NORTHWESTERN UNIVERSITY

Ordering of DNA-Coated Colloids in Concentrated Electrolytes: X-ray Scattering Studies

A DISSERTATION

SUBMITTED TO THE GRADUATE SCHOOL
IN PARTIAL FULFILLMENT OF THE REQUIREMENTS

for the degree

DOCTOR OF PHILOSOPHY

Field of Materials Science and Engineering

By

Roger J.E. Reinertsen

EVASTON, ILLINOIS

June 2024

Abstract

Liquid electrolytes lie at the heart of a plethora of critical technologies and mediate the biochemical processes that underpin life. Despite this ubiquity, comprehensive descriptions of these materials remain elusive, owing to the complex interplay between collective short-and-long ranged interactions governing ions and solvent molecules. Interactions between highly charged macromolecules and concentrated electrolytes are particularly challenging, as the distributions of mobile ions are necessarily dictated by a combination of the electric fields of the macromolecular surface and those of neighboring ions. Model experimental systems are necessary to detect both the presence and functional significance of such "ion-ion correlations" in high-salt conditions. To address this need, this thesis investigates the assembly DNA-grafted nanoparticles in concentrated aqueous salt solutions, with the goal of elucidating the relationships between the molecular-scale interactions within the electrolyte to the mesoscopic responses of the highly charged nanoscale probes. Experimental measurements, including X-ray, neutron, and visible light scattering, are combined with molecular dynamic simulations to achieve a rigorous description of this system across a wide range of length scales. Of particular interest are attractive forces between DNA molecules manifested by divalent cations, which induce the formation of colloidal crystals; these ion-driven forces evolve considerably as salt concentration is elevated, resulting in considerable structural evolution of the nanoparticle assemblies. The influences of macromolecular solvation and ion-ion correlations are deduced, and these understandings are utilized to characterize more complex systems, such as mixtures of salts and temperature-varying conditions. These results serve to inform future theories of electrolytes and outline phenomena pertinent to biology and nanotechnology.

Acknowledgments

I would like to begin with thanking my advisor Professor Michael Bedzyk; learning to "think in reciprocal space" as a member of his research group during my graduate career has been a privilege. I would also like to thank rest of my committee, including Professor Monica Olvera de la Cruz, Kenneth Shull, Pulak Dutta, and Sumit Kewalramani. I must particularly emphasize my gratitude to Dr. Kewalramani, who has been an excellent mentor.

I want to also acknowledge the collaborators I have worked with along the way. I thank members of the Olvera de la Cruz group at Northwestern, in particularly Dr. Felipe Felipe Jiménez-Ángeles, who was willing to design simulations for the challenging systems that I've worked with. I must also thank the various beamline scientists who have helped make the experiments in this thesis possible, beginning with Dr. Steven Weigand of Sector 5-ID-D of the APS, who conducted scattering measurements for this work when general user access was not permitted on site. I also thank Dr. Soenke Seifert of Sector 12 of the APS, Dr. Wellington Leite of Oak Ridge National Lab, and Dr. Richard Gillilan and Dr. Qingqui Huang of the Cornell High Energy Photon Source.

I thank various current and former members of the Mirkin group at Northwestern, who have helped me with DNA synthesis and nanoparticle functionalization, including Robert Stawicki, Jennifer Delgado, Vinzenz Mayer, Alexa Wong, Dr. Tanushri Sengupta, Dr. Kaitlin Landy, Dr. Matthew Vasher, and Dr. Heather Calcaterra.

I'm very grateful for the current and former members of my research group that have been my friends and mentors, including Dr. Elise Goldfine, Dr. Joseph McCourt, Dr. Carlos Torres, David Garcia-Wetten, Amol Agarwal, Dan Duplessis, Dr. Anusheela Das, Dr. Yanna

Chen, Dr. Katherine Harmon, Dr. V. L. V. Narayanachari (Achari) Kondapalli, and Dr. Guennadi Evmenenko. I also thank Tanvi Panchumarthy and Paula Lee for the research they conducted during the summer 2023 SHyNE REU; it was a pleasure to be your mentor,

Finally, I would really like to express my deepest gratitude to the rest of my family and friends, who helped support me during this time. Regardless of where in the country you all are, your love and assurance have kept me going. And to person who has been by my side throughout this whole experience, my girlfriend Lele Mathis, I thank you from the bottom of my heart.

List of Terms and Abbreviations

[X]	Denotes molar concentration of species X (mol/liter)
APS	Advanced Photon Source
AuNP	Gold (Au) Nanoparticle
BCC	Body-Centered Cubic
CHESS	Cornell High-Energy Synchrotron Source
CPG	Controlled Pore Glass
DH	Debye-Hückel
DI	Deionized
DMTO	4,4'-dimethoxytrityl
DNA	Deoxyribonucleic Acid
DNA-NP	DNA-coated Nanoparticle
DND-CAT	DuPont-Northwestern-Dow Collaborative Access Team
D_{nn}	Nearest Neighbor Distance
DTT	Dithiothreitol
FCC	Face-centered Cubic
ID	Insertion Device
HFIR	High Flux Isotope Reactor
MALDI-TOF	Matrix-Assisted Laser Desorption/Ionization-Time of Flight
MAXS	Medium-Angle X-ray Scattering
MD	Molecular Dynamics
MS	Mass Spectrometry
NTE	Negative Thermal Expansion
OD	Optical Density
PB	Poisson-Boltzmann
ORNL	Oak Ridge National Lab
$\boldsymbol{q}$	Scattering Vector
q	Magnitude of scattering vector
RCF	Relative Centrifugal Force
RCP	Random Close Packed
RP-HPLC	Reverse-Phase High Performance Liquid Chromatography
RPM	Revolutions per Minute
SANS	Small-Angle Neutron Scattering
SAXS	Small-Angle X-ray Scattering
SLD	Scattering Length Density
T35	Oligonucleotide consisting of 35 Thymine nucleotides
TCEP	tris(2-carboxyethyl)phosphine
UV-Vis	Ultraviolet-Visible Spectroscopy
WAXS	Wide-Angle X-ray Scattering

Dedicated to my cousin and godfather, Glenn Grossarth

Table of Contents

List of Figures

List of Tables

Chapter 1: Introduction

The interactions of charged surfaces and macromolecules with solutions of mobile ions are of eminent importance to the properties of a wide range of material classes. In particular, interfaces with highly concentrated electrolytes are directly pertinent to a variety of technical applications. For example, controlling charge carrier migration in such systems is critical to developing reliable supercapacitors[1] and batteries[2] for energy storage. The salinity of subsurface brine deposits modifies the solubility of CO_2[3] and organic contaminants[4] , thus determining the suitability of such reservoirs for carbon capture and storage and for establishing potential groundwater contamination risks. Salt-dependent solubility changes are fundamental to many chemical[5] and biological[6] separation processes. The stabilization of inorganic colloidal particles in molten salts opens up new synthetic routes for quantum dots and other light-converting systems[7, 8]. Polyelectrolyte-based coatings can be used to enhance emulsion-based oil recovery from brine[9] or instill antimicrobial properties in wound dressings, which interface with complex biological solutions[10]. Additionally, many open questions exist concerning the biochemistry of extremophilic organisms that thrive at high salinities (dubbed halophiles[11] or chaophiles[12]), which efficiently carry out biological processes in environments where most proteins are expected to be denatured; the presence of high charge densities in the proteomes of these organisms[13, 14] suggest a utilization of electrostatic interactions, an understanding of which could enable the development of new enzymatic or biomimetic industrial processes.

However, the manifestations of electrostatic forces in such dense, multicomponent systems are complicated by surface charges, ions, and dielectric constants varying in correlated manners on comparable length scales[15]. Even in “simple” aqueous solutions of monovalent salts, arrangements of charged boundaries[16] and ions[17] can promote counterintuitive phenomena such

as attractions between like charges. In a biological context, various functionalities of anionic, gene-encoding DNA molecules result from interactions with the ionic environment; distributions of multivalent cations dynamically regulate the condensation state and topology of nucleic acids[18], and lower-valency ions tune the binding and activity of DNA-affiliated enzymes[19]. DNA also retains functionality in organisms with remarkably high intracellular ionic strengths[13]. Salts also influence the performance of DNA arrays in biochips,[20] the efficiency of nanopore genome sequencing[21] , and the stability of DNA for information storage[22]. By thoroughly characterizing the interactions of nucleic acids with a diverse range of ionic environments, models for electrolyte behavior, as well as DNA-based technologies, can be refined.

This thesis aims to characterize the structure and assembly of highly charged macromolecules in a wide variety of electrolyte of types and concentrations, and to elucidate the relationship between electrolyte properties and apparent electrostatic intermolecular forces. More specifically, gold nanoparticles grafted with high densities of DNA are utilized (DNA-AuNPs), as the high negative charge of the DNA results in a large electrostatic contribution to inter-particle interactions, and the gold nanoparticle cores interact strongly with X-ray and visible photons, providing multiple useful signals for characterizing suspensions and assemblies of these conjugates. A myriad of charge-driven interactions is uncovered, with particular emphasis placed on attractive interactions between DNA-NPs resulting from divalent cations in solution; these forces are found to evolve throughout the full accessible range of salt concentrations (ranging from dilute to saturated solution), actuating a variety of responses in DNA-AuNP assemblies including phase transitions, contraction, and expansion. This evolution is connected to experimentally measured correlations between electrolyte ions within the bulk electrolyte, as well as to the role of solvent ions in tuning macromolecular solubility and said ion-ion

correlations. Interpretation of the results of these experiments are aided by complementary Molecular Dynamics (MD) simulations conducted by collaborators at Northwestern. The findings from these studies are utilized to explain a number of additional counterintuitive phenomena discovered in the DNA-AuNP-electrolyte system, demonstrating the significance of these effects in additional contexts. These explorations of electrostatic forces in extreme ionic conditions should allow for appraisal of existing theories for the behavior of these complicated fluids, and elucidate the properties of grafted DNA in a wide variety of solution environments, potentially informing the design of novel, stimuli-responsive materials.

To conclude the introduction, the structure of the thesis will be briefly summarized. Chapter 2 serves as an overview to the classical models for electrolytes, as well as a review of work highlighting the apparent complexity of concentrated electrolytes. Summaries of pertinent terminology and phenomena are also provided, in addition to background on DNA and DNA-NPs. Chapter 3 introduces methods utilized to synthesize and characterize DNA-NP suspensions and summarizes the X-ray and neutron scattering techniques that serve as the experimental backbone of this work. Chapter 4 studies the assembly of DNA-NPs in solutions of alkaline earth chlorides, utilizing a combination of small-and-wide angle X-ray scattering (SAXS, WAXS) and coarse-grained MD simulations to demonstrate how ion-ion correlations present at high salt concentrations reverse the effect of added salt on lattice swelling. Chapter 5 combines SAXS and small-angle neutron scattering (SANS) measurements with all-atom MD simulations to reach a molecular-level description of how the competition between macromolecular hydration and Ca^{2+} binding determines the crystal structure (FCC or BCC) of the DNA-NP assemblies. Chapter 6 extends these investigations to solutions containing mixtures of salts of monovalent and divalent salts, demonstrating how the effects uncovered in this thesis lead to variations in apparent

competition and cooperation between different cations. Chapter 7 applies the obtained understandings to apparent novel thermal responses of DNA-NP structures, including tunable thermal expansion coefficients and melting transitions. Chapter 8 tests the generality of the findings detailed in prior chapters to particles functionalized with oligonucleotides of varied length and base composition. Chapter 9 summarizes preliminary investigations into the effects of additional salts, including attempts to resolve repulsive interactions in solutions of monovalent cations, as well as efforts to interrogate the influence of anion identity or cation valency. Chapter 10 serves as a summary of the thesis, and outlines directions for additional experiments.

Chapter 2: Background

2.1. Electrostatics in Liquid Electrolytes

2.1.1. Classical Electrolyte Theories

Within a liquid of high dielectric permittivity, ionization reactions lead to the disassociation of compounds into ionic constituents. The ions present in these solutions are mobile charge carriers capable of responding to internal and applied electric fields. As a result, the manifestation of electrostatic forces may differ dramatically from vacuum conditions. In the classical Debye-Hückel theory [23], a mean-field approach is utilized; the distribution of ions in the solution are presumed to follow a Boltzmann distribution, controlled by the mean electrostatic potential near a given charge. This results in the "Poisson-Boltzmann" equation for a solution:

$$\nabla^2\Phi(\boldsymbol{r}) = -\frac{\rho(\boldsymbol{r})}{\epsilon} = -\frac{\sum c_i z_i e^{-\frac{z_i e\Phi(r)}{k_B T}}}{\epsilon} \quad \textbf{(2.1)}$$

With $\Phi(r)$ representing the electric potential at position $\boldsymbol{r}$, $\rho(\boldsymbol{r})$ the charge density, ε dielectric constant of the solution (here presumed to spatially invariant), c_i and z_i the concentration and valency of a given ion, respectively. of vacuum and the medium, respectively, k_B the Boltzmann constant, T the solution temperature, and e the elementary charge. Analysis of a linearized version of this equation valid at low potentials yields the form:

$$\nabla^2\Phi(\boldsymbol{r}) = \frac{\Phi(\boldsymbol{r})}{\lambda_D^2} \quad \textbf{(2.2)}$$

which predicts that, from a given charge, the electrostatic potential and distribution of oppositely charged ions decay as exponential functions of the Debye screening length (λ_D), defined as

$$\lambda_{\mathrm{D}} = \sqrt{\frac{\epsilon_r \epsilon_0 k_B T}{\sum_{\mathrm{i}} \mathrm{c_i} \mathrm{z_i^2} \mathrm{e}^2}} = \sqrt{\frac{1}{4\pi L_B I}}$$

(2.3)

With ε_0 and ε_r representing the dielectric constant of vacuum and the medium, respectively. L_{b} is the Bjerrum length, which corresponds to a separation at which the electrostatic energy between two elementary charges approaches the thermal energy, and I is ionic strength, which is a sum of the concentrations of all charged components in the electrolyte multiplied by the square of their valency. Such an approach has proven to be a tremendously useful approach to analyzing freezing points[23], the formation of electrical double layers at charged interfaces[24], and the activity of dilute electrolytes via the Debye–Hückel limiting law[25]:

$$\log \gamma_{\pm} \sim \frac{-e^2 |z_-||z_+|}{\lambda_D 8\pi \epsilon_r \epsilon_0 k_B T}$$

(2.4)

The Debye–Hückel theory is also employed in the DLVO (Derjaguin, Landau, Verwey and Overbeek) theory for the stability of charged colloidal particles, which successfully predicts that the addition of electrolytes can drive the precipitation of charged macromilecules.[26]. More rigorous approaches, based on statistical mechanical analysis of liquids find results similar to the Debye-Hückel theory in the dilute case, namely exponentially decaying charge-correlations [27-29]. However, these more rigorous approaches also predict a crossover to damped oscillatory interactions when the value of the Debye length approaches the diameter of ions in the system [27-29]. Results from classical, Poisson-Boltzmann-based approaches [30, 31], and those derived from liquid state theory [32-34] have been extended to the case of electrolytes with asymmetric size and charges.

2.1.2. Underscreening and Ion Correlation Effects

Interestingly a series of surface force apparatus (SFA) studies recorded long-range (1-10 nm) electrostatic repulsions in concentrated monovalent electrolyte solutions and room temperature ionic liquids [35-38]. Interactions between the surfaces in these studies were found to be exponentially decaying, with characteristic decay lengths substantially higher than the calculated Debye lengths for these solutions. Furthermore, for a variety of electrolytes, this "screening length" was found to increase with added salt according to:[38-40]:

$$\lambda_S \sim a^3 I L_B = a^3 I \frac{e^2}{4\pi\epsilon_r\epsilon_0 k_B T} \quad \textbf{(2.5)}$$

Where *a* represents the average unhydrated radius of the ion, and the other quantities have their usual meanings. At low salt concentrations, repulsions decayed with the classical Debye length; the crossover to the region governed by **Equation 2.5** occurs when the Debye length approaches the ionic radius. The observed scaling was rationalized with a mechanism where the potential imposed on an ion by neighboring ions is great enough to impair mobility; as a result, the effective concentration of ions free to screen electrostatic forces is lowered [39, 40].

As the aforementioned SFA measurements require nanometric confinement of liquid films between surfaces, it is unclear whether these results describe behavior of bulk electrolytes. Qualitatively similar results have been recorded indirectly, based on fluorescence measurements of the surface excess of anionic dye in concentrated alkali halide solutions confined between silica; however, the observed decay lengths scaled differently with ion size [41].While long screening lengths were recorded by colloidal probe atomic force microscopy (AFM) measurements in neat ethylammonium nitrate (EAN), they were only present at elevated

temperature, which quantitatively conflicts with the observed scaling in **Equation 2.5** [42]. Primitive model [43, 44] or all-atom [45-47] molecular dynamics simulations have demonstrated decaying oscillatory forces which increase with salt concentration, but of significantly shorter range. Additional experimental evaluations of the effective range of electrostatic forces in concentrated electrolytes are needed in order to resolve the present ambiguity. Additionally, a systematic investigation into salts of higher, or mixed, valency has not yet been conducted.

2.2. Solubility in Electrolytes: Salting-Out

Generally, the presence of dissolved ions in water modifies the solubility of other solutes (or the stability of suspended colloidal particles). For example, solubility constants of gasses in liquids (as defined in Henry's Law, $C_{gas} = HP_{gas}$) can be related to solution ionic strength through the empirical Sechenov (or Setschenow) Equation[48]:

$$\log\frac{H}{H_o} = k_s b_s \qquad \textbf{(2.6)}$$

Where H represents the Henry's Law coefficient for the gas (directly relating concentration in solution to partial pressure above the liquid), H0 represents this quantity in pure water, b represents the molal concentration of salt in solution, and ks is an experimentally determined coefficient, typically negative in sign. These findings can be generalized to nonvolatile solvent types by modifying the empirical equation to reflect activity coefficients (and thus solubility):

$$\log\frac{\gamma_0}{\gamma} = \log\frac{S}{S_0} = K_s C_s \qquad \textbf{(2.7)}$$

Where gamma denotes the activity coefficient of the solute and S the solubility, with subscript $_0$ denoting values in pure water, C_s the solution molar salt concentration, and Ks a generally positive coefficient. Intriguingly, this empirical equation accurately describes the dependence of a large number of neutral solutes of salinity[48], including complex macromolecules such as proteins at high ionic strengths; in the context of protein solubility, this relationship is often referred to as the Cohn equation[49].

While **Equation 2.7** is broadly applicable, its empirical nature limits its predictive power, and does not necessarily provide a complete description of the system. For example, different salts (which generally increases the surface tension of water) are experimentally found to either increase ("salting in") or decrease ("salting out") protein solubility, as described by Hofmeister[50]. These effects have been rationalized in various ways. One model postulates that the effect of salts on the bulk water either serves to strengthen (kosmotropes) or weaken its hydrogen bond structure (chaotropic), in turn increasing or decreasing the energetic cost of accommodating a solute or macromolecule[51, 52]. Others argue that repulsive interactions between electrolyte ions and image charges within the region of reduced permittivity formed by most solutes leads to "salting out" [53]. Many recent explanations highlight the significance of the specific chemical details of macromolecular surfaces [54]. Finally, recent work highlights the significance of apparent clustering between electrolyte ions, leading to attractive "depletion-type" forces that can drive colloid precipitation[17], "Salting out" and "ion-specific" effects remain areas of controversy and active research[55, 56].

The complexity of a macromolecule's response to salt concentration extends beyond the dependence on ionic type. Many proteins, such as hemoglobin, have solubilities that depend non-monotonically on the concentrations of certain salts[57]. More specifically, such proteins are

rendered more soluble by a modest increase in ionic strength (typically up to 0.5 M) but are "salted out" at higher concentration. Green successfully described this behavior by adding a term of Debye-Hückel type (**Eq. 2.1-2.4**) to **Equation 2.7**[57]:

$$\log \frac{S}{S_0} = K_i \sqrt{C_s} - K_s C_s \quad \textbf{(2.8)}$$

Where Ki and Ks are positive salting-in and salting-out coefficients. Green found Ki to be invariant on the identity of the salt used, suggesting that the "salting-in" term arises from attractive electrostatic interactions described satisfactorily by Debye-Hückel theory. The applicability of this equation to zwitterionic (containing both positively and negatively charged groups) proteins suggest that attractive intermolecular interactions are significant, even when the charge of a protein is net neutral (as is true at the so-called isoelectric point)[58]. Thus, any complete picture of the salt-dependence of charged macromolecule solubility needs to account for interactions between regions of varied charge (sometimes referred to as "patches")[59].

2.3. Polyelectrolyte Brushes

The DNA-AuNPs that will be utilized in this study are spherical polyelectrolyte brushes[60]. When polyelectrolyte chains are grafted onto a substrate, steric hindrance and electrostatic repulsion modify the conformation of the "brush"; these repulsive interactions drive extension of the polyelectrolyte chains at the expense of chain entropy. Increasing solution salt concentration modifies the phase behavior of dense brushes, driving transitions into the "salted-brush" regime, where brush height decreases as $I^{1/3}$, and eventually the "quasi-neutral" regime, where neutralized, collapsed brushes become insensitive to added salt [61, 62]. The presence of

multivalent ions can complicate this behavior, potentially introducing bridging attractions between chains [63-65].

The grafting of chains onto a spherical substrate, or "core", substantially modifies brush behavior. The curvature of these "spherical polyelectrolyte brushes" results in the accessible volume for grafted strands increasing further from the core. Gel electrophoresis measurements on 10nm DNA-AuNPs reflect this: at low salt, the 30 bases nearest the core are fully extended, with subsequent segments of the polymer adopting random coil geometries [66]. Such effects are included in the modified Daoud-Cotton (mDC) model [67, 68]:

$$\left(\frac{t}{R_c}+1\right)^{5/3} = 1 + \frac{kNl_k}{R_c}\left(\frac{v\,\sigma}{l_k}\right)^{1/3} \quad \textbf{(2.9)}$$

where t represents brush height, R_c the radius of the core, k a constant on the order of unity, l_k the electrostatic Kuhn length, N the number of repeat units, v the excluded volume, and σ the grafting density. Though approaches vary [62, 69, 70], the ratio of the excluded volume to Kuhn length is typically calculated as scaling as a positive power of the electrostatic screening length, preserving the prediction that added salt condenses the brush. It should be noted that more complex models for these systems have been proposed, which predict inhomogeneous extension of polyelectrolyte chains [71] .

Many existing experimental studies on spherical polyelectrolyte brushes utilize adsorption or grafting of polyelectrolytes onto polymer cores; the generalization of these results to DNA-AuNPs is unclear, as such structures tend to have lower grafting densities (~0.01 strand per nm^2) and larger sizes (~100nm)[60, 67, 68, 72-74]. Diblock copolymer micelles consisting of hydrophobic cores and polyelectrolyte shells can exhibit comparable dimensions (determined by

aggregation number and degree of polymerization) [75-77]; however, the reliance on hydrophobic forces to stabilize the micelle structure may prohibit compatibility with solvents of widely varying ionic strength and dielectric constant [78]. Empirical extensions of the mDC have been applied to DNA-AuNPs [79, 80], or nanoparticles with sulfonated polyelectrolyte shells [81]. However, quantitative assessment of DNA brush height in highly concentrated electrolytes has not yet been conducted.

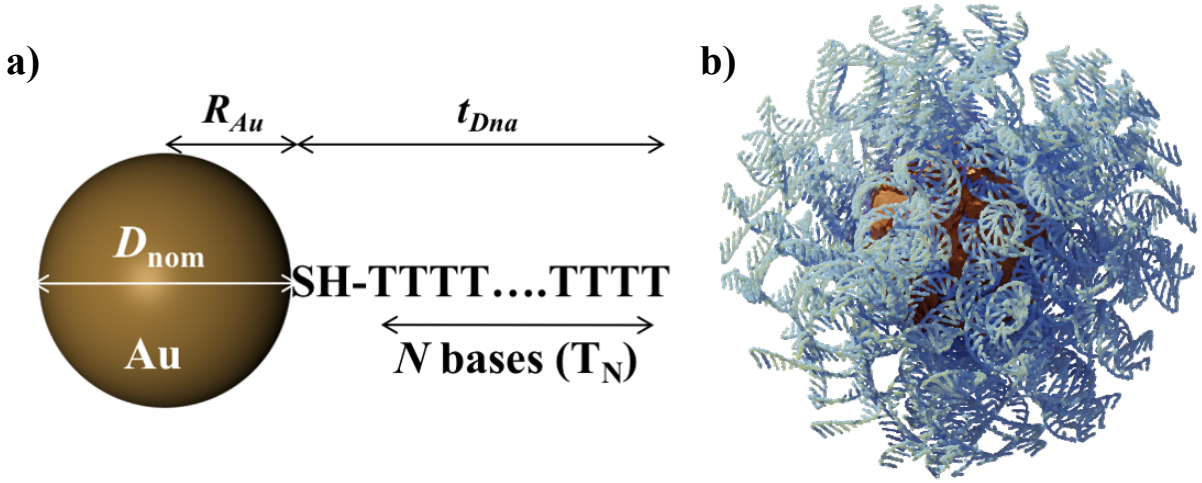

Figure 2.1: (a) A schematic representation of a AuNP functionalized with variable lengths of DNA. *N* denotes the number of thymine bases in the sequence. A thiolated linker tethers the oligonucleotide to the gold surface. (b) A cartoon render of the DNA-AuNP structure functionalized with many DNA molecules. The high grafting density drives the extension of the DNA shell.

2.4. DNA-NPs: Structure and Ionic Interactions

One method for probing electrostatic forces in the solution bulk is to study the ordering of highly charged objects resulting from coupling to their ionic environment. In particular, gold nanoparticles coated with DNA represent suitable candidates; DNA is a strongly anionic polyelectrolyte (containing highly acidic phosphate groups along its backbone), and thiolated DNA strands can be grafted with high coverage (on the order of 10 molecules per nm^2) on curved gold surfaces [82], resulting in nanoparticles with high net charge density. Additionally,

monodisperse populations of DNA molecules can be synthesized via solid-state support synthesis, permitting a high degree of structural control. The properties of these DNA-AuNPs are well-characterized, owing to their frequent utilization in nanotechnological applications. Many of these applications capitalize on the capacity of DNA to exhibit sequence-specific base-pairing interactions with other DNA molecules; such approaches permit the detection of DNA oligomers [83], the assembly of colloidal crystals [84], and even the detection of trace quantities of transition metal ions, such as Hg^{2+}[85]. While these base-base interactions are of great technical relevance, they may confound the exploration of general electrostatic behavior; thus, particles functionalized with oligomers consisting of one base should be utilized. **Figure 2.1** demonstrates a schematic representation of such particles, portraying a particle functionalized with thymidine homopolymers of variable degree of polymerization *N*; of all standard bases, poly-dT sequences deposit in the highest density on gold surfaces [86].

The behavior of DNA-functionalized nanoparticles has been explored in a variety of ionic environments, which will be summarized briefly. Heavy Ion Replacement SAXS and Anomalous SAXS have demonstrated that the environment surrounding the DNA shell is highly enriched in cations [87, 88]. Particles with single-stranded DNA shells of insufficient length and loading density precipitate at high ionic strength, likely due to insufficient electrostatic stabilization [86, 89]. In colloidal lattices formed via base-pairing interactions, the addition of monovalent, divalent, and trivalent ions induces contraction of bridging DNA, with this behavior being ascribed to the screening of electrostatic repulsions [90]. Particles functionalized with double-stranded DNA precipitate in high salt concentrations; this “blunt-end attraction” requires the presence of a terminal base-pair and is thought to be mediated by hydrophobic and base-stacking interactions

[91], rather than electrostatic forces. Considering the results summarized thus far, particles functionalized with high densities of single-stranded, homopolymer DNA sequences are the best candidate for isolating the influence of electrostatic forces. Interestingly, the presence of divalent alkaline earth cations drive the formation of 2D [79, 92]and 3D [93]; colloidal crystals from DNA-AuNPs functionalized with homogenous oligo-dT sequences. 2D Gibbs monolayers of nanoparticles at the liquid-vapor interface could be achieved at concentrations of Mg^{2+} between 5 and 800 mM [79, 92] and at concentrations of Ca^{2+} between 5 and 50 mM [92]. Concentrations of Ca^{2+} greater than 300mM drive the formation of 3D assemblies [93]. Since such crystallization is mediated by the distribution of divalent ions in solution, it should be sensitive to the properties of the bulk electrolyte, such as the electrostatic screening length. A systematic study on attractions and repulsions between DNA-AuNPs with single-stranded oligo-dT molecules in highly concentrated solutions of monovalent and divalent electrolytes would thus yield insight into the electrostatic properties of these solutions.

Chapter 3: Experimental Methods

This chapter provides a brief overview of the experimental methods utilized in this thesis. Detailed experimental procedures are given in the corresponding chapters.

3.1. DNA-NP Synthesis

DNA-coated gold nanoparticles (DNA-NPs) were synthesized using established methods[94] which will be summarized here. DNA can be attached to gold surfaces via a strong bond between Au and S. Thus, oligonucleotides terminated on the 3' side with thiol groups is were synthesized using phosphoramidite chemistry with a MerMade solid-state controlled pore glass (CPG) DNA synthesizer. The work in Chapters 4-7 makes use of a sequence consisting entirely of 35 thymine nucleotides. Following synthesis, the DNA is separated from the pore glass via aqueous methylamine and NH_4OH and purified via reverse-phase high-performance liquid chromatography. Successfully synthesized olignucleotides are capped with 5'-Dimethoxytrityl (DMT) groups, enabling separation from prematurely truncated strands. The DMT group is removed via reaction with acetic acid and liquid-liquid extracionn with ethyl acetate. Oligonucleotides are then lyophilized, before being re-dispersed in deionized water to enable determination of yield by UV-Vis spectrophotometry, and purity by matrix-assisted laser desorption/ionization mass spectrometry (MALDI).

In preparation for grafting onto AuNPs, the terminal thiol groups of the oligonucleotides are reduced with dithiothreitol (DTT) or tris(2-carboxyethyl)phosphine (TCEP), and purified utilizing Cytiva NAP Sephadex™ G-25 DNA grade gel columns. To begin functionalization, small quantities of Tween 20 detergent are added to 10 nm AuNPs (purchased from Ted Pella), followed by the reduced oligonucleotides. The mixture is stirred and allowed to incubate

overnight. The following day, DNA loading is increased via the addition of sodium chloride (NaCl) and sodium dodecyl sulfate (SDS); the NaCl concentration is increased in 0.1 M increments every 30-60 minutes, until a final concentration of 1 M NaCl is attained. At this point, excess SDS, free DNA, and NaCl are removed through centrifugal filtration with 50 or 100 kDa Amicon spin filters. The DNA-NPs are then removed from the filters and dispersed in 0.02% SDS, before being transferred to DI water through 4 rounds of centrifugation in 1.5 mL tubes. Upon completion of the final centrifugation process, the supernatant above the highly concentrated DNA-NP suspensions is removed, enabling the storage (4° C) of DNA-NPs as highly concentrated stocks. Suspension concentrations can be determined by UV-Vis spectrophotometry (see below), and the average number of DNA per AuNP ca be determined by Oligreen Assay.

3.2. X-ray Scattering Methods

X-rays, or photons of wavelength between 10^{-2} and 10^{2} nm, are highly useful tools for investigating the structure of materials at the atomic and nanometric scale. While a wide variety of techniques have been developed based on the elastic and inelastic scattering of X-rays by matter, the primary characterization techniques utilized in this work are based on the elastic scattering of monochromatic X-rays beams by liquid solutions and colloidal suspensions. In such experiments, the measured quantity will be the intensity of scattered X-rays in various directions; the directional relationship between the incident X-ray beam and scattered radiation is quantified by the scattering vector, $\boldsymbol{q}$:

$$\boldsymbol{q} = \boldsymbol{k_s} - \boldsymbol{k_i} \qquad \textbf{(3.1)}$$

where k_s denotes the wavevector of the scattered X-rays, and k_i that of the incident X-rays. In an elastic scattering process, the X-ray energy (and thus wavelength and magnitudes of wave vectors) does not change. The magnitude of q can thus be calculated as:

$$q = |\boldsymbol{q}| = |\boldsymbol{k_s} - \boldsymbol{k_i}| = |\boldsymbol{k_i}| 2\sin\theta = \frac{4\pi}{\lambda}\sin\theta \quad \textbf{(3.2)}$$

where θ is half the scattering angle (2θ), and λ the X-ray wavelength. Such scattering processes are highly useful for deducing the distances between components scattering from the sample, whether they be atoms or nanoparticles. The length scale of the separations being probed by these experiments can be approximated as:

$$d \sim \frac{2\pi}{q} \quad \textbf{(3.3)}$$

This relationship serves to emphasize two considerations: that larger values of q correspond to smaller separations within the sample, and that information about relative positions can be obtained for wide variety of length scales by measuring scattering over a wide angular range. **Figure 3.1** details the instrument setup of beamline 5-ID-D of the Advanced Photon Source (APS), which utilizes three area detectors positioned at various distances from the sample in order to investigate a wide range of length scales simultaneously [95]. As the goals of this thesis include relating the characteristics of electrolytes (which tend to manifest at length scales below 5 nm, detectable by WAXS) to the ordering of nanoparticles (which can range from 10-1000 nm, detectable by SAXS), this instrument is an invaluable tool and is used for the majority of X-ray scattering measurements in this work.

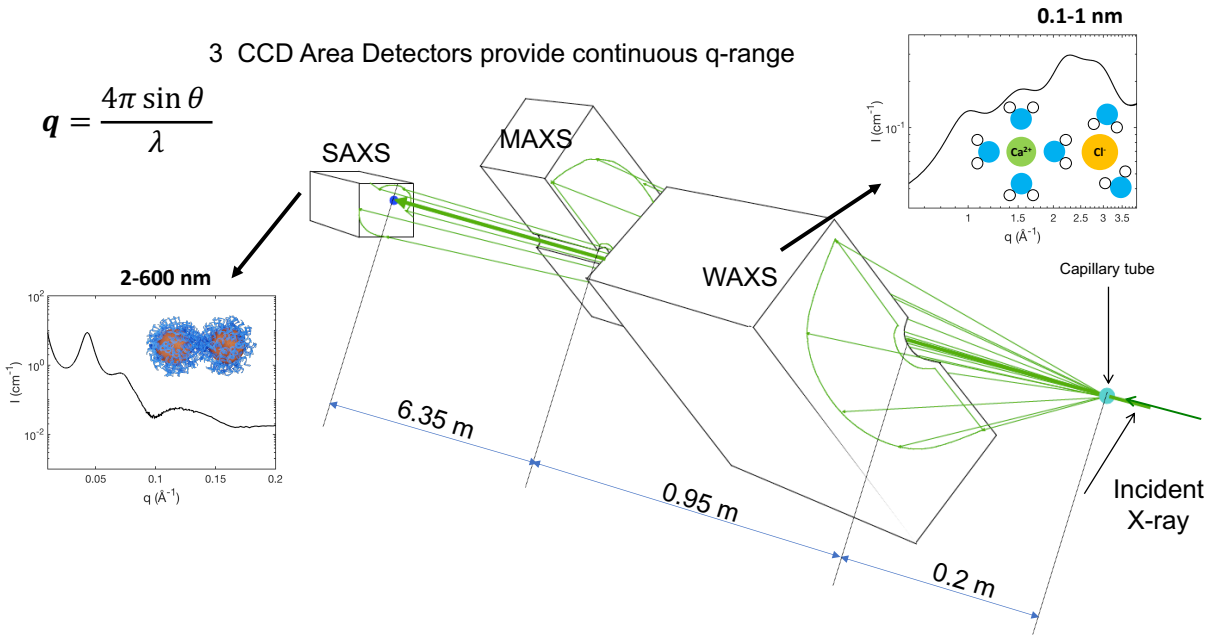

Figure 3.1: An example SAXS/MAXS/WAXS setup (Beamline 5-ID-D of the APS). By utilizing multiple detectors, positional information on length scales from 1.26Å to 6200Å can be collected simultaneously. Representative SAXS and WAXS data of a DNA-AuNP assembly and an electrolyte are shown. The observed SAXS scattering is the product of a gold-nanoparticle form factor and a lattice structure factor, while the WAXS scattering arises from positional correlations of ions and solvent molecules.

Because SAXS probes separations on the 10-1000 nm scale, X-rays are typically modeled as scattering from continuous distributions of matter, rather than discrete atoms. More specifically, since X-rays scatter from electrons, colloidal objects studied with SAXS are modeled as spatial distributions of electron density (or more generally, scattering length density). The scattering amplitude from an isolated nanoscale object can thus be computed as:

$$F(\boldsymbol{q}) = r_e \int_{V_p} \rho(\boldsymbol{r}) e^{(i\boldsymbol{q}\cdot\boldsymbol{r})} dV \qquad \textbf{(3.4)}$$

where the scattering amplitude, F(q) is often labeled the form factor of the object, r_e is the classical electron radius, and V_p denotes the volume of the nanoscale object, which serves as the bound of the integration. To provide a pertinent example, the form factor for a spherical particle of homogenous electron density, ρ_p, and radius R_p can be written as:

$$F(q) = r_e \int_{V_p} \rho(\boldsymbol{r}) e^{(i\boldsymbol{q}\cdot\boldsymbol{r})} dV = r_e \rho_p \int_0^{R_p} \frac{sinqr}{qr} 4\pi r^2 dr = \frac{4\pi r_e \rho_p}{q^3} [\sin qR_p - qR_p \cos qR_p]$$

(3.5)

Note that the form factor of a spherically symmetric object depends only on the magnitude of the scattering vector.

In a typical solution SAXS experiment, scattered intensity is recorded from nanoscale objects dispersed in a solvent (with electron density ρ_s) at a large number of angles; for dilute objects with homogenous electron density (e.g., AuNPs), the scattered intensity, I(q), measured can be written as:

$$I(q) = \frac{N}{V_{samp}} \left(\rho_p - \rho_s\right)^2 \langle F(\boldsymbol{q}) F^*(\boldsymbol{q}) \rangle = \frac{N}{V_{samp}} \Delta\rho^2 \langle |F(\boldsymbol{q})|^2 \rangle$$

(3.6)

where N denotes the number of nanoscale objects and V_{samp} the total sample volume. Angle brackets denote orientational averaging of the form factor, which leads to scattered intensity only depending on the scattering vector magnitude. Thus, it is typical to represent data collected with area detectors as azimuthal averages in for solution SAXS experiments; such data is typically plotted as 1D, averaged profiles of Intensity versus scattering vector magnitude q.

The present work concerns interactions between nanoscale objects, which introduce additional components to the scattered intensity. Since AuNPs (and DNA-AuNPs) are

approximately spherically symmetric, the formula for scattered intensity can be modified in this case as:

$$I(q) = \frac{N}{V_{samp}} \left(\rho_p - \rho_s\right)^2 |F(q)|^2 S(q)$$

(3.7)

where a term, S(q), known as a structure factor, has been introduced. Note that this equation only holds if any ordered structures of nanoparticles are dispersed orientationally randomly in solution. Preferential ordering of such structures would necessitate weighted orientational averaging of S(**q**) and introduce apparent azimuthal anisotropy in I(**q**). Generally, SAXS patterns associated with DNA-NP structures in this work are found to be radially symmetric, suggesting that these structures are well-distributed, and warranting analysis in terms of orientally averaged structure factors, succinctly denoted *S(q)*.

The term S(q) arises from constructive and destructive interference between X-rays scattered from different nanoscale objects within a sample, resulting in intensity modulations. These modulations can be related to the distribution of objects in an isotropic sample as:

$$S(q) = \frac{4\pi}{q} \int_0^\infty r\left[\mathrm{P}_p(r) - \bar{\mathrm{P}}\right] \sin qr \, dr$$

(3.8)

Where $P_p(r)$ denotes the number concentration of objects in a spherical shell distance r from the origin, and P the average concentration of objects within the sample. When positional correlations between objects become particularly strong, as is the case of a colloidal crystal, sharp peaks (known as “diffraction peaks”) manifest in the structure factor. If said correlations are weak or occur over a range of length scales (as in a disordered aggregate of nanoparticles), only low-intensity and/or broad diffraction peaks manifest in the structure factor.

3.3. Neutron Scattering Methods

As shown in **Equation 3.6** and **3.7**, signal in a small-angle scattering experiment depends on the contrast in scattering length density between the nanoscale object and the surrounding medium. For X-ray scattering experiments, scattering length density (SLD) is proportional to the electron density of a material. Considering the DNA-AuNP utilized in the present work, it is apparent that the electron density of elemental gold is an order of magnitude greater than both water and DNA (see Table 2). Thus, the intensity of scattered X-rays from the gold nanoparticle cores is dramatically higher than that of the "shell" of DNA ligands; this asymmetry is so pronounced that the scattering from the DNA shell is essentially negligible in most solution SAXS data concerning DNA-NPs. While this simplifies analysis, ensuring that a spherical gold particle represents a sufficient model for the DNA-AuNP form factor, it also means that information concerning the structure of the grafted DNA (e.g., radial extent) can only be deduced indirectly by SAXS experiments, if determinable at all.

In addition to the X-ray photon, the neutron also represents a highly useful tool for studying the properties of matter at the atomistic or nanometric scale. Because neutrons have comparable wavelengths to X-rays, and also interact weakly with matter, most of the formalisms described in the previous section can be applied to the elastic scattering of neutrons, in particular small-angle neutron scattering (SANS). The primary distinction between the techniques becomes apparent when considering the physical origin of neutron scattering; whereas X-rays scatter from electrons surrounding nuclei via the electromagnetic interaction, neutrons scatter from nuclei via the strong force. The very short range of this interaction (10^{-15} m) results in apparent q-independence of a neutron scattered from an isolated nucleus (that is, the scattered neutron taking the form of a spherical wave). More relevant to scattering experiments at small angles,

however, is the apparently erratic manner in which the amplitudes of scattered neutrons vary depending on isotope[96] ; put differently the scattering length (b) of neutrons varies with chemical isotope, whereas the scattering length of an X-ray from an electron is consistently r_e. Scattering length density (SLD), the quantity most relevant to SANS experiments, can be computed as:

$$SLD = \sum_i b_i \rho_i \quad \textbf{(3.9)}$$

Where b_i denotes the neutron scattering length of nucleus i, and ρ_i the density of that nucleus within the material. Table 3.1 tabulates the X-ray and neutron SLDs for various materials relevant to this thesis. Of particular interest is the large differences in the values of water (H_2O) and deuterium oxide (D_2O). By varying the composition of a mixture of the two isotopes, it is possible to tune the SLD of a solvent to match that of different components within as suspension (such as polypeptides or DNA)[97]. Thus, SANS experiments often provide very useful complimentary information about samples, particularly concerning the configuration of materials consisting of elements of lower atomic number.

Table 3.1: Scattering length densities (SLD) for the various components of the DNA-AuNP system. The X-ray SLD contrast between DNA and water is almost 20-times less than that of Au and water. The magnitude of the neutron SLD contrast between DNA and D_2O is greater than that of Au and D_2O.

Component	**X-ray SLD (10^{-6} Å^{-2})**	**Neutron SLD (10^{-6} Å^{-2})**
Au	124.694	4.662
H_2O	9.469	-0.561
D_2O	9.369	6.335
$CaCl_2$	18.120	2.783
DNA	~15.5	~3

3.4. UV-Vis Spectrophotometry

The scattering and/or absorbance of visible and ultraviolet light are useful processes for characterizing the composition and concentrations of colloids and biomaterials. In a relatively dilute solution or suspension, the absorbance can be modeled with the Beer-Lambert law[98]:

$$A = \log I_o(\lambda) - \log I(\lambda) = \varepsilon(\lambda) C l \quad \textbf{(3.10)}$$

where A denotes the absorbance, I_o the transmitted intensity through a reference (often a sample-free buffer), I the transmitted intensity of the sample, epsilon a species-dependent molar absorptivity coefficient, C the molar concentration of that species, and l the path length of the light through the sample. In many modern UV-Vis spectrophotometers, path length is fixed by the size of the cuvette used to hold the sample, allowing for determination of the concentrations of solution components with known absorptivity coefficients, such as DNA[99].

The optical properties of AuNPs vary depending on their size, as this parameter determines which optical wavelengths are absorbed by the surface plasmon resonance (SPR) mode of electrons within the nanoparticle[100]. Interest in this phenomenon has led to the establishment of absorptivity coefficients and wavelengths of peak absorbance for AuNPs of a variety of sizes [101], allowing for reliable determination of concentration of suspensions of these materials; for example, 10 nm AuNPs feature peak absorbance at 520 nm, with a molar absorptivity coefficient of $9.550 * 10^7$ $M^{-1}cm^{-1}$

Intriguingly, the optical properties of AuNPs[102] and DNA-NPs[103] change if the particles cluster or aggregate. When a large number of DNA-NPs are co-localized within a volume of dimension comparable to optical wavelengths, the electrons in adjacent particles oscillate in a

coordinated manner in response to visible light; the increasingly collective nature of this response as DNA-NPs become more aggregated results in apparent red-shifting of the surface plasmon resonance absorbance peak[104]. This transition is visually apparent, allowing for rapid determination of the presence of aggregated DNA-NP phases with the eye. Additionally, UV-Vis spectrophotometry can be utilized to monitor the aggregation state of DNA-NPs as parameters such as temperature are varied, allowing for the determination of melting points (or lack thereof) of DNA-NP structures[103].

Chapter 4: DNA-NP Structure in Concentrated Electrolytes

The work in this chapter is published in *Proceedings of the National Academy of Sciences of the United States of America* as Reexpansion of charged nanoparticle assemblies in concentrated electrolytes (Roger J. E. Reinertsen, Sumit Kewalramani, Felipe Jiménez-Ángeles, Steven J. Weigand, Michael J. Bedzyk, and Monica Olvera de la Cruz)[105]

Concentrated electrolytes are relevant to a wide variety of fields, ranging from the development of electrochemical devices, such as supercapacitors [106], to extremophile biology [13]. Electrostatics in dilute solutions of salts have been extensively described by mean-field theories such as the Debye-Hückel theory [23]. In such theories, mobile salt ions reorganize in response to the electrostatic potential of the charged macro-ions (e.g., colloids and membranes). In particular, salt ions concentrate near oppositely charged surfaces and screen their electrostatic field. The effective range of electrostatic interactions (screening length) is expected to decay with salt concentration C as $\lambda_D \propto C^{\frac{-1}{2}}$. Therefore, a direct extension of this theory to high salinity would imply that the range of charge-driven effects decreases to negligible distances. In reality, interactions between the dissolved ions, which are ignored in the Debye-Hückel theory, become increasingly important at high salt concentrations, resulting in ionic correlations that are influenced by ion size and valency [32, 34, 107], and strongly regulate ion distributions in confinement by dielectric surfaces [108]. These ionic correlations in concentrated monovalent and multivalent electrolytes drive overscreening of charged surfaces [109], and stabilize colloidal nanoparticles against aggregation in molten salts [7]. Furthermore, high degrees of ionic organization are theorized to underlie the unexpectedly long electrostatic screening lengths measured via surface force apparatus (SFA) in

highly saline solutions [38, 39, 110]. Interest in the generality of such findings has motivated additional research[17, 41, 42, 44, 45, 111, 112], which has revealed the need for further investigations through experimental studies probing electrostatic interactions in concentrated salt solutions.

In the present study, we investigate the assembly of highly negatively charged DNA-functionalized Au nanoparticles (DNA-NP) in concentrated aqueous solutions of alkaline earth chlorides: $CaCl_2$, $MgCl_2$, and $SrCl_2$. The grafted DNA sequences are designed to exclude interparticle attractions via DNA base-pairing. Even then, these dissolved salts at moderate concentrations ($\lesssim$ 1M) induce attractive interactions between the like-charged particles, driving their assembly into crystalline and non-crystalline aggregates [17, 93]. We utilize a combination of small-and-wide-angle X-ray scattering (SAXS/WAXS) to analyze the structures formed by these nanoparticles over the whole accessible range of electrolyte concentrations (via SAXS), while also assessing the ion-ion correlations present in the bulk electrolyte (via WAXS). As would be expected from Debye-Hückel theory, SAXS measurements show that the observed structures contract with added salt. However, this trend holds only until a threshold concentration, above which the structures expand as salt concentration increases. This lattice re-expansion is connected to enhanced cation-anion ordering in the bulk solutions resolved by WAXS measurements and is explained through molecular dynamics (MD) simulations, which reproduce the nonmonotonic swelling of the nanoparticle aggregates. Overall, the combined experimental and computational results demonstrate how interactions mediated by dissolved ions continue to evolve at high salt concentrations, and provide insight into how ion-ion correlations manifest in interactions between charged nano-scale objects dispersed in concentrated electrolytes.

4.1 Experimental Methods

4.1.1 Sample Preparation

The sequence 5'-T_{35}-C_3SH- 3' was selected to prepare grafted DNA layers with minimal secondary structure formation. The 3' propyl-thiol terminated oligonucleotides were synthesized using a MerMade solid-state controlled pore glass (CPG) DNA synthesizer (BioAutomation) via phosphoramidite chemistry [113]. Following synthesis, the DNA was released from the CPG beads using a 1:1 mixture (by volume) of methylamine and NH_4OH at 55°C for 30 minutes. The DNA was then transferred to deionized water (18.2 MΩ·cm). Successfully synthesized strands were separated from failed syntheses via reverse-phase high-performance liquid chromatography (RP-HPLC, 1260 Infinity II LC System, from Agilent Technologies). The 5'-DMT group, which enables separation via HPLC, was then removed via reaction in 20% acetic acid and subsequent extraction with ethyl acetate. The purity and molecular weight of the synthesized sequences were verified with matrix-assisted laser desorption/ionization time-of-flight spectroscopy (Bruker AutoFlex MALDI-TOF). Concentrations of DNA solutions were determined via UV-Vis spectroscopy, using Beer's Law and absorbance of the oligonucleotide at 260 nm [114] (Nanodrop 1000 UV Visible Spectrophotometer, from Thermo Scientific).

The thiol-terminated oligonucleotides were grafted to colloidal gold nanoparticles following established methods [82]. In brief, the thiolated DNA molecules were reduced in 100 mM dithiothreitol (DTT) maintained at pH ~8 via phosphate buffer. Following reaction for 30-60 minutes, the DNA was transferred to water via purification through size-exclusion NAP5 columns (from Cytiva). The reduced DNA was added to ~10 nM solutions of colloidal AuNP (nominally 10 nm diameter, from Ted-Pella) at a ratio of ~372 DNA/AuNP and allowed to incubate overnight. Sodium chloride (NaCl 99.99% purity from Millipore-Sigma) and small quantities of 0.1%

Sodium Dodecyl Sulfate (SDS) were then slowly added to the solution over ~ 8 hours until a final concentration of 1 M NaCl was achieved. This process enables high grafting density on the nanoparticles. Unbound DNA was removed via centrifugation using 50 kDa spin-filters (from Amicon). DNA-NPs were then transferred to DI water (18.2 MΩ·cm), and purified through three rounds of centrifugation, in order to minimize the presence of NaCl, unbound DNA, and SDS in the final nanoparticle stock solutions. Final DNA-NP concentrations were determined via application of Beer's Law to the UV-Vis-measured absorbance (Cary Series UV-Vis-NIR Spectrophotometer, from Agilent Technologies) of the AuNP at 520 nm [101].

The number of DNA strands per particle was determined via Quant-iT Oligreen Assay from Invitrogen. Suspensions of known DNA-NP concentrations were briefly reacted in 20 mM KCN solution at 50°C, in order to dissolve the gold cores and release the DNA into solution. Oligreen fluorescent dye, diluted in Tris-EDTA buffer (pH 8, from Sigma-Aldrich), was used to stain the liberated oligonucleotides. The fluorescence of these solutions at 480 nm was measured using a Biotek Cytation 5 plate reader. The measured fluorescence intensities were compared with those measured for Oligreen-stained 5'-T_{35}-C_3SH- 3' solutions of various known concentrations. Thereby, the average loading DNA loading per particle was determined. Results for the two batches are listed in **Table 4.1**. DNA-NPs with higher DNA loading formed crystals with higher interparticle separations but showed similar responses with regard to phase transitions and contraction/expansion to particles with lower DNA loading (**Fig. 4.7**).

To prepare samples with exceptionally high alkaline earth chloride concentrations, saturated solutions of these salts in water were prepared at ~22°C and allowed to equilibrate with the precipitated hydrate phase in sealed polypropylene tubes at ~ 22°C for at least 12 hours before use. Solutions were prepared using Calcium Chloride Dihydrate (99.5% purity, from Sigma-

Aldrich), anhydrous $MgCl_2$ (99.9% purity, from Sigma-Aldrich), and anhydrous $SrCl_2$ (99.9% purity, from Sigma-Aldrich). Samples for SAXS analysis were prepared in total volumes of 30 – 50 μL, with final DNA-NP concentrations of 50 nM (unless otherwise stated), and the alkaline earth chloride solution being the final component added to the mixtures. Following the addition of the salt solution, each solution was homogenized via pipette and transferred to either a 1.0 mm or a 1.5 mm quartz glass capillary (Charles Supper) within one minute. The capillaries were then sealed with quick-drying epoxy, and 24-36 hours elapsed prior to measurements. Salt solution samples for WAXS analysis were prepared in 500 μL volumes in 1.5mL centrifuge tubes.

4.1.2 X-ray Scattering Measurements

SAXS measurements on nanoparticle suspensions were primarily carried out at beamline 5ID-D of the Advanced Photon Source. To reduce the X-ray attenuation due to the concentrated salt solutions, the X-ray energy of 16 keV (wavelength, l = 0.7749 Å) or 17 keV (l = 0.7293 Å wavelength) was used. In particular, to avoid the strong fluorescence from Sr^{2+}, 16 keV was used as this energy is below the K absorption edge for Sr ($E_{K,Sr}$ = 16.1 keV). The SAXS/WAXS scattered intensities were measured simultaneously using three Rayonix CCD detectors positioned at 0.2 m, 1.0 m, and 7.5 m from the sample, allowing for simultaneous and continuous data collection in the range ($0.02\ nm^{-1} < q < 30\ nm^{-1}$). The X-ray spot size at the sample position was 0.25 mm x 0.25 mm, and the incident flux was ~ 3×10^{11} photons/s. Capillary samples were mounted horizontally on a translation stage. Samples were scanned for sets of three 5-second exposures, with the capillaries being translated continuously at ~ 0.5 mm/s during measurement to minimize radiation damage. For bulk electrolyte WAXS measurements, the X-ray energy was tuned to 15 keV (0.8270Å), and samples were flowed through a 1.5 mm capillary at 7 μL/s for 5-second exposures. 5-6 measurements were made per sample to improve statistics. Measurements were also made on

the empty capillary before and after each sample. The 2D data was reduced to 1D intensity profiles via azimuthal integration (using GSAS-II), following corrections for polarization, detector solid angle, and transmission.

4.1.3 Data Analysis

For all samples, the 1D intensity profiles from the three detectors were merged. "Background-subtracted" data was obtained by subtracting the measured intensities ($I_{sol}(q)$) from capillaries containing the salt solutions (no DNA-NPs) from the measured intensity of capillaries containing DNA-NPs in the corresponding salt solutions ([$I_{samp}(q)$]):

$$I_{DNA-AuNP}(q) = I_{samp}(q) - (1-\phi) \times I_{sol}(q) \quad \textbf{(4.1)}$$

In **Eq. 4.1**, ϕ is the volume fraction of the DNA-NP (of the order of 10^{-3}).

In the SAXS regime (0.02 nm^{-1} < q < 1 nm^{-1}), $I_{DNA-AuNP}(q)$ is primarily due to the electron-dense Au nanoparticle cores. The scattering amplitude [form factor, $F(q, R_{Au})$] due to a single spherical Au particle is given as:

$$F(q, R_{Au}) = V_{Au} \times (\rho_{Au} - \rho_{sol}) \times \frac{[\sin(qR_{Au}) - (qR_{Au}) \times \cos(qR_{Au})]}{(qR_{Au})^3} \quad \textbf{(4.2)}$$

V_{Au} ($= \frac{4\pi}{3} R_{Au}^3$) and ρ_{Au} (= 4660 e/nm^3) are the volume and electron density of the gold core, respectively, and ρ_{sol} is the electron density of the surrounding solvent. The solution electron density depends on the salt concentration and in this study varied between ρ_{sol} = 334 e/nm^3 (for pure water) and 460 e/nm^3 (for 5.6 M $CaCl_2.2H_2O$). The scattering amplitude of an object scales linearly with the difference in the electron densities for the object and the solution (e.g., **Eq. 4.1**) electron density difference between the object and solution. Therefore, the scattered intensity

scales as the absolute square of the electron density difference. As a result, the scattered intensity from a DNA (ρ_{DNA} ~ 550 e/nm^3) [115] is typically at least 400 times weaker than that from a gold core (should the objects have comparable volumes). Thus, the scattering from the DNA is taken to be negligible in this study.

For the dispersed DNA-NPs showing no assembly, the scattered intensity *P(q)* is calculated as:

$$P(q) = A \times \langle |F(q, R_{Au})|^2 \rangle_{R_{Au}} + B \quad \textbf{(4.3)}$$

The angle brackets denote the averaging of the absolute square of the form factor over a Schulz distribution for size-dispersity [116]. Briefly:

$$\Pr(R_{Au}) = \left(\frac{z+1}{\langle R_{Au} \rangle}\right)^{z+1} \times \frac{R_{Au}^{z}}{\Gamma(z+1)} e^{-(z+1)\frac{R_{Au}}{\langle R_{Au} \rangle}} \quad \textbf{(4.4)}$$

Here, $\langle R_{Au} \rangle$ denotes the average nanoparticle radius, Γ the gamma function, and z is a parameter related to the distribution variance (Σ^2) as $z = \frac{\langle R_{Au} \rangle^2}{\Sigma^2} - 1$. The coefficient *A* is proportional to the concentration of nanoparticles in solution. The constant term *B* arises due to the difficulties in precisely correcting for the background due to the slight differences in the thicknesses of capillaries used for measurements of samples and solutions.

For the case where DNA-NPs were freely dispersed (no assembly), $I_{DNA-AuNP}(q)$ was analyzed using **Eq. 4.3**. Otherwise, **Eq. 4.5** (below) was used.

$$I_{DNA-AuNP}(q) = S(q) \times P(q) \quad \textbf{(4.5)}$$

Here, $S(q)$, is the structure factor arising due to interference between X-rays scattered from positionally correlated particles. For non-correlated systems, $S(q)$=1. For correlated DNA-NPs, the analysis procedure for $S(q)$ is described below.

The "decoupling approximation" [117] is used to model the structure factors for DNA-NP aggregates displaying crystalline ordering:

$$S(q) = 1 + \beta(q)G(q)[Z(q) - 1] \quad \textbf{(4.6)}$$

β(q) reflects the role of polydispersity in variations in nanoparticle positions within crystalline domains:

$$\beta(q) = \frac{|\langle F(q, R_{Au})\rangle|^2}{\langle |F(q, R_{Au})|^2\rangle} \quad \textbf{(4.7)}$$

As described in the previous section, a Schulz size distribution was used, with average radius $\langle R_{Au}\rangle$ and z being determined while fitting $P(q)$. $G(q)$ reflects lattice disorder due to positional fluctuations of nanoparticles about their mean positions:

$$G(q) = e^{-\sigma^2 D_{nn}^2 q^2} \quad \textbf{(4.8)}$$

D_{nn} is the mean separation between nearest-neighbor nanoparticle cores in the lattice, and σ parametrizes the relative displacement of the DNA-NPs about their lattice sites. *Z(q)* describes the crystalline diffraction peaks associated with the lattice symmetry:

$$Z(q) = \frac{C}{q^2}\left[\sum_{\{hkl\}} m_{hkl}\left|\sum_j e^{i2\pi(hx_j+ky_j+lz_j)}\right|^2 L_{hkl}(q)\right] + bkg \quad \textbf{(4.9)}$$

The outer sum extends over each set of symmetry-equivalent reflections, denoted by Miller indices h, k, and l. m_{hkl} denotes the multiplicity of the reflections, or the number of all reflections in each set $\{h\ k\ l\}$. The inner sum extends over j particles in the unit cell, with particle positions described by fractional coordinates (x_j,y_j,z_j). $L_{hkl}(q)$ represents a line shape for a given reflection; in the present analysis, Lorentzian functions of constant widths were utilized:

$$L_{hkl}(q) = \frac{\frac{w}{2\pi}}{(q - q_{hkl})^2 + \left(\frac{w}{2}\right)^2}$$

(4.10)

The q^{-2} dependence is the Lorentz factor due to the averaging over all possible orientations of the crystal lattice in 3 dimensions. *Bkg* issued to account for small imprecisions in the extracted structure factors. Since the structures observed here have cubic symmetry, q_{hkl} is calculated as:

$$q_{hkl} = a^*\sqrt{h^2 + k^2 + l^2} = \frac{2\pi}{a}\sqrt{h^2 + k^2 + l^2}$$

(4.11)

a is the lattice parameter of the cubic unit cell, which relates to D_{nn} through $D_{NN} = \frac{a}{\sqrt{2}}$ for FCC lattices, and $D_{NN} = \frac{\sqrt{3}a}{2}$ for BCC lattices.

The extracted crystalline $S(q)$ profiles were fit using a, w, σ, C, and bkg, as well as the known fractional atomic coordinates for FCC and BCC unit cells. This analysis allowed for deduction of the structure types and interparticle separation. Fit parameters, as well as values of D_{nn} estimated from the first diffraction peak q_1 ($D_{nn} = \frac{\sqrt{6}\pi}{q_1}$) are listed in **Table 4.2**. We observe that the values of D_{nn} obtained from the two methods differ minimally.

Structure factors displaying a lack of long-range order (broad diffraction peaks) were analyzed by calculating the corresponding radial distribution function, *g*I, which is calculated via Fourier transform of the renormalized structure factor [116]:

$$g(r) = \frac{\rho(r)}{\rho_0} = 1 + \frac{H(r)}{4\pi r \rho_0} = 1 + \frac{1}{2\pi^2 r \rho_0} \int_0^\infty q[S(q) - 1] \sin(qr)\, dq$$

(4.12)

$$H(r) = \frac{2}{\pi} \int_0^\infty q[S(q) - 1] \sin(qr)\, dq$$

(4.13)

$\rho(r)$ denotes the number density of particles found at radial distance r from the center of any given DNA-NP, and ρ_o denotes the average number density of particles in the solution. Renormalized RDFs (**Eq. 4.14**) are displayed in **Fig. 4.8**. The integral in **Eq. 4.13** was evaluated numerically, on the interval 0.1 $nm^{-1} < q < 3$ nm^{-1}. Due to this finite range, there are oscillatory artifacts visible in RDFs corresponding to the q range. The position of the first maximum in the RDF is used to determine D_{nn}, as tabulated for various salt concentrations in **Table 4.3**. Comparison of these D_{nn} values to those calculated from the first peak in *S(q)* via $D_{nn} = \frac{\sqrt{6\pi}}{q_1}$ yields only small (> 2%) differences, suggesting that this formula applies to the RCP phase as well.

$$g_0(r) = \frac{\rho_0(g(r) - 1)}{\rho_0(g(r_1) - 1)} + 1 = \frac{H(r)}{H(r_1)} + 1$$

(4.14)

The 1D intensity profiles from salt solutions were obtained by subtracting the scattered intensity from the empty capillary from that measured with the concentrated salt solution. Furthermore, to better visualize scattering peaks associated with the added salt, the scattering

contribution of bulk water molecules was subtracted. This was done by subtracting the scattering profile of DI water, weighted by the number fraction of bulk-like water molecules in the solution (**Figs. 4.11a-c**) [118]. WAXS peak positions are defined as the maxima of the corresponding peaks in the residual scattering signal following these subtractions.

4.2. Results and Discussion

As discussed, The nanoparticles utilized in this study were prepared by grafting thiolated single-stranded DNA molecules consisting of 35 thymine bases (T_{35}) onto Au cores (nominal radius, R_{Au} = 4.5 nm). The grafting density was ~ 60 – 80 DNA/Au nanoparticle, with loading varying between synthesis batches (see chapter supporting information, **Table 4.1**). Unless specified otherwise, samples for measurements were prepared with DNA-NP concentration of 50 nM, corresponding to a dilute suspension (volume fraction ~ 10^{-3}). Additional sample preparation details are provided in the preceding section. Despite the exclusion of canonical base pairing between neighboring DNA-NP, such particles assemble into colloidal crystals in solutions containing sufficient amounts of divalent cations. In such a condensed state, the proximity of the AuNP cores causes redshifting of the absorbance corresponding to the surface plasmon resonance (SPR), resulting in the suspensions changing color from red to purple [119] (**Fig. 4.1a**). Given sufficient time, the nanoparticle aggregates precipitate from the solution. Lowering the salt concentration results in the "melting" of the aggregates and redispersion of the particles, as visualized by the restoration of the suspension's red color (**Fig. 4.1a**). This reversibility implies that the assemblies are equilibrium phases, with salt-concentration-determined structures.

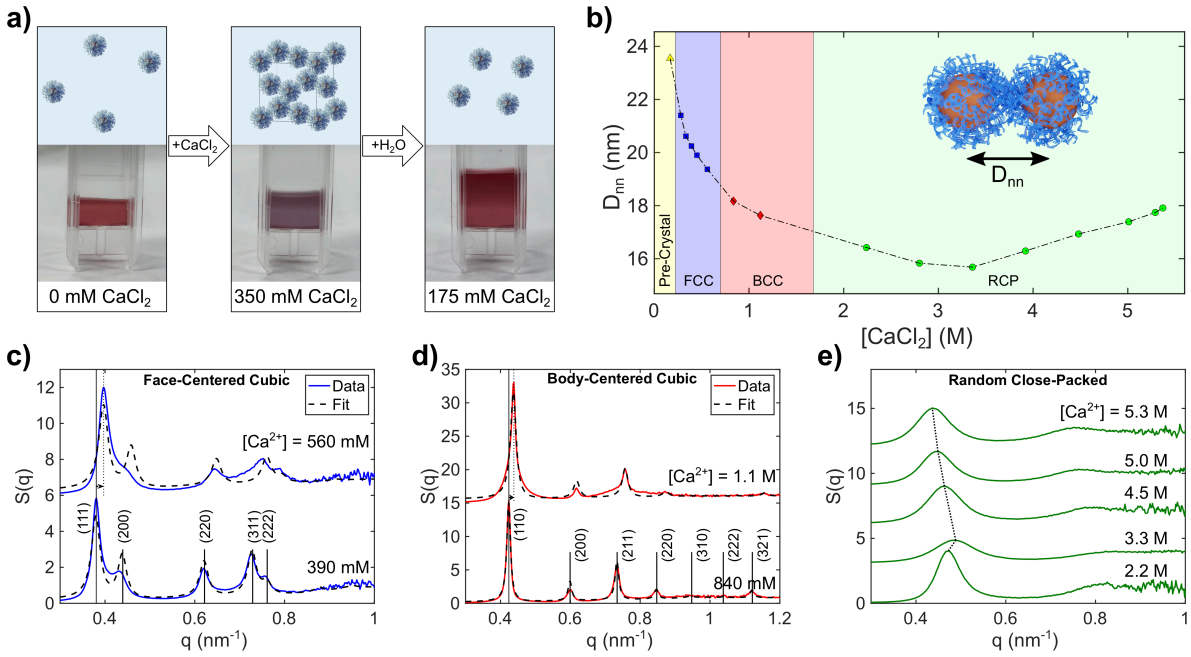

Figure 4.1: Assembly of DNA-NPs in $CaCl_2$ solutions. (a) Schematic (top) and photographs (bottom) of $CaCl_2$-induced reversible crystallization of DNA-functionalized nanoparticles (DNA-NP). Increasing the salt concentration results in nanoparticle aggregation, which is reflected in the suspension color changing from red to purple (middle). Decreasing the salt concentration restores the red color, showing that the aggregation of the nanoparticles is reversibly controlled by salt concentration. Note that while the salt concentration is varied, the DNA-NP concentration is held fixed at 50 nM. (b) DNA-NP structural phase diagram and center-to-center interparticle separations, D_{nn}, as a function of $CaCl_2$ concentration. Note that the effective volume per particle, calculated after correcting for the packing fractions in different assembly structures, shows the same trend as D_{nn} (**Fig. 4.10**). (c, d) Representative structure factors with corresponding model fits for DNA-NP face-centered cubic [FCC, (c)] and body-centered cubic [BCC, (d)] lattices. (e) Structure factors for the assemblies formed at high $CaCl_2$ concentration, which display no long-range order. The position of the primary diffraction peak initially shifts to higher q with added $CaCl_2$, consistent with a contracting structure; this trend reverses at high $CaCl_2$ concentrations (> 3.3 M). In c-e, the structure factors are offset vertically for clarity.

To investigate the assembly structures, we analyzed DNA-NP dispersions over the whole accessible range of $CaCl_2$ concentrations (0 - 5.3 M) via in situ SAXS. All dispersions were allowed to equilibrate in epoxy-sealed quartz capillaries for 24 - 36 hours prior to measurements. For details of SAXS measurements and data processing, see Experimental Methods section.

Figs. 4.1c - 1e, show examples of SAXS-derived structure factors $S(q)$ at varied salt

concentrations. Here, $q = 4\pi \sin\theta/\lambda$ is the scattering vector magnitude, 2θ is the scattering angle, and λ is the X-ray wavelength (here, $\lambda = 0.729$ Å). $S(q)$ results from the interference of X-rays scattered from distinct particles in the assemblies and yields assembly phases and interparticle distances. DNA-NP dispersed in [$CaCl_2$] $\lesssim$ 0.25 M remain suspended, with the suspension retaining its red color. However, very weak diffraction peaks are discernible in S(q) for [$CaCl_2$] $\gtrsim$ 0.2 M (**Fig. 4.6**), likely corresponding to fluid-like correlations between small numbers of particles. Such dispersed phases are referred to as pre-crystalline. By contrast, **Figs. 4.1c-1d** show sharp diffraction peaks corresponding to DNA-NP organization into crystal lattices over [$CaCl_2$] ~ 0.3 -1.7 M . For [$CaCl_2$] $\gtrsim$ 1.7 M, much broader intensity modulations corresponding to short-ranged positional correlations between DNA-NP are observed (**Fig. 4.1e**). Detailed analysis of these structure factors reveals that the DNA-NP assemble into face-centered cubic lattices (FCC) for [$CaCl_2$] ~ 0.3 to 0.8 M (**Fig. 4.1c**), as observed in our previous work [93]. Furthermore, here we find that for [$CaCl_2$] ~ 0.8 – 1.7 M, DNA-NP assemblies convert from FCC to body-centered cubic (BCC) (**Fig. 4.1d**). Above [$CaCl_2$] ~ 1.7 M, the intensity profiles exhibit broad peaks with a ratio $q_2/q_1 \sim \sqrt{3}$, between the positions of the first 2 intensity maxima. This is consistent with random close packing (RCP) [120, 121]. These results were reproduced using multiple batches of DNA-NPs (**Fig. 4.7**), and were influenced minimally by decreasing the DNA-NP concentration from 50 nM to 20 nM. (**Fig. 4.5**).

Apart from the salt-concentration-induced structural transformations, analysis of $S(q)$ (**Figs. 1c-1e**) also demonstrates that the distances between the nanoparticles vary with $CaCl_2$ concentration. We note that for both FCC and BCC structures, the nearest neighbor distance (D_{nn}) is related to the position of the principal diffraction peak (q_1) as: $D_{nn} = \sqrt{6}\pi/q_1$ (**Table**

4.2). This relationship also extends to RCP, which lacks long-range ordering, as demonstrated by nearly identical D_{nn} values extracted through this formulation and via Fourier analysis of the $S(q)$ (**Fig. 4.8, Table 4.3**). **Figs. 4.1c-4.1e** show that q_1 increases (D_{nn} decreases) with added salt up to [$CaCl_2$] ~ 3.3 M. Over this range, D_{nn} decreases from ~ 24 nm to ~16 nm. Assuming that there is minimal interdigitation between the DNA shells from neighboring particles, this corresponds to a contraction of DNA shell [$t_{DNA} = {(D_{nn} - 2R_{Au})}/{2}$] from 7.5 nm to 3.5 nm. These lengths are much smaller than the T_{35} contour length of ~ 0.65 × 34 ~ 22 nm [79], implying that DNA acts as a flexible oligomer in compact conformations in the ionic conditions used here. Above the threshold of [$CaCl_2$] ~ 3.3 M, the trend in q_1 (and thus D_{nn}) reverses, signifying that the aggregates expand. The phase transformations of DNA-NP assemblies and the variation of the interparticle separation with $CaCl_2$ concentration are summarized in **Fig. 4.1b**.

At first glance, the observed structural transformations, particularly the FCC to BCC transition, are surprising. This is because long-ranged, softer electrostatic interactions expected in the low salt concentration regime favor BCC, as observed in the assembly of like-charged colloids interacting via screened Coulomb potential [121]. In that work, the assemblies transformed from BCC to FCC with increasing salt concentration. This is also consistent with observations on colloids and nanoparticles with hard cores and soft polymer shells, for which the BCC phase is favored in systems with longer and more flexible shells, which lead to "softer" interparticle interactions [122, 123]. We analyze the observed FCC to BCC transformation in the following chapter[124] and have show that interparticle attractive interactions coupled with the dehydration of the DNA shell at elevated salt concentrations lead to the observed FCC to BCC transitions. In this work, we will focus on the surprising contraction and re-expansion of the assemblies at high salinity.

The observed lattice contraction is consistent with a picture where increasing the divalent cation concentration (1) increases attractive interactions between the DNA in the overlap region of the neighboring DNA-NP and (2) screens the repulsions between charged phosphate groups along the DNA strands, allowing more compact DNA conformations. Similar contraction of nanoparticle lattices in a moderate salt concentration regime (< 2 M) has also been observed for DNA-NP assembled via Watson-Crick hybridization[80, 90]. Therefore, the re-expansion of aggregates above a threshold concentration is non-intuitive. To test whether aggregate re-expansion is an effect of specific Ca^{2+} - DNA interactions or a more general phenomenon, we repeated SAXS measurements in $MgCl_2$ (0 - 4.5 M) and $SrCl_2$ solutions (0-3 M) (**Fig 4.2**).

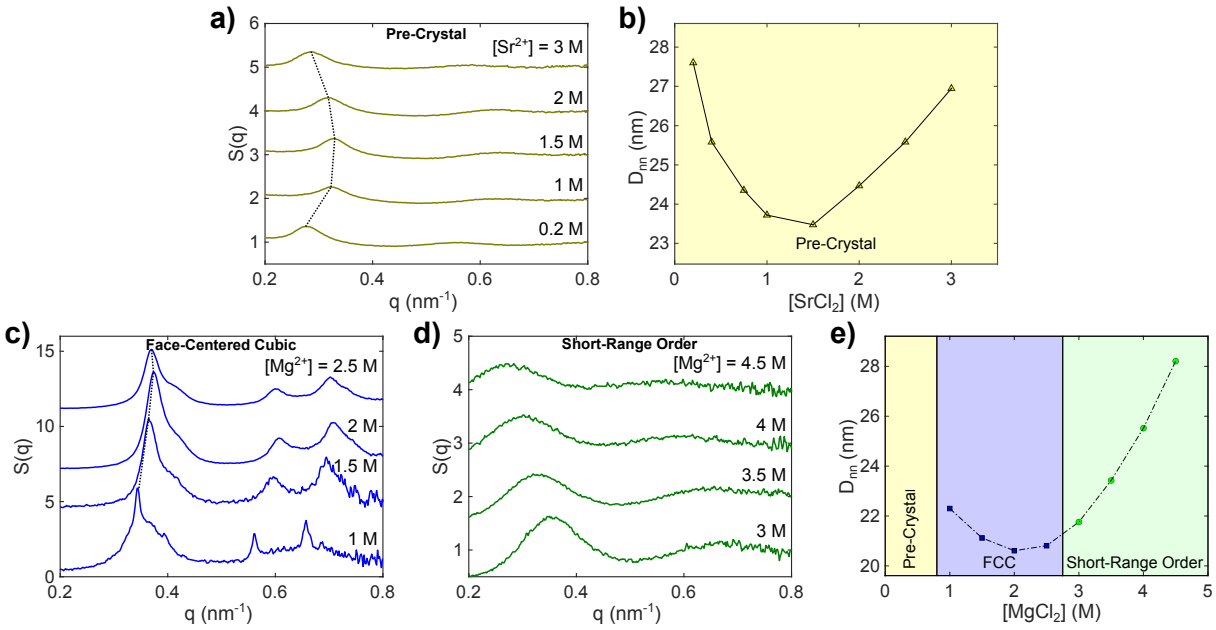

Figure 4.2: Assembly of DNA-NPs in $SrCl_2$ and $MgCl_2$ solutions. (a) Structure factors for DNA-NP assemblies at varied $SrCl_2$ concentrations. The dotted line is a guide to the eye and indicates the variation in the position of the principal peak. The corresponding inter-DNA-NP distances as a function of [$SrCl_2$] are shown in (b). (c-d) Structure factors observed at various $MgCl_2$ concentrations. Note that the position of the principal peak shifts to higher q up to 2 M (lattice contracts with added $MgCl_2$). Above this concentration, added salt leads to lattice expansion. (e) Summary of structural phases and interparticle separations observed as a function of $MgCl_2$ concentration. No detectable scattering peaks were observed in solutions below ~ 1M. In a, c-d, the structure factors are offset vertically for clarity.

There are clear distinctions between the assembly structures observed in $CaCl_2$ (**Fig. 4.1b**), $SrCl_2$ (**Fig. 4.2b**), and $MgCl_2$ (**Fig. 4.2e**). For example, DNA-NP dispersed in $SrCl_2$ solutions do not form precipitates. The suspensions at all concentrations retain their red color. The SAXS-derived structure factors for these dispersions (**Fig. 4.2a**) display a weak, broad diffraction peak, indicative of a fluid-like ordering [125], here defined as pre-crystalline. In $MgCl_2$ solutions, DNA-NP assemble into FCC for [$MgCl_2$] ~ 1 – 2.5 M (**Fig. 4.2c**) and convert to structures with short-ranged ordering above 2.5 M (**Fig. 4.2d**). This behavior is comparable to that observed in $CaCl_2$ solutions (**Fig. 4.1b**), with the exceptions that (1) no BCC phase is observed in $MgCl_2$ solutions and (2) the salt concentration for DNA-NP crystallization into FCC is higher (1M for $MgCl_2$ vs 0.3 M for $CaCl_2$). These contrasting properties of the assemblies reflect specific cation-DNA interactions. For example, the observed assembly behavior is consistent with the established understanding that the smaller Ca^{2+} or Mg^{2+} cations associate more strongly with DNA than larger Sr^{2+} or Ba^{2+} cations [126]. Interestingly, the smaller size of Mg^{2+} (as compared to Ca^{2+}) would suggest a stronger electrostatic interaction with DNA. However, we observe that higher concentrations of $MgCl_2$ are required to induce nanoparticle crystallization and that assemblies in $MgCl_2$ solutions feature larger interparticle separations than those in $CaCl_2$ solutions (**Figs.** 4.**1b** and 4.**2e**). We speculate that this weaker interaction arises due to the tendency of Mg^{2+} to retain its primary hydration shell when interacting with the DNA phosphate backbone [127, 128]. Despite these distinctions in the assembly behavior, the SAXS-extracted D_{nn} values show the same qualitative trend of aggregate contraction followed by re-expansion for assemblies in each of the three salt solutions (**Figs. 4.1b, 4.2b,** and **4.2e**).

There are some interesting phenomenological observations associated with the observed re-expansion. (1) The re-expansion occurs regardless of whether the structures exhibit crystalline

($MgCl_2$), short-ranged ($CaCl_2$), or liquid-like order ($SrCl_2$). (2) The value of the threshold concentration C_{th} for the upturn in D_{nn} is cation-dependent, increasing in the sequence Sr^{2+} (1.5 M) < Mg^{2+} (2.0 M) < Ca^{2+} (3.3 M). A potentially related phenomenon to this re-expansion has been observed in high charge density polyelectrolytes, which precipitate from solution at low concentrations of cationic multivalent ions and polyamines with $Z \geq 3$, and redisperse at higher salt concentrations [129, 130]. The redissolution was speculated to be due to a charge reversal [131], in which the charge due to adsorbed counterions, at the macro-ion surface, exceeds the charge required to neutralize the macro-ion. However, DNA charge reversal has not been documented in aqueous concentrated electrolytes with $Z \leq 3$ cationic proteins or ions, [132]. Additionally, this charge reversal model does not consider the association of cations to anions in the bulk [133], which can lead to redissolution without charge reversal [134]. Furthermore, if a charge-reversal mechanism were to underlie the presently observed DNA-NP re-expansion, then the C_{th} would be expected to be lowest for the cation that interacts most strongly with the DNA-NP (Ca^{2+}). The observed C_{th} sequence is, in fact, the reverse of this prediction. Rather, the sequence follows that of the solubility limits of the corresponding chloride salts in water [135]. Notably, for each salt, C_{th} is consistently ~ 40 - 60 % of the salt's solubility limit in water at room temperature (**Fig. 4.9**). Furthermore, our molecular simulations (discussed below) reveal that the effective electric field outside the DNA shells remains weakly negative at all salt concentrations (**Fig. 4.14**). These observations suggest that it is the interactions between electrolyte ions in close proximity, which become prominent at high salinities, that drive the non-monotonic interparticle separation behavior.

To gain insights into the electrolyte ion-DNA-NP and inter-electrolyte interactions, we performed molecular dynamics (MD) simulations using a coarse-grained model to analyze a

dense phase of DNA-NP in equilibrium with MX_2 reservoirs (**Figs. 4.3a-b**). The model used implicit solvent, but explicit ions. Due to computational constraints, the simulations utilized smaller nanoparticles, ($R_{Au,MD}$ = 2.25 nm) coated by 18 DNA, each represented by 16 charged (-*e*) beads with monovalent counterions, here labeled M^+ (for more details, see supporting information following this chapter). MD results of the equilibrium ion concentration distributions ($[M^{2+}]$, $[X^-]$, $[M^+]$) and D_{nn} as a function of reservoir concentration are shown in **Figs. 4.3c and 4.3e**, respectively. **Fig. 4.3d.** illustrates the method for extracting D_{nn} at a given concentration. **Fig. 4.3e** corroborates the experimentally observed (**Fig. 4.1b**) D_{nn} non-monotonic behavior. The transition molar concentration $C_{th,MD}$ ~ 2.0 M for the upturn in D_{nn} is lower than the experimentally observed C_{th} for Ca^{2+}(~ 3.3 M), but close to C_{th} for Mg^{2+}. We note that the implicit solvent utilized in the MD simulations does not consider ion hydration effects. Furthermore, below 2.0 M, in the regime where D_{nn} decreases with increasing salt concentration, MD simulations (**Fig. 4.3f**) reveal that the divalent ions' molar concentration in the dense DNA-NP phase is higher than in the reservoir ($[M^{2+}]_{DNA} > [M^{2+}]_{Bulk}$). Interestingly, in the expansion regime, the concentration of the divalent cations in the DNA-NP phase is slightly lower than in the reservoir ($[M^{2+}]_{DNA} < [M^{2+}]_{Bulk}$). It should be noted that, across the whole salt concentration regime for DNA-NP assembly, the DNA brush contains high concentrations of both cations and anions. Details of the radial ion distribution profiles are provided in the chapter supplemental information (**Fig. 4.13**). In the aggregate contraction regime, these results suggest that the system's equilibrium is driven by the internal energy decrease due to DNA-M^{2+} interactions. In contrast, in the aggregate expansion regime, the system's equilibrium is dictated by (1) the entropy gained through DNA adapting more extended conformations, enabling ions

redistribution in a larger volume of the DNA shell, and (2) favorable electrostatic interactions between salt ions.

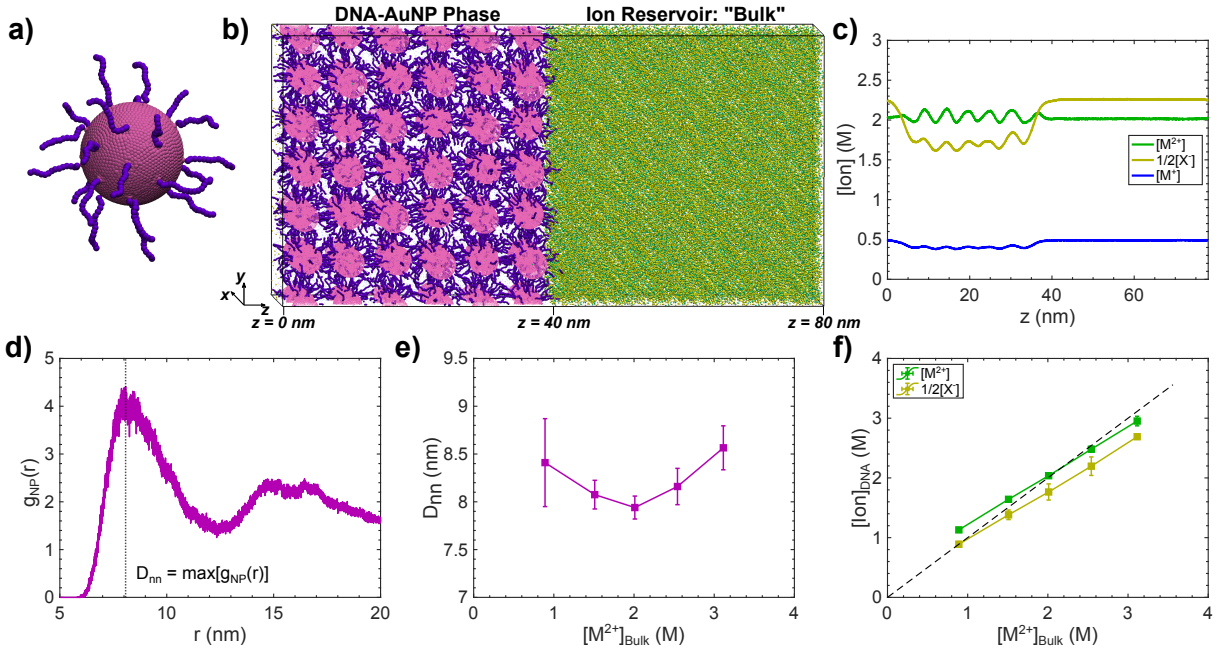

Figure 4.3: MD simulations on DNA-NP assemblies at different salt concentrations. (a) Coarse-grained model for a DNA-NP. The 16 DNA beads, representing a single DNA, bear a negative elementary charge (-e), and are connected using a harmonic potential. (b) To form the dense phase, 108 nanoparticles are initially arranged in an FCC lattice and surrounded by monovalent counterions. An ion solution containing divalent cations and monovalent anions is in contact with the dense phase. c) The ionic concentration profiles in the z-direction, after equilibration, for divalent cations, and monovalent cations and anions. (d) Radial distribution functions $g_{NP}(r)$ for DNA-NP are calculated using the equilibrium configurations. (e) The nearest-neighbor separation distance D_{nn} [defined as the position of the maxima of the radial distribution functions (d)] shows a non-monotonic behavior as a function of the divalent ion concentration in the reservoir. Note that the shorter contour length of the DNA (~7.6 nm vs ~22 nm in experiments) and smaller core (4.5 nm vs 9 nm in experiments) in the simulations lead to notably smaller D_{nn} values. (f) The mean ionic concentrations in the dense phase as a function of the divalent ion concentration in the reservoir. Note that in the DNA-NP aggregate expansion regime (> 2.0 M), the divalent ion concentration in the reservoir exceeds that in the DNA-NP dense phase. The dashed line signifies where the concentration in the dense phase is equal to that of the reservoir. These results were corroborated via chemical potential calculations (**Table 4.6**)

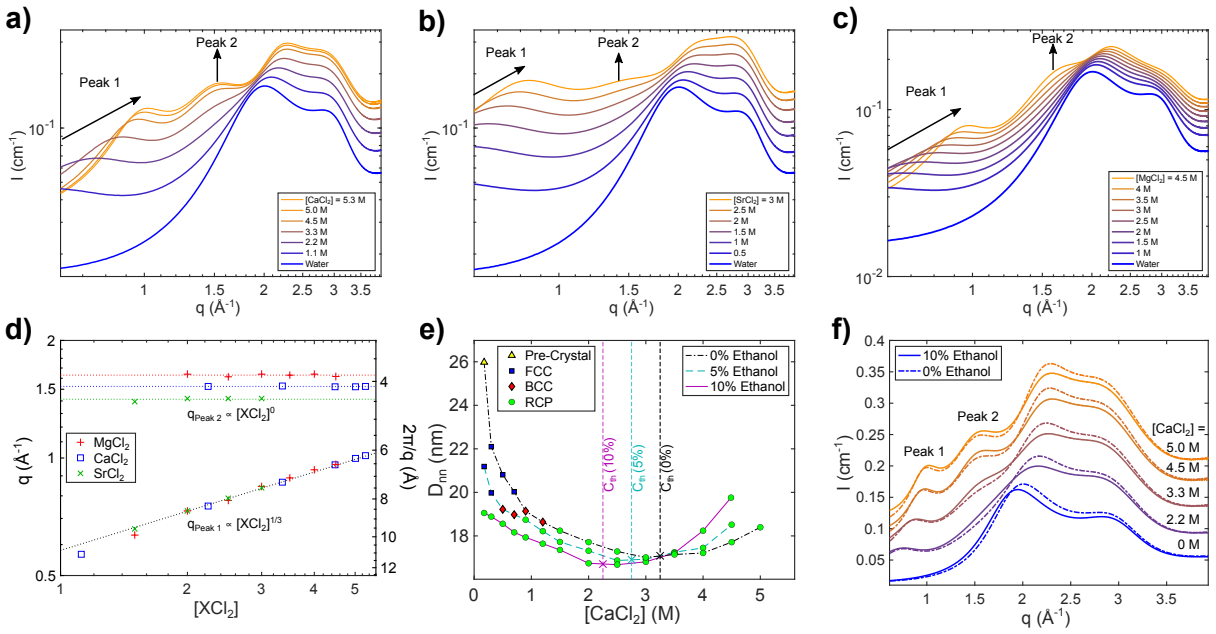

Figure 4.4: Electrolyte ion-ion interactions studied with WAXS and varied solvent composition. (a-c) Capillary-subtracted WAXS intensity profiles for aqueous $CaCl_2$ (a), $SrCl_2$ (b), and $MgCl_2$ (c) solutions. Two sets of peaks, which are not apparent in deionized water (blue profiles in a-c), are denoted as "Peak 1" and "Peak 2". (d) Plot demonstrating the concentration-dependence of the peak positions, and their corresponding real-space separations. The position of Peak 1 scales with the cube root of concentration and is consistent with a repulsive interaction. Peak 2 does not shift appreciably with the salt concentrations; but does shift to lower q (larger d spacing) with increasing cation size. Determination of peak positions is detailed in the methods section, and **Fig. 4.11**. (e) Interparticle separation (D_{nn}) as a function of [$CaCl_2$] in solutions with 0%, 5%, and 10% ethanol (v/v). Yellow markers denote pre-crystals, blue FCC, red BCC, and green RCP. Vertical lines mark the estimated salt concentrations corresponding to the minimum spacings observed in each sequence. The transition between contraction and expansion occurs more rapidly with higher ethanol volume fractions. Additionally, higher ethanol volume fractions lead to more contracted structures at low [$CaCl_2$], and more expanded structures at high [$CaCl_2$]. Corresponding SAXS patterns can be found in **Fig. 4.12**. (f) A comparison of capillary-subtracted WAXS intensity profiles of $CaCl_2$ solutions of various concentrations, with and without 10% ethanol. Notably, the peak at q ~ 1.5 Å ("Peak 2") is enhanced in the presence of ethanol.

The results of our MD simulations suggest that altered ionic distributions in the DNA shell and in the bulk solutions at high salinity underpin the observed lattice swelling. It is challenging to directly measure the ionic distributions surrounding DNA-NP via X-ray scattering because the scattered intensities are dominated by the electron-dense Au cores [88]. However, WAXS can be used to measure Å to nm scale interionic structuring in the bulk solution. Thus,

we prepared solutions of $CaCl_2$, $MgCl_2$, and $SrCl_2$ of the same concentrations used in the assembly experiments and conducted in situ WAXS measurements. Background subtracted WAXS intensity profiles for $CaCl_2$, $MgCl_2$ and $SrCl_2$ salt concentration series are shown in **Figs. 4.4a-c**. The scattering peaks for $q > 2$ Å^{-1} correspond to water structure and ion hydration [136, 137]. The present analysis will focus on $q < 2$ Å^{-1}, which corresponds to ion ordering beyond local solvation.

For all salt solutions, a low q intensity modulation (labeled "Peak 1") is observed. The corresponding intensity maxima shift monotonically to higher q, with a direct dependence on the cubic root of the salt concentration ($q_{Peak1} \propto C^{\frac{1}{3}}$, **Fig. 4.4d**). Based on previous studies on multivalent metal halide salts [138-140], Peak 1 can be assigned to arise from repulsions between divalent cations. This is because the separation between the scattering ions decreases with increasing salt concentration ($d \propto C^{\frac{-1}{3}}$) in a manner consistent with the distribution of repulsive objects in confinement in three dimensions. This is also verified by noting that q_{Peak1} depends on the salt concentration, but not on the cation type. In fact, the $q_{Peak1} \propto C^{\frac{1}{3}}$ dependence for all salt solutions follows a "universal" curve (**Fig. 4.4d**). At higher salt concentrations ($C \gtrsim C_{th}$), where the DNA-NP structures expand with added salt, an additional modulation (labeled "Peak 2") near q ~1.5 Å^{-1} (d ~ 4 Å) becomes prominent (**Figs. 4.4a-c**). The positions of this peak are independent of salt concentration, but vary with cation type. In fact, the corresponding distance increases with cation size (**Fig. 4.4d**). It is concluded that Peak 2 arises from attractive interactions between the divalent cations and anions. Previous scattering studies have also observed such intensity modulations [137, 140], and attributed them to positional correlations between hydrated cations and anions. This is further verified by the observations that the

intensity of this peak is enhanced in salt solutions with anions of higher atomic number, e.g., $CaBr_2$ vs $CaCl_2$ [139]. For the specific case of $CaCl_2$, additional evidence from dielectric relaxation spectroscopy [141] and Raman spectroscopy [142] support that Ca^{2+} and Cl^- form complexes with shared hydration shells, called solvent-separated ion pairs.

The ionic ordering induced by attractive electrostatic interactions in our WAXS measurements provides a plausible explanation for the observed ion redistributions in the MD simulations. In particular, at high salt concentrations, cations are no longer independent. Complexation with anions increases the effective volumes occupied by the ions in the DNA-NP condensed phase and restricts the ability of the cations to organize densely in the DNA shells, thereby driving the local cation concentration below that of the bulk solution. Furthermore, the cation-anion pairing/correlations can effectively reduce the number of free cations that can interact with the DNA-NP, thus explaining the observed DNA-NP re-expansion at high salinities. That is, since increasing the number of counterions in the DNA-NP shell at low salt concentrations leads to compression of the assemblies, reducing the effective concentration of free counterions by clustering could lead to a reverse effect. Such a reduction in free ion concentration caused by the formation of electrolyte ion clusters has been recently proposed in theoretical treatments of concentrated electrolytes [143].

To further establish the role of ion-ion interaction in the aggregate re-expansion, we analyzed the DNA-NP assemblies in $CaCl_2$ solutions with solvents of varied permittivity. Specifically, we utilized ethanol-water mixtures with 5% and 10% v/v ethanol. Ethanol and water are fully miscible and increasing ethanol content decreases the static dielectric constant of the mixture [144], thus increasing the electrostatic coupling within the solution [145]. For example, enhanced interactions between DNA and ions in ethanol are known to lower the salt

concentrations required to precipitate DNA [146]. Therefore, in the low salt concentration regime, the enhanced DNA-ion attractions in ethanol should lower the minimum $CaCl_2$ concentration required for DNA-NP crystallization. Furthermore, cation-anion interactions are enhanced in ethanol-water mixtures [147]; based on our prior observations implicating ionic correlations as driving re-expansion, we hypothesized that increasing ethanol fractions will shift C_{th} to lower $CaCl_2$ concentrations.

SAXS/WAXS measurements reveal the effects of enhanced DNA-ion and cation-anion attractive interactions in solutions with ethanol. With regards to DNA-ion interactions at low salt, we find that, as hypothesized, the $CaCl_2$ concentration required for DNA-NP assembly into crystals decreases with increased ethanol content, and that the boundaries for transitions to BCC and RCP structures shift to lower $CaCl_2$ concentrations. For example, in a 5% ethanol solution, $[CaCl_2] \sim 0.175$ M (vs 0.3 M in 0% ethanol) is sufficient for forming DNA-NP FCC structures (**Fig. 4.4e**). Below C_{th}, for a given $CaCl_2$ concentration, the D_{nn} is lowest for the 10% ethanol case and highest for the 0% ethanol case. By contrast, at high salinities ($[CaCl_2] > 3.5$ M), i.e., in the regime where electrolyte cation-anion interactions drive lattice re-expansion, D_{nn} is found to increase with ethanol content (**Fig. 4.4e**). Furthermore, C_{th} shifts downward with increasing ethanol fraction: $C_{th} \sim 3.3$, 2.8 and 2.3 M for 0%, 5% and 10% ethanol, respectively. This enhanced re-expansion and the above-described lowering of C_{th} are directly correlated to the enhanced propensity for short-ranged ordering of cations and anions in the solution as verified by WAXS (**Fig. 4.4f**). Specifically, WAXS intensity profiles exhibit higher amplitudes for the intensity modulations associated with Ca^{2+}-Cl^- ion paring (Peak 2) in 10% ethanol solutions, as compared to the 0% ethanol solutions, thus implying a higher degree of ionic clustering in the ethanol-containing solutions. These observations establish an empirical connection between the

enhanced ion-pairing in bulk solution and the anomalous expansion of the DNA-NP aggregates in high salinities.

The effects of the ordered structure of electrolyte solution at high salinities have been invoked in other systems where non-monotonic changes are observed. Most notably, in the aforementioned series of surface force measurements [38, 39, 110], an upturn in the range of electrostatic interactions (screening length) was observed (dubbed "underscreening"), which was attributed to strong positional correlations between the electrolyte cations and anions. It is also hypothesized that this underscreening effect is the cause of re-entrant swelling and redissolution of polyelectrolytes at high salt concentrations [148]. Parsimony suggests a unified explanation for all the non-monotonic system responses: namely, underscreening, polyelectrolyte redissolution, gel re-entrant swelling, and nanoparticle aggregate expansion observed at high salinities. However, some differences must be noted. The underscreening effect in 1:1 electrolytes (e.g. NaCl) was observed for $\lambda_D \leq a$. Here a is the average diameters of the unhydrated electrolyte ions and λ_D is the classical electrostatic screening length. Extending this result to the present study, using the average of the unhydrated diameters of Ca^{2+} (0.20 nm) and Cl^- (0.362 nm) [149], would imply $C_{th} \sim 0.3 - 0.4$ M for $CaCl_2$, which is much smaller than the experimentally observed 3.3 M. Furthermore, the experimentally observed C_{th} sequence ($Sr^{2+} < Mg^{2+} < Ca^{2+}$) seemingly depends on salt solubility limit, rather than ion size (**Fig. 4.9**). Additional experiments on DNA-NP assembly, such as anomalous X-ray scattering measurements on low electron density cores (e.g., proteins) functionalized with DNA in specific salt solutions (e.g., $SrBr_2$) could measure the composition and extent of the ionic atmosphere near these particles, thus, resolving ion-ion correlations at DNA-NP interfaces in the assembly contraction and expansion regimes.

4.3. Conclusions

To summarize, the present study demonstrates that ionic correlation at interfaces and in bulk solutions modulate interactions between charged macromolecules over the full range of achievable salinities, up to saturation. The assembly behavior of DNA-coated nanoparticles was analyzed concomitantly with the structure of the bulk electrolyte by combining X-ray scattering and molecular dynamics simulations. Our study identifies two regimes. First, in solutions with salinities below half the solubility limit of the dissolved salts, divalent cations are free to organize around DNA molecules, inducing net attractive forces between DNA-NPs that drive the aggregation of DNA-nanoparticles. In this regime, adding salt strengthens DNA-NP interactions, causing assemblies to become more compact. Second, in the regime of salinities approaching the solubility limit, divalent cations form clusters with neighboring anions in the dense electrolyte solution. In this regime, these clusters partition favorably into the bulk solution away from the DNA-NP aggregates. Adding salt strengthens this electrolyte ordering, with the net effect of reducing the effective counterion concentration that can interact with the nanoparticles. This reverses the trend of aggregate compression with added salt. Strengthening electrolyte ion ordering by lowering solution permittivity shifts the transition between these two regimes to lower concentrations. Overall, our study provides insight on how ion-ion correlations shape interactions of electrolytes with charged materials at the nanoscale, and furthers the discussion on electrostatics in concentrated electrolytes.

4.4. Chapter 4 Supplemental Information

4.4.1 Additional Experimental Results

In order to evaluate if the concentration of DNA-NPs influenced crystallization, additional SAXS measurements on capillary samples with 20 nM DNA-NP concentrations were carried out

at beamline 12-ID-C,D of the APS. SAXS data was collected using a Pilatus single photon counting area detector positioned ~ 2.3 m from the sample. The X-ray energy was tuned to 13 keV (0.954 Å wavelength), the beam size at the sample position was ~ 0.4mm x 0.2mm, and the flux was ~ 2×10^{12} photons/s. Ten measurements, each a 0.1 second exposure, were recorded for each sample. Azimuthal averaging was performed by the procedure outlined above to obtain the 1D scattering profiles of the DNA-NPs at various salt concentrations. Comparison of the phases and interparticle separations of aggregates formed in 20 and 50 nM suspensions of DNA-NPs revealed minimal variation (**Fig. 4.5**).

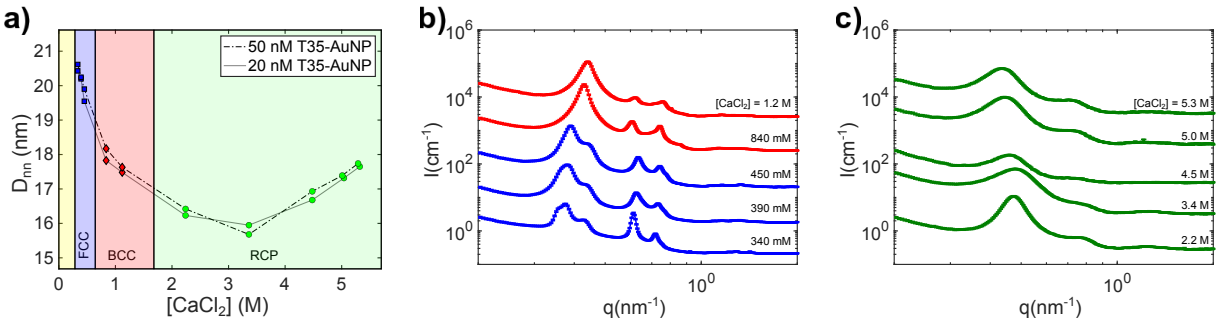

Figure 4.5: (a) DNA-NP structural phase diagram and center-to-center interparticle separations, D_{nn}, as a function of $CaCl_2$ concentration for 50 nM and 20 nM DNA-NP suspensions. Phases and interparticle separations are highly comparable across the two nanoparticle concentrations. (b,c) Buffer-subtracted SAXS data for DNA-NPs dispersed at a concentration of 20 nM in solutions of $CaCl_2$

4.4.2 Supplemental Figures and Tables

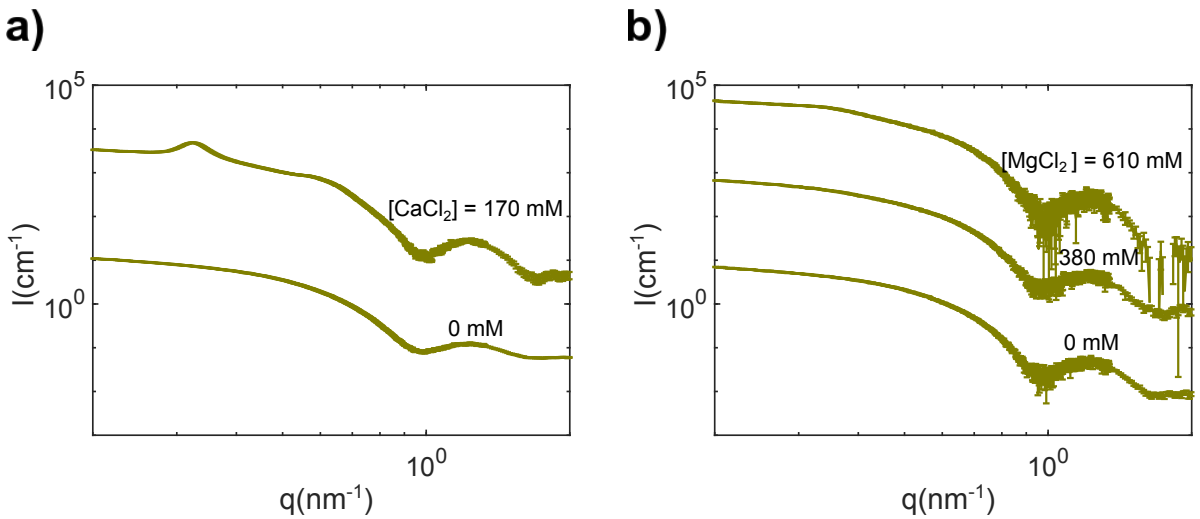

Figure 4.6: Buffer-subtracted SAXS data for DNA-NPs dispersed in low-concentration solutions of $CaCl_2$ (a) and $MgCl_2$ (b) insufficient to induce crystallization (pre-crystalline phases); A weak scattering peak is recorded for $CaCl_2$ solutions, enabling approximation of interparticle separations. No clear peaks are recorded in low-concentration $MgCl_2$ solutions.

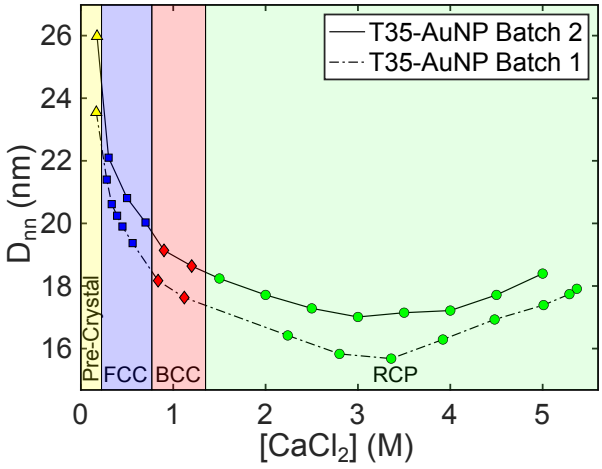

Figure 4.7: DNA-NP structural phase diagram and center-to-center interparticle separations, D_{nn}, as a function of $CaCl_2$ concentration for 2 separately functionalized batches of DNA-NPs. Between the batches, the absolute value of the interparticle separations differed but the responses to added salt (phase transitions and lattice contraction and expansion) are highly comparable. SAXS patterns for Batch 2 are displayed in **Fig. 4.12**.

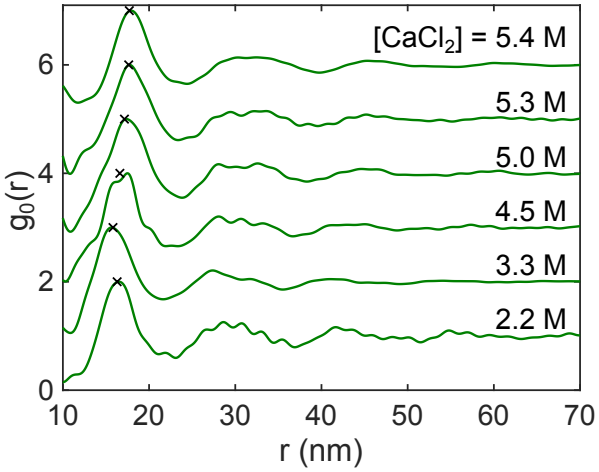

Figure 4.8: Normalized radial distribution functions calculated from SAXS data for DNA-NP aggregates at high $CaCl_2$ concentration. The cross marks denote the values $r = \frac{\sqrt{6\pi}}{q_1}$, where q_1 denotes the position of the primary scattering peak associated with the aggregates at the corresponding salt concentration. High-frequency oscillations arise from the finite size of the dataset.

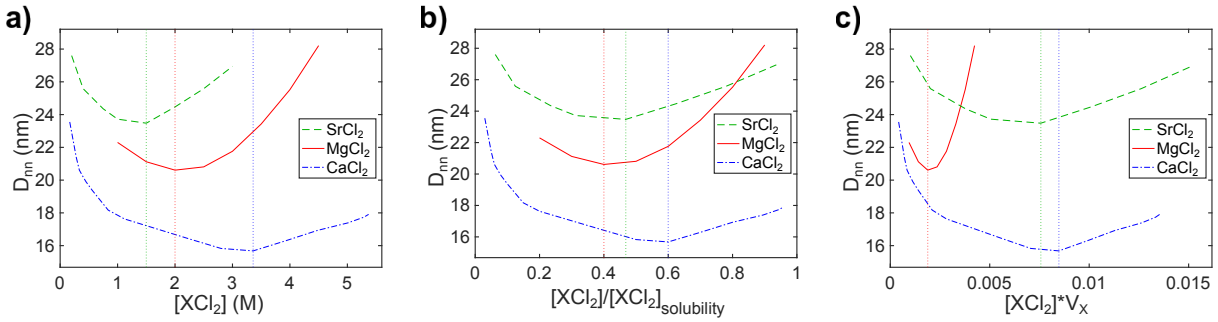

Figure 4.9: (a) Plots of DNA-NP center-to-center interparticle separations, D_{nn}, as a function of $CaCl_2$, $MgCl_2$, and $SrCl_2$ concentration. (b) Similar plot of D_{nn}, with concentration normalized to the solubility limits of the salts. (c) Similar plot of D_{nn}, with concertation being multiplied by the non-hydrated volume of the appropriate cation (equating to the volume fraction of the cation in the bulk solution). Vertical lines denote the transition from the contraction to expansion regimes. Pertinent quantities are listed in **Table 4.4**.

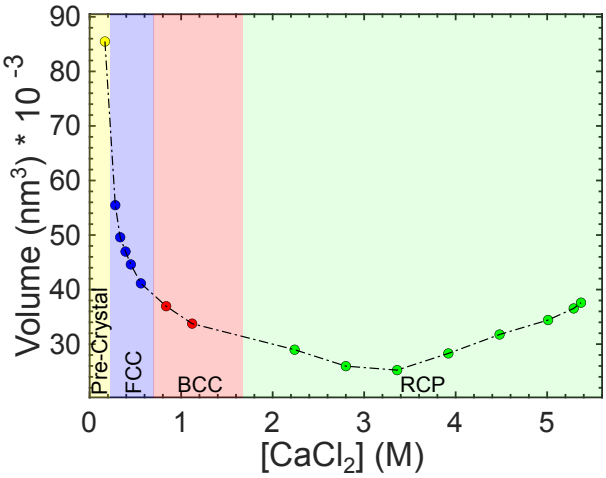

Figure 4.10: DNA-NP structural phase diagram and effective volume per particle as a function of $CaCl_2$ concentration. Effective volumes were calculated from the experimentally determined D_{nn}, and the packing fraction of the phase (0.74 for FCC, 0.68 for BCC, and 0.64 for phases lacking long-range order). The dependence of salt on the effective volume matches that of D_{nn}

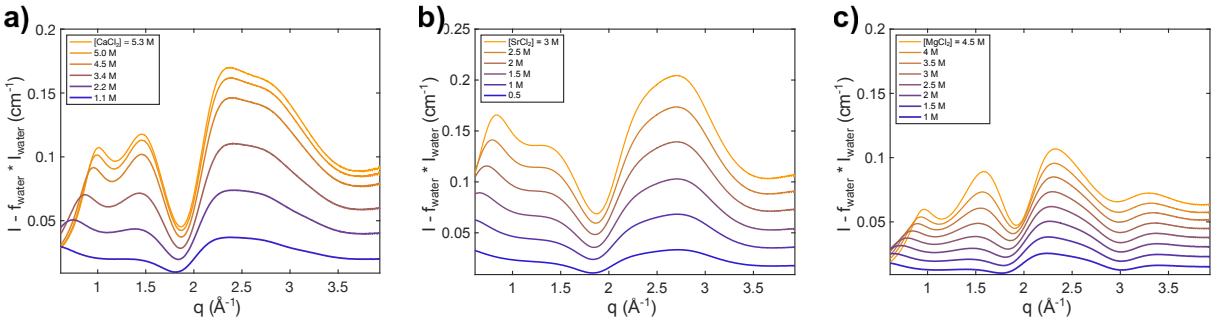

Figure 4.11: (a-c) Residual WAXS signals after subtracting the scattering from bulk water, weighted by the number fraction of water in the solution for $CaCl_2$ (a), $SrCl_2$ (b), and $MgCl_2$ (c).

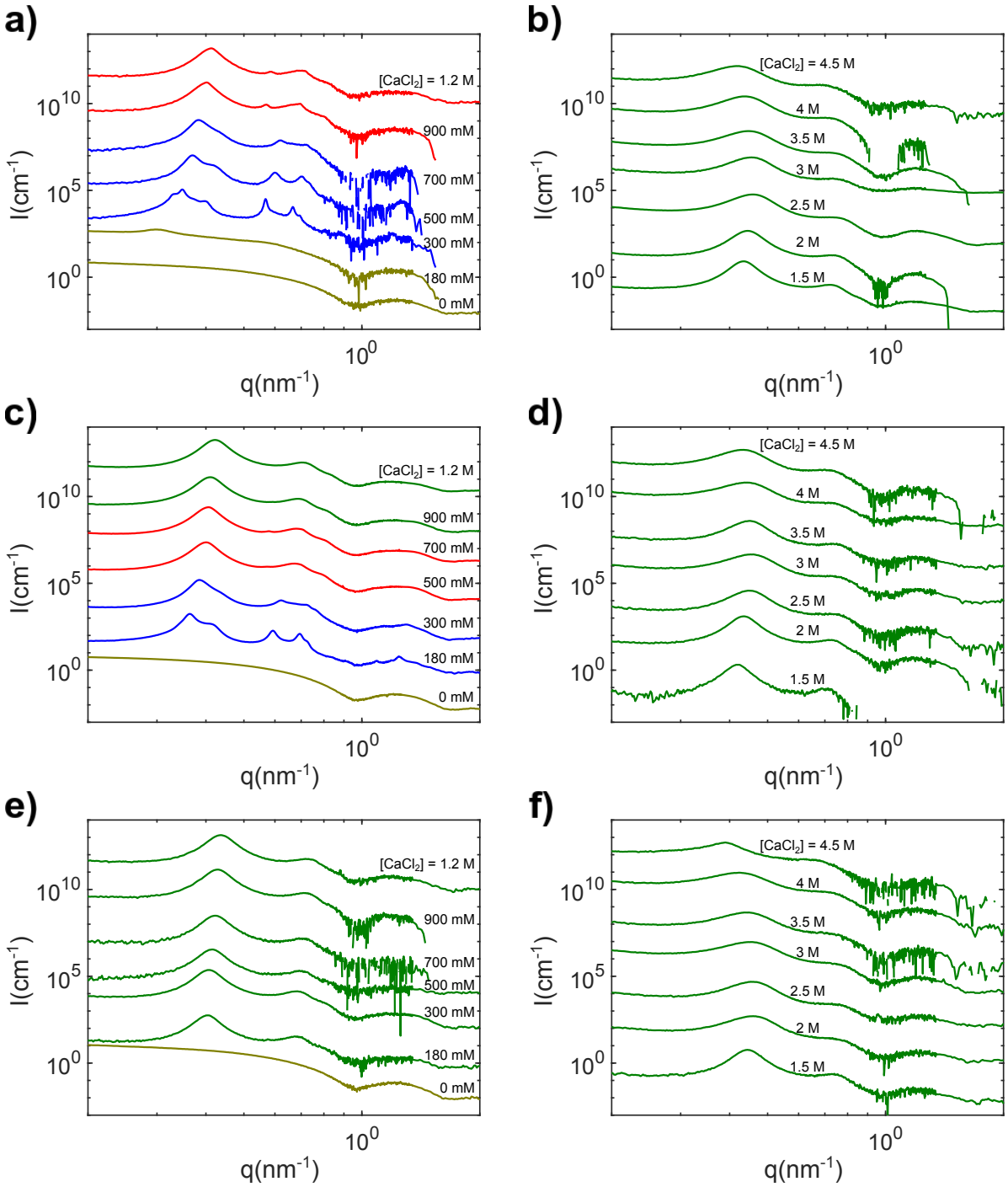

Figure 4.12: Buffer-subtracted SAXS data for DNA-NP dispersed in solutions of varied $CaCl_2$ concentration and 0% ethanol (a-b), 5% ethanol (c-d), and 10% ethanol (e-f).

Table 4.1: Physical parameters for the two batches of DNA-NPs studied in this work. Nanoparticle diameter was determined from SAXS measurements, while the average number of DNA per nanoparticle was determined via Oligreen Assay.

Batch	AuNP diameter	DNA/NP	St. dev (DNA/NP)	Loading density (nm^{-2})
1	9.1	63	5	0.242
2	9.2	84	5	0.316

Table 4.2: Parameters determined from fitting in **Eq. 4.6-4.11** to extracted crystalline structure factors for DNA-NP assembled in solutions of $CaCl_2$. Interparticle separations determined from fits are compared to values calculated from the primary scattering peak position, q_1, showing good agreement.

[$CaCl_2$] (M)	Structure	a (nm)	w (nm^{-1})	σ	C	bkg	D_{nn} (nm)	$\frac{\sqrt{6}\pi}{q_1}$ (nm)
0.33	FCC	29.15	0.0214	0.0556	268.6	0.0764	20.61	20.61
0.39	FCC	28.63	0.0235	0.0535	235.0	0.0857	20.24	20.22
0.45	FCC	28.15	0.0250	0.0560	286.9	0.0490	19.90	19.84
0.56	FCC	27.39	0.0250	0.0780	331.9	0.1040	19.37	19.39
0.84	BCC	20.98	0.0128	0.0679	1515.0	0.0667	18.17	18.16
1.1	BCC	20.40	0.0191	0.0700	1119.0	-0.0933	17.67	17.64

Table 4.3: Interparticle separations determined from maxima in calculated RDFs for DNA-NPs assembled in concentrated CaCl2 solutions, compared to values calculated from primary scattering peak position, q_1. Values show good agreement.

Concentration (M)	PDF Peak 1 Position (nm)	$\frac{\sqrt{6}\pi}{q_1}$ (nm)
2.2	16.42	16.29
3.3	15.68	15.81
4.5	16.93	16.61
5	17.39	17.14
5.3	17.74	17.64
5.4	17.91	17.71

Table 4.4: Solubility of the salts studied in this work at laboratory temperature (22°C), and tabulated anhydrous radii of the corresponding cations.

Salt	Water Solubility (M)	Cation Radius (Å)
$CaCl_2$	5.6	1.0
$SrCl_2$	3.2	1.26
$MgCl_2$	5.0	0.72

4.4.3 Computational Methods and Additional Results

The MD simulations and this section were prepared by Dr. Felipe Jiménez-Ángeles

We simulate a dense phase of nanoparticles functionalized with single-stranded DNA chains in equilibrium with a reservoir containing an electrolyte solution. The spherical nanoparticles are 4.5 nm in diameter and are decorated by 18 single-stranded DNA chains represented by 16 charged beads. Each DNA bead bears a negative unit charge -*e*. The spherical nanoparticles are made of uncharged non-polarizable atoms. The dense phase is built by placing 108 nanoparticles in a cubic simulation box of 42 nm per side. Free monovalent cations in the simulation box neutralize the nanoparticle's charge. The nanoparticles are arranged into an FCC crystal using a unit cell of 14 nm per side. Initially, the nanoparticle's dense phase is placed next to an electrolyte solution contained in a region of 42 nm per side. The simulation box is 42 nm in the *x*- and *y*-directions and 84 nm in the *z*-direction and contains the nanoparticles' dense phase and the electrolyte solution. The solvent is considered implicitly as a uniform background of dielectric constant ε_r.

The beads forming the spherical nanoparticles, the DNA chains, and the ions interact via a shifted and truncated Lennard-Jones potential that only includes the repulsive part. The electrostatic interactions between charged beads are considered using the Coulombic interaction. The interactions between the beads are expressed as:

$$u_{ij}(r) = \begin{cases} 4\epsilon\left[\left(\frac{\sigma}{r}\right)^{12} - \left(\frac{\sigma}{r}\right)^{6} + \frac{1}{4}\right] + \frac{z_i z_j e^2}{4\pi\varepsilon_0\varepsilon_r r} & \text{for } r \le 2^{1/6}\sigma \\ \frac{z_i z_j e^2}{4\pi\varepsilon_0\varepsilon_r r} & \text{for } r > 2^{1/6}\sigma \end{cases}$$

(4.15)

For all the beads σ = 0.475 nm and ϵ = 0.55 kJ/mol; z_i is the valence of species *I*, ε_0 is the vacuum permittivity, $\varepsilon_r = 78.5$ is the water relative dielectric constant, and e is the positive elementary charge. We use harmonic-potential interactions between neighboring atoms of the spherical nanoparticle, between neighboring DNA beads, and to attach the DNA chains to the nanoparticle's surface.

The MD simulations were conducted using the package GROMACS [150, 151]. Newtons' equations of motion are integrated using stochastic Langevin dynamics, and the electrostatic interactions are calculated using the PME algorithm. We apply periodic boundary conditions in the *x*, *y*, and *z* directions. We performed MD simulations using a 5-fs time-step at T = 298 K. The equilibration is performed in three stages. First, we perform an MD simulation of 2×10^6 time-steps at constant *NVT* using constraints on the grafted nanoparticles to maintain them in place. This stage is performed to allow the two regions to exchange ions. In the second stage, we perform an MD simulation of 2×10^6 time-steps at constant NP_zT with no constraints on the nanoparticles; P_z implies that only the *z*-direction of the simulation box is allowed to fluctuate while the *x*- and *y*-directions are fixed. **Table 4.5** contains the composition and conditions of the systems. The production run is performed over at least 4×10^7 time steps at constant NPT. The temperature is controlled using the Langevin thermostat, and the pressure is maintained using the Parrinello-Rahman barostat. The initial 10^7 time-steps are discarded from the production run. The equilibrium

ionic density profiles and the nanoparticles' pair correlation function are calculated from the production run

Fig. 4.13 shows the ionic density profiles $\rho_i(r)$ around the nanoparticles from simulation runs with different concentrations of the divalent ions in the reservoir. The profiles are calculated from the last 100 ns of the simulation runs, considering the average over each nanoparticle in the dense phase. The density profiles of the grafted chains beads show modulations from about 2.5 to 2.8 nm due to the beads attached to the nanoparticle's surface. The peak at around 3.3 nm indicates the radial distance at which interdigitation between DNA on adjacent particles begins. From about 3.3 nm, the chains' density profiles decrease smoothly due to the interaction with the grafted chains of neighboring nanoparticles. At the low reservoir concentration of 0.9 M. (**Fig. 4.13b**), the ionic profiles show that the divalent ions are adsorbed strongly, whereas the concentration of monovalent anions near the nanoparticles' surface is much lower than the bulk concentration. As the ionic concentration increases, the divalent cations and the anions increasingly adsorb at the nanoparticle surfaces (**Fig. 4.13c-d**), and the profiles display an oscillatory behavior due to the enhancement of the ionic correlations [152]. From about 3.7 nm, the density of divalent ions decreases whereas the density of anions increases. This behavior indicates that the overall charge in the brush (including the nanoparticle's charge plus the ions) is negative. Below we discuss in further detail the charge distribution around the nanoparticles. At distances above $r \approx 5.5$ nm the profiles reach a bulk value of the dense phase, and further away, reach the concentrations in the reservoir.

To investigate the charge distribution near the nanoparticles, we use the local charge density $\rho_{el}(r)$ given by:

$$\rho_{el}(r) = \sum_{i=1}^{4} z_i \rho_i(r))$$

(4.16)

where z_i and $\rho_i(r)$ are the valences and local number densities, respectively, and i = 1,…,4 represent the chains beads, divalent cations, monovalent cations, and monovalent ions, respectively. **Fig. 4.14a** shows the average charge density profiles around the nanoparticles $\rho_{el}(r)$ at different ionic concentrations. We observe that near the nanoparticle's surface, $\rho_{el}(r)$ is negative because only the negatively charged chains' beads are located within the region r < 2.7 nm. The minimum located at $r \approx$ 2.7 nm coincides with the ions' closest approach distance to the nanoparticles. As the distance from the nanoparticles' surface increases, $\rho_{el}(r)$ increases reflecting the ions adsorbed to balance the charge of the grafted chains. Due to the ionic correlations, the charge density profiles oscillate within the grafted chains region. The profiles show a maximum at $r \approx$ 2.85 nm and then a minimum at $r \approx$ 3.3 nm due to the chains' end and the starting of the ionic diffuse layer outside the brush region. The peak at about $r \approx$ 3.5 nm is due to the divalent cations' adsorption. Outside the brush region, the charge profiles exhibit small oscillations due to the ionic correlations. The following analysis of the cumulative charge density and mean electric field shows that the nanoparticle's charge is not inverted by the adsorbed divalent ions.

Following Gauss' law, we define the cumulative charge density $\sigma(r)$ as:

$$\sigma(r) = \frac{1}{4\pi r^2} \int_0^r \rho_{el}(y)\, 4\pi y^2 \mathrm{d}y$$

(4.17)

This is related to the mean electric field profile around the nanoparticles as $E_r(r) = \frac{\sigma(r)}{\epsilon_0 \epsilon_r}$. In **Fig. 4.14b**, the cumulative charge density profiles for three different ionic concentrations. Inside the brush, the ionic correlations induce regions where the electric field oscillates and changes direction. Outside the grafted chains region, from the minimum at about $r \approx 3.5$ nm, the cumulative charge density increases and goes to zero away from the nanoparticle. This implies that outside the nanoparticle the electric field remains negative, namely, there is no charge inversion.

Here we present a consistency analysis of the system's chemical equilibrium and the ionic concentrations in the two phases. We consider that the system is formed by *n* different species each with number density $\rho_i = \frac{N_i}{V}$ and chemical potential μ_i; N_i is the number of particles of species *I*, *V* the total volume, and $i = 1, \ldots, n$. The components are divided into two regions (α and β phases) with corresponding number densities ρ_i^{α} and ρ_i^{β}, where the subscript designates the species and the superscript represents the phase and $\rho_i^{\alpha} \neq \rho_i^{\beta}$, in general. The equilibrium ion concentration in the reservoir and the nanoparticle dense phase are determined by the chemical equilibrium, namely, $\mu^{\alpha}{}_i = \mu^{\beta}{}_i$, where μ_i is the chemical potential of species *i*.

In terms of the Gibbs free energy, the chemical potential is given as:

$$\mu_i = \left(\frac{\partial G}{\partial N_i}\right)_{T,P,N_{j\neq i}} \qquad \textbf{(4.18)}$$

where N_i is the number of particles of species i and n is the number of species in the system. The chemical potential is the change in the Gibbs free energy by introducing one 'molecule' into the system:

$$\mu_i = \left(\frac{\Delta G}{\Delta N_i}\right)_{p,T,N_{j\neq i}} = G(T,p,N_1,\dots,N_i,\dots,N_n) - G(T,p,N_1,\dots,N_i-1,\dots,N_n)$$

(4.19)

We calculate the change of the free energy using the slow-growth method in thermodynamic integration [151, 153] to transform the system from state A to state B as follows:

$$\Delta G = G^B(T,p) - G^A(T,p) = \int_0^1 \left\langle \frac{\partial H}{\partial \lambda} \right\rangle_\lambda d\lambda$$

(4.20)

λ is a coupling parameter that varies from 0 to 1 to modulate the interaction between the target molecule and the medium that is gradually turned in the system's Hamiltonian H, such that the interaction between the medium and the molecule is switched off at state A ($\lambda = 0$) and is on in state B ($\lambda = 0$).

In a non-uniform system, the chemical potential is given as:

$$\mu_i = \mu_i^{id}(\mathbf{r}) + \mu_i^{ex}(\mathbf{r})$$

(4.21)

where the ideal part is given by [154]:

$$\mu_i^{id}(\mathbf{r}) = k_B T \ln(\rho_i(\mathbf{r})\Lambda_i^3)$$

(4.22)

where $\Lambda_i^3 = \sqrt{h^2/(2\pi m_i k_B T)}$ is the de Broglie thermal wavelength and m_i is the mass of species i. In a non-uniform system, both the ideal and the excess chemical potential contributions depend

on the position in the system, but the total chemical potential is independent of the position. The excess chemical potential is equal to the free energy of inserting the ions into the system:

$$\mu_i^{ex}(\mathbf{r}) = \Delta G(\mathbf{r})$$

(4.23)

The excess chemical potential can be split into the Lennard-Jones and Coulombic contributions as:

$$\mu_i^{ex}(\mathbf{r}) = \mu_i^{LJ}(\mathbf{r}) + \mu_i^{C}(\mathbf{r})$$

(4.24)

where each of the contributions is computed by performing a slow-growth thermodynamic integration for each of the interactions (see **Eq. 4.20**).

To evaluate the chemical potential, we consider reduced systems for the dense phase and the bulk. The dense phase consists of four nanoparticles in an FCC unit cell and the ions. The reduced bulk phase contains only the ions. The ionic concentrations are taken from the data reported in **Fig. 4.3**. The composition of the systems and the results are presented in **Table 4.6**. We employed 20 λ -steps to turn on the interactions, the first 10 are for the Lennard-Jones interactions and the other 10 are for the Coulombic interactions. Each simulation for a fixed value of λ is performed for 20 ns. To maintain the system's electroneutrality during the free energy calculation, we consider inserting an artificial 'molecule' with no internal bonds consisting of one Ca^{2+} ion and two Cl^- ions. We refer to this artificial molecule as a *triplet*. In the dense phase, we fixed the ions at a position away from the grafted nanoparticles to avoid the position dependence of the excess chemical potential.

The results of the chemical potential are presented in the last column of **Table 4.6**. In the dense phase systems, we see that the system that is in closer agreement with the chemical potential

in bulk is that with the lower ionic concentration than in the bulk. This result further supports our finding presented in **Fig. 4.3**, in which the systems with divalent ions reservoir concentrations above 2M, the ionic concentration is higher in the reservoir than in the dense phase.

We performed additional MD simulations employing systems consisting of 32 nanoparticles within a simulation box of dimensions $L_x = L_y = 28$ nm, and $L_z \approx 56$ nm. We employed a similar approach as described for the larger systems consisting of 108 nanoparticles. The initial configuration consists of nanoparticles dense phase arranged into an FCC crystal placed next to a reservoir containing initially the divalent cations and the monovalent anions. The crystal is formed of 2×2×2 unit cells replicated in the *x*-, *y*-, and *z*- directions and contains the necessary monovalent cations to neutralize the nanoparticles' charge. The compositions of the systems are provided in **Table 4.7**. These smaller systems allowed us to perform MD simulations of up to 2 μs. The results of the pair correlation functions are presented in **Fig. 4.15**. The mean separation distance between the nanoparticles (the positions of the maxima in the pair correlation functions) are 8.7 nm, 8.0 nm, and 8.8 nm at the molar concentrations of 1, 1.5, and 2.0 M, respectively. We recover the non-monotonic behavior as observed in the larger systems of 108 nanoparticles. The longer simulations allowed us to see the nanoparticles expand to occupy the whole simulation box, reflecting weakening attractive interactions at higher salinities, and properties resembling a fluid-like phase.

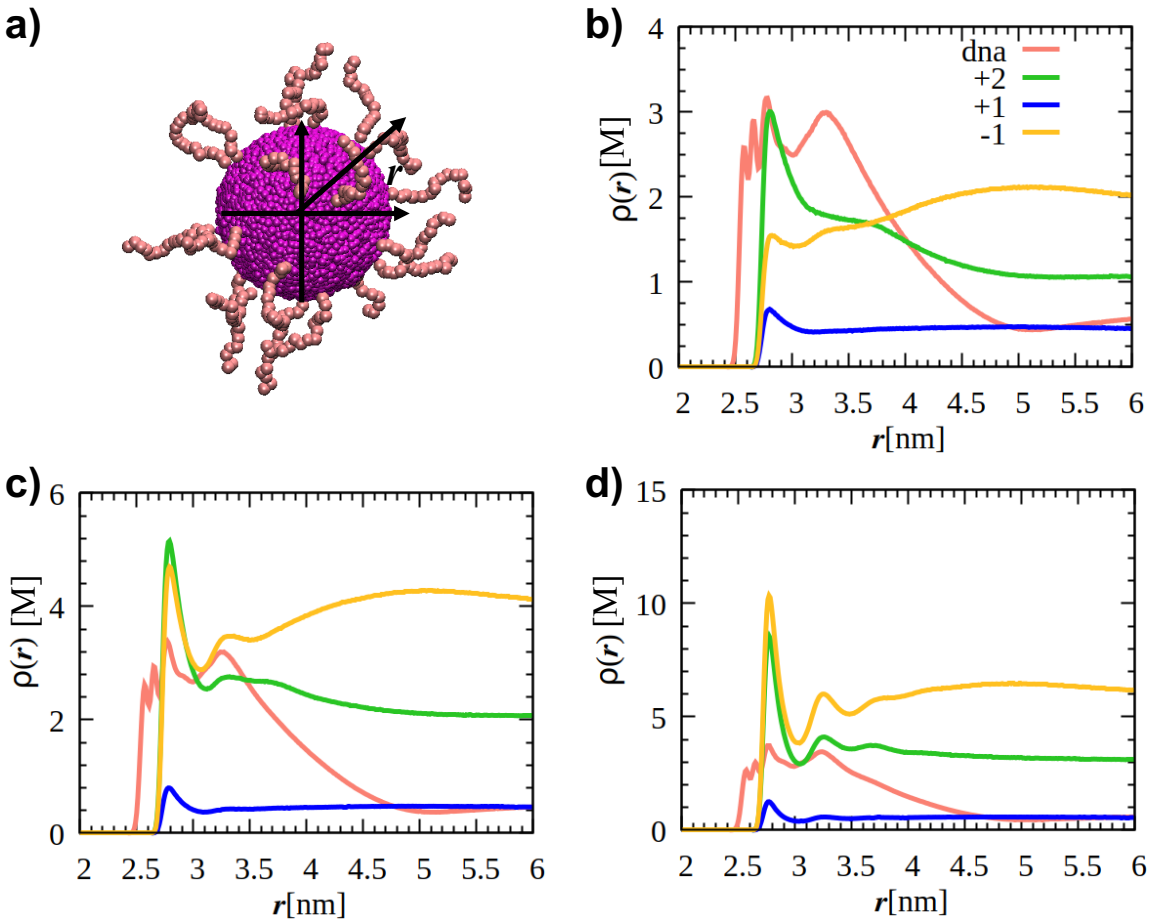

Figure 4.13: (a) Coordinate system employed to compute the density profiles of the species in the system as a function of the radial distance from the center of the nanoparticles, r. The divalent ions concentrations in the reservoir are (b) 0.9M, (c) 2.0 M, and (d) 3.1 M; the light-red lines represent the profiles of the beads forming the grafted chains; the green, blue, and yellow lines represent the profiles of divalent cations, monovalent cations, and monovalent anions, respectively.

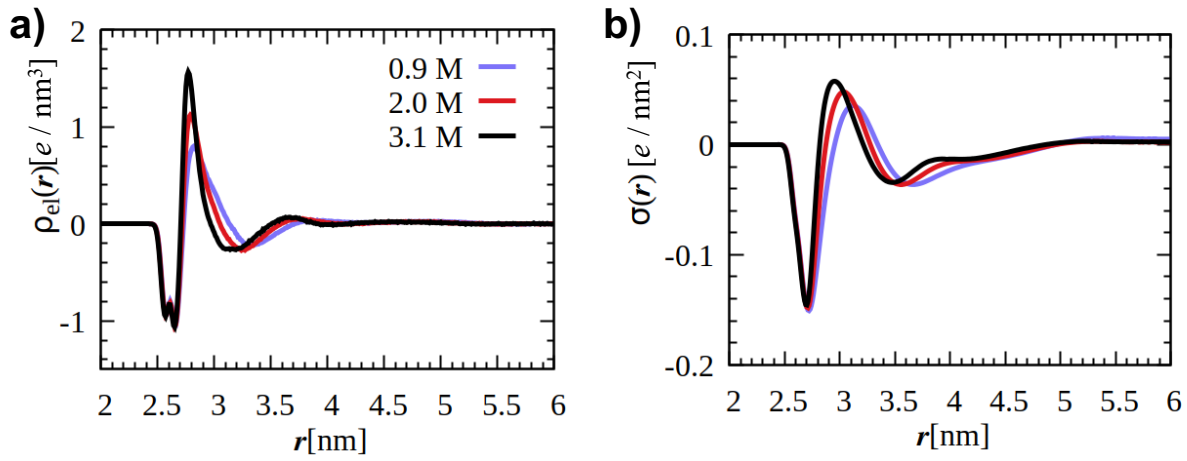

Figure 4.14: (a) Charge density profiles $\boldsymbol{\rho_{el}(r)}$ and (b) cumulative charge density profiles $\boldsymbol{\sigma(r)}$ at three ionic concentrations, 0.9, 2.0, and 3.1M.

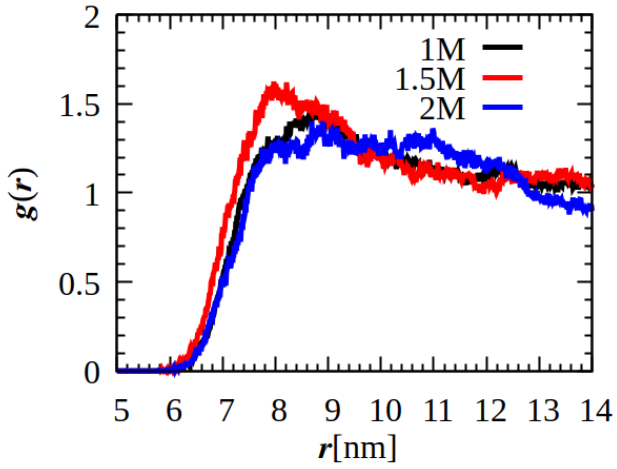

Figure 4.15: Pair correlation functions between the nanoparticles at the overall ionic concentrations of 1, 1.5, and 2 M. The results correspond to systems formed by 32 nanoparticles which allowed to run the simulation up to 2 μs.

Table 4.5: Composition of the simulation box. N_{2+} is the number of divalent ions, N_{+} is the number of monovalent cations, and N_{-} is the number of anions in the simulation box. P is the pressure.

System	N_{2+}	N_{+}	N_{-}	P [bar]
1	133893	39744	267786	240
2	178524	39744	357048	370
3	223155	39744	446310	570
4	223155	39744	446310	750
5	223155	39744	446310	950

Table 4.6: Composition of the systems employed to calculate the chemical potential. N_{2+} is the number of divalent ions, N_+ is the number of monovalent cations, and N_- is the number of monovalent anions; $\boldsymbol{\rho_{2+}}$ is the number density of the divalent ions, $\boldsymbol{\rho_+}$ is the number density of monovalent cations, and $\boldsymbol{\rho_-}$ is the number density of monovalent anions. The simulation boxes are cubic with 11.8 nm per side.

System	N_{2+}	N_+	N_-	$\boldsymbol{\rho_{2+}}$**[M]**	$\boldsymbol{\rho_+}$ **[M]**	$\boldsymbol{\rho_-}$ **[M]**	$\boldsymbol{\mu_{trp}}$**[kJ/mol]**
Dense phase	3140	513	5321	3.17	0.512	5.376	-1652 ± 7
Dense phase	3040	513	5121	3.07	0.512	5.175	-1623 ± 4
Bulk	3140	513	6793	3.17	0.512	6.863	-1628 ± 4

Table 4.7: Composition of the systems formed by 32 grafted nanoparticles. N_{2+} is the number of divalent ions, N_+ is the number of monovalent cations, and N_- is the number of anions in the simulation box. P is the pressure.

System	N_{2+}	N_+	N_-	P **[bar]**
1a	26400	11776	52800	110
2a	39600	11776	79200	195
3a	52800	11776	195600	310

Chapter 5: Mechanisms of FCC-to-BCC Transitions in DNA-NPs

Much of the work in this chapter is published in *Faraday Discussions* as Transformations in crystals of DNA-functionalized nanoparticles by electrolytes (Roger J.E. Reinertsen, Felipe Jiménez-Ángeles, Sumit Kewalramani, Michael J. Bedzyk, and Monica Olvera de la Cruz[155]

Colloidal dispersions of like-charged particles in deionized water are stable due to the particles' mutual electrostatic repulsion; however, the mobile ions in the medium screen the electrostatic interactions, resulting in a decrease in the strength and range of these interactions with increasing salt concentration[156]. The screened Coulombic interactions can be considered using the potential derived in the Derjaguin-Landau-Verwey-Overbeek (DLVO) theory [157, 158], which depends on a screening length $\lambda = \kappa^{-1}$. The screening length can be adjusted by changing different parameters in the system. In particular, the inverse of the screening length κ increases by increasing the ions' concentration and valence and decreases by increasing the temperature and the medium dielectric constant. In certain solution ionic conditions, charged particles form highly ordered arrays of particles known as colloidal crystals[159-161].

Like-charged, spherical colloidal particles interacting via repulsive screened Coulombic interactions assemble into different lattice types depending on screening length; typically, larger screening lengths, allowing for "softer", longer-ranged repulsions, favour the body-centered cubic (BCC) structure, while smaller screening lengths, leading to "harder", shorter-ranged interactions, favour the face-centered cubic (FCC) structure [162-164]. Here, we show that nanoparticles functionalized with highly charged flexible ligands, assemble into FCC crystals at low salt concentrations, and BCC crystals at high salt concentrations. This is quite unexpected, as in charged systems, FCC structures do not transition to BCC, including when co-assembled

with highly size-asymmetric oppositely charged nanoparticles [165, 166]; exceptions typically require specific interactions or the presence of an external field.[159] Our analysis of the present system suggests that water-mediated interactions between the ions and the charges in the nanoparticles are responsible of transforming FCC to BCC as the salt concentration increases.

Some insights into the relative stability of FCC and BCC structures in ligand-coated nanoparticles may be gleaned from experimental observations and phenomenology in systems of particles consisting of hard cores and *neutral* polymer brush shells (grafted particles or diblock copolymer micelles). In these systems, the stability of FCC and BCC structures varies depending on the particle properties. A small ratio of the brush length-to-core radius favours FCC structures, while a large ratio favours BCC micelles [122]. Low surface densities of grafted polymer chains favour BCC structures [123]. The role of the effective softness has been quantified [167, 168]. Soft brushes (long and sparse) stabilize second-nearest neighbour interactions in BCC structures. High chain flexibility and large brush-to-core ratios favouring BCC structures also apply to nanoparticle superlattices assembled via DNA-bases pairing [169]. Small nanocrystals grafted with alkyl ligands favour BCC structures when the ligands are longer [170]. These results are explained in a model by assuming that the "packing frustration" of the ligands decreases in BCC structures. Consequently, a smaller number of chains needs to be compressed or extended to accommodate packing constraints than in the FCC structure [171].

FCC to BCC transitions have been observed in some systems such as diblock copolymer micelles in water upon increasing temperature due to a decrease in the aggregation number of the micelles, thus making the brush sparser (and "softer) [172]. Alkyl-grafted nanocrystals assembled via slow solvent removal [173 174] transition from FCC to BCC structures as they dry. Lattices of oleic-acid functionalized nanocrystals transition from FCC to BCC structures as a non-solvent

(such as ethanol) is added, which should pull solvent away from the ligands, destabilizing the particles[175]. Related studies show that swelling of a nanocrystal lattice with solvent vapor drives a transition from BCC to FCC.[176]

In ligand-coated systems, FCC structures appear to be favourable over BCC structures in the presence of solvents favourable to the ligands. One hypothesis is that the swelling of the alkyl ligands by a solvent makes the particles behave as hard sphere, so the ligands do not deform (or interdigitate) favouring FCC structures [177]. Similar reasoning appears in a molecular dynamics study of nanocrystals suspended in toluene and hexane [178]. Missoni and Tagliazucchi use a molecular theory to show that the presence of solvents in nanoparticle superlattices favours FCC over BCC structures[179]. Extending these considerations to a charged, ion-containing aqueous system would be an exciting step forward.

5.1. Experimental Methods

We select the sequence 5'-T_{35}-C_3SH- 3' to prepare grafted DNA with a minimal propensity for base-pairing and forming secondary structure. The 3' propyl-thiol terminated oligonucleotides are synthesized using a MerMade solid-state controlled pore glass (CPG) DNA synthesizer (BioAutomation) via phosphoramidite chemistry. Following the synthesis, the DNA is released from the CPG beads using a mixture of methylamine and NH_4OH (1:1 volume ratio) at 55°C for 30 minutes. The DNA is then transferred to DI water and purified via reverse-phase high-performance liquid chromatography (RP-HPLC). The 5'-DMT group, which enables separation via HPLC, is then removed via a reaction with 20% acetic acid and subsequent extraction with ethyl acetate. The purity and molecular weight of the synthesized sequences are verified with matrix-assisted laser desorption/ionization time-of-flight spectroscopy (MALDI-

TOF, from Bruker). The concentration of the DNA solutions is determined via UV-Vis spectroscopy at 260 nm.

The thiol-terminated oligonucleotides are grafted to the surfaces of the colloidal gold nanoparticles following established methods[82] . Briefly, the thiolated DNA molecules are reduced in 100 mM dithiothreitol (DTT) maintained at an approximate pH of 8 via phosphate buffer. Following the reaction for 30-60 minutes, the DNA is transferred to the water via purification through size-exclusion NAP5 columns. The reduced DNA is added to colloidal AuNP solutions of about 10 nM at an approximate ratio of 372 DNA/AuNP. The solutions are incubated overnight. Sodium chloride (NaCl) and small quantities of 0.1% Sodium Dodecyl Sulfate (SDS) are then slowly added to the solution for 8 hours until a final concentration of 1 M NaCl is achieved. This process enables high grafting density on the nanoparticles. Unbound DNA is removed via centrifugation using 50 kDa spin filters. To minimize the presence of NaCl, unbound DNA, and SDS in the final nanoparticle stocks, we transfer the DNA-AuNPs to DI water and purify them through three centrifugation rounds. Final DNA-AuNP concentrations are determined by applying Beer's Law to the UV-Vis-measured absorbance of the AuNP at 520 nm.

The number of DNA strands per particle is measured using[180] a Quant-iT Oligreen Assay from Invitrogen. To dissolve the gold cores and release the DNA into the solution, suspensions of known DNA-AuNP are briefly reacted in 20 mM KCN solution at 50°C. The liberated DNA is then stained with the Oligreen fluorescent dye (diluted in TE buffer as per manufacturer instructions). The fluorescence of these solutions at 480 nm is measured using a Biotek Cytation 5 imaging reader. These values are compared to those measured for Oligreen-stained 5'-T_{35}-C_3SH- 3' solutions of various known concentrations. Comparison to the calibration curve's

fluorescence allows for quantifying the amount of DNA associated with a known quantity of DNA-AuNPs, thus determining average loading.

To prepare samples with high salt concentrations, saturated solutions of $CaCl_2$ and NaCl in water were prepared at ~22°C and allowed to equilibrate with precipitated hydrate phase at least 12 hours before use. Solutions were prepared using Calcium Chloride Dihydrate (99.5% purity, Sigma-Aldrich) and Sodium Chloride (99.99% purity Suprapur®, Millipore-Sigma). Samples for SAXS analysis were prepared in total volumes of 30-50 μL, with final DNA-AuNP concentrations of 50 nM, and the $CaCl_2$ solution being the final component added to the mixture. Following the addition of the salt, the solution was promptly (within 60 seconds) homogenized via pipette and transferred to 1.0 mm or 1.5 mm quartz glass capillaries (Charles Supper). The capillaries were then sealed with epoxy, and 24-36 hours were allowed to elapse prior to measurement.

SAXS measurements on nanoparticle suspensions were conducted at beamline 5ID-D of the Advanced Photon Source. To compensate for the X-ray attenuation of the concentrated salt solutions, the X-ray energy was tuned to 17 keV (0.7293 Å wavelength). The scattered intensities were measured simultaneously using three Rayonix CCD detectors positioned ~0.2m, ~1.0m, and ~7.5m from the sample, allowing for data collection over the range $0.02\ nm^{-1} < q < 30\ nm^{-1}$. The X-ray spot size on the sample position was 0.25 mm x 0.25 mm, and the incident flux was ~ 3×10^{11} photons/s. Capillary samples were mounted horizontally on a translating capillary stage. Samples were scanned for sets of three 5-second exposures, with the capillaries being translated continuously at 0.508 mm/s during measurement to minimize radiation damage. The 2D data was reduced to 1D intensity profiles via azimuthal integration (using GSAS-II), following corrections for polarization, detector solid angle, and transmission.

Additional SAXS measurements on separately synthesized DNA-NP samples in aqueous solutions [$CaCl_2$] varied in 50-100 mM increments were carried out in the J.B. Cohen X-ray Lab at Northwestern University. A Rigaku SMAXS-3000 setup was utilized, equipped with a Cu microbeam anode, multilayer focusing mirrors, and an Eiger R1M 75uM pixel single photon counting 2D detector positioned 1.56 m from the samples stage. CuKα X-rays (8.04 keV energy, or 1.542 Å wavelength) were utilized. "High resolution" slit sizes were selected for measurements, where incident vertical and horizontal slits focus the beam to around 0.5 x .0.5 mm on the sample. Samples were contained in 1.0 mm quartz capillaries from Charles Supper kept in air at ambient conditions. SAXS patterns were collected for 20 minutes each, scattering being recorded via the Xenocs Instrument Control Center (XICC) software. Following collection, the 2D scattering patterns were converted to 1D profiles via azimuthal integration, carried out by the instrument software.

In order to gain insight into the configuration of the DNA shell, small angle neutron measurements were carried out at beamline CG3 BioSANS of the High Flux Isotope Reactor (HFIR)[181, 182]. The instrument is equipped with a dual two-dimensional linear position-sensitive ^{3}He 2D detectors. For these measurements, the small angle detector was positioned 7 m from the sample, and the wing detector at 1.13 m from the sample, angled 3.2°. Neutrons with 6Å wavelength were selected, a relative wavelength spread ($\Delta\lambda/\lambda$) of 14%. This configuration allowed measurement of scattered neutrons for $0.007 < q < 0.925$. Collected data was corrected for instrument background, detector sensitivity, and instrument geometry and converted into combined 1D Intensity profiles using drt-SANS[183]. In preparation, DNA-NPs were prepared dispersed in D_2O, to avoid the large incoherent scattering of H_2O. 400 μL of 500 nM DNA-NP suspensions with either 0 or 1.5 M $CaCl_2$ were added to 1.0 mm path length banjo cells. The

cells were placed in a tumbler stage, and tumbled at low speeds, to prevent sedimentation of the DNA-NP aggregates. Each sample was measured for a total of 6 hours. Cells containing DNA-NP, but otherwise compositionally equivalent solutions were also measured under the same circumstances, enabling the isolation of the signal associated with scattering from the DNA-NPs via background subtraction.

5.2. X-ray Scattering Results

Single-stranded (ss)-DNA-functionalized gold nanoparticle conjugates (DNA-NP) have a high net negative charge, which results in repulsive electrostatic interactions between particles. These repulsions prevent the nanoparticles' precipitation even in concentrated NaCl solutions. By contrast, in the presence of sufficient concentrations of Ca^{2+} ions (as provided by the addition of $CaCl_2$), attractive forces drive the precipitation of the conjugates within minutes. In-situ small-angle X-ray scattering (SAXS) measurements reveal that the conjugates pack into FCC lattice just above a threshold $CaCl_2$ concentration of ~ 280 mM (**Fig. 5.1a-b**). SAXS also shows that increasing the $CaCl_2$ concentration drives the compression of the lattices (**Fig. 5.1b, e**). Above 700 mM $CaCl_2$, the aggregates transition into BCC crystals, with the interparticle separation continuing to decrease with added salt (**Fig. 5.1c, e**). While the BCC phase features a lower packing efficiency than the FCC phase, we calculate that the volume per particle within the lattice continues to decrease across the transition (**Fig. 5.1f**). We note here that our previous study on non-base pairing, ssDNA-grafted nanoparticles assembled via Ca^{2+} cations instead displayed a transition from FCC to an amorphous, glassy state at higher $CaCl_2$ concentration.[184] We attribute this difference to more homogenous DNA coverages in the present study, as well as

greater intervals between sample preparation and measurement enabling additional growth of colloidal crystals.

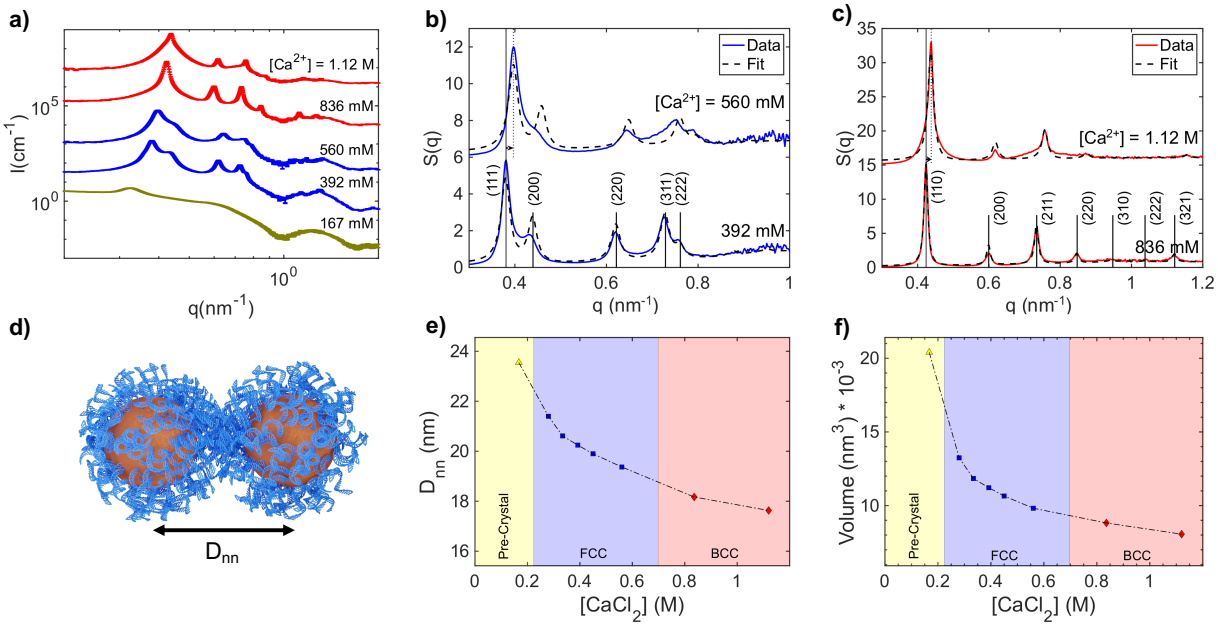

Figure 5.1: (a) Background-subtracted small-angle X-ray scattering data for the DNA-grafted nanoparticles assembled at various $CaCl_2$ concentrations. (b and c) Extracted structure factors for the nanoparticle aggregates, compared to model fits for FCC (b) and BCC (c) crystals. (d) A schematic defining the nearest-neighbor interparticle separation, D_{NN}, which the nanoparticles assume in the colloidal crystals. (e) A plot of phase and nearest-neighbor separation (D_{NN}) as a function of $CaCl_2$ concentration. "Pre-crystal" refers to nanoparticle suspensions with no visible sedimentation, and very weak scattering peaks. (f) A plot of volume per nanoparticle in the structures, as calculated from the lattice parameters and packing efficiencies; the volume per particle decreases across the FCC–BCC transition.

Based on **Figure 5.1**, the transition between the two crystal structures DNA-NP appears rather sharp with respect to salt concentration, with no signature of a second structure detected at 560 or 832 mM $CaCl_2$. The range of salt concentrations that permit coexistence of the two structures provides insight into the factors influencing assembly. Whether multiple phases occur in "coexistence regions" over a range of variables (such as temperature and compositions), or at specific "coexistence boundaries", provides insight into the number of degrees of freedom in the

system[185]. In the context of the present, a wide region of coexistence (with respect to salt) would result from varied partitioning of Ca^{2+} across different DNA brushes (potentially being influenced by any polydispersity of the DNA-NPs). Indeed, FCC-BCC coexistence in colloidal crystals formed from highly asymmetric particles has been demonstrated to be stabilized by such factors[186]. While the present boundary between the phases appears sharp, we conducted additional SAXS measurements to investigate the transition more closely, with [$CaCl_2$] being varied in reduced 50-100 mM increments. The results of these measurements are shown in Figure 5.2. For these DNA-NP samples, the FCC-to-BCC transition occurs sharply between 500 mM and 550 mM, contrasting with that of other DNA-NPs. This apparent variance between nanoparticle batches reflects the significance of the properties of the grafted DNA; specifically, relevant is the grafting density, which varies between batches (see Table 4.1), and has been implicated in influencing the relative stability of FCC and BCC structures[123]. While **Figure 5.2** serves to reduce any potential "coexistence region" to a range of less than 50 mM, the distortions of the diffraction peaks of samples between 500 and 600 mM $CaCl_2$ likely reflect small energetic differences between the two structures manifesting as potential disorder and/or intermediate phases. The latter explanation is particularly intriguing considering that assemblies of nanoparticle tectons [187] undergo diffusionless transitions between these two structures as solvent quality is decreased [188]. In this case, the FCC-to-BCC transition occurs via the Bain distortion mechanism, where a pathway is accessed through body-centered tetragonal (BCT) intermediate phases[189]. Additional, higher-resolution (e.g., synchrotron) measurements near the transition in the present system could yield further mechanistic insight. To conclude, our measurements suggest that DNA-NP structures reflect equilibration with the surrounding electrolyte and implicate the configurations of the DNA brushes as mediating FCC-to-BCC structural

transitions. These apparent changes in grafted polyelectrolyte configuration resemble those induced by reduced solvent quality, here apparently arising from increased ionic strength of the solutions. Such an effect resembles the "salting out" of proteins[190]. In the next sections, we employ neutron scattering measurements and molecular dynamics simulations to test(?) these hypotheses.

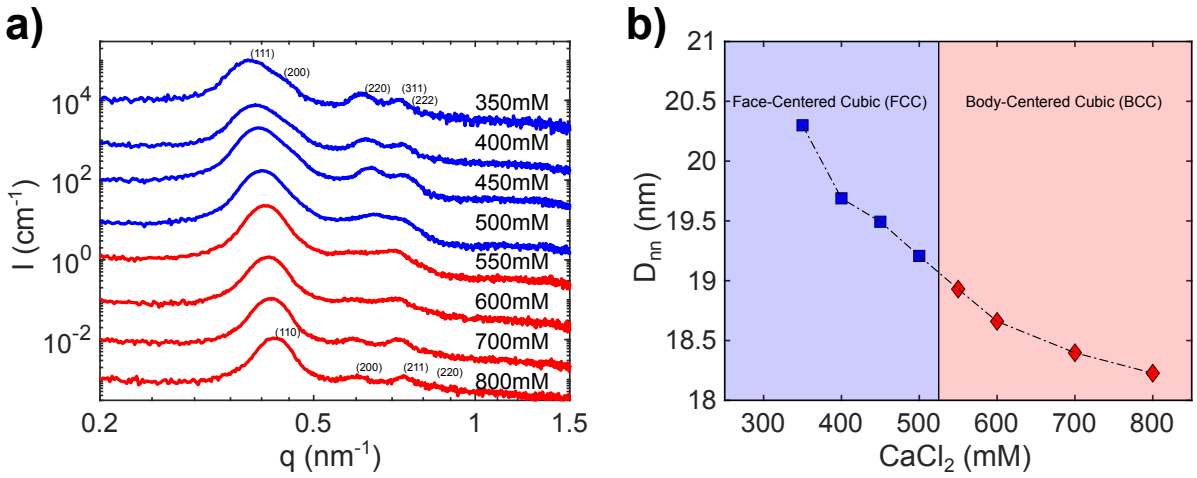

Figure 5.2: (a) SAXS intensity profiles for DNA-NPs assembled at $CaCl_2$ concentrations incrementally varied across the FCC-to-BCC transition. Blue curves demote FCC structure factors, and red BCC structure factors. Note that the patterns recorded at 500, 550 and 600 mM appear disordered. The phase and nearest-neighbor separation (D_{nn}) are plotted as a function of $CaCl_2$ concentration in (b).

5.3. Neutron Scattering Results

While our X-ray scattering results provide information concerning the positioning of the nanoparticle cores, information concerning the conformation and solvation of the grafted DNA manifests as a signal too weak to resolve. Considering the evidence that lattice type is influenced by the interactions between ligands and solvents, this missing information is of interest. Thus, we turn to the results of our SANS measurements to resolve directly resolve the effects of [$CaCl_2$] on DNA. In **Figure 5.3**, SAXS and SANS intensifies are compared for DNA-NPs in pure D_2O

(and therefore dispersed), and in 1.5 M $CaCl_2$ solution (aggregated). The diffraction peak associated with the DNA-NP core ordering is present in both sets of data at 1.5 M $CaCl_2$. Additional intensity modulations are present both sets of SANS data when compared to the SAXS data, reflecting the scattering contribution of the DNA. These modulations appear to be relatively weak, potentially reflecting the hydration state of the DNA. More specifically, strong hydration of the grafted oligonucleotides will decrease the effective scattering length density of the "shell" surrounding the nanoparticle.

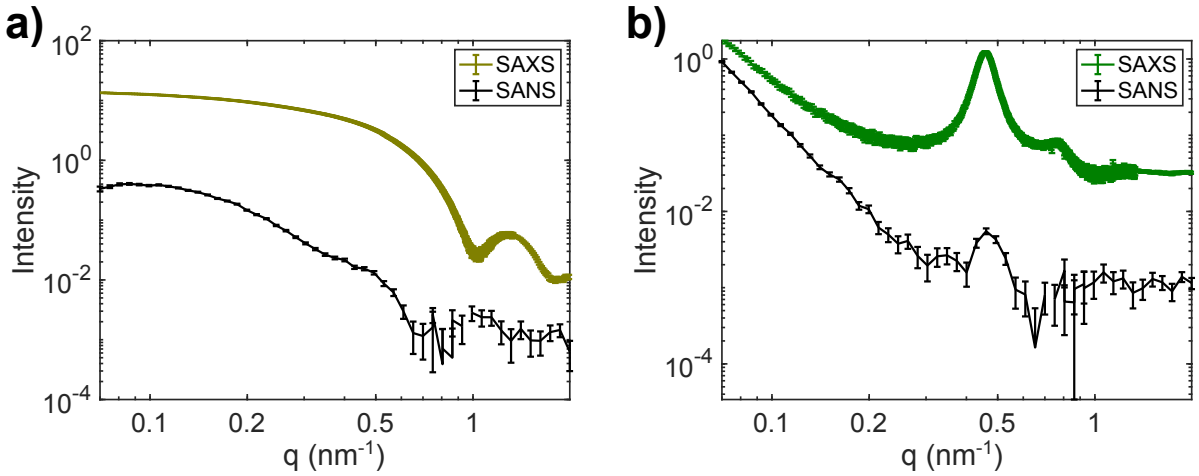

Figure 5.3: SAXS and SANS intensity profiles for DNA-NPs in 0 M (a) and 1.5 M (b) $CaCl_2$ solutions. Additional intensity modulations appear in the SANS profiles, reflecting the scattering contribution of the DNA. The large peak found in both measurements of the 1.5 M samples arises from DNA-NP ordering (here a broad peak corresponding to structures lacking long-ranged order). The large relative error bars of the SANS data reflect the lower total detected counts.D_2O was used as the solvent to minimize incoherent scattering in the SANS measurements.

The applicability of a core-shell form factor for modeling the data was evaluated. Such a model has previously been applied to DNA-NPs grafted with 7-15 base sequences[191] . For this approach, a radius of the nanoparticle core (R_{au}, here determined from SAXS to be 4.5 nm) and a radial extent of the shell are selected (T_s). The neutron SLD values of the DNA, gold, and solvent are input as well (**Table 5.1**). Based on these values, as well as the grafted number of DNA

molecules and the molecular dimensions of DNA[192] , an "average" SLD for the shell is computed, weighted by the volume fractions of DNA and solvent. **Figure 5.4** shows some of the results of these efforts. For DNA-NPs in 0-salt conditions, the core-shell model over-estimates the sharpness of the various minima; indeed, in low salt conditions, the DNA would be mostly stretched due to electrostatic repulsions. This stretching would introduce radial dependence to the SLD distribution within the shell, smearing the features of the form factor. In spite of this inapplicability, it is in interesting to note that the minima in the model form factor align with that of the data, suggesting that the proposed dimensions may be a good first approximation; this would correspond to an effective total diameter of the T35-DNA-NPs, which is physically reasonable, considering DLS data[193].

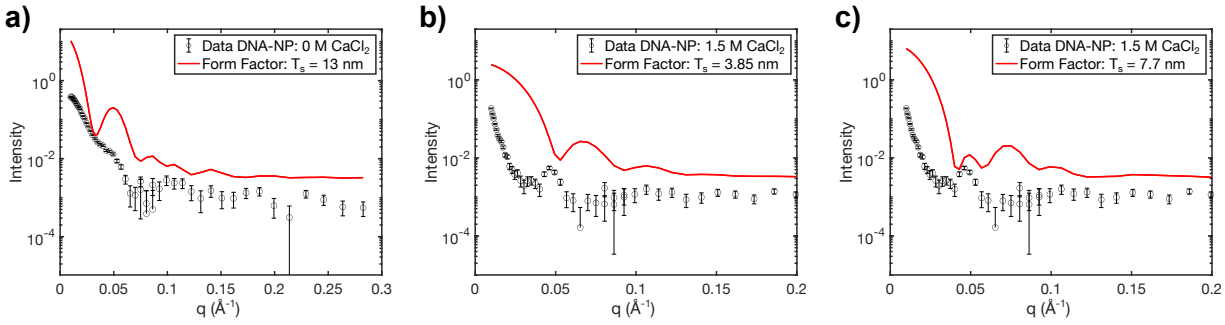

Figure 5.4: SANS profiles and simulated core-shell form factors for DNA-NPs at 0 M (a) and. 1.5 M (b). Form factors are offset using a multiplicative scale factor for ease-of-viewing. The core shell form model consistently overestimates the sharpness of the minima in the data, as it does not account for the radial-dependency or polydispersity of the DNA shell. Nonetheless, the first two minima of the models align with the data in (a) and (c). The compact shell model simulated in (b) fails to capture any features of the data.

Two versions of a core-shell model for the DNA-NPs at 1.5 M are plotted in **Figure 5.4b-c**. The selected values of 3.85 nm and 7.7 nm correspond to the minimum and maximum shell thicknesses, as determined by the distances between the AuNP surfaces at these concentrations. Phrased differently, the former case corresponds to the DNA shells being fully collapsed, whereas the latter corresponds to the DNA on adjacent particles interdigitating,

extending all the way to the surface of the adjacent nanoparticle; as an aside, the question of whether spherical polyelectrolyte brushes is an open question arising from conflicting experimental evidence[77, 194]. Here, it is apparent that the "fully collapsed" model (Tc=3.85) fails to reproduce features in the data, with the primary minima aligning with the diffraction peak, and no evidence of the intensity modulation below 0.05$Å^{-1}$. Rather, the extended model produces minima that align roughly with that of the data. While a more refined model would provide more accurate information, one can conclude from these results that the DNA on a given particle interdigitates with that of its neighbor. This understanding informs the current study, suggesting that the second nearest-neighbor interactions that stabilize the BCC structure may be attained here by a given brush exhibiting simultaneously varying degrees of interpenetration with its neighbors. Finally, such interdigitated conformations become more favored as monomer-monomer interactions become stronger than monomer-solvent interactions, reflecting how the addition of $CaCl_2$ modifies both the electrostatic and solvation environment of DNA.

5.4. MD Simulations Results

The MD simulations and this section were prepared by Dr. Felipe Jiménez-Ángeles

We performed all-atom explicit solvent molecular dynamics (MD) simulations using the setup shown in **Figure 5.5**. The system consists of a DNA-grafted gold nanoparticle immersed in an electrolyte solution made of Ca^{2+} and Cl^- ions. The simulation box is replicated multiple times by applying periodic boundary conditions in the *x*-, *y*-, and *z*- directions. The box sizes considered in our study allow the interaction between the nanoparticles in the neighboring image boxes. Therefore, the simulation box is considered a unit in a three-dimensional crystalline

system. We explored different ion concentrations. The system details are provided in the methods section at the end of the chapter.

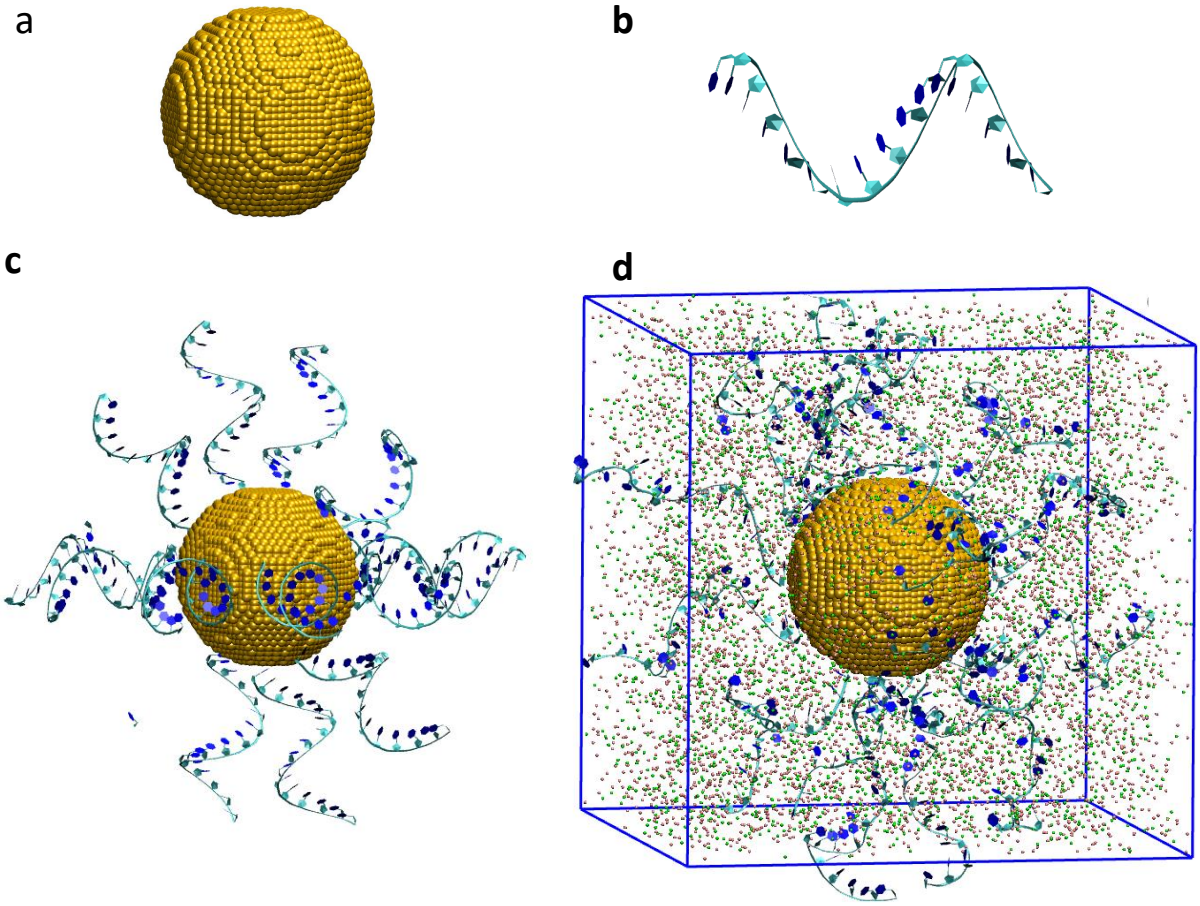

Figure 5.5: Simulation setup employed to analyze the chemical equilibrium of a dense phase made of DNA-grafted gold nanoparticles and a $CaCl_2$ ion reservoir. (a) Nanoparticle of 4.5 nm diameter, (b) all-atom model of a single-stranded DNA molecule made of 17 T-bases, (c) composite system consisting of 18 single-stranded DNA molecules grafted on the surface of the nanoparticle, and (d) simulation box containing a DNA-grafted nanoparticle immersed in an electrolyte solution made of Ca^{2+} and Cl^- ions. Water is included explicitly in the system (not shown). Note that due to computational constraints, the DNA-NPs in simulations have been scaled down by a factor of ~2. The number of DNAs per Au nanoparticle is correspondingly reduced to roughly match the DNA grafting density in experiments.

The DNA molecules are grafted to the nanoparticle's surface; however, they adopt different configurations around the nanoparticle as a function of the electrolyte concentration.

Fig. 5.6a shows the density profiles of the DNA molecules as a function of the distance to the

nanoparticles' center. All the DNA profiles have a common peak at $r \approx 2.7$ nm due the grafting on the nanoparticle's surface, and a second peak at $r \approx 3.3$ nm. At $r \gtrsim 3.3$ nm, we see significantly different behaviors of the grafted DNA molecules at different electrolyte concentrations. At the two highest electrolyte concentrations a third peak appears at about $r \approx 3.8$ nm; the higher the electrolyte concentration, the sharper the third peak becomes. Interestingly, at lower electrolyte concentrations ($[CaCl_2] \leq 1.2$ M), the DNA extends beyond $r \gtrsim 3.8$ nm, decaying monotonically, whereas at the higher electrolyte concentrations the profiles do not extend past this value. This behavior indicates that the electrolyte concentration modifies the correlation of the DNA molecules with the nanoparticle's surface. At low electrolyte concentrations the DNA molecules are correlated at longer distances whereas at high concentrations the DNA molecules are more structured near the nanoparticles surface.

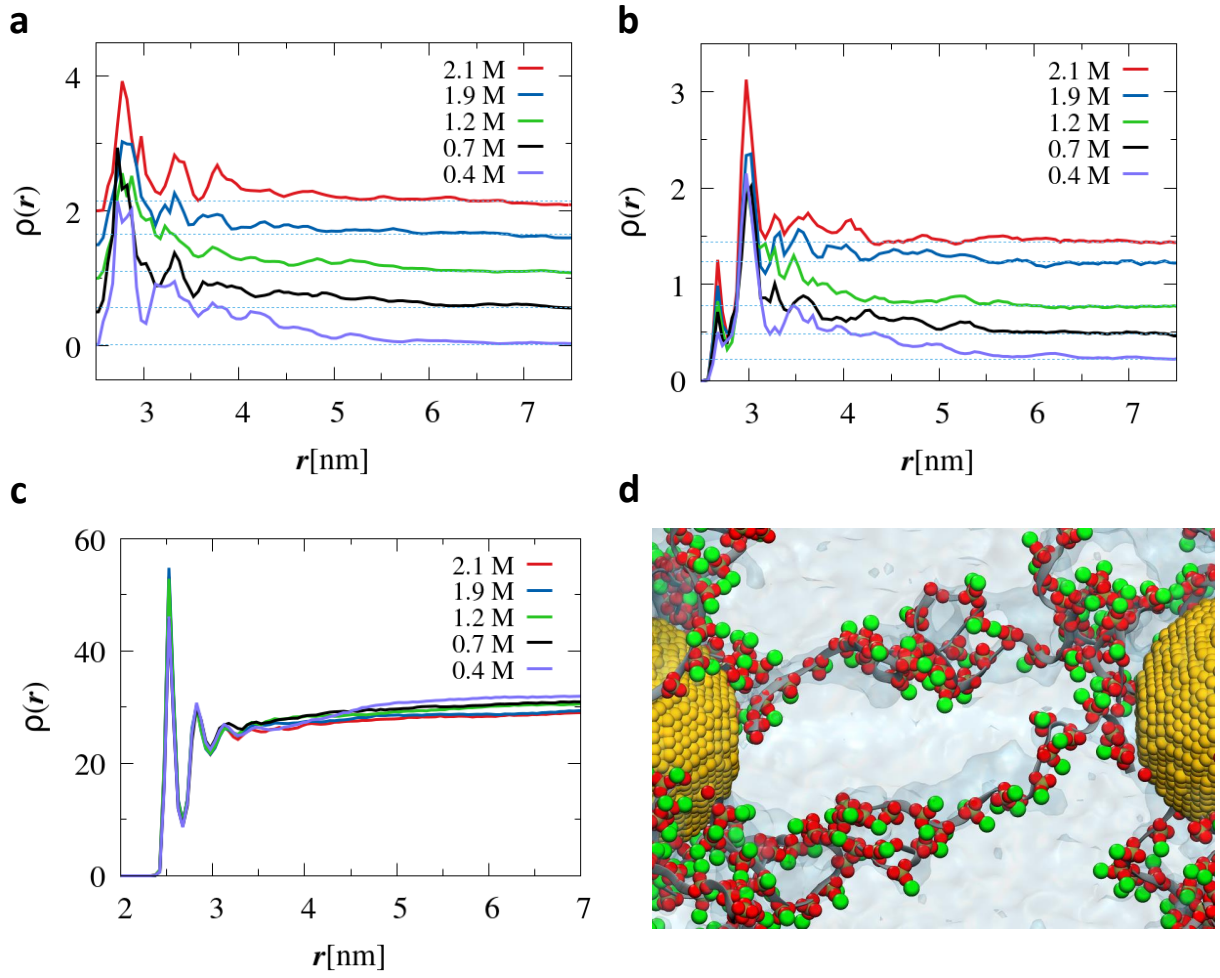

Figure 5.6: Structure of DNA, ions, and water around the nanoparticle. Density profile of (a) the DNA molecules, (b) Ca^{2+} ions, and (c) water as a function of the distance to the nanoparticle's center. The DNA density profiles are calculated using the P atom of the PO_4^- group of the DNA molecules (see **Fig. 5.5b**). To aid visualization, the DNA density profiles are shifted upwards by 0.5 with respect to the contiguous profile; the DNA density profile at 0.4 M is not shifted. In the Ca^{2+} profiles, the shifts result naturally from the different concentrations. The line colors represent different $CaCl_2$ molar concentrations. The density units are number of particles per nm^3. Light-blue lines are included to show when the profiles reach a uniform value. (d) Instantaneous snapshot of the simulation box showing the aqueous environment around the DNA-grafted nanoparticle. The nanoparticle is shown in yellow, Ca^{2+} ions within 0.5 nm from the P atoms are in green, and the DNA backbone is shown as a grey ribbon. The PO_4^- groups from DNA are displayed as spheres; P: ochre, and O: red. The image is produced using two contiguous image boxes that self-interact through the DNA strands.

By analyzing the Ca^{2+} distribution around the nanoparticle, we notice interesting changes as a function of the electrolyte concentration. The density profiles in **Figure 5.6b** show a peak at

around $r \approx 2.5$ nm which implies the adsorption of Ca^{2+} ions on the nanoparticle's surface. This peak is due to the electrostatic attraction of the grafted Ca^{2+} cations by the DNA on the surface. The ionic correlations enhance the Ca^{2+} adsorption on the nanoparticle's surface, therefore, the adsorption is small at the lowest concentration and increases as the ionic concentration increases. A secondary peak is at $r \approx 3$ nm and some ionic structure between $3\ \text{nm} \lesssim r \lesssim 4\ \text{nm}$ because of the interaction between the Ca^{2+} and the DNA molecules. The density profiles show that the correlation length decreases as the electrolyte concentration increases. For example, at 0.2 M the ionic density profile decay monotonically from $r \approx 4$ nm and becomes uniform at about $r \approx 6$ nm, whereas at 2.1 M the profile is uniform from $r \approx 4.5$ nm. These changes in the correlation length and ionic structure around the nanoparticle impact the overall interaction between the nanoparticles.[195, 196]

Water mediates the interactions of biomolecules with ions and other molecules.[197] In Figure 4c, we analyze the aqueous environment using the water density profile. The water density profiles show a main peak at $r \approx 2.5$ nm that increases as the $CaCl_2$ concentration increases, and three more peaks of decreasing height as the distance to the nanoparticle's surface increases. Then, the density profiles tend to a constant value that is reached at a closer distance from the surface as the electrolyte concentration increases. For the highest electrolyte concentration (2.1 M), the water density plateau is reached at $r \approx 4.5$ nm, whereas at the lowest concentration (0.4 M) the plateau is reached at a $r \approx 6.5$ nm. **Fig. 6d** shows an instantaneous configuration of the DNA strands and the ionic environment that mediates the nanoparticles' interaction in the dense phase.

The correlation between the nanoparticles and the ions occurs primarily via the DNA charged groups. In **Fig. 7a** we investigate the correlations between the DNA PO_4 groups and the

Ca^{2+} ions using the radial distribution functions (RDF) at different electrolyte concentrations. We find that the PO_4 groups strongly adsorb the Ca^{2+} ions, which is seen as a peak in the RDF profiles at about $r \approx 0.3$ nm.

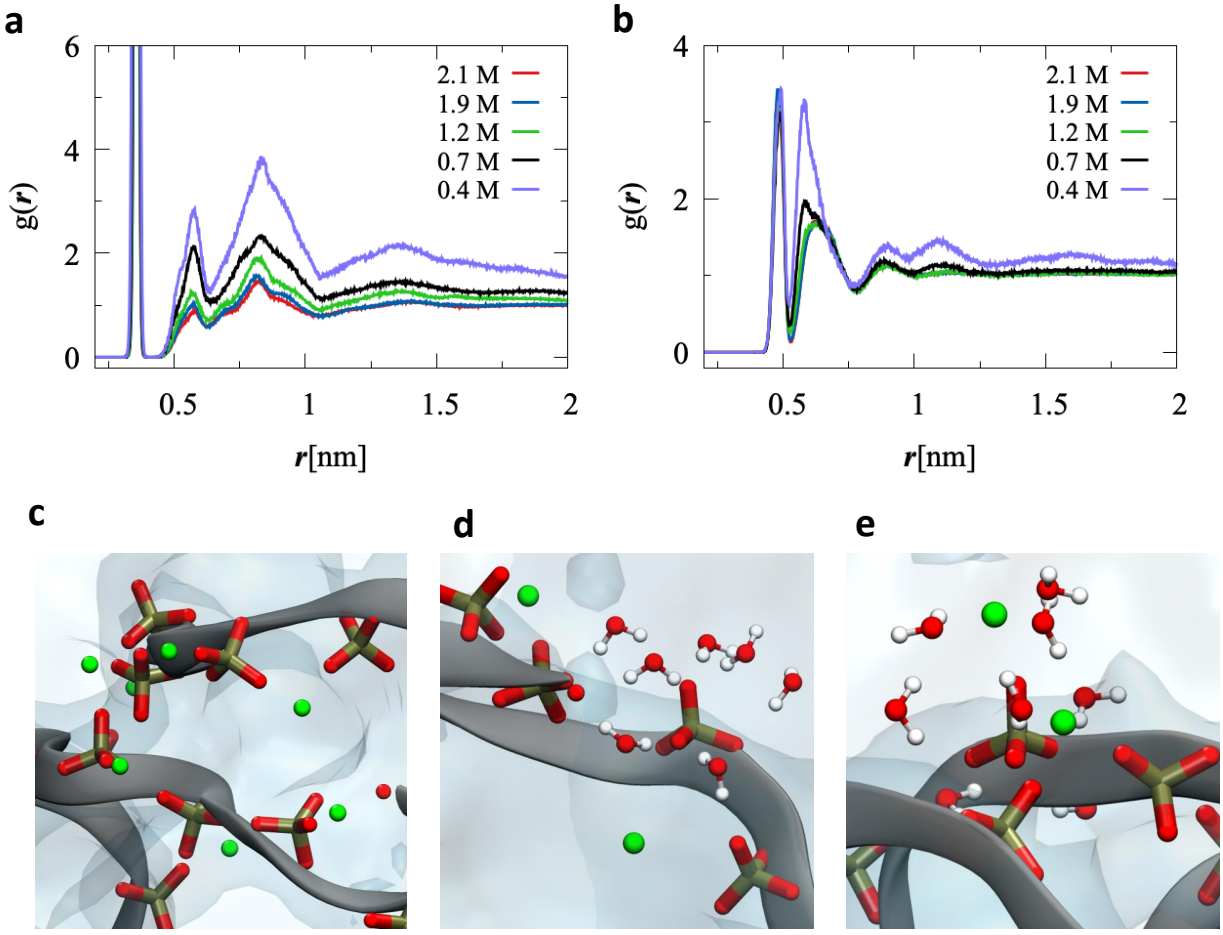

Figure 5.7: Radial distribution functions of (a) PO_4^-–Ca^{2+} and (b) Ca^{2+}–Ca^{2+} at different $CaCl_2$ concentrations. Snapshots of the environment around the PO_4^- groups of DNA: (c) Ca^{2+} ions in the system at 2.1 M, and water molecules and Ca^{2+} ions near a PO_4^- group in a system at (d) 0.4 M and (e) 2.1 M.

Furthermore, we observe other peaks at $r \approx 0.6$, 0.8, and 1.25 nm caused by the crossed correlation via neighbouring PO_4 groups in the DNA molecule. By increasing the electrolyte concentration, the crossed correlations gradually decrease. Consequently, at 2.1 M the third peak at $r \approx 1.25$ nm, almost disappears, and the profile is uniform at long distances. At the lowest

concentration (0.4 M) the correlations between the PO_4 groups and the Ca^{2+} ions are of a much longer range than 2 nm.

It is worth noticing that the grafted DNA nanoparticle enhance the correlations between the ions. In **Fig. 5.7b**, the RDF profiles between Ca^{2+} ions peak at about $r \approx 0.47$ nm, also observed in the bulk solution. At the lowest electrolyte concentration, the secondary peak at $r \approx$ 0.6 nm is much more pronounced in the presence of the DNA molecules than in bulk. In addition, the ion-ion correlations are of longer range at the lowest concentration than at the higher ones.

Fig. 5.7c-e show snapshots of the ions and water around the PO_4 DNA groups. We can see that the Ca^{2+} ions coordinate with multiple PO_4 groups and induce the bridging between them. **Fig. 5.7d-e** shows that the PO_4 groups are better hydrated at low than at high electrolyte concentrations because the Ca^{2+} remove water from the PO_4 groups.[198]

In summary, the DNA molecules adopt extended configurations at low electrolyte concentrations, and they become more compact and layered near the nanoparticle's surface at high concentrations

Similarly, the range or spatial extension of ionic correlations reduces with increasing electrolyte concentration. Furthermore, by increasing the salt concentration in the system, the Ca^{2+} ions replace the hydration water around the DNA chains. These dehydrated (or less-hydrated) ligands lead to changes in the effective nanoparticles' interaction favor configurations that better

accommodate the BCC structure. In other words, a low electrolyte concentration favors the FCC phase, whereas the BCC is more favorable at high electrolyte concentrations.

A change in the separation distance D_{nn} implies a change in the number of water molecules per unit cell. Therefore, the equilibrium separation distance D_{nn} between the nanoparticles results from a balance in the interaction forces and the chemical equilibrium between the crystal and the surrounding ions reservoir. *Hence, we analyze the stable hydration scenarios of the nanoparticles as a function of the $CaCl_2$ concentration.* We consider the system outlined in **Fig. 5**, and three hydration states represented by the number of water molecules in the box, N_w = 45000, 55000, and 70000. The corresponding box size varies from L =11.5 nm to L =13.5 at the lowest and highest hydration, respectively.

The equilibrium ion concentration in the reservoir and the nanoparticle dense phase are determined by the thermodynamic equilibrium conditions, namely, $p^a = p^b$ and $m^a_i = m^b_i$ where p and m_i are, respectively, the pressure and the chemical potential of species i (see methods at end of chapter). The superscripts a and b designate the nanoparticles' dense phase and the aqueous phase (b), respectively. The chemical potential is expressed in terms of the Gibbs free energy as

$$\mu_i = \left(\frac{\partial G}{\partial N_i}\right)_{p,T,N_{j\neq i}} \quad \textbf{(5.1)}$$

where N_i is the number of particles of species i and n is the number of species in the system. To maintain the system electroneutrality during the free energy calculation, we consider inserting an artificial 'molecule' with no internal bonds formed by one Ca^{2+} ion and two Cl^- ions. We refer to

this artificial molecule as a *triplet*. We calculate the chemical potential as the change of the Gibbs free energy by introducing the 'molecule' into the system as

$$\mu_i = (\frac{\Delta G}{\Delta N_i})_{p,T,N_{j\neq i}} = G(T,p,N_1,\ldots,N_i,\ldots,N_n) - G(T,p,N_1,\ldots,N_i-1,\ldots,N_n) \quad \textbf{(5.2)}$$

The change of the free energy is calculated using the slow-growth method in thermodynamic integration[199, 200] to transform the system from state A to state B as follows

$$G^B(T,p) - G^A(T,p) = \Delta G = \int_0^1 \langle \frac{\partial H}{\partial \lambda} \rangle_\lambda d\lambda \quad \textbf{(5.3)}$$

l is a coupling parameter that varies from 0 to 1 to modulate the interaction between the target molecule and the medium that is gradually turned in the system's Hamiltonian, such that the interaction between the medium and the molecule is switched off at state A (λ =0) and is on in state B (λ =1).

Figure 5.8a shows the change in the Gibbs free energy by inserting a triplet into the system as a function of the electrolyte concentration and at three different hydration states, namely, $N_w =$ 45000, 55000, and 70000. At the highest hydration state (N_w =70000), the change in Gibbs free energy decreases by increasing the electrolyte concentration, implying that the insertion of a new triplet into the system is favorable at this hydration state. For the two lower hydration states, the change in the Gibbs free energy shows states that are as likely as the states with the highest hydration. Hence, our analysis shows that the dehydrated states are energetically favorable as the electrolyte concentration increases. In **Figure 5.8b**, the simulation box volume shows sensitive

increments by increasing the $CaCl_2$ concentration. By changing the number of water molecules, the changes in the volume are significantly more pronounced. This simple analysis supports our hypothesis about a significant dehydration by increasing the salt concentration.

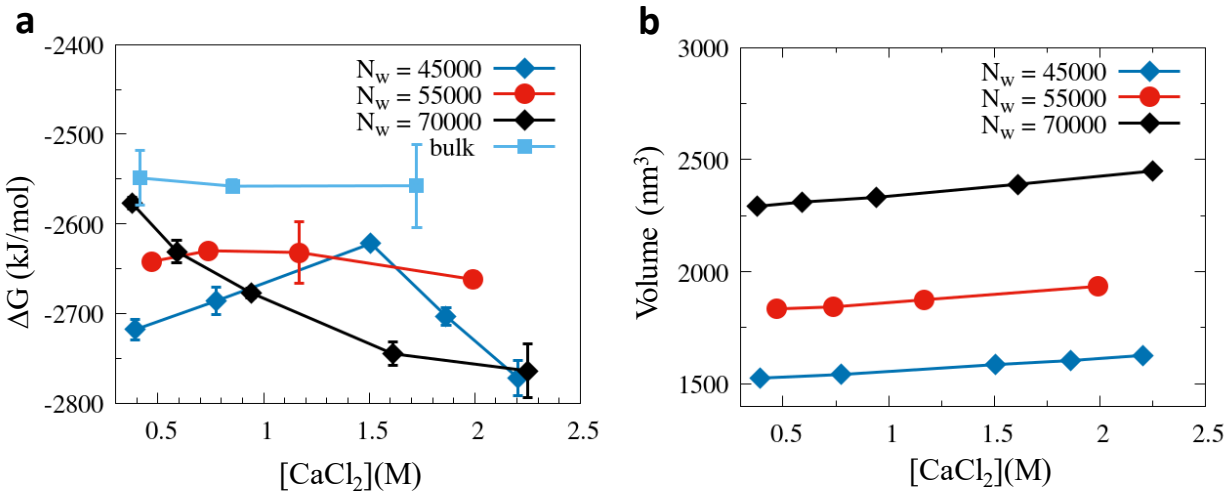

Figure 5.8: (a) Gibbs free-energy change due to inserting a triplet consisting of one Ca^{2+} ion and two Cl^- ions into the simulation box containing one DNA-grafted nanoparticle, and (b) the equilibrium simulation box volume. The calculations are performed as a function of the $CaCl_2$ concentration and for different hydration states defined by the number of water molecules, N_w, in the simulation box.

We analyzed the changes in the Gibbs free energy in a system consisting of a $CaCl_2$ electrolyte solution. The Gibbs energy changes by inserting a triplet in bulk are higher than in the system containing the grafted DNA nanoparticle. Therefore, our simulation method is limited to determining the equilibrium conditions between the reservoir and the crystalline system. We speculate that this limitation is due to a missing concentration of nanoparticles, free DNA, or other components in the reservoir that are present in the real system.

5.5. Conclusions

In summary, we have presented a system in which nanoparticles grafted with highly charged polyelectrolytes form lattices of different symmetries depending on salt content. While

divalent cations are necessary to induce the attractive forces that stabilize the condensed states, increasing the salinity of the solution with divalent or monovalent salts drives contraction of the aggregates, as well as FCC to BCC phase transitions. We hypothesize that the additional salt dehydrates the grafted DNA, strengthening phosphate-cation interactions, as well as more compact, structured DNA conformations amenable to the BCC structures, as evidenced by our molecular dynamics studies. Our neuron scattering studies elaborate upon this picture, revealing that the increasingly dehydrated DNA adopts conformations that increase the number of monomer-monomer contacts between molecules on adjacent particles, thus forming an interpenetrating structure capable of stabilizing the second nearest-neighbor interactions that favor the BCC structure. Taken together, these results provide insight on how electrolytes influence charged biomolecule hydration, and demonstrate how these factors can be utilized to produce systems which actuate in response to varied ionic conditions. Our results also demonstrate the importance of surface-electrolyte interactions in concentrated electrolytes.

5.6. Chapter 5 Supplemental Information

5.6.1 Neutron Scattering Data Analysis

The SANS data is modeled using a core-shell sphere model:

$$F(q, R_{Au}) = \frac{4\pi}{q^3} \times [(\rho_{Au} - \rho_{shell}) \times [\sin(qR_{Au}) - (qR_{Au}) \times \cos(qR_{Au})] + (\rho_{Au} - \rho_{shell})[\sin(qR_{shell}) - (qR_{shell}) \times \cos(qR_{shell})]] \quad \textbf{(5.4)}$$

To account for variations in background and scale, and the polydispersity of the gold nanoparticle cores, the intensity associated with the form factor is compute as:

$$P(q) = A \times \langle |F(q, R_{Au})|^2 \rangle_{R_{Au}} + B \quad \textbf{(5.5)}$$

The angle brackets denote the averaging of the absolute square of the form factor over a Schulz distribution for size-dispersity [116]. Briefly:

$$\Pr(R_{Au}) = \left(\frac{z+1}{\langle R_{Au} \rangle}\right)^{z+1} \times \frac{R_{Au}^{z}}{\Gamma(z+1)} e^{-(z+1)\frac{R_{Au}}{\langle R_{Au} \rangle}} \quad \textbf{(5.6)}$$

Here, $\langle R_{Au} \rangle$ denotes the average nanoparticle radius, Γ the gamma function, and z is a parameter related to the distribution variance (Σ^2) as $z = \frac{\langle R_{Au} \rangle^2}{\Sigma^2} - 1$. The coefficient A is proportional to the concentration of nanoparticles in solution, while B accounts for background. The values used to produce the models plotted in **Figure 5.4** are provided in **Table 5.1.**

Table 5.1: Parameters utilized in the core-shell form factor models plotted in Figure 5.4. The volume of the DNA is computed as the product of the volume of a given oligonucleotide, here modeled as a cylinder with 0.5 nm radii and a height of 0.65 nm per base (here 35) and the number of DNA per particle (determined by Oligreen assay to be 70). The outer radius of the particle, R_s, is computed as $R_s = R_{au} + T_c$. SLD values are provided in Table 3.1.

[$CaCl_2$]: Geometry	R_{Au} (nm)	T_c (nm)	Vol Shell (nm^3)	Vol DNA nm^3	Vol Fraction of DNA in "shell"
0 M: Fully Extended	4.5	13	22067.594	1250.74658	5.66779766 %
1.5 M: Fully compressed	4.5	3.85	2056.93842	1250.74658	60.8062237 %
1.5 M: Fully Extended	4.5	7.7	7224.50281	1250.74658	17.3125627 %

5.6.2 Simulations Methods

The MD simulations and this section were prepared by Dr. Felipe Jiménez-Ángeles

Classical all-atom explicit solvent MD simulations are conducted using the CHARM force field parameters[201, 202] to model the system's interactions. The dense phase is represented by a unit cell that contains a single DNA-grafted spherical nanoparticle replicated in x, y, and z directions using periodic boundary conditions. The spherical nanoparticle is 4.5 nm of diameter, approximately, and is made of uncharged non-polarizable atoms. The spherical nanoparticle surface is decorated using 18 single-strand DNA chains formed of 17 thymine bases bearing a total charge of -16e distributed along its length; e is the positive elementary charge. The structure of DNA is built using the conformational parameters taken from experimental fiber-diffraction studies[203]. The nanoparticle's shape is maintained using harmonic-potential interactions between neighboring atoms. The DNA chains are attached to the nanoparticle's surface using a harmonic potential between a carbon atom at the end of the DNA strand and an atom at the nanoparticle's surface. The decorated spherical nanoparticle is placed at the center of a cubic simulation of side L, including (N +144) Ca^{2+} ions 2N Cl ions, and N_w water molecules; the extra 144 Ca2+ ions are necessary to maintain the system electroneutrality. The simulations are performed using the package GROMACS[150, 151]. To model the electrostatic and van-der-Waals interactions in the system, we employ the CHARM force field parameters[201, 202] to model the system's interactions. The electrostatic interactions are calculated the PME algorithm. To equilibrate the molecules in bulk and at the interface we performed microsecond MD simulations using a time-step of 2.5 fs at $T = 298$ K. The temperature is controlled using the Nose-Hoover thermostat, and the pressure is maintained using the Parrinello-Rahman barostat.

The thermodynamic equilibrium of the system is governed by the exchange of water and ions between the nanoparticles' dense phase and the surrounding reservoir. Hence, here we revise the thermodynamics of phase equilibrium in multicomponent systems. We will employ this

formulation to develop a method to investigate the system formed by the DNA-grafted gold nanoparticles immersed in a multivalent ions solution. Let us consider a system formed by K different species (which maybe atoms, ions, and molecules), of number density $\rho_i = \frac{N_i}{V}$ and chemical potential μ_i; being N_i the number of particles of species *i*, *V* the total volume, and $i = 1, \dots, K$. In the phase equilibrium, the components are divided into *J* regions (phases) with corresponding number densities $\rho_i^{\alpha_1}, \rho_i^{\alpha_2}, \dots, \rho_i^{\alpha_J}$, where the subscript and superscript designate the species and the phase, respectively. In general, $\rho_i^{\alpha_1} \neq \rho_i^{\alpha_2} \neq \cdots \rho_i^{\alpha_J}$. The phase equilibrium is determined by the thermal equilibrium,

$$T \equiv T^{\alpha_1} = T^{\alpha_2} = \cdots = T^{\alpha_J} \tag{5.7}$$

the mechanical equilibrium,

$$p \equiv p^{\alpha_1} = p^{\alpha_2} = \cdots = p^{\alpha_J}, \tag{5.8}$$

and the chemical equilibrium

$$\mu_i \equiv \mu_i^{\alpha_1} = \mu_i^{\alpha_2} = \cdots = \mu_i^{\alpha_J} \tag{5.9}$$

T, p, and μ_i represent the temperature, the pressure, and the chemical potential of *i*-th species, respectively; the superscript designates the phase. In processes at constant *p* and *T*, the Gibbs free energy is the thermodynamic potential that is minimized in equilibrium,

$$dG = -SdT + Vdp + \sum_{i=1}^{J} \mu_i \mathrm{d}N_i \tag{5.10}$$

At constant V and T, the corresponding thermodynamic potential is the Helmholtz free energy, given by

$$dF = -SdT - pdV + \sum_{i=1}^{J} \mu_i \mathrm{d}N_i \quad \textbf{(5.11)}$$

The chemical potential in terms of the Gibbs free energy is given as

$$\mu_i = \left(\frac{\partial G}{\partial N_i}\right)_{T,P,N_{j\neq i}} \quad \textbf{(5.12)}$$

In terms of the Helmholtz free energy, the chemical potential is given as

$$\mu_i = \left(\frac{\partial F}{\partial N_i}\right)_{T,V,N_{j\neq i}} \quad \textbf{(5.13)}$$

In our study, we deal with small changes due to the insertion/deletion of one ionic triplet in an aqueous phase. Therefore, $pdV \approx Vdp \approx 0$, and $\Delta F \approx \Delta G$.

Chapter 6: Competition and Cooperation Between Cations

Dissolved ions govern the functionalities of charged biological macromolecules, such as by stabilizing conformations [204], serving as catalytic centers[205], or driving phase transitions[206]. Accordingly, it is common for both natural and synthetic materials to utilize interactions with specific ions to drive actuation. However, natural biological solutions are crowded, complex mixtures containing high concentrations of a wide variety of ions[207]. Poisson-Boltzmann theory suggest that "off-target" ions tend to disrupt charge-based interactions through electrostatic screening and competition for charged sites[208-210]. Indeed, the presence of high concentrations of monovalent salts tends to suppress the protamine-induced condensation of DNA [211, 212] and the calcium-induced gelation of alginate[213]. However, a variety of factors not included in the Poisson-Boltzmann formalism, such as hydration effects[214] and ion-ion correlations[215], frequently become significant in relevant conditions. Due to the considerable complexity of multicomponent aqueous mixtures, studies on model systems are necessary to elucidate how ion-controlled interactions manifest in these environments.

DNA-coated gold nanoparticles (DNA-NPs) represent an attractive model system for studying ion-induced effects, owing to the high negative charge of the spherical DNA-brush, strong optical properties of the gold cores[216] , and relevance to a number of nanotechnologies[217]. We have previously demonstrated that DNA-NPs can be assembled into various structures through the addition of divalent cations, even in the absence of favorable base pairing interactions[184]. The phases and densities of these DNA-NP assemblies depend on cation identity (differing between Ca^{2+}, Mg^{2+}, and Sr^{2+}), and evolve with added salt throughout the full accessible range of salinities, including a previously unexpected swelling of the structures at

exceptionally high concentrations driven by ionic correlations[105]. Here, we extend the use of this system to study aqueous mixtures of alkali chlorides (monovalent cations) and alkaline earth chlorides (divalent cations). Small-angle X-ray scattering (SAXS) results reveal that the assembly of DNA-NPs by monovalent cations differs from that of divalent cations, showing a generally lower propensity for aggregation and no re-swelling at high ionic concentration. However, in mixtures of monovalent and divalent cations, DNA-NPs form structures associated with the divalent cations; in fact, as the ratio of monovalent cations to divalent cations increases, the influence of the latter is enhanced, resulting in the favorability of structures typically seen at higher divalent cation concentrations. We explore this apparent "cooperativity" with additional SAXS experiments, finding that it is driven by a "salting-out" mechanism [49, 218], where the effects of desolvation of DNA-NPs by added solute overwhelms the influence of electrostatic screening at high concentration. Intriguingly, we also demonstrate that the DNA-NP aggregates also swell in highly concentrated mixtures of salts, suggesting that the effects of ion-ion correlations on these materials extends beyond solutions highly enriched in divalent cations.

6.1. Experimental Methods

6.1.1 Sample Preparation

Oligonucleotides were synthesized via phosphoramidite chemistry[113]. using a MerMade solid-state controlled pore glass (CPG) DNA synthesizer from BioAutomation and DNA phosphoramidites from Glen Research. The selected sequence, 5'-T_{35}-C_3SH- 3, is terminated on the 3' end with a propyl-thiol group (denoted C_3SH). Upon completion of synthesis, the DNA was cleaved from the CPG via reaction with a 1:1 mixture of NH_4OH and methylamine, held at 55°C for 30 minutes. After removing volatile reactants with a Multivap® Nitrogen Evaporator

from Organomation, the DNA was dispersed in deionized water (18.2 MΩ·cm), and isolated from the CPG with 0.2 micron syringe filters. “Successfully” synthesized oligonucleotides are capped with 5’-DMT groups, enabling separation from prematurely truncated strands via reverse-phase high-performance liquid chromatography (RP-HPLC). Here, a 1260 Infinity II LC System from Agilent Technologies was utilized to isolate the desired, 35-base sequence. Following separation, the oligonucleotides were lyophilized; the 5’-DMT groups were then cleaved via reaction with a 20% (by volume) acetic acid solution (in water) and separated from the water-soluble DNA via liquid-liquid extraction with ethyl acetate. The aqueous oligonucleotide mixtures were then lyophilized. The molecular weights of the final products were determined via matrix-assisted laser desorption/ionization time-of-flight spectroscopy (AutoFlex MALDI-TOF, from Bruker), which matched the desired sequence, confirming the success of the synthesis.

The thiol-terminated oligonucleotides were grafted to colloidal gold nanoparticles following established methods [82]. In brief, the thiolated DNA molecules were reduced in 100 mM dithiothreitol (DTT) maintained at pH ~8 via phosphate buffer. Following reaction for 30-60 minutes, the DNA was transferred to water via purification through size-exclusion NAP5 columns (from Cytiva). The reduced DNA was added to ~10 nM solutions of colloidal AuNP (nominally 10 nm diameter, from Ted-Pella) at a ratio of ~372 DNA/AuNP and allowed to incubate overnight. Sodium chloride (NaCl 99.99% purity from Millipore-Sigma) and small quantities of 0.1% Sodium Dodecyl Sulfate (SDS) were then slowly added to the solution over ~ 8 hours until a final concentration of 1 M NaCl was achieved. This process enables high grafting density on the nanoparticles. Unbound DNA was removed via centrifugation using 50 kDa spin-filters (from Amicon). DNA-NPs were then transferred to DI water (18.2 MΩ·cm), and purified

through three rounds of centrifugation, in order to minimize the presence of NaCl, unbound DNA, and SDS in the final nanoparticle stock solutions. Final DNA-NP concentrations were determined via application of Beer's Law to the UV-Vis-measured absorbance (Cary Series UV-Vis-NIR Spectrophotometer, from Agilent Technologies) of the AuNP at 520 nm [101].

In order prepare solutions with very high salt concentrations, samples were prepared from saturated aqueous solutions of various alkali chlorides and alkaline earth chlorides. Saturated salt solutions (concentrations provided in Table 6.3) were allowed to equilibrate for at least 24 hours with the precipitated solid phases in sealed polypropylene tubes at ~22°C. Utilized salts were obtained from MilliporeSigma, and include Sodium Chloride (99.99% purity), Lithium Chloride (99.98% purity), Calcium Chloride Dihydrate (99.5% purity), $MgCl_2$ (99.9% purity), and $SrCl_2$ (99.9% purity). H_2O (18.2 MΩ·cm) was produced by a Synergy® Water Purification System, and D_2O (99.9% purity) was obtained from MilliporeSigma. Samples for SAXS analysis were prepared such that the final DNA-NP concentrations were 50 nM, and final volumes ranged from 30-50 μL. Here, the DNA-NPs were the final component added to the mixtures; following this addition, the suspensions were homogenized via pipette and transferred (within 1 minute) to quartz capillaries. 1.0 mm or 1.5 mm quartz capillaries, from Charles Supper, were used. After transfer, the capillaries were sealed with epoxy. 24-48 hours elapsed prior to measurement.

6.1.2 X-ray Scattering Measurements

SAXS measurements on nanoparticle suspensions were primarily carried out at beamline 5ID-D of the Advanced Photon Source. To reduce the X-ray attenuation due to the concentrated salt solutions, the X-ray energy of 16 keV (wavelength, l = 0.7749 Å) or 17 keV (l = 0.7293 Å wavelength) was used. In particular, to avoid the strong fluorescence from Sr^{2+}, 16 keV was used

as this energy is below the K absorption edge for Sr ($E_{K,Sr}$ = 16.1 keV). The SAXS/WAXS scattered intensities were measured simultaneously using three Rayonix CCD detectors positioned at 0.2 m, 1.0 m, and 7.5 m from the sample, allowing for simultaneous and continuous data collection in the range ($0.02\ nm^{-1} < q < 30\ nm^{-1}$). The X-ray spot size at the sample position was 0.25 mm x 0.25 mm, and the incident flux was ~ 3×10^{11} photons/s. Capillary samples were mounted horizontally on a translation stage. Samples were scanned for sets of three 5-second exposures, with the capillaries being translated continuously at ~ 0.5 mm/s during measurement to minimize radiation damage. The 2D data was reduced to 1D intensity profiles via azimuthal integration (using GSAS-II), following corrections for polarization, detector solid angle, and transmission. Data from the 3 detectors was corrected for high-energy noise ("zingers") and merged into continuous scattering profiles.

SAXS measurements on DNA-NP samples in mixtures of $MgCl_2$ and LiCl (**Fig. 6.10**) were carried out at beamline 12-ID-C,D of the APS. SAXS data was collected using a Pilatus single photon counting area detector positioned ~ 2.2 m from the sample. The X-ray energy was tuned to 18 keV (0.689 Å wavelength), the beam size at the sample position was ~ 0.4mm x 0.2mm, and the flux was ~ 2×10^{12} photons/s. Each measurement consisted of a 0.2 second exposure. Azimuthal averaging was performed by the procedure outlined above to obtain the 1D scattering profiles.

SAXS measurements on DNA-NP samples in aqueous (H_2O) solutions of low [$CaCl_2$] (**Fig 6.15a**) were carried out at Beamline ID7A1 (BioSAXS) of the Cornell High Energy Synchrotron Source (CHESS)[219, 220]. SAXS data was collected using a Pilatus single photon counting area detector positioned ~ 1.8 m from the sample. The X-ray energy was tuned to 13.3 keV (1.094 Å wavelength), the beam size at the sample position was ~ 0.25mm x 0.25mm, and

the flux was ~ 7×10^{12} photons/s. Each measurement consisted of a 0.5 second exposure. Azimuthal averaging was performed with BioXTAS RAW[221] to obtain the 1D scattering profiles.

SAXS measurements on DNA-NP samples in aqueous (D_2O) solutions of low [$CaCl_2$] (**Fig. 6.15b**) were carried out in the J.B. Cohen X-ray Lab at Northwestern University. A Rigaku SMAXS-3000 setup was utilized, equipped with a Cu microbeam anode, multilayer focusing mirrors, and an Eiger R1M 75uM pixel single photon counting 2D detector positioned 1.56 m from the samples stage. CuKα X-rays (8.04 keV energy, or 1.542 Å wavelength) were utilized. "High resolution" slit sizes were selected for measurements, where incident vertical and horizontal slits focus the beam to around 0.5 x .0.5 mm on the sample. SAXS patterns were collected while the samples were kept at ambient conditions, for 10 minutes each, scattering being recorded via the Xenocs Instrument Control Center (XICC) software. Following collection, the 2D scattering patterns were converted to 1D profiles via azimuthal integration, carried out by the instrument software.

6.1.3 Data Analysis

"Background-subtracted" data was obtained by subtracting the measured intensities ($I_{sol}(q)$) from capillaries containing the salt solutions (no DNA-NPs) from the measured intensity of capillaries containing DNA-NPs in the corresponding salt solutions ([$I_{samp}(q)$]):

$$I_{DNA-AuNP}(q) = I_{samp}(q) - (1 - \phi) \times I_{sol}(q) \quad \textbf{(6.1)}$$

In **Eq. 6.1**, ϕ is the volume fraction of the DNA-NP (of the order of 10^{-3}).

In the SAXS regime (0.02 $nm^{-1} < q < 1\ nm^{-1}$), $I_{DNA-AuNP}(q)$ is primarily due to the electron-dense Au nanoparticle cores. The scattering amplitude [form factor, $F(q, R_{Au})$] due to a single spherical Au particle is given as:

$$F(q, R_{Au}) = V_{Au} \times (\rho_{Au} - \rho_{sol}) \times \frac{[\sin(qR_{Au}) - (qR_{Au}) \times \cos(qR_{Au})]}{(qR_{Au})^3} \quad \textbf{(6.2)}$$

V_{Au} ($= \frac{4\pi}{3} R_{Au}^3$) and ρ_{Au} (= 4660 e/nm^3) are the volume and electron density of the gold core, respectively, and ρ_{sol} is the electron density of the surrounding solvent. The solution electron density depends on the salt concentration and in this study varied between ρ_{sol} = 334 e/nm^3 (for pure water) and 460 e/nm^3 (for 5.6 M $CaCl_2.2H_2O$). The scattering amplitude of an object scales linearly with the difference in the electron densities for the object and the solution (e.g., **Eq. 6.1**) electron density difference between the object and solution. Therefore, the scattered intensity scales as the absolute square of the electron density difference. As a result, the scattered intensity from a DNA (ρ_{DNA} ~ 550 e/nm^3) [115] is typically at least 400 times weaker than that from a gold core (should the objects have comparable volumes). Thus, the scattering from the DNA is taken to be negligible in this study.

For the dispersed DNA-NPs showing no assembly, the scattered intensity *P(q)* is calculated as:

$$P(q) = A \times \langle |F(q, R_{Au})|^2 \rangle_{R_{Au}} + B$$

(6.3)

The angle brackets denote the averaging of the absolute square of the form factor over a Schulz distribution for size-dispersity [116]. Briefly:

$$\Pr(R_{Au}) = \left(\frac{z+1}{\langle R_{Au} \rangle}\right)^{z+1} \times \frac{R_{Au}^{z}}{\Gamma(z+1)} e^{-(z+1)\frac{R_{Au}}{\langle R_{Au} \rangle}}$$

(6.4)

Here, $\langle R_{Au} \rangle$ denotes the average nanoparticle radius, Γ the gamma function, and z is a parameter related to the distribution variance (Σ^2) as $z = \frac{\langle R_{Au} \rangle^2}{\Sigma^2} - 1$. The coefficient A is proportional to the concentration of nanoparticles in solution. The constant term B arises due to the difficulties in precisely correcting for the background due to the slight differences in the thicknesses of capillaries used for measurements of samples and solutions.

For correlated DNA-NPs, **Eq. 6.5** (below) should be used.

$$I_{DNA-AuNP}(q) = S(q) \times P(q)$$

(6.5)

Here, $S(q)$, is the structure factor arising due to interference between X-rays scattered from positionally correlated particles. For non-correlated systems, $S(q)$=1.

6.2. Results and Discussion

The intensities of scattered X-rays in solutions of varied NaCl concentration are displayed in **Fig. 6.1A**. When no salt is added to the DNA-NP suspensions, the scattering pattern corresponds to that of isolated DNA-NP particles (dubbed the nanoparticle form factor), as the system is sufficiently dilute such that interparticle interaction are minimal. The introduction of NaCl results in the emergence of small diffraction peaks in the scattering patterns; these features, known at the Structure Factor (S(q)), arise due to positional correlations of DNA-NPs (**Fig. 6.1b**). The low magnitudes of these diffraction peaks suggest the presence of weak, liquid-like DNA-NP clusters [222]. Additional evidence of the weakness of interparticle interactions in NaCl solutions arises from the lack of any apparent phase transition in the suspensions; 10 nm AuNPs have a characteristic red color, which changes to purple should the particles aggregate, due to redshifting of surface plasmon resonance absorbances[223] Interparticle separations (D_{nn}) within the clusters can be calculated as[105]:

$$D_{nn} = \frac{\sqrt{6}\pi}{q_1} \quad \textbf{(6.6)}$$

where q_1 denotes the position of the first diffraction peak. Plotting Dnn and apparent DNA-NP phase versus [NaCl] reveals that the DNA brushes within the clusters compress with added salt, with D_{nn} decreasing from ~35nm at 1 M to ~29 nm at 5 M, (**Fig. 6.1c**). This result is qualitatively consistent with Poisson-Boltzmann theory, which projects that added salt should screen electrostatic repulsive forces between anionic DNA[69].

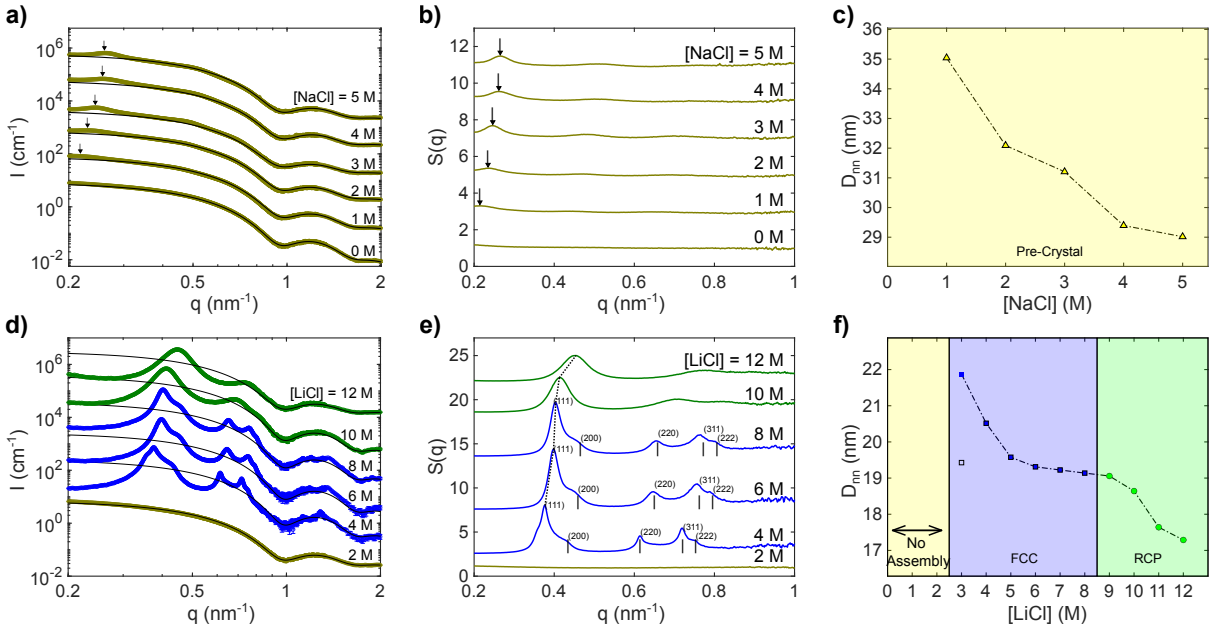

Figure 6.1: a) 1D SAXS intensity profiles for DNA-coated AuNPs suspended in aqueous solutions with varied NaCl (a) concentration. Black curves denote expected intensities for isolated nanoparticles. b) Structure factors, S(q), for DNA-NP assemblies in NaCl. Arrows denote positions of first intensity modulation. c) The corresponding phases and inter-DNA-NP separations (D_{nn}) as a function of [NaCl]. d) 1D SAXS intensity profiles for DNA-coated AuNPs suspended in aqueous solutions with varied LiCl concentration. e) Structure factors for DNA-NP assembled in LiCl solutions. Vertical lines and Miller indices peaks correspond to expected peak positions for diffraction from FCC structures (**Table 6.1**). f) Phases and D_{nn} as a function of [LiCl]. Additional SAXS patterns are presented in **Fig. 6.11** of the chapter supporting information.

Fig. 6.1c displays the scattered intensities of DNA-NPs dispersed in solutions of varied concentrations of LiCl, and **Fig. 6.1d** the corresponding structure factors. In solutions with [LiCl] < 2M, no diffraction peaks are recorded, suggesting minimal interparticle ordering. When [LiCl] > 3M, however, DNA-NPs assemble and precipitate from solution reflecting the presence of strong attractive interparticle forces. DNA-NPs order into have face-centered cubic (FCC) arrays when 3M < [LiCl] < 8M, and form disordered structures when [LiCl] > 9M. Previous analysis of similar structures suggest that these phases correspond to Random Close Packing (RCP)[224, 225], and that **Eq. 6.6** also relates D_{nn} to the position of the primary scattering peak (q_1) for these structures[105]. Li^+ ions drive the condensation of the DNA-NPs to a much greater degree

than Na^+ ions (**Fig. 6.1e**), likely owing to the higher charge density and water affinity[226] of the former. While the strength of the interaction between the DNA-NPs and monovalent Li^+ is somewhat surprising, D_{nn} decreases monotonically with [LiCl].

Comparison of the assembly of these DNA-NPs in solutions containing monovalent and divalent cations yields interesting insights. While the smaller Mg^{2+} and Ca^{2+} cations drive crystallization and precipitation, similarly to Li^+, the larger Sr^{2+} cation drives only weak clustering, similarly to Na^{+}[105]. Lower concentrations of $CaCl_2$ (~300 mM) and $MgCl_2$ (~1 M) are required to induce precipitation than LiCl (3M). DNA-NP structures formed in Mg^{2+} and Li^+ solutions are similar, showing no detectable ordering at low concentrations, forming FCC structures over a relatively wide concentration wide range, and forming amorphous structures at concentrations approaching saturation. Ca^{2+} has a particularly profound interaction with these DNA-NPs, forming pre-crystalline, FCC, body-centered cubic (BCC), and RCP structures as [$CaCl_2$] is increased (Fig 2A). While the addition of the various alkaline earth chlorides similarly decreases Dnn, the nanoparticle aggregates switch to swelling with added salt above threshold salt concentrations (typically 40-60% of the solubility limit, as evidenced by the non-monotonic shift of the primary diffraction peak in S(q) (**Fig 6.2a**). The distinct structures and re-swelling effects associated with Ca^{2+} make it a natural candidate for studying DNA-NP assembly in mixtures of cations.

In order to investigate how the presence of other salts modulates DNA-NP assembly by divalent cations, we prepared samples with fixed $CaCl_2$ concentration (200 mM or 400 mM) and varied NaCl concentration (0 to 4 M.). Nanoparticles do not precipitate in solutions with 0 or 1 M NaCl, instead forming precrystalline clusters (**Fig 6.2a-b**). However, increasing [NaCl] to 2M, 3M, and 4M leads to the formation of FCC, BCC, and RCP precipitates, respectively (Fig 2B).

These structures typically form in solutions with increasingly high [$CaCl_2$] (~250 mM, ~800 mM, and ~ 1.5 M), suggesting that NaCl enhances the efficiency with which Ca^{2+} drives interactions between the DNA brushes. This behavior is in stark contrast to the prediction of classical solution electrostatics, which suggest that high concentrations of Na^+ should displace Ca^{2+}bound by the negative charge of the phosphate groups ("competitive" interactions) [210, 227]; in the present system, said displacement would result in the "melting" of the Ca^{2+}-bound aggregates, returning the DNA-NPs to the "pre-crystalline" state present in NaCl solutions. Instead, the large amounts of dissolved NaCl interact in a "cooperative" manner with Ca^{2+}. Aggregates prepared at 400 mM [$CaCl_2$] provide similar results, with phase transitions shifted to lower [NaCl] (**Fig. 6.12**). Extraction of the interparticle separations (D_{nn}) from the various structures establishes that varying [$CaCl_2$] by 200 mM has a clear influence on the aggregates, even when [NaCl] is a factor of 10-20 greater Fig 2C); the values for D_{nn} of these structures (~15-24 nm) is also consistently less than those prepared in NaCl (~29-35 nm), further reflecting the strong influence of Ca^{2+}.

To establish the generality of this apparent "cooperative" effect of NaCl, we also tested samples with varied [NaCl] (0 to 4 M) and 200 mM concentrations of either $MgCl_2$ or $SrCl_2$. In $MgCl_2$ solutions where [NaCl] < 2M, the apparent dominance of Mg^{2+} is sufficient to suppress the "pre-crystalline" clustering observed in NaCl solutions (**Fig 6.2d**). Higher [NaCl] drives the formation of FCC structures (**Fig 6.2d**), observed previously in solutions for which 1 M < [$MgCl_2$] < 2.5 M[105]. Therefore, the addition of NaCl also appears to increase the "effective" Mg^{2+} concentration. The strong influence of the divalent cation is further demonstrated in the mixed $SrCl_2$ and NaCl solutions; while $SrCl_2$ does not drive DNA-NP precipitation, instead forming pre-crystalline clusters, the addition of NaCl leads to increasingly compact clusters (**Fig.**

6.9), with D_{nn} values (~24.5 – 30 nm) less than those observed in NaCl solutions. Thus, crystallization is not a requisite for the cooperative interactions of interest

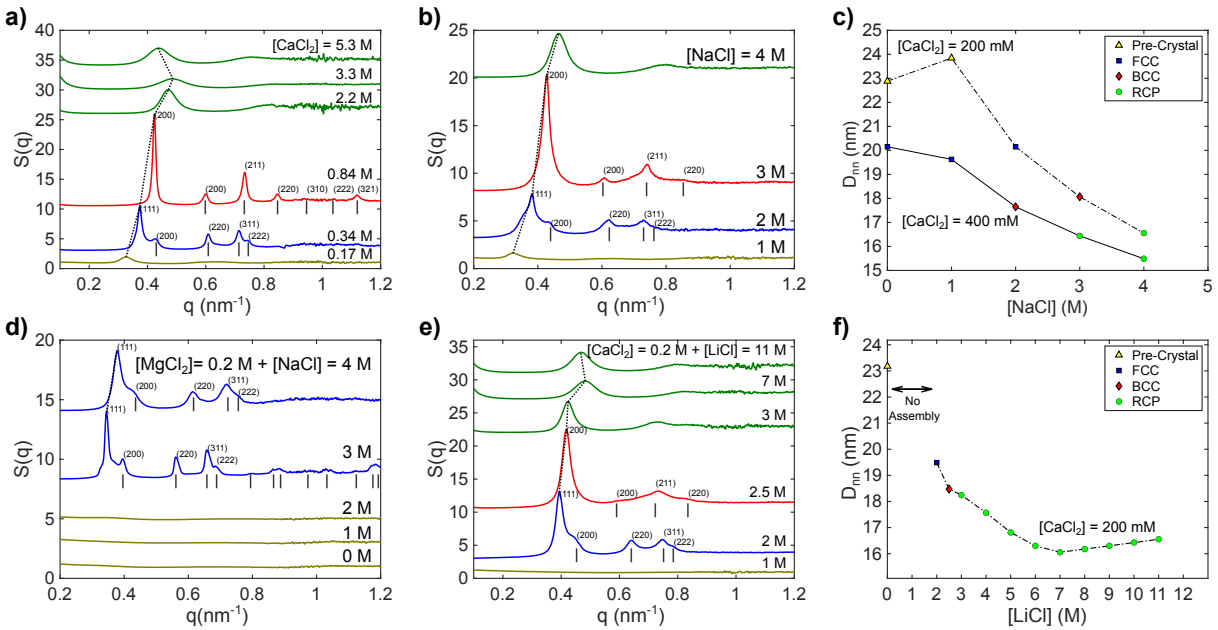

Figure 6.2: a) Structure factors for DNA-NP structures assembled at varied $CaCl_2$ concentrations. Vertical lines and miller indices denote expected peak positions for face-centered cubic (FCC) and body-centered cubic (BCC) lattices (see **Tables 6.1** and **6.2** in the chapter SI). The dotted line connects the primary scattering peaks, revealing a non-monotonic dependence on peak position, and thus interparticle separation, on $[CaCl_2]$. b) Structure factors for DNA-NP structures assembled at fixed $[CaCl_2]$ and varied [NaCl]. Interparticle separations and phases are plotted in c). Increased [NaCl] drives the formation of structures associated with higher $[CaCl_2]$. d) Structure factors for DNA-NP structures assembled at fixed $[MgCl_2]$ and varied [NaCl]. Consistent with behavior of DNA-NPs in $MgCl_2$ solutions observed previously[105], no structuring is observed at low salt concentration, while FCC structures are formed at higher salinities. e) Structure factors for DNA-NP structures assembled at fixed $[CaCl_2]$ and varied [LiCl]. The phases and interparticle separations are plotted in f), demonstrating that increasing [LiCl] drives the formations of structures associated with higher $[CaCl_2]$. Additionally, the DNA-NP aggregates begin to expand with [LiCl] at high concentrations, matching the behavior observed at high $[CaCl_2]$. Additional structure factors and 1D SAXS profiles are provided in chapter supporting formation (**Fig. 5.12-5.13**)

Samples with 200 mM $[CaCl_2]$ and varied [LiCl] (0-11 M) were also prepared to evaluate whether the influence of a monovalent cation capable of crystallizing DNA-NPs differed from that of NaCl. Indeed, the presence of 1 M LiCl leads to the suppression of pre-crystalline ordering. However, FCC, BCC, and RCP structures are formed when [LiCl] was increased to 2,

2.5, and 3 M, respectively (**Fig 6.2e**). The emergence of disordered structures shifts to lower monovalent salt concentrations when LiCl is utilized (3 M LiCl vs 4 M NaCl), and considerable peak broadening is apparent in the BCC structure factor recorded at [LiCl] = 2.5M. In spite of this increased propensity for disorder, the effect of added LiCl is qualitatively similar to that of added NaCl, leading to phases and D_{nn} values corresponding to higher [$CaCl_2$] (**Fig 6.2f**). In addition to establishing this commonality, utilizing the highly soluble LiCl allowed us to probe our system in solutions of extremely high ion concentrations, where ion-ion interactions can have significant effects [143, 228]. Indeed, we find that DNA-NPs, in the presence of 200 mM $CaCl_2$, begin to expand with added LiCl when [LiCl] exceeds 7 M. This behavior is comparable to that observed in solutions for which [$CaCl_2$] > 3.3 M (Fig 2A) and suggests that sufficiently high concentrations of ions can induce the ionic correlations driving DNA-NP reswelling[105], even when the divalent cations are minority components. DNA-NPs suspended in mixtures of MgCl2 and LiCl also exhibit this phenomenon (**Fig. 6.11**). The absence of this re-swelling in structures formed in simple LiCl solutions (**Fig 6.1d**) establishes the necessary participation of divalent cations in driving this transition, and further emphasizes the striking influence of divalent cations on DNA-NP structures, even in solutions where the concentration of other ions is as much as 50 times higher.

The effects of NaCl and LiCl displayed in **Figure 6.2** are counterintuitive considering experimental evidence that cations compete to neutralize the negative charge of the DNA backbone[126, 229]. Additionally, since the assembly of DNA-NPs by divalent cations appears to be at least partly electrostatic in nature[184], the screening effects associated with the addition of other salts would be expected to lead to some degree of suppression of assembly. Notably, pre-crystalline ordering driven by $CaCl_2$ appears to be suppressed by 1 M LiCl (**Fig 6.2e-f**).

Additionally, scrutinization of the D_{nn} values (**Fig. 6.2c**) suggest that increasing [NaCl] to 1 M in 200 mM $CaCl_2$ solutions causes the DNA-NP clusters to expand rather than contract. In order to verify the consistency of these effects, we analyzed additional samples, with [$CaCl_2$] and [NaCl] varied in smaller increments. From **Figure 6.3**, it is apparent that the addition of NaCl in concentrations up to 0.5 M increases D_{nn}: above 0.5 M, the effect of added NaCl switches to decreasing D_{nn}, eventually driving the precipitation of FCC structures. For samples in which [$CaCl_2$] = 250 mM, 0.5 M NaCl suppresses crystallization, reflecting a relationship between D_{nn} and the solution stability of the nanoparticles. At higher $CaCl_2$ concentrations (i.e., 300 mM), any apparent suppression of aggregation by NaCl is eliminated, with structures only compressing with added salt.

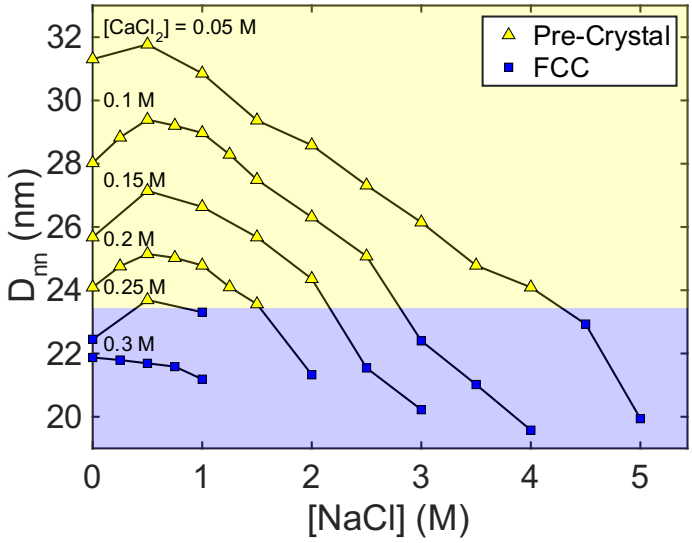

Figure 6.3: Phases and interparticle separations for DNA-NPs assembled at various concentrations of NaCl and $CaCl_2$. At 0.25 M and below, the addition of up to 0.5 M NaCl suppresses crystallization and increases D_{nn}. At [NaCl] greater than 0.5 M, additional NaCl drive aggregate contraction and crystallization. Structure factors are provided in **Fig. 6.14** of the chapter supporting formation.

The net effect of added NaCl thus varies depending on the concentrations of the salts within the system, with low concentrations favoring less condensed, freely dispersed DNA-NP

structures, and high salinities favoring compressed, aggregated structures. Thus, DNA-NPs equilibrated with a fixed, low concentration of $CaCl_2$ thus exhibit subsequent "salting-in" and "salting-out" transitions with increasing [NaCl], in analogy to the dependency of protein solubility on concentrations of certain salts [57, 58]. This analogy, while simplified, provides certain insights into the mechanisms underlying the complex behavior of the DNA-NP system. At low concentrations, where "salting-in" occurs, the effect of added NaCl is dominated by the electrostatic screening of attractive interactions between DNA-NPs[57, 58, 230], thus increasing D_{nn}. However, increasing quantities of ionic species present in solution disrupt the hydration structure of DNA molecules[231] and drive additional cation binding[232]. At higher salinities, these modifications to DNA solvation increase the relative favorability of attractive interactions between DNA-NPs, resulting in "salting-out". While the addition of poorer solvents such as ethanol are required to precipitate dispersed nucleic acids in solutions of salts of monovalent and/or divalent cations[233], DNA origami pyramids can be "salted out" with ammonium sulfate[234], reflecting the enhanced role of hydration in DNA assembled into nanomaterials. Indeed, we have previously demonstrated the significance of desolvation to the FCC-to-BCC transition observed in the DNA-NP-$CaCl_2$ system[155]. Additionally, we present additional evidence of the significant role of hydration by comparing DNA-NP assemblies in $CaCl_2$ solutions utilizing H_2O or D_2O as the solvent (**Fig. 6.4**). The stronger hydrogen bonding between D_2O molecules results in decreased favorability of macromolecule hydration[235]. Here, structures formed in D_2O are more compressed (showing lower D_{nn}), with the transitions to FCC, BCC, and RCP structures occurring at consistently lower [$CaCl_2$] than in H_2O solutions, reflecting a causal role for solvation in the observed "salting out" behavior. Additional evidence is provided from the effects of glycerol and urea on the assembly (**Fig. 6.7**).

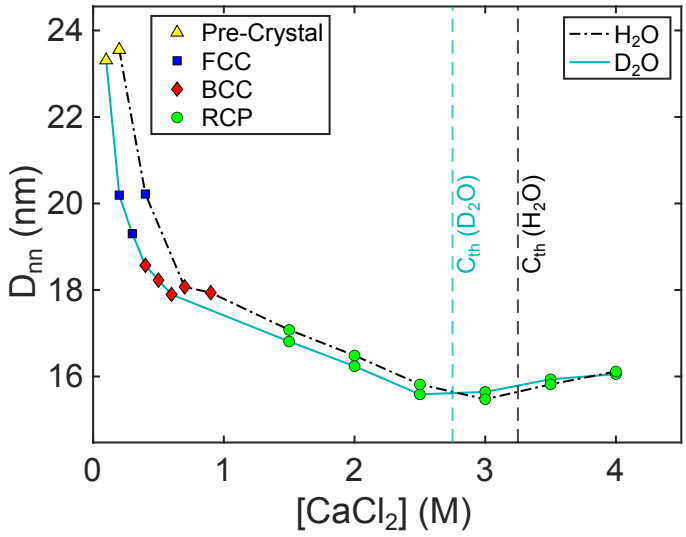

Figure 6.4: Interparticle separation (D_{nn}) and phases of DNA-NP assemblies as a function of [$CaCl_2$] in solutions with H_2O or D_2O as the solvent. Vertical lines mark the estimated salt concentrations between the two lowest spacings observed in each sequence. When D_2O is the solvent, the crystallization transition, the FCC-to-BCC transition occur at lower [$CaCl_2$]. The transition from contraction to expansion also occurs at lower [$CaCl_2$] in D_2O solutions.

As shown in **Figure 6.2e-f**, added LiCl drives reswelling of DNA-NPs above a threshold concentration if Ca^{2+} is present. While our analysis suggests that hydration-related "salting out" effects should be considerably more influential than electrostatic "salting in" effects at these extreme salinities, additional competition between Li^+ and Ca^{2+} to bind to phosphates manifesting at ion high concentration could in principle explain the observed reswelling behavior. If such competitive interactions were present, increasing [Ca^{2+}] should suppress this effect, requiring higher [LiCl] in order to induce reexpansion. Appraisal of DNA-NP suspensions with varied $CaCl_2$ concentration (200, 400, and 900 mM) reveals that this threshold concentration of LiCl instead shifts downward with [Ca^{2+}] (**Fig. 6.4**). Thus, the reexpansion also appears to be driven by cooperative effects of Ca^{2+}, Li+, and Cl^-, which is consistent with a

mechanism in which ion-ion correlation effects prominent in concentrated electrolytes modulate DNA-NP interactions[105].

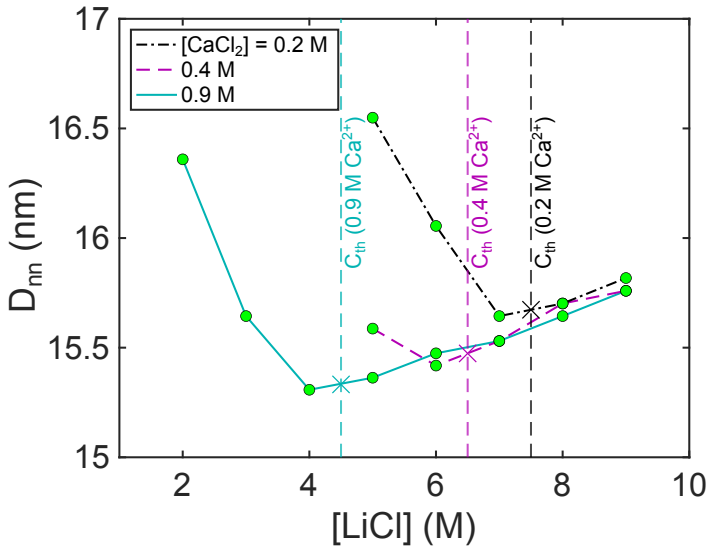

Figure 6.5: Interparticle separation (D_{nn}) as a function of [LiCl] in solutions with 0.2 M, 0.4 M, and 0.9 M CaCl2. The green markers signify all structures as being random close packed. Vertical lines mark the estimated salt concentrations between the two lowest spacings observed in each sequence. The transition between contraction and expansion occurs at lower [LiCl], suggesting that cooperative effects between ions, instead of competition between Ca^{2+} and Li^{+}, are responsible the reswelling. 1D SAXS profiles are provided in **Fig. 6.16** of the chapter supporting formation.

6.3. Conclusions

Here, we have demonstrated that mixtures of cations can induce in DNA-coated nanoparticles a rich array of behaviors, arising from a complex interplay of electrostatic screening, hydration effects, and ion-ion correlations. **Figure 6.6** summarizes these results in a schematic plot. DNA-NPs interact strongly with divalent cations, forming characteristic structures even in the presence of very high concentrations of other ions. These structures are "salted in" by the addition of small quantities of monovalent salts, but "salted out" above a

threshold salinity, thus displaying behavior comparable to that of zwitterionic proteins. At very high ionic concentrations, aggregates containing divalent cations reexpand with added salt, showcasing a manner in which ion-ion correlations tune material behaviors. It is apparent that the response of nucleic acids nanomaterials to solution composition can be varied considerably, with the present study elucidating several principles that may be used in the engineering of these materials, which find applications in detection[236] and medicine[237].

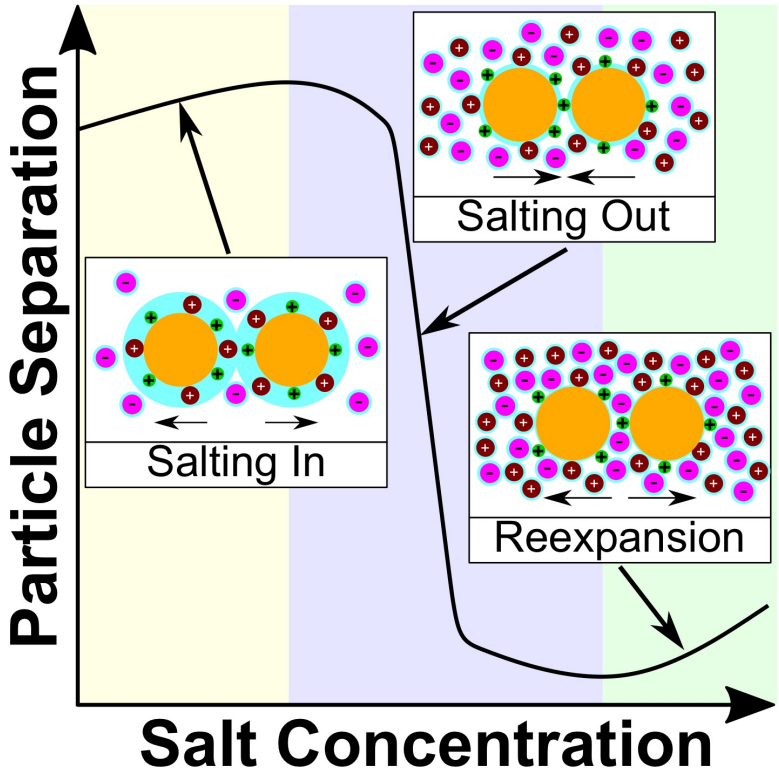

Figure 6.6: A schematic summary of the responses of DNA-NPs in solutions of low $CaCl_2$ concentration as a monovalent salt is added (here denoted by increasing "Salt Concentration"). Insets depict the dominant mechanism in a region of the diagram.

6.4. Chapter 6 Supplemental Information

6.4.1 Additional Experimental Results

The effect of other solution additives was tested with additional SAXS experiments, conducted as described in this chapter. Specifically selected were glycerol and urea, both of which have been shown to decrease the melting temperature of double-stranded DNA, arising from their capacity to increase the solubility of single-stranded DNA[238, 239]. These additives also modify the dielectric properties of the solution, with glycerol decreasing the static permittivity[240], and urea increasing it[241]. DNA-NP suspensions with varied [$CaCl_2$] were prepared in solutions of 10% glycerol (v/v) or 1 M urea.

Results of these experiments are shown in **Figure 6.7**, where they are compared to the results from pure $CaCl_2$ solutions. The tested concentrations of urea and glycerol stabilize the DNA-NPs against electrolyte-induced assembly, and lead to structures with larger interparticle separations, which reflects enhanced DNA solvation. At high [$CaCl_2$], the transition from salt-induced contraction to expansion shifts to lower values in glycerol, as a result of bulk ion-ion correlations manifesting at lower salt concentrations in solutions of lower permittivity (or $CaCl_2$ solubility). This transition is unaffected by the presence of urea, which is likely not present in high-enough concentration to influence the interactions between ions. These results provide additional evidence of the role of "salting out" and ion correlation effects in this system, and demonstrate how these forces may be tuned independently by careful selection of solution composition.

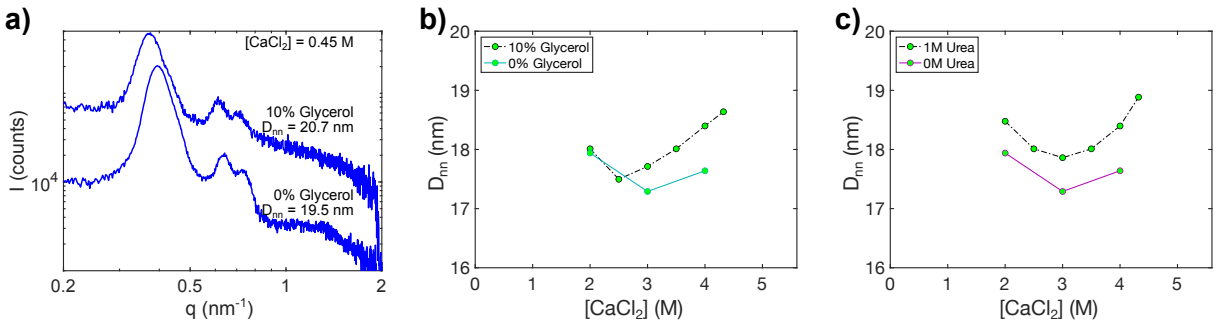

Figure 6.7: $CaCl_2$-induced Assembly of DNA-NPs in 10% glycerol (a-b) and 1 M urea (c), compared to assembly in purely aqueous solutions of the same concentrations. (a) depicts example SAXS patterns, with that of glycerol displaying scattering peaks at lower q, denoting a more expanded structure. (b) and (c) display plots of interparticle separation as functions of $[CaCl_2]$. The concentration at which D_{nn} begins to incase with $[CaCl_2]$ is shifted downward when glycerol is added, but unaffected when urea is present.

While this work demonstrates that the presence of high concentrations of monovalent salts is "cooperative" to Ca^{2+} binding, it is unclear whether these results extend to mixtures of divalent cations. So, additional samples were prepared with fixed $[CaCl_2]$ (200 or 400 mM) and varied $[SrCl_2]$. Results of these experiments are presented in **Figure 6.8**. Comparably to the cases of NaCl and LiCl, the addition of $SrCl_2$ apparently magnifies the influence of Ca^{2+}, leading to structural compression and favoring crystallization. However, at higher $[SrCl_2]$ (1-1.5 M), the structures instead expand with added $SrCl_2$. Recall that ion-ion correlations become prominent at lower concentrations of $SrCl_2$, with the DNA-NP reswelling commencing at concentrations as low as 1.5 M in these solutions. This consideration, as well as the fact that the threshold between salt-induced contraction and expansion shifts to lower $[SrCl_2]$ when $[CaCl_2]$ is increased to 400 mM, suggests that this reswelling arises from ion-ion correlations, rather than competition between Sr^{2+} and Ca^{2+}. At very high $[SrCl_2]$ in these mixtures, the DNA-NPs return to suspension as pre-crystals, with D_{nn} values lower than pre-crystals in concentration-equivalent $SrCl_2$ solutions (~27 nm), suggesting that Ca^{2+} remains bound even after this "re-solubilization" transition. Whether the "melting" of the FCC structures results from increasing dominance of the

Sr^{2+} or is a natural consequence of the apparent DNA configuration in these concentrated ionic mixtures, is currently ambiguous. Nonetheless, it appears that many of the principles outlined in this chapter also apply to mixtures of $SrCl_2$ $CaCl_2$, serving as a promising indicator of generatability.

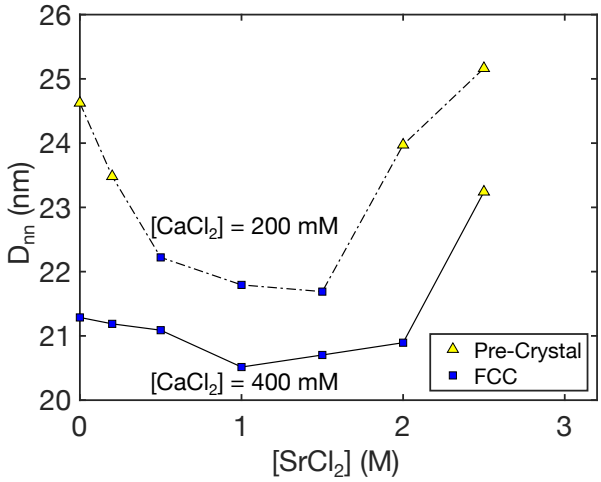

Figure 6.8: A plot of phase and interparticle separation of DNA-NPs as a function of [$SrCl_2$] in the presence of fixed concentrations of $CaCl_2$.

6.4.2 Supplemental Figures and Tables

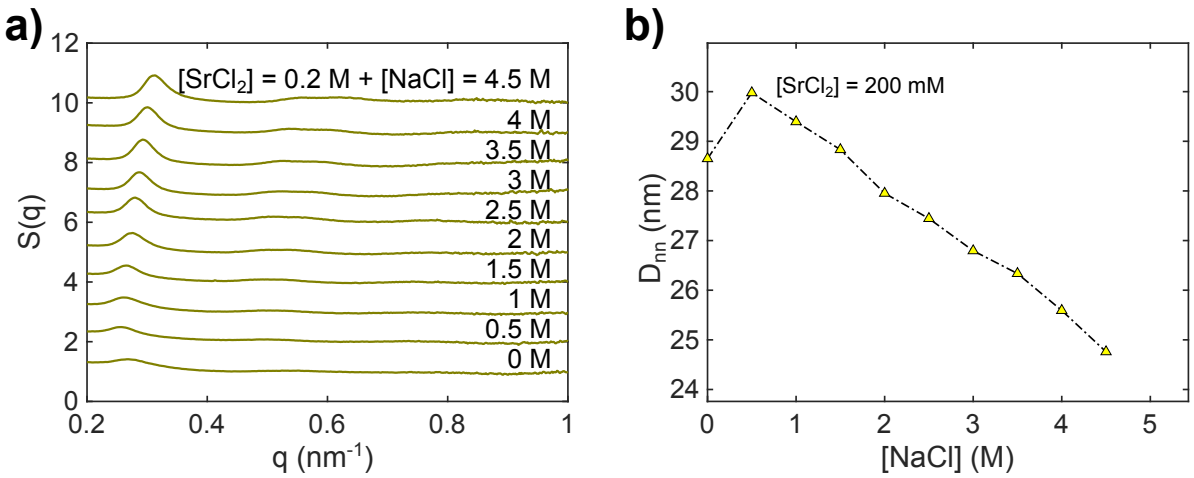

Figure 6.9: a) Structure factors for DNA-NP structures assembled at fixed [$SrCl_2$] = 0.2 M and varied [NaCl]. Interparticle separations and phases are plotted in (b). Yellow triangular markers denote that all observed structures are precrystalline. Note that "salting in" and "salting out" transitions are observed, depending on [NaCl].

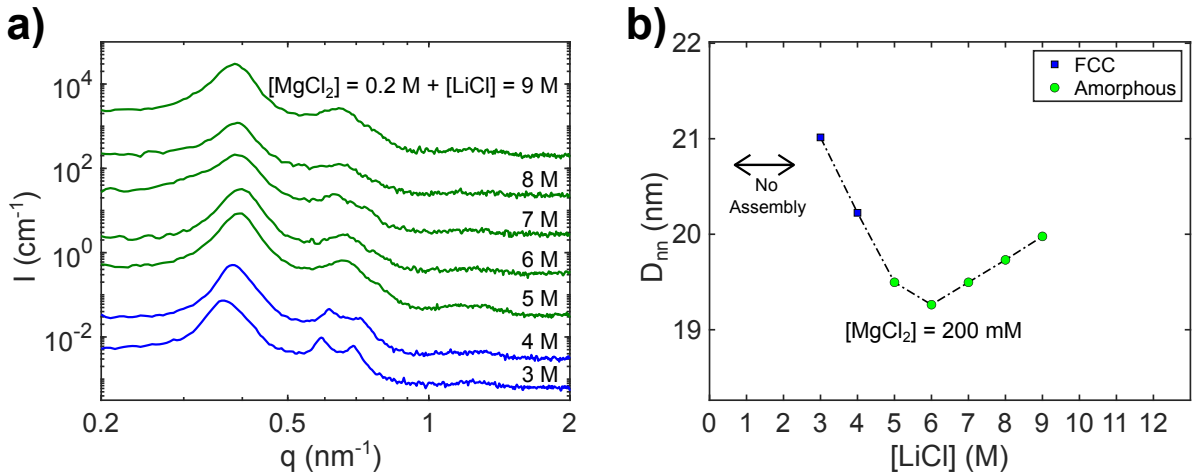

Figure 6.10: a) 1D SAXS intensity profiles for DNA-coated AuNPs suspended in aqueous solutions of at fixed [$MgCl_2$] (0.2 M) and varied LiCl concentration. Interparticle separations and phases are plotted in (b).

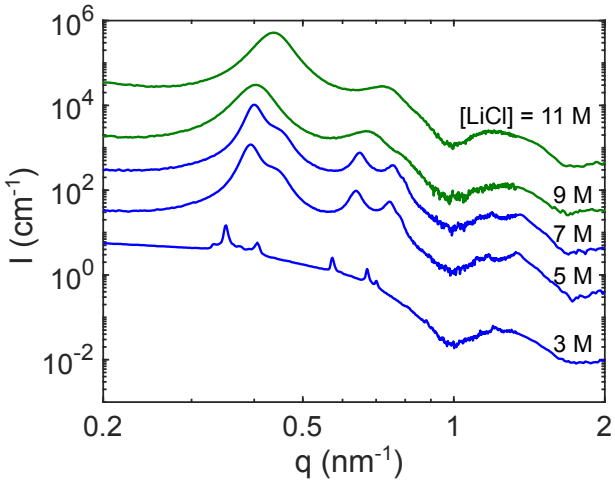

Figure 6.11: Buffer-subtracted SAXS data for DNA-NP dispersed in solutions of varied LiCl concentration, summarized in **Fig. 6.1.**

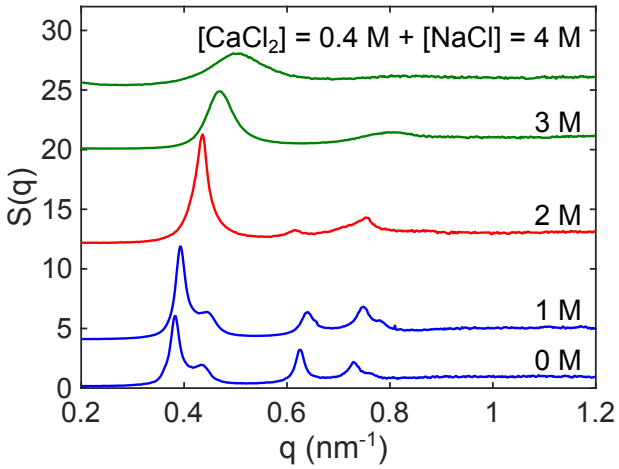

Figure 6.12: Structure factors for DNA-NP structures assembled at fixed [$CaCl_2$] = 0.4 M and varied [NaCl]. Interparticle separations and phases are plotted in **Fig. 6.2c**.

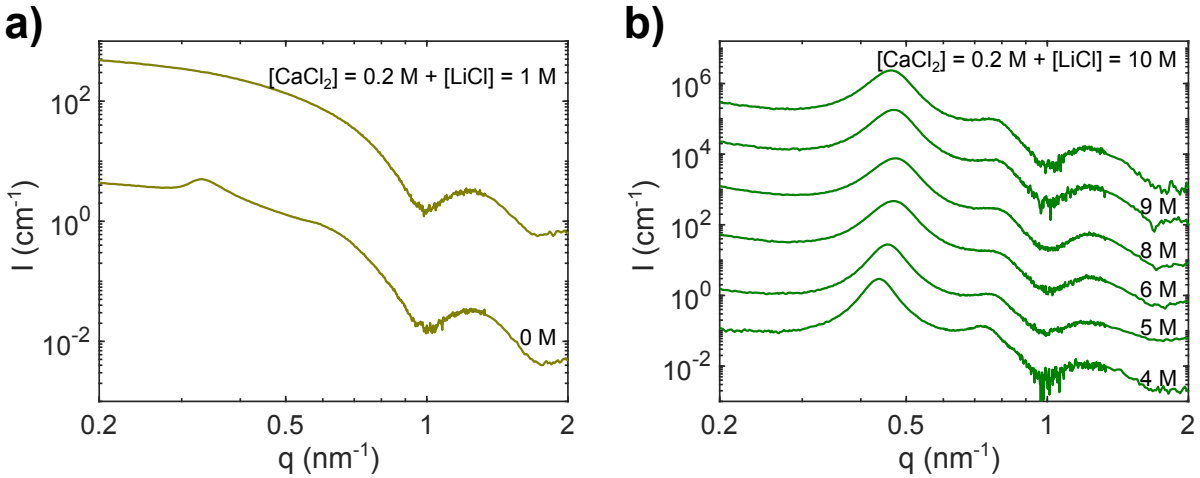

Figure 6.13: Buffer-subtracted SAXS data for DNA-NP dispersed in solutions of fixed at fixed [$CaCl_2$] (0.2 M) and varied LiCl concentration, ranging from low (a) to high (b) concentration, as summarized in **Fig. 6.2f**. The addition of 1 M LiCl eliminates precrystalline ordering associated with $CaCl_2$. The primary scattering peak shifts non-monotonically with [LiCl].

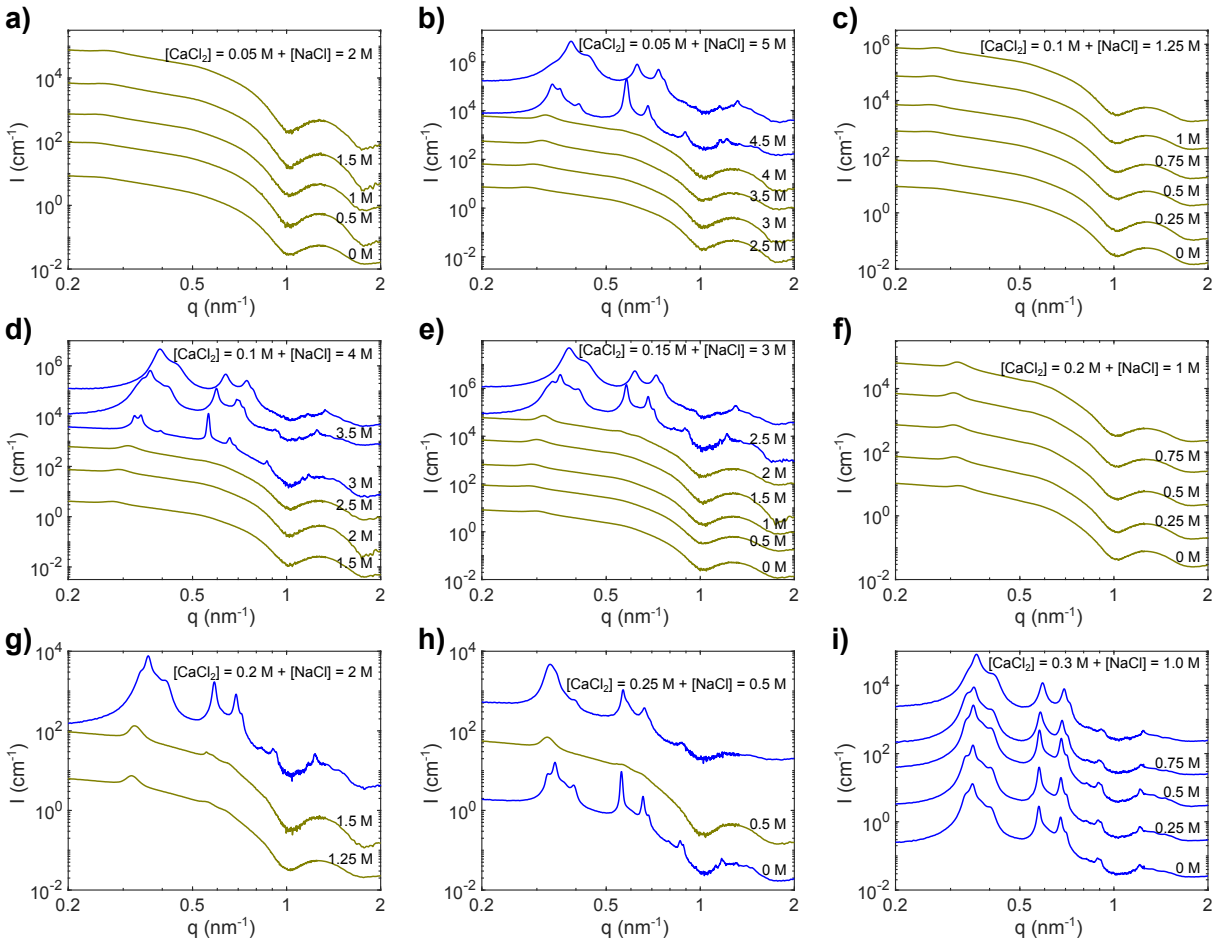

Figure 6.14: Buffer-subtracted SAXS data for DNA-NP dispersed in solutions of fixed at varied [NaCl] and [$CaCl_2$] fixed at different valuers, including 50 mM (a-b), 100 mM (c-d), 150 mM (e), 200 mM (f-g), 250 mM (h) and 300 mM (i). Results are summarized in **Fig. 6.3**

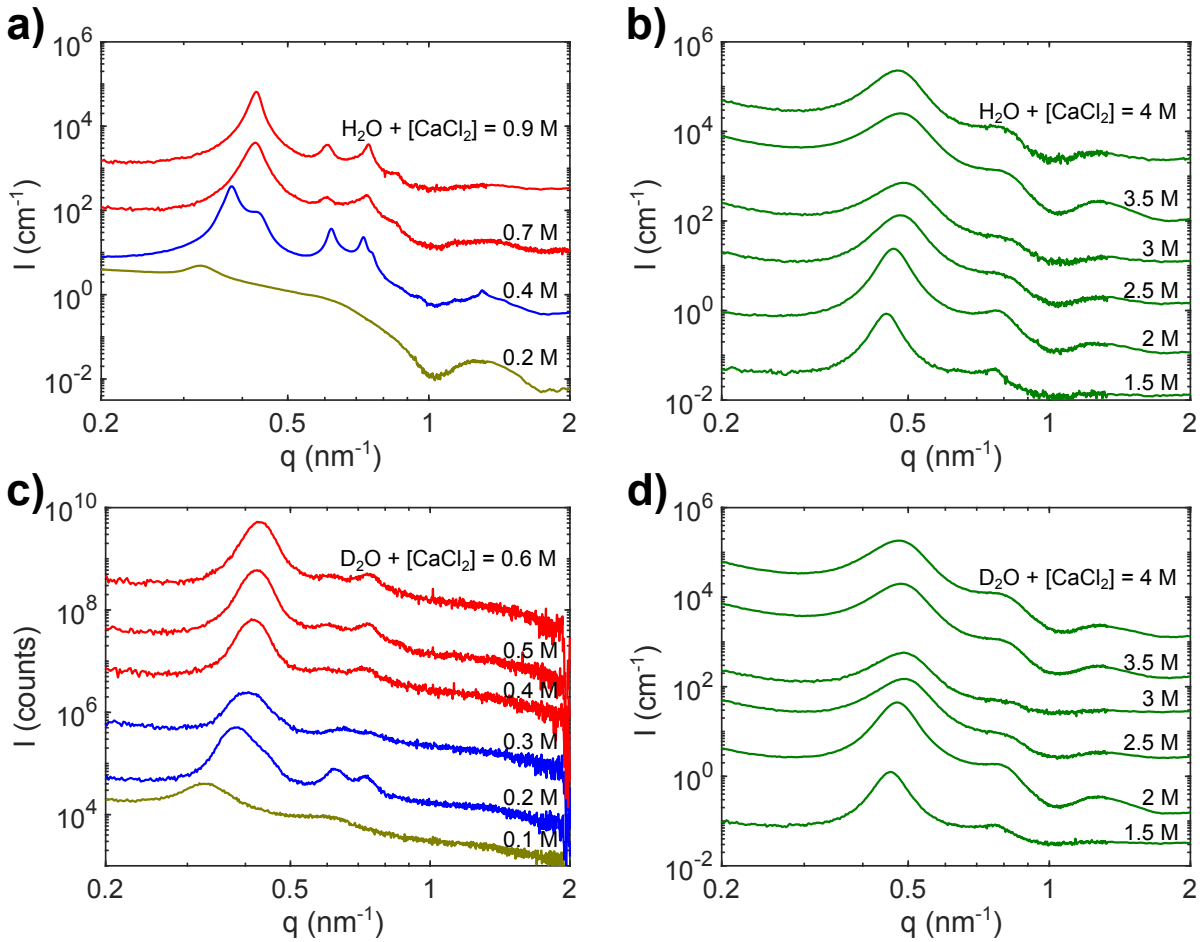

Figure 6.15: 1D SAXS intensity profiles for DNA-coated AuNPs suspended in solutions of varied [$CaCl_2$], with H_2O (a-b) or H_2O (c-d) as the solvent. Results are summarized in **Fig. 6.4.**

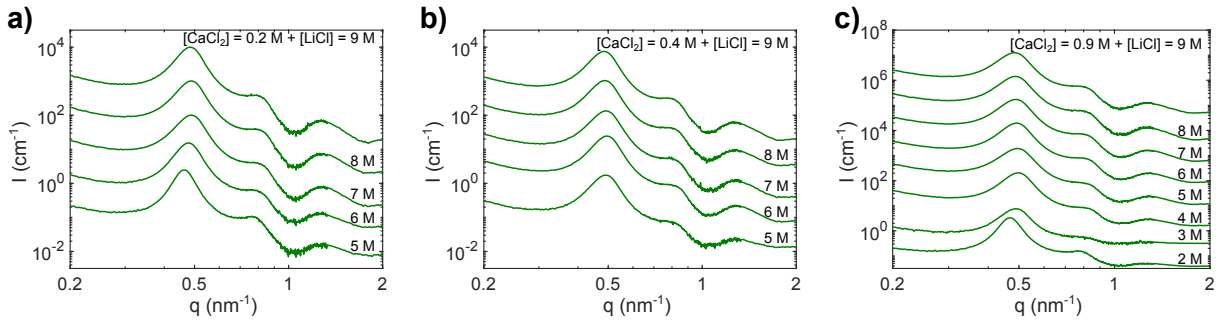

Figure 6.16: Buffer-subtracted SAXS data for DNA-NP dispersed in solutions of fixed at varied [LiCl] and [$CaCl_2$] fixed at different valuers, including 0.2 M (a), 0.4 M (b), and 0.9 M (c). Results are summarized in **Fig. 6.5.**

Table 6.1: Miller indices and relative scattering peak positions for the first 13 peaks associated with the FCC structure, referenced to the position of the first scattering peak. Here, q_1 corresponds to the (111) peak.

(hkl)	$h^2+k^2+l^2$	q_{peak}/q_1
111	3	1
200	4	1.15470054
220	8	1.63299316
311	11	1.91485422
222	12	2
400	16	2.30940108
331	19	2.51661148
420	20	2.5819889
422	24	2.82842712
333,511	27	3
440	32	3.26598632
531	35	3.41565026
442,600	36	3.46410162

Table 6.2: Miller indices and relative scattering peak positions for the first 7 peaks associated with the BCC structure, referenced to the position of the first scattering peak. Here, q_1 corresponds to the (110) peak.

(hkl)	$h^2+k^2+l^2$	q_{peak}/q_1
110	2	1
200	4	1.15470054
211	6	1.41421356
220	8	1.63299316
310	10	1.82574186
222	12	2
321	14	2.1602469

Table 6.3: Aqueous solubilities for the various salts utilized in this work (at 22°C).

Salt	Water Solubility (M)
NaCl	5.5
LiCl	13.
$CaCl_2$	5.6
$MgCl_2$	5.0
$SrCl_2$	3.2

Chapter 7: Temperature-Dependent Effects

The influence of environmental temperature on material properties is a topic of pervasive influence. Many products rely upon the applications of heat in order to enable processing or actuation. Materials that will be subject to fluctuations in temperature throughout the duration of their usage may wear or deform. From the standpoint of studying the fundamental origins of a material's properties, temperature represents an accessible parameter to vary in the pursuit of disambiguating the governing thermodynamic factors. For example, the stiffening of rubber in response to heat provides insight into the entopic origin of its elasticity [242]. In this chapter, *in situ* X-ray scattering experiments are employed to elucidate how the electrolyte-mediated assembly of DNA-NPs evolves with solution temperature.

Most materials respond to increases in temperature by expanding and/or undergoing phase transitions, such as melting or sublimation. The pervasiveness of the former is readily explained by the anharmonicity of atomic bonds, which tend to drive larger interatomic separations when internal energy is increased [243]. However, some materials exhibit apparent contraction upon heating, dubbed negative thermal expansion (NTE)[244]. Generally, materials exhibiting NTE feature highly directional bonds or exhibit phase transitions, though NTE in assemblies of monodisperse particles governed by isotropic interactions has been predicted[245]. While DNA-NPs assembled via base-pairing interaction have been shown to thermally expand and melt upon heating[84], polyethylene glycol (PEG)-grafted nanoparticles instead precipitate as colloidal crystals and contract at elevated temperatures[246]. Here, the thermal responses of DNA-NPs are found to vary considerably with salt concentration, exhibiting melting transitions,

thermal expansion, and negative thermal expansion in different regimes. These phenomena are analyzed in the context of ionic correlations and solvation.

7.1 Methods

Samples of 10 nm AuNPs grafted with the T35 sequence dispersed in solutions of varying salt concentrations were synthesized as described in prior chapters. *In situ* SAXS/MAXS/WAXS experiments were conducted at beamline 5-ID-D of the APS, utilizing 17 keV X-rays. An array capillary heater was used, capable of holding nine 1.5 mm capillaries between metal plates, with temperature controlled by cartridge heaters and monitored by thermocouples. To reach sub-ambient temperatures, cold N_2, from the vented cap of a liquid nitrogen tank, was utilized as the cooling gas for active cooling. The system was controlled by National instruments hardware and Labview software. A thermocouple sealed in a 1.5 mm quartz capillary filled with mineral oil was placed in one of the sample positions to monitor the expected temperatures of the liquid samples. Generally, temperatures fluctuated 1-2°C around set points. To enable equilibration, 30 minutes were allowed to elapse between the attainment of a set point and measurement. For each point, three measurements, each at different positions in the capillary, were collected, each consisting of 0.15 s exposures; this low time was selected to minimize X-ray-induced sample damage accumulated over the course of measurement. The instrumental correction and radial averaging of the data was performed as described in other chapters.

Additional measurements were performed at Northwestern University in the J.B. Cohen X-ray Diffraction Facility. SAXS measurements were done with a Rigaku SMAXS-3000 setup, equipped with a Cu microbeam anode (8.04 keV energy), multilayer focusing mirrors, and an Eiger R1M 75uM pixel single photon counting 2D detector positioned 1.56 m from the samples

stage. Samples in epoxy-sealed 1.5 mm quartz capillaries were mounted in a Linkam temperature control stage; liquid nitrogen was utilized to achieve sub-ambient temperatures. “High resolution” slit sizes were selected for measurements, where incident vertical and horizontal slits focus the beam to around 0.5 x 0.5 mm on the sample. SAXS patterns were collected 20 minutes each, scattering being recorded via the Xenocs Instrument Control Center (XICC) software. Following collection, the 2D scattering patterns were converted to 1D profiles via azimuthal integration, carried out by the instrument software. Temperature-controlled UV-Vis spectrophotometry was performed using a Varian Cary 5000 UV-vis spectrophotometer equipped with an external temperature controller that employs a Peltier heat pump. 1 mL of sample (with DNA-NP concentration of 1-2 nM) were deposited in quartz cuvettes with magnetic stir bars. Absorbance at 520 nm (corresponding to non-aggregated DNA-NPs) was measured as temperature was increased from 25°C to 65°C, and decreased to 10°C in 0.2°/minute increments, with one measurement at each setpoint.

SAXS data was primarily analyzed by monitoring the position of the first major diffraction peak at different temperatures. For the FCC, BCC, and RCP structures encountered in this study, the position of this peak can consistently be related to the average distance of closest approach between the DNA-NPs in the structures by the relationship: $D_{nn} = \frac{\sqrt{6\pi}}{q_1}$. The positions of these primary scattering peaks were determined utilizing MATLAB; briefly, for each measurement, the three frames were averaged, and a gaussian filter with a 10-point window was applied to smooth the data. From here, q_1 was extracted as the maximum value of the 1D scattering profile, with data below 0.3 nm^{-1} omitted to avoid other scattering contributions.

7.2 Tunable Thermal Expansion

As DNA-NPs are commonly applied in ambient and biological conditions, we begin with analyzing how DNA-NP structures evolve with temperature at $CaCl_2$ concentrations between 0 and 1 M. Recall that at room temperature, T35-DNA-NPs generally assemble into FCC structures above ~0.25 M, and into BCC structures above ~600 mM**. Figure 7.1** shows example SAXS data, corresponding to an FCC scattering pattern at 375 mM [$CaCl_2$], and a BCC pattern at 900 [$CaCl_2$]. Comparing the diffraction patterns obtained at sub-ambient (~5°C) and biological (~37°C) temperatures, it is apparent that the positions of the scattering peaks shift. More specifically, the peaks of the FCC pattern shift to lower q values, corresponding to apparent expansion of the lattice, while the peaks of the BCC pattern shift to higher q values, signifying that the lattice contracts upon heating. Thus, salt concentration appears to determine not only the structure of DNA-NP assemblies, but also their thermal properties.

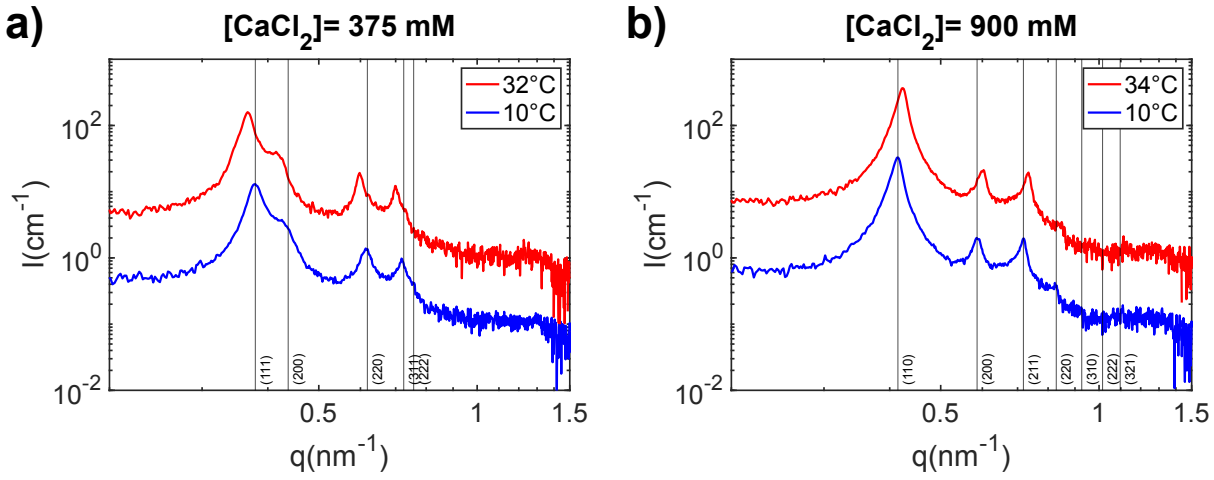

Figure 7.1: SAXS patterns for DNA-NPs assembled at 375 mM (a) or 900 mM (b) CaC_{l2}, each measured at a low and high temperature. Mille indices and vertical lines label the positions of FCC (a) and BCC (b) peaks at the lower temperature. Comparing the two samples, the diffraction peaks shift in opposite directions when the sample is heated, indicating the FCC structure thermally expands, whereas the BCC structure thermally contracts

These apparent shifts in lattice dimensions can be quantified by defining a coefficient of thermal expansion, α:

$$\boldsymbol{\alpha_a = \frac{1}{a}\left(\frac{\partial a}{\partial T}\right)_{P,N} \sim \frac{1}{a_o}\left(\frac{a_1 - a_o}{T_1 - T_2}\right)}$$

(7.1)

where a denotes a lattice parameter of the structure. For the structures in this work, all having cubic symmetry, this coefficient can be written as:

$$\alpha_V = \frac{1}{V}\left(\frac{\partial V}{\partial T}\right)_{P,N} = \frac{1}{a^3}\left(\frac{\partial a^3}{\partial T}\right)_{P,N} = \frac{3}{a}\left(\frac{\partial a}{\partial T}\right)_{P,N} = 3\alpha_a \sim \frac{3}{a_o}\left(\frac{a_1 - a_o}{T_1 - T_2}\right)$$

(7.2)

Average volumetric coefficients of thermal expansion over the 5° to 35° C range can thus be computed from the positions of the diffraction peaks from DNA-NP structures at various $[CaCl_2]$.

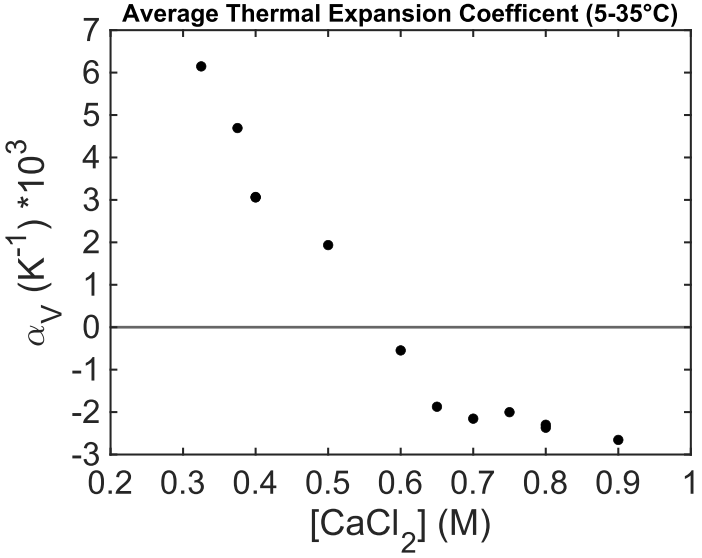

Figure 7.2: A plot of average volumetric thermal expansion coefficient of DNA-NPs structures versus $[CaCl_2]$, calculated from the SAXS diffraction peaks measured at the temperature endpoints of the range. $[CaCl_2]$ influences both the sign and magnitude of the thermal expansion coefficient

Figure 7.2 plots these coefficients against the corresponding salt concentrations, demonstrating continuous evolution of this parameter. At low salt concentrations, α_V is positive, decreasing in magnitude with [$CaCl_2$] until 500-600 mM. Around these concentrations, α_V becomes negative, and subsequently increases in magnitude more slowly with [$CaCl_2$].

It is interesting to note that the apparent transition from positive to negative thermal expansion aligns roughly in [$CaCl_2$] with the FCC to BCC transition. While this may reflect the underlying solvation thermodynamics, additional SAXS experiments establish that the phase transition is not a causative factor. For example, **Figure 7.3** compares the thermal responses of DNA-NP structures formed in solutions of 300 mM $CaCl_2$, with or without the presence of 1 M NaCl. In both electrolyte compositions, DNA-NPs form FCC structures. However, while structures in 300 mM $CaCl_2$ expand when heated from 5 to 25°C, consistent with prior results, structures in 300 mM $CaCl_2$ and 1 M NaCl instead contract. Therefore, the BCC structure does not represent a requirement for NTE in this system. Instead, it appears that the most significant factor is the total ionic content of the solution.

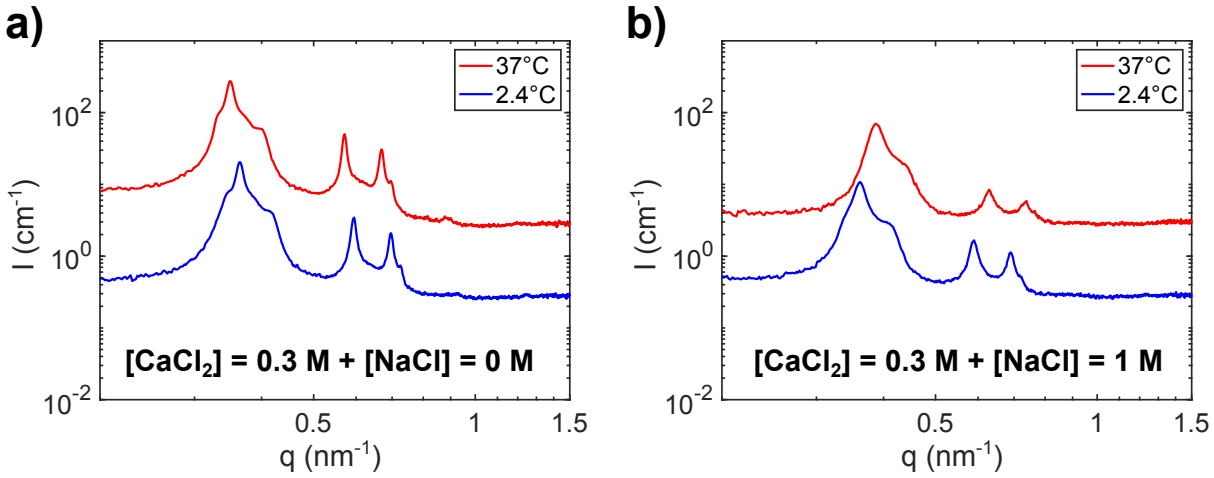

Figure 7.3: SAXS patterns for DNA-NPs assembled at 0.3 M CaCl2, and either 0 M (a) or 1 M (b) CaCl2, each measured at a low and high temperature. Despite displaying the same lattice type, the diffraction peaks shift in opposite directions when the sample is heated, suggesting that the sign of the thermal expansion coefficient differs between the samples.

7.3 Melting Transitions

In addition to expansion or contraction, increases in temperature can drive materials to change phase, as by melting structural transitions. For colloidal materials and macromolecules, temperature changes can modify the stability and/or solubility of components, possibly leading to precipitation[247] or complex liquid-liquid phase separations[248]. Thermally induced phase separation of nucleic acids in solutions of divalent cations has been studied, with higher degrees of solution stability occurring at higher[249] or lower[250] temperatures, depending on the sequence and structure of the molecules. Since geometry of nucleic acids influencing their interactions with ions, an extension of such investigations to DNA-NPs is warranted.

Evidence of melting transitions in DNA-NP structures is apparent from both *in situ* SAXS measurements and temperature-varied UV-Vis spectrophotometry. **Figure 7.4** displays such results for DNA-NPs in 300 mM $CaCl_2$ solutions. SAXS measurements reveal that the DNA-NP structures transition from showing clear FCC diffraction peaks to showing broad, low-intensity features as temperature is increased from 21 to 34 °C. The latter is consistent with weak, liquid-like, pre-crystalline ordering observed in DNA-NP suspensions at lower [$CaCl_2$]. UV-Vis measurements provide complimentary measurements, as the relative intensity of the optical absorbance at 520 nm reflects the concentration of non-aggregated DNA-NPs in the solution. Melting transitions of electrolyte-assembled DNA-NP structures are broad, taking place over a range of roughly 20 to 32°C; this is 2-4x wider than the temperature range over which base-paired DNA-NP structures undergo melting transitions[251]. In addition, these melting transitions are very sensitive to [$CaCl_2$]; structures in 200 mM solutions melt between 7 and 15°C, and DNA-NPs in 350 mM remain in stable FCC aggregates in excess of 60°C. The presence of NTE at higher [$CaCl_2$] suggests that higher temperatures favor more compact DNA-

NP configurations (thus aggregates); accordingly, no melting transitions were detected in solutions of higher [$CaCl_2$]. Thus, melting transitions appear accessible only at [$CaCl_2$] below 350 mM.

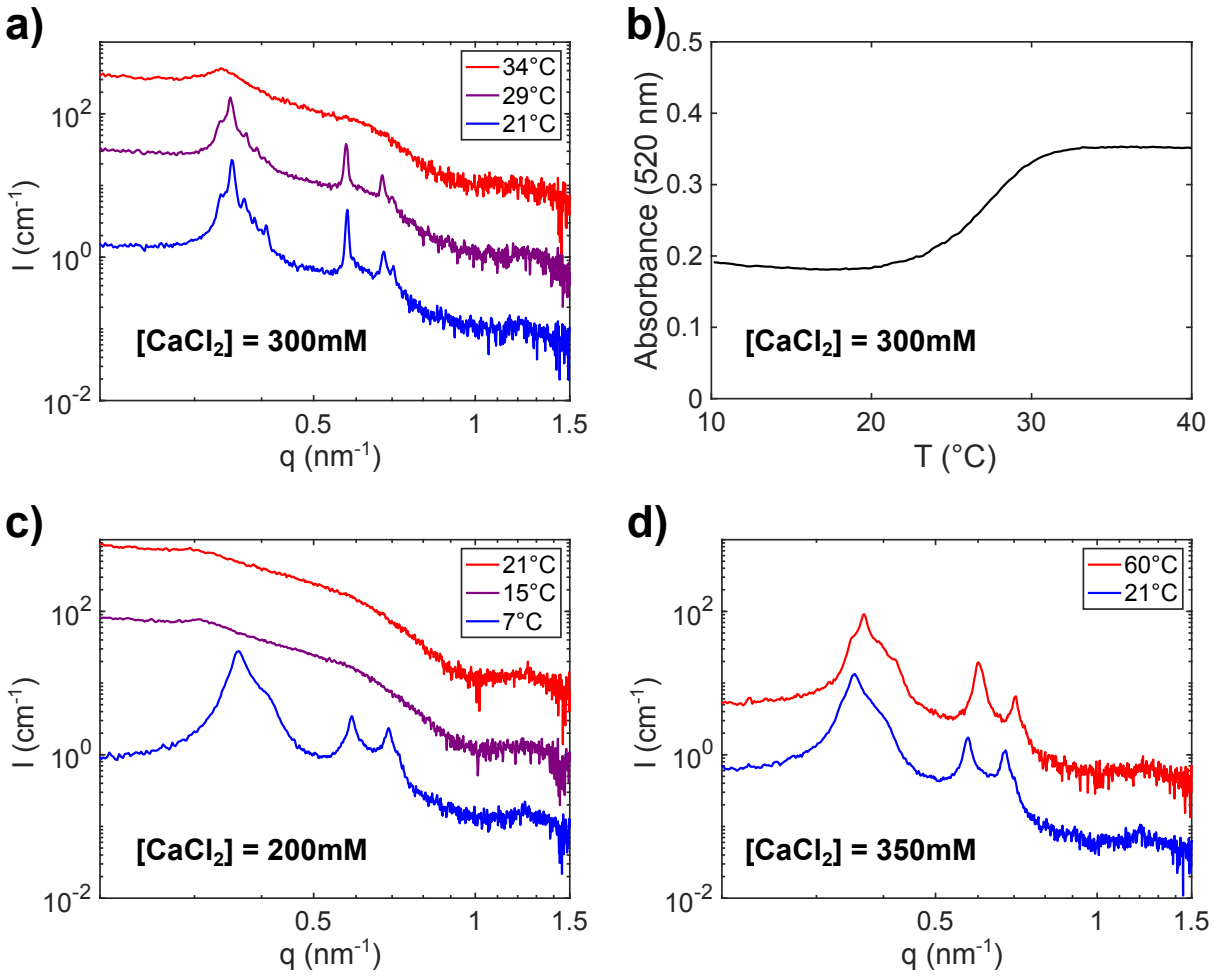

Figure 7.4: (a) SAXS patterns for DNA-NPs assembled at 300 mM $CaCl_2$ with varying temperatures. The sharp diffraction peaks disappear upon heating to 34°C, indicating the melting of the structures. (b) A UV-VIS melting curve, showing absorbance at 520 nm versus solution temperature for DNA-NPs in 300 mM $CaCl_2$. When the absorbance is maximized, the concentration of unassembled DNA-NPs is the greatest, indicating that aggregate melting has completed. (c) SAXS patterns for DNA-NPs assembled at 200 mM $CaCl_2$ with varying temperatures. The aggregates melt at 15°C.(d) SAXS patterns for DNA-NPs assembled at 350 mM $CaCl_2$ with varying temperatures. The FCC structures do not melt at 60°C

7.4 Characterizing the Full T vs [$CaCl_2$] Space

With several interesting thermal responses of DNA-NPs now having been highlighted, the effects over a wider range of temperatures and salt concentrations will now be discussed. Analysis of *in situ* SAXS data at smaller temperature intervals allows for the tracking of nearest-neighbor particle separation (D_{nn}) as temperature is varied. **Figure 7.5** plots evolution of this value for several DNA-NP structures as temperature is varied incrementally between 5 and 65°C. DNA-NPs at [$CaCl_2$] between 0.35 and 0.5 M display the previously described thermal expansion between 5 and 25°C, with D_{nn} increasing with temperature. However, the structures instead begin to contract with heating at higher temperatures; the transition shifts to lower temperatures as [$CaCl_2$] is increased. At higher [$CaCl_2$], such as 0.8 or 0.9 M, this transition is not observed, with D_{nn} instead only showing a negative correlation with temperature. Both higher temperatures and higher salt concentrations lead to negative thermal expansion responses.

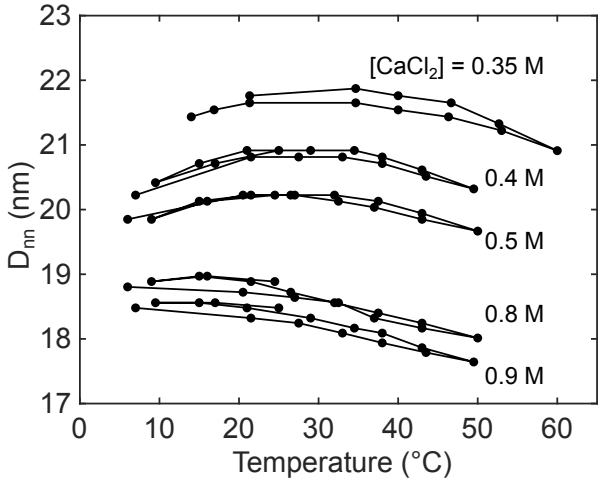

Figure 7.5: Interparticle separations (D_{nn}) for DNA-NPs assembled at various [$CaCl_2$] as functions of temperature. Negative slopes correspond to negative thermal expansion, while positive slopes correspond to positive thermal expansion. For [$CaCl_2$] below 0.5M, the temperature at which the temperature-dependence of D_{nn} changes sign shifts to lower temperatures. At higher [$CaCl_2$], this dependence is only negative

At higher concentrations of $CaCl_2$, DNA-NPs tend to form disordered aggregates (random close packed, RCP), and the dependency of D_{nn} on temperature evolves further (**Figure 7.6**). As [$CaCl_2$] is increased to 2 M, the primary response remains negative thermal expansion, with D_{nn} decreasing with heating and increasing with cooling. As concentrations of 3-5 M are reached, dramatic differences between the effects of heating and cooling appear. At these very high $CaCl_2$ concentrations, increases in temperature still result in contraction of the DNA-NP aggregates; however, cooling does not result in re-expansion of the precipitates, with D_{nn} remaining at the lower values associated with higher temperatures. Thus, the positions of the particles display an apparent hysteresis, with heating driving apparent compression that is not reversed by cooling.

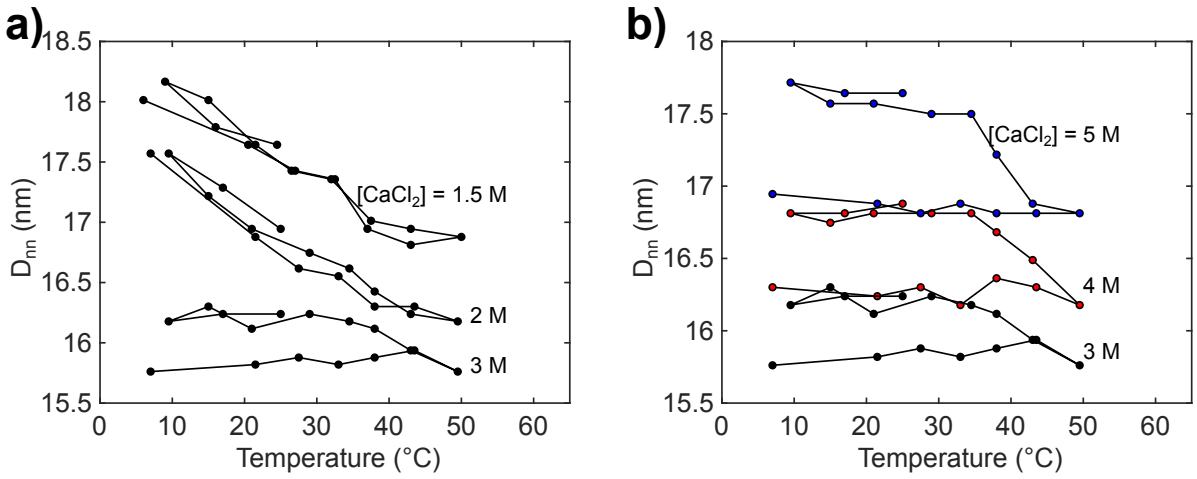

Figure 7.6: Interparticle separations (D_{nn}) for DNA-NPs assembled at various [$CaCl_2$] above (a) and below (b) the salt concentration at which structures begin to expand with added salt. D_{nn} decreases upon heating. At very high salt concentrations, the structure do not fully reexpand upon cooling, with D_{nn} values remaining ~1-1.5 nm below the initial state.

The myriad of behaviors exhibited by this system is charted with respect to the salt concentration and temperature in **Figure 7.7**. The strong dependency of the melting temperature on [$CaCl_2$] reflects the strong interaction between Ca^{2+} and DNA-NPs, which was shown in the previous chapter to remain significant even in crowded solutions of many other cations. Indeed,

any increase in entropy arising from abstracting Ca^{2+} from the DNA-NP structures appears insufficient to induce melting above 350 mM. This entropy, however, may be significant enough to serve as a driving force for the positive thermal expansion behavior observed. Indeed, increases in temperature enable the overcoming of electrostatic inter-monomer attractions in polyzwitterions[252] and polyelectrolytes cross-linked by multivalent counterions[253, 254]. Conversely, it is clear that a separate factor favors the contraction of the DNA-NPs at higher salinities, as well as higher temperatures. Many otherwise hydrophilic macromolecules, including PEG[255] and Poly(N-isopropylacrylamide) (PNIPAM)[256] are precipitated from water at elevated temperatures, owing to "salting out" effects. Generally, this is rationalized in terms of the entropy gained by the liberation of water molecules from hydration shells[257]. Such a model has been invoked to explain the negative thermal expansion of PEG-grafted NPs, where the decreasing water solubility of the PEG chains causes them to adopt more compact configurations[246] . Increasing ionic strength would decrease the activity of "free" water, thus magnifying this effect[258]; appropriately, it was demonstrated that the addition of NaCl can also drive NTE. Thus, it seems reasonable to suppose that entropic costs of binding water molecules and Ca^{2+} to the DNA exist in opposition, with increasing ionic strength magnifying the weight of the former, thus pushing the effective range of positive thermal expansion to lower temperatures. Finally, it is worth emphasizing that the region of high [$CaCl_2$] where apparent hysteresis is observed coincides with the interval in which bulk ion-ion correlations strongly influence the DNA-NP structures. One hypothesis is that increased thermal energy enables Ca^{2+} to escape from ion clusters and bond more tightly with DNA; a similar explanation arises in apparent decreases in Ca^{2+} hydration[259], which might have similar effects. Additional studies investigating

the stability of these apparent thermal hysteresis effects against dilution and mechanical agitation will provide highly useful insight.

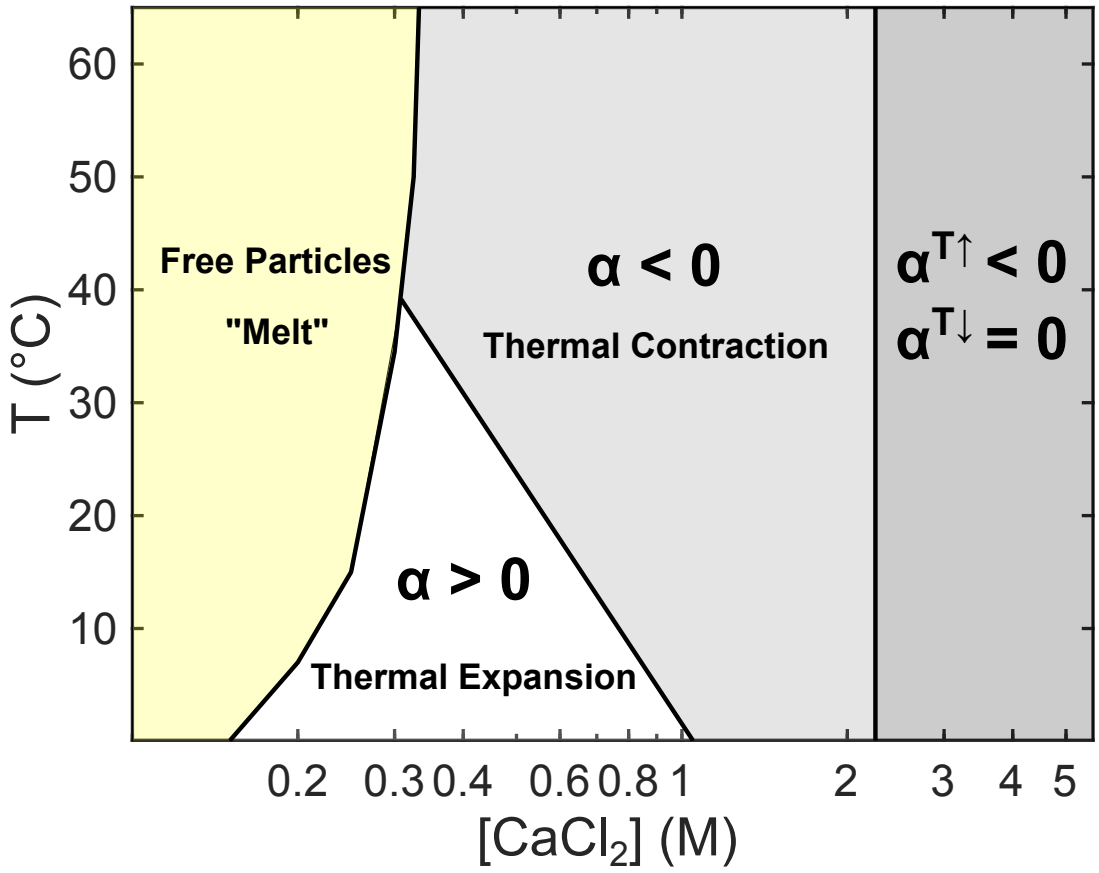

Figure 7.7: A schematic plot illustrating the various responses to heating exhibited by the DNA-NPs, as dictated by salt concentration and temperature.

7.5. Conclusions

We have studied how electrolyte-mediated DNA-NP assembly is modulated by temperature. The benefits of these investigations are twofold. Firstly, we have established the dependence of melting temperatures and thermal expansion coefficients of these constructs on salt concentrations. Careful manipulation of melting (or precipitation) of DNA-AuNPs can be utilized in sensing applications[260], or in the preparation of large colloidal crystals[261]. Similarly,

characterizing the thermal expansion of these nanoscale constructs is necessary before deployment in applications where temperature may vary. Additionally, these thermal responses may inform the development of viable actuation strategies in DNA-based nanomaterials. Secondly, we have gained fundamental insights into the thermodynamic factors governing this colloid-in-electrolyte system. At low salt concentrations, increasing thermal energy can overcome the electrostatically driven binding of DNA and Ca^{2+}, leading to melting and thermal expansion. At higher ionic strengths and temperature, however, elevated temperatures decrease the favorability of water-DNA interactions, causing the DNA to adopt more compact conformations and driving negative thermal expansion. At high salt concentrations, where ion-ion correlations influence the system, temperature increases may disrupt ion correlations or hydration in a manner which is not reversible by simple cooling, thus manifesting as hysteresis effects in the DNA-NP structure. In summary, we have demonstrated additional flexibility in the DNA-NP-electrolyte system and have gained insight into the thermodynamic considerations of the interactions between charged colloids and concentrated electrolytes.

Chapter 8: Effects of DNA Brush Composition

Thus far, this thesis has focused on the study of 10 nm gold nanoparticles grafted with identical, 35-base sequences consisting entirely of thymine bases. However, the length and base compositions of oligonucleotides influence their chemical and physical properties[262], including in the DNA-NP geometry[236]. Of particular interest to this work is the manner in which nucleic acid characteristics modify interactions with electrolyte ions, leading to potential differences in assembly.

Here, DNA-NPs prepared with varying nucleic acids are utilized to test the generality of several cation-driven phenomena described in prior chapters. Particles are(?) grafted with longer oligothymidylic acid sequences (55 bases) and short, polydisperse sequences containing other bases aggregate in the presence of sufficient concentrations of $CaCl_2$; while no crystalline order is observed in these assemblies, the reswelling behavior of T35 aggregates (as described in Chapter 4) is observed, suggesting that this effect arises from ion interactions with general features of nucleic acids (e.g., the phosphate backbone), rather than specific base-dependent motifs. Additionally, the assembly of AuNPs grafted with oligothymidylic acid sequences of varying length (20-40 bases) was investigated, revealing the influence of DNA-NP polydispersity on aggregate crystallinity. Sufficient length of the monodisperse DNA strands compensates for the inherent polydispersity of AuNPs; lattices formed of particles grafted with shorter sequences contain defects, or are disordered, while those featuring longer sequences display long-range order. Co-assembly of DNA-NPs with different sequence lengths further evidences this effect, with wider size distributions leading to increased lattice disorder through the formation of stacking faults.

8.0. Methods

The various oligonucleotides utilized in this chapter were synthesized in 5 umol batches using a MerMade solid-state controlled pore glass (CPG) DNA synthesizer from BioAutomation (see **Table 8.1**). Methods for oligonucleotide purification, characterization, and grafting onto 10 nm AuNPs are described in prior chapters. All scattering experiments described in this chapter were performed on DNA-NP samples contained in sealed quartz capillaries, using the combined SAXS/MAXS/WAXS instrument at 5-ID-D of the APS, as detailed elsewhere.

Table 8.1: Relevant properties of DNA Sequences utilized in this chapter. All oligonucleotides are tagged at the 3' end with a propyl-thiol group.

Name	Sequence (5' to 3')	Molecular Weight (Da)	ε_{260} ($Lmole^{-1}cm^{-1}$)	Notes
T20	TTT TTT TTT TTT TTT TTT TT	6575.4	171500	
T25	TTT TTT TTT TTT TTT TTT TTT TTT T	8096.4	212000	
T30	TTT TTT TTT TTT TTT TTT TTT TTT TTT TTT	9617.4	252500	
T35	TTT TTT TTT TTT TTT TTT TTT TTT TTT TTT TTT TT	11138.4	293000	
T40	TTT TTT TTT TTT TTT TTT TTT TTT TTT TTT TTT TTT TTT T	12659.3	333500	
T55	TTT TTT TTT TTT TTT TTT TTT TTT TTT TTT TTT TTT TTT TTT TTT TTT TTT TTT TTT T	17222.3	455000	Required 2 days on synthesizer
A	TAC TTC CAA TCC AAT TCT TGT GTC GAT AGG TCG GTT GCT TTT TTT TTT TT	15829.4	459100	Required 2 days on synthesizer. HPLC failed, leaving sample polydisperse
B	ATT GGA TTG GAA GTA TCT TGT GTC GAT AGG TCG GTT GCT TTT TTT TTT TT	16029.5	476900	Required 2 days on synthesizer. HPLC failed, leaving sample polydisperse

8.1. Effect of Long Sequence Length: T55

AuNPs grafted with 55-base thymine sequences were prepared, dispersed in aqueous solutions of varying [$CaCl_2$], and studied with SAXS. Interestingly, DNA-NPs functionalized with these longer T55 chains displayed apparent red shifting of their optical properties, resulting in suspensions of these particles appearing purple, rather than the typical red color. This red shifting does not result from aggregation or close proximity of the DNA-NPs in pure water, as SAXS measurements indicate a lack of interparticle ordering, and no particle precipitation occurs. Modification of the dielectric environment surrounding the AuNP surface can modify optical properties[263], e.g., by adsorbing large quantities of DNA[264]. As the functionalization process of AuNPs with longer DNA has not yet been optimized, repeating these experiments with additional batches to test the reproducibility of the apparent color should be a priority.

SAXS measurements demonstrate that larger [$CaCl_2$] are required to drive the formation of pre-crystalline clusters and aggregates (**Figure 8.1**) from particles grafted with shorter thymine sequences. This difference may arise from higher total charge or enhanced steric stability of the longer chains. At salt concentrations large enough to drive aggregation, structures displaying no long-range order formed, with larger interparticle separations than those seen in T35 structures. Nonetheless, the interparticle separations decrease with [$CaCl_2$] until a concertation of ~3 M, switching to expanding with [$CaCl_2$] above this value. This suggests that the crystallization thresholds and structural phases of DNA-NPs are influenced by DNA length, the contraction and re-expansion effect driven by salts such as $CaCl_2$ is independent on the DNA, instead arising from properties of the bulk electrolytes.

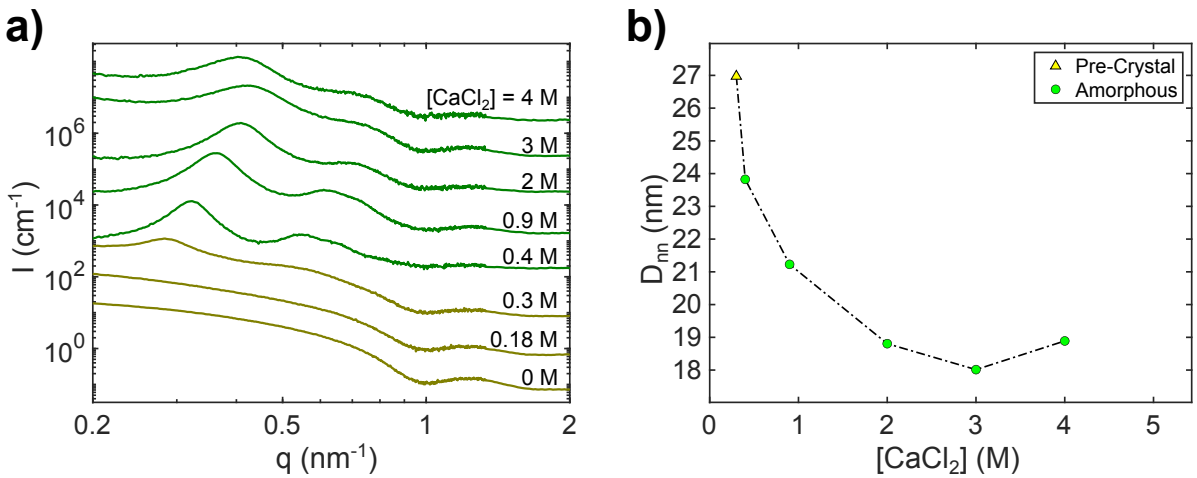

Figure 8.1: Assembly behavior of DNA-NP functionalized with a 55-base thymine sequence (T55). (a) SAXS intensity of T55-grafted NPs a various [$CaCl_2$]. Interparticle separation (D_{nn}) values and phases are summarized in (b). Larger salt concentrations are required to form pre-crystals and precipitates of particles with longer sequences, and larger D_{nn} values are measured in these structures. The transition from salt-induced contraction to expansion is present.

8.2. Effect of Varied Sequences

An attempt was made to prepare DNA-coated nanoparticles which interact by Watson-Crick base pairing through the 15 bases most distal from the AuNP core. Sequence A and B were selected from the literature[84] for this purpose (see **Table 8.1**). However, it was apparent from MALDI results that the sequences consisted of oligonucleotides of various lengths, suggesting either that the HPLC process failed to remove strands that had not completed the full sequence on the synthesizer, or that the DNA had cleaved into fragments during processing. Unfortunately, HPLC cannot be repeated after the DMTO tags are removed, so the final products of the synthesis were a polydisperse mixture of thiol-terminated and non-thiol-terminated DNA fragments of uncertain composition.

In spite of this uncertainty, DNA-AuNPs could still be successfully synthesized from these sequences (note that all DNA not grafted to the AuNPs is removed following synthesis).

For SAXS measurements, particles grafted with sequence A were mixed 1:1 with particles grafted with sequence B and dispersed in solutions of varied [$CaCl_2$] (**Figure 8.2**). While the particles remained suspended in water and 10 mM $CaCl_2$, SAXS revealed weak ordering, suggesting some degree of interparticle interaction (potentially weak base-pairing effects). The DNA-NPs precipitated at 100 mM $CaCl_2$, forming disordered aggregates with D_{nn} notably lower than those formed from oliogthymine strands. DNA polydispersity, short sequence length, and potential Watson-Crick base pairing interactions all may destabilize DNA-NPs against salt. Despite these differences, a non-monotonic dependence of D_{nn} on [$CaCl_2$] was observed(?), again reflecting that the reswelling behavior–in contrast with DNA-NPs crystallization and structure–arises from the properties of the bulk electrolyte.

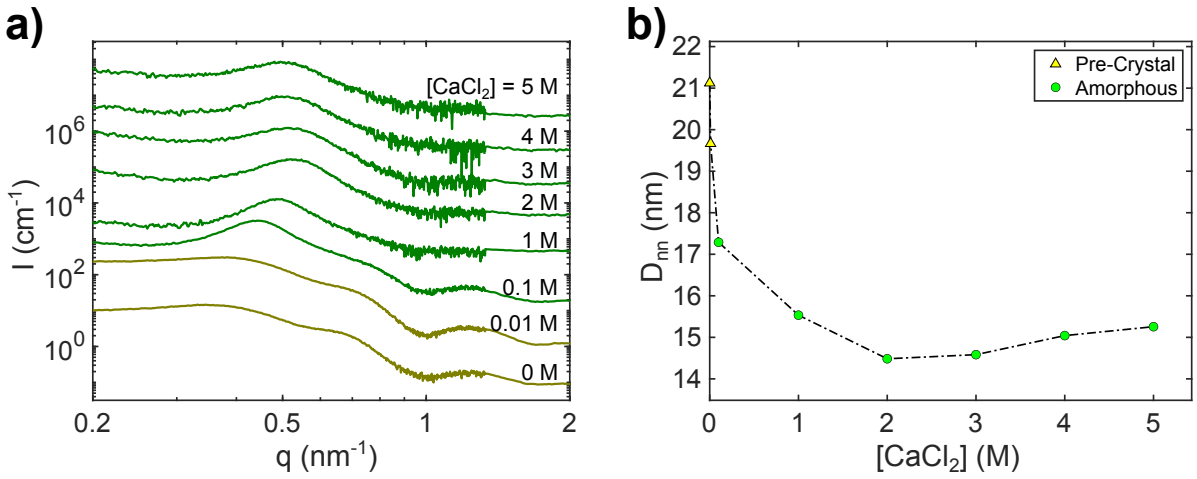

Figure 8.2: Assembly behavior of DNA-NP functionalized with polydisperse, short oligonucleotides (sequence A and B). (a) SAXS intensity of these DNA-NPs a various [$CaCl_2$]. Interparticle separation (D_{nn}) values and phases are summarized in (b). Disordered ordering is observed even with no added $CaCl_2$], and notably smaller D_{nn} values are measured in these structures. The transition from salt-induced contraction to expansion is present.

8.3. Effect of Thymine Sequence Length

It is well established that by co-assembling nanoparticles with different ligand shell sizes, different binary structures can be achieved via solvent precipitation[265, 266] and DNA-base pairing[267]. However, it is unclear how such size variation will influence the divalent ion-based assembly studied in this work. If interparticle separation is mediated by DNA brush height, increasing the number of bases in the grafted oligonucleotide should tune the effective particle size (**Equation 2.9**). The single-base control possible with solid-state assembly presents a unique opportunity to explore assembly of particles with size variation on the order of single monomers, which may have general implications in understanding how polydispersity influences colloidal crystallization[268].

8.3.1. Sequence Length Influences Lattice Ordering

To test how DNA sequence length influenced crystallization behavior, 10 nm AuNPs functionalized with oligo-dT strands of varying length were assembled at 350 mM CaCl2 and characterized via SAXS. **Figure 8.3** display representative structure factors of the assemblies (**Fig. 8.3a-c**), as well as the observed interparticle separations for the different sequence lengths (**Fig. 8.3d**), which serve as a metric for effective particle size. As expected, longer contour lengths resulted in larger brush heights. Particles functionalized with 30-40 monomer sequences formed FCC structures, while DNA-AuNPs with ligands of insufficient length (20 bases) form structures lacking long-range order (RCP). Other groups have observed a similar lack of long-range order in crystals of DNA-AuNPs assembled via Watson-Crick base pairing when the length of the utilized DNA was less than that of the core diameter[269]; mechanistically, this was attributed to greater flexibility of longer DNA compensating for non-uniformity of the AuNP

cores[269]. Another approach is to consider the effective polydispersity of core-shell DNA-AuNP structures. Generally, polyelectrolytes of a given length extend more in spherical brushes of smaller cores (**Equation 2.9**). As a result, nanoparticles of smaller radii will have more extended DNA shells, with the reverse also being true. Thus, longer DNA chains decrease the total polydispersity of DNA-AuNPs. This polydispersity influences the degree of order observed in colloidal assemblies (**Fig. 8.3**), with lower polydispersity driving the formation of more-ordered structures.

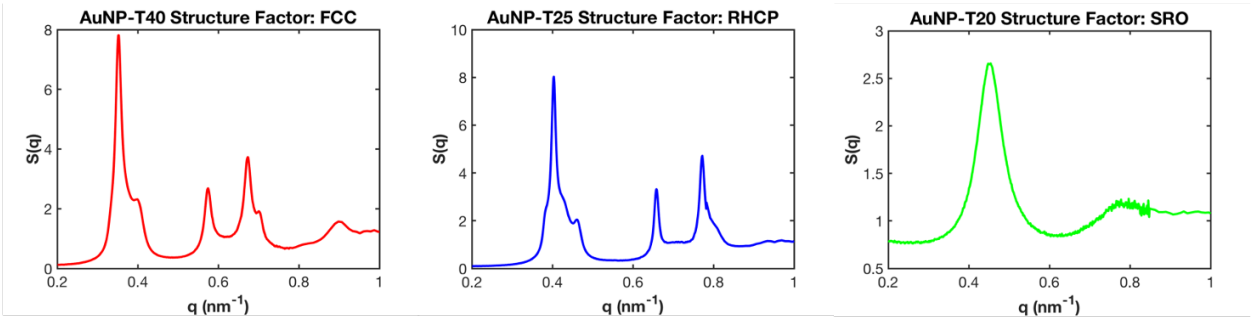

DNA-AuNP	D_{nn} (nm) in 350mM $CaCl_2$
T40-2	21.89
T35-1	20.69
T30-2	20.24
T25-1	19.09
T20 (Old)	17.04

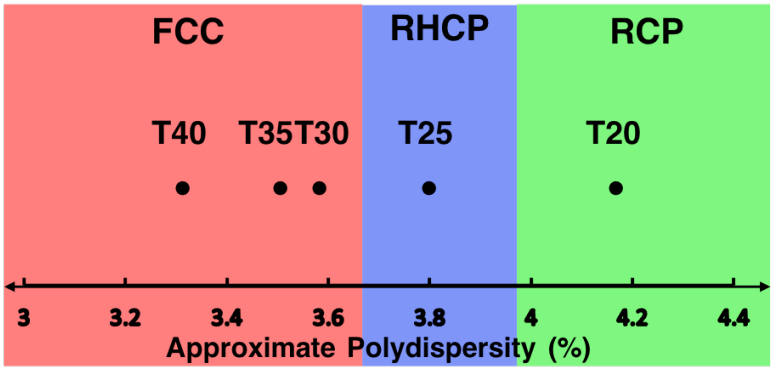

Figure 8.3: (SAXS demonstrates how polydispersity of AuNP cores leads to disorder in assemblies. (a-c) Extracted structure factors of assemblies with various ligand lengths at 350mM $CaCl_2$, displaying FCC (a), RHCP (b) and RCP (c) lattices. (d) A list of interparticle separations in the observed structures. Longer sequences of grafted dT lead to larger D_{nn}. (e) A plot of structure type versus polydispersity for the DNA-AuNPs, demonstrating that lower particle polydispersity favors structures with higher order. Polydispersity values for the gold cores were determined by fitting X-ray scatting data. Values of polydispersity for DNA-AuNPs were approximated by assuming a uniform DNA shell surrounding polydisperse gold cores.

8.3.2. Size Dispersity Creates Defects in Latices

Interestingly, grafted DNA of intermediate length (25 bases) resulted in the formation of a Random Hexagonal Close-packed (RHCP) structure (**Fig. 8.3b**), characterized by consistent disruption of the ABCABC or ABAB stacking observed in FCC or Hexagonal-close packed structures, respectively. This suggests that, while high degrees of component size variation prevent crystallization, there may be a range where this variability drives the formation of stacking faults. The degree of faulting can be assessed by fitting to an appropriate model [270, 271]. To further investigate the influence of the size distribution of constituent particles in these assemblies, binary mixtures of the various particles were crystalized and analyzed via SAXS. The results of these studies are summarized in the phase diagram in **Figure 8.4**. Mixtures of particles with comparable mean particle size tend to form FCC and RHCP structures, while greater size disparities promote the formation of disordered structures. Smaller number fractions of "impurity" particles tend to disrupt order less than the degree observed in near-equimolar mixtures, though this is influenced by the size differences of the component particles. Thus, the length of the grafted DNA can dramatically influence crystallization behavior, with variance in this parameter influencing stacking disorder.

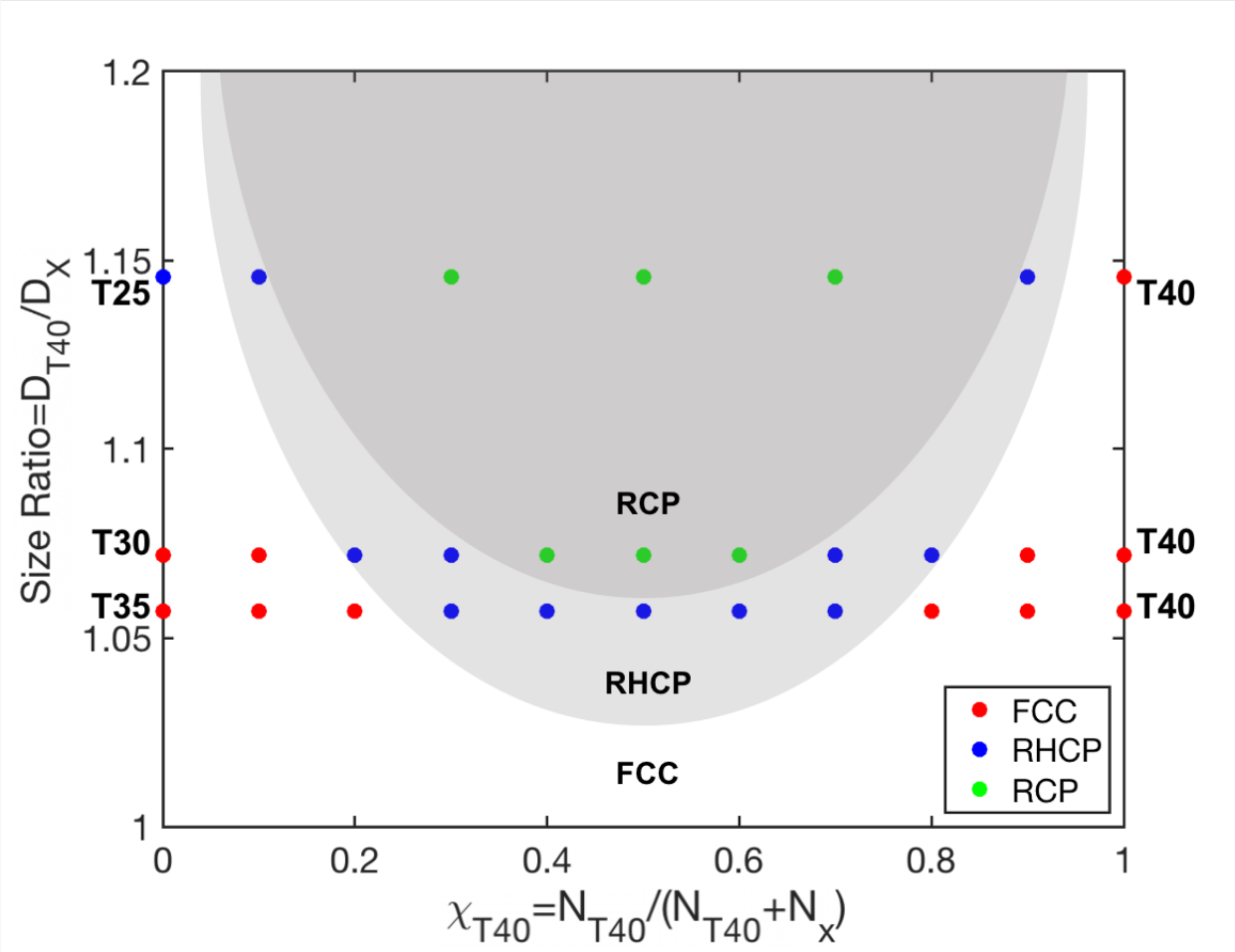

Figure 8.4: The observed phases of binary assemblies of DNA-AuNPs with different DNA length at 350 mM $CaCl_2$, dependent on component size asymmetry and composition. Composition is represented as the number fraction of the larger particle (with total particle concentration 50 nM). Asymmetry is calculated as the ratio of the effective particle sizes, as determined by SAXS measurements on assemblies of the unmixed components. Disordered structures are favored by greater asymmetry and component mixing.

8.4. Conclusions

Here, we have studied the $CaCl_2$-induced assembly of AuNPs grafted with DNA sequences of different length and composition, gaining insight into the factors that control the properties of formed structures. The salt concentration required to induce nanoparticle precipitation generally increases with DNA length and decreases if the base composition is

diversified. Highly ordered lattices are only possible if DNA length is sufficient to compensate for the polydispersity of the DNA core, but sequences of significantly greater length do not result in apparent ordering of the nanoparticle cores. Engineering crystallinity in these systems will likely require correlated selection of core size and DNA. Finally, regardless of the DNA brush composition, structures formed of contract with [$CaCl_2$] at low salt, and expand with [$CaCl_2$] at high salt, further evidencing that this effect arises from the ion correlations present in the bulk electrolyte.

Chapter 9: Effects of Additional Salts

Here, several additional series of SAXS experiments on DNA-NPs in concentrated electrolytes of other types are detailed. No ordering of DNA-NPs is detected in solutions of cesium chloride and the ionic liquid ethylammonium nitrate, which can both be prepared in high molar concentration. In contrast, DNA-NPs precipitate in concentrated solutions of the ionic liquid 1-Ethyl-3-methylimidazolium [EMIM] chloride. Additional experiments reveal that the identity of the electrolyte's anion strongly influences DNA-NP interactions, potentially explaining the stark differences observed between the ionic liquids and reflecting the significant role of anions in both "salting out" and ion-correlation-driven phenomena. Finally, the role of cation valency is further investigated by studying chloride salts of trivalent cations (lanthanum chloride, $LaCl_3$); in these solutions, the stronger electrostatic interaction between La^{3+} and DNA results in DNA-NP precipitation at much lower salt concentrations. However, the DNA-NP aggregates are found to swell with [$LaCl_3$], eventually resulting in complete re-dispersal of the particles at salt concentrations approaching saturation.

9.1. Cesium Chloride (CsCl)

DNA-NPs (grafted with 40-base thymine) were prepared as described in the preceding chapters. CsCl (99.995% purity) was obtained from Millipore-Sigma. SAXS experiments were conducted using the flow-cell SAXS/MAXS/WAXS setup of 5-ID-D of the APS. For these measurements, X-ray energy was tuned to 15 keV, and samples were flown continuously during measurement. DNA-NP suspensions at 0, 47 nM, and 211 nM concentrations in solutions of varying [CsCl]. In between measurements, iodine and DI water were used to wash the capillary. Measurements were also made on the empty capillary before and after each sample. Data was

radially integrated and processed as described in prior chapters. 1D scattering profiles of the capillary and DNA-NP-free solutions are subtracted from that of the DNA-NP suspensions for each salt concentration. The DNA-NP form factor is then calculated as a population of polydisperse gold spheres and used to isolate the scattering signal associated with interparticle correlations, *S(q)*.

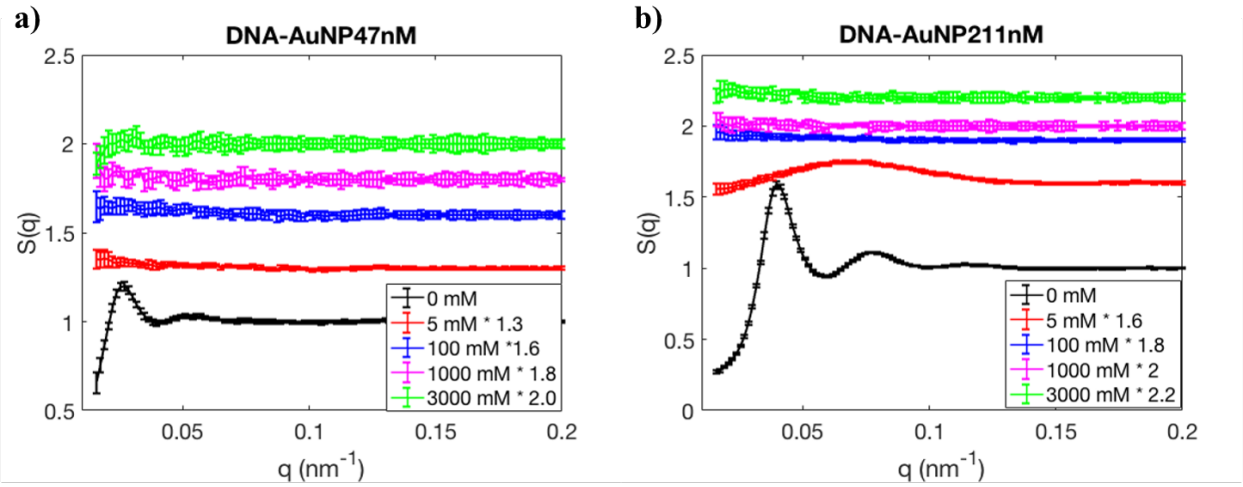

Figure 9.1: Low-q structure factors of 47 nM (a) and 211 nM (b) solutions of T40-0 DNA-AuNPs at various concentrations of CsCl. Solutions with higher particle volume fractions display structuring due to electrostatic repulsion. Evidence of repulsive forces at high ionic strength was not observed.

Figure 9.1 shows the results of these experiments, detailing *S(q)* at various [CsCl]. At 0mM CsCl, a correlation peak is observed at very low q (< 0.05 nm^{-1}), corresponding to separations of over 100 nM. This suggests that the DNA-NPs organize due to long-range electrostatic repulsion. Increasing [CsCl] to 5 mM eliminates apparent ordering in the 47 nM suspensions, and greatly smears the correlation peak in the 211 nM suspensions; this reflects the weakening of electrostatic repulsions by the addition of salt. From 0.1 to 3 M CsCl, no correlations are detected, suggesting that particles are dispersed and interacting minimally. Thus, no evidence of attractive or long-ranged repulsive interactions was obtained. However, since

these measurements were obtained under flow conditions, ordering may have been disrupted by hydrodynamic forces. Additionally, aqueous solutions of CsCl in excess of 7 M can be prepared[272], and DNA-NP suspensions can be concentrated further; future experiments should investigate the effects of higher concentrations of either of these components.

9.2. Ionic Liquids

9.2.1 Ethylammonium nitrate

DNA-NPs (grafted with 30-base thymine) were prepared as described in the preceding chapters. Ethylammonium Nitrate (EAN) (97% purity) was obtained from Iolitec. SAXS experiments were conducted at 5-ID-D of the APS, using samples contained in sealed 1.0 mm quartz capillaries. For these measurements, X-ray energy was tuned to 8 keV. DNA-NP suspensions at 500 nM concentrations in solutions of varying [EAN] were prepared in DI water, as well as DNA-NP-free solution of matching [EAN]. Samples were scanned for sets of three 5-second exposures, with the capillaries being translated continuously at ~ 0.5 mm/s during measurement to minimize radiation damage. Data processing was as described in prior chapters, enabling the extraction of *S(q)*.

Figure 9.2 shows the signatures of structuring in DNA-NP in solutions of EAN and water. As previously observed, correlation peaks at low q, associated with long-range repulsive interactions in DI water. At 0.5 M and 7 M EAN concentrations, no peaks are present in the full SAXS range, suggesting that DNA-NPs do not order repulsively in the conditions tested. Additionally, no clustering associated with weak attractive forces is apparent, even at exceptionally high salt concentration (7M) indicating that the presence of salt-induced attractive interactions depends on cation and anion type. Additional simple optical experiments revealed

that DNA-NPs precipitate in concentrated solutions of Ethylammonium chloride (98% from MilliporeSigma), implicating a significant role of the anion in regulating DNA-NP solubility.

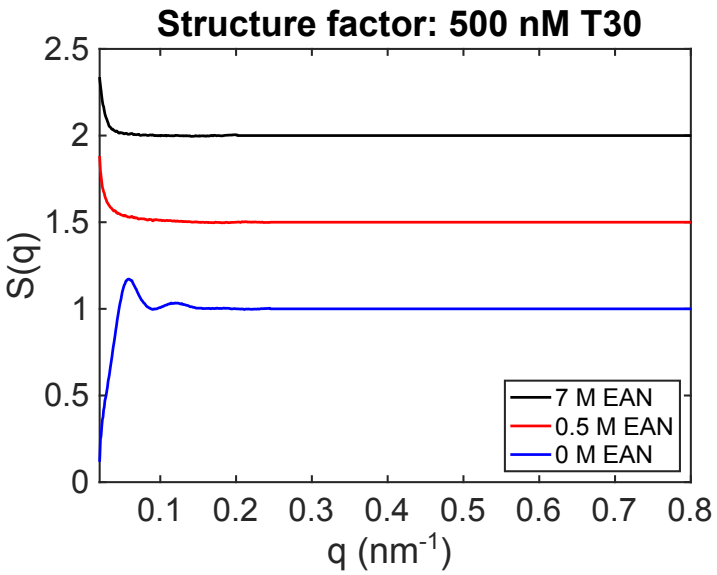

Figure 9.2: Low-q structure factors of 500 nM (b) suspensions of T30-functionalized DNA-AuNPs at various concentrations of Ethylammonium Nitrate (EAN). Structuring due to repulsive forces is observed in water, but not at higher ionic strength. In fact, no apparent ordering is observed in EAN solutions.

9.2.2 1-Ethyl-3-methylimidazolium (EMIM) chloride

To further test the interaction of ionic liquids with DNA-NPs, T35-grafted particles were suspended at 50 nM in aqueous solutions of 1-Ethyl-3-methylimidazolium (EMIM) chloride (98% purity) obtained from Millipore-Sigma. DNA-NPs precipitate in concentrated EMIMCl solutions, contrasting with the effects of EAN, while matching those of Ethylammonium chloride.

SAXS experiments were performed on sealed-capillary samples at 5-ID-D of the APS, as previously described. Samples were prepared in EMIMCl solutions of varying concentration, as well as mixtures of EMIMCl and $CaCl_2$ (with 200- or 400-mM concentration). Results are presented in **Figure 9.3**. EMIMCl drives the formation of pre-crystalline aggregates at low-to-

moderate concentrations (similarly to NaCl), and amorphous aggregates at very high concentration (similarly to LiCl). The clusters/aggregates contract monotonically with [EMIMCl], corresponding to the behavior of the alkali chlorides. In solutions containing $CaCl_2$, DNA-NP precipitate and contract with increased [EMIMCl], until high (~4-5 M) concentrations, above which structures modestly expand with elevating [EMIMCl]; this is comparable to effects observed in concentrated LiCl solutions containing $CaCl_2$, reflecting that other salts can induce the correlations necessary to induce the re-expansion phenomenon.

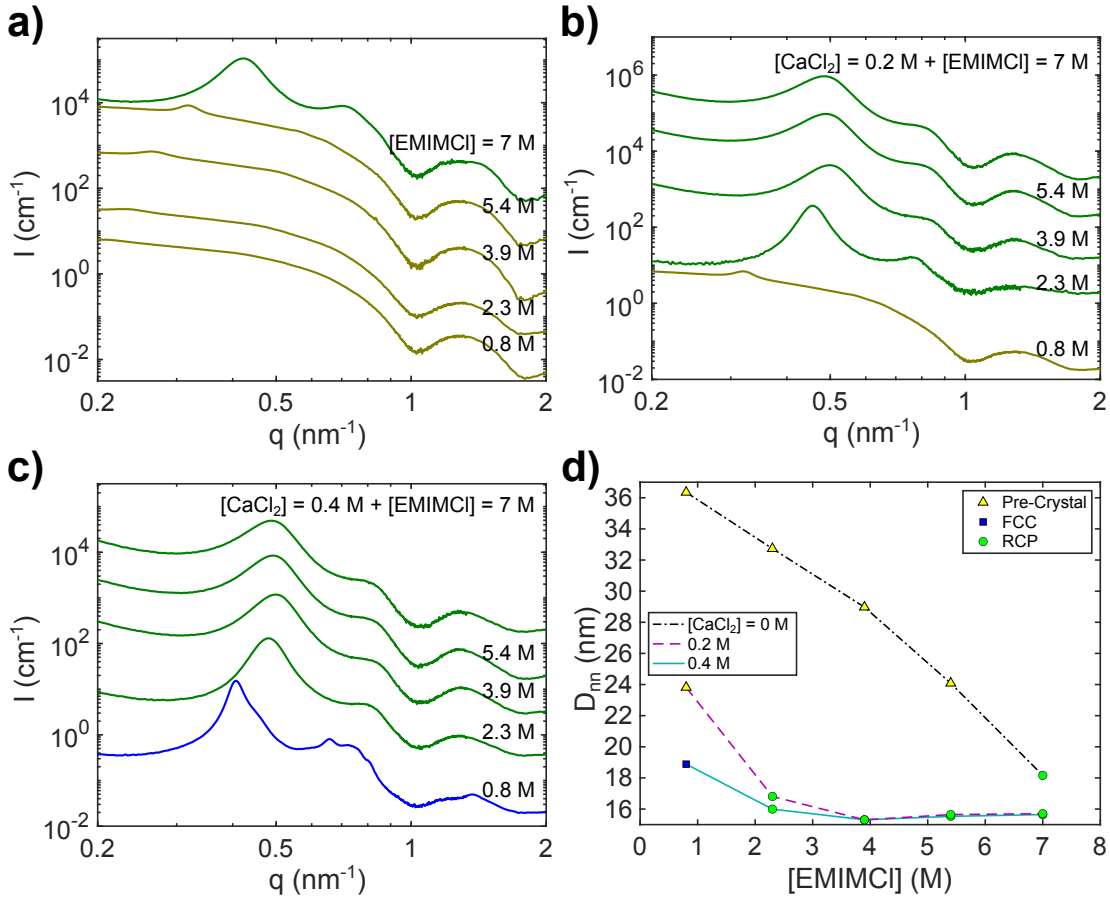

Figure 9.3: Assembly of T35-grafted DNA-NPs in aqueous solutions of 1-Ethyl-3-methylimidazolium chloride (EMIMCl). (a-c) Scattered X-ray intensity of DNA-NPs at different [EMIMCl], in the presence of 0 (a) 200 (b) or 400 (c) mM $CaCl_2$. Phases and interparticle separations (D_{nn}) are summarized in (d). While EMIMCl induces DNA-NP contraction and precipitation even in the absence of $CaCl_2$, reexpansion is only observed if Ca^{2+} is present.

9.3. Anion Effects

9.3.1 Magnesium Sulfate

To test the effects of a divalent anion, T35-grafted particles were suspended at 50 nM in aqueous solutions of magnesium sulfate ($MgSO_4$) (99.5% purity) obtained from Millipore-Sigma. Comparable to the case of $MgCl_2$, DNA-NPs precipitate in $MgSO_4$. SAXS experiments were performed on sealed-capillary samples at 5-ID-D of the APS, with results summarized in **Figure 9.4**. DLVO theory would predict that DNA-NPs would precipitate in lower concentrations of $MgSO_4$ than $MgCl_2$, as a given molar unit of the former will raise the ionic strength by a larger factor due to the higher anion valency, thus decreasing the Debye length more rapidly (See **Equation 2.3**). However, a higher [$MgSO_4$] (~1.5M) is required to precipitate DNA-NPs than [$MgCl_2$] (~1.0M), reflecting the inapplicability of a simple model where the screening of repulsive interactions alone induces precipitation. Despite this distinction, DNA-NP structures in $MgSO_4$ solutions tend to be more compact, forming BCC and RCP structures not found in $MgCl_2$ solutions. Additionally, no reexpansion occurs at high [$MgSO_4$], potentially due to distinctions in the how Mg^{2+} and SO_4^{2-} form ionic clusters and induce “salting out” effects. The behavior observed here suggests that the effects of anions on DNA-NP crystallization vary depending on concentrations, with higher anion valency inhibiting crystallization at low concentration, but driving more pronounced precipitation at high concentrations.

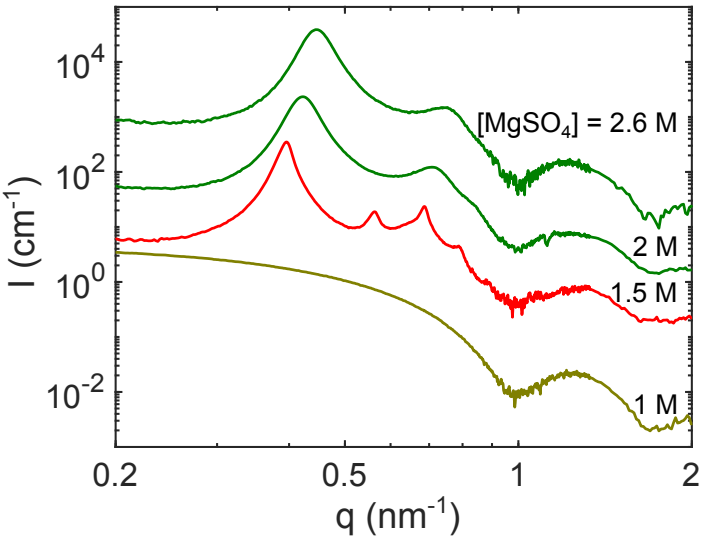

Figure 9.4: Scattered X-ray intensity of DNA-NPs at different [$MgSO_4$]. Similarly to behavior observed in [$MgCl_2$] solutions, no precrystalline ordering is observed. However, unlike $MgCl_2$. $MgSO_4$ drives the formation of aggregates with BCC structure and lower separations and does not drive re-expansion at high concentrations.

9.3.2 Calcium Acetate and Calcium Nitrate

The notably different effects of chloride and nitrate salts motivated additional investigation into the role of the monovalent anion. Solutions of calcium nitrate (99% from Alfa Aesar), calcium acetate (99% from Millipore-Sigma), sodium nitrate (99.99% from Alfa Aesar) and sodium acetate (99.5% from Millipore-Sigma) were prepared, and T35-DNA-NPs were dispersed in them. Capillary SAXS measurements were carried out at Beamline ID7A1 (BioSAXS) of the Cornell High Energy Synchrotron Source (CHESS)[219, 220]. SAXS data was collected using a Pilatus single photon counting area detector positioned ~ 1.8 m from the sample. The X-ray energy was tuned to 13.3 keV (1.094 Å wavelength), the beam size at the sample position was ~ 0.25mm x 0.25mm, and the flux was ~ 7×10^{12} photons/s. Each measurement consisted of a 0.5 second exposure. Azimuthal averaging was performed with BioXTAS RAW[221] to obtain the 1D scattering profiles.

Figure 9.5 displays the scattered intensities of DNA-NPs in solution of the aforementioned calcium salts. It is apparent that no precipitation, and minimal ordering, of DNA-NPs occurs in concentrated $Ca(NO_3)_2$ solutions, resembling the effects of EAN, and suggesting that the nitrate cation disfavors DNA-precipitation. In contrast, DNA-NPs precipitate in calcium acetate solutions, though a higher concentration is required (~ 0.5 M) than that of $CaCl_2$ (~ 0.25 M). Nonetheless, DNA-NP aggregates in calcium acetate solution contract monotonically with added salt, suggesting that the manifestation of ion correlations vary with anion type.

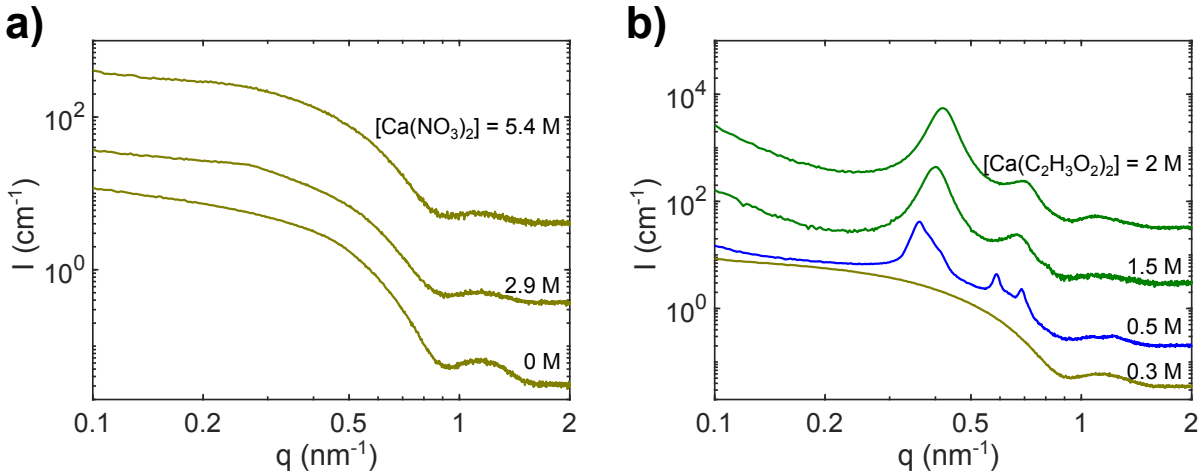

Figure 9.5: Scattered X-ray intensities of DNA-NPs in solutions of calcium salts with different anions, including calcium nitrate (a), and calcium acetate (b). Very little ordering is apparent in calcium nitrate solutions, while DNA-NP aggregation occurs in calcium acetate solutions.

9.3.3 Sodium Nitrate and Sodium Acetate

DNA-NPs dispersed in solutions of the aforementioned sodium salts were characterized with SAXS as described in the previous section, with results presented in **Figure 9.6**. DNA-NPs do not precipitate in $NaNO_3$ solutions of any concentration, instead forming very weakly ordered clusters with large interparticle separations (~ 35 nm), a value comparable to particle hydrodynamic diameters deduced from dynamic light scattering measurements of DNA-NPs in

pure water[193]. However, the presence of sodium acetate is sufficient to precipitate DNA-NPs, contrasting with the effects of sodium chloride and sodium nitrate. Aggregates in these solutions contract with added salt throughout the full accessible range.

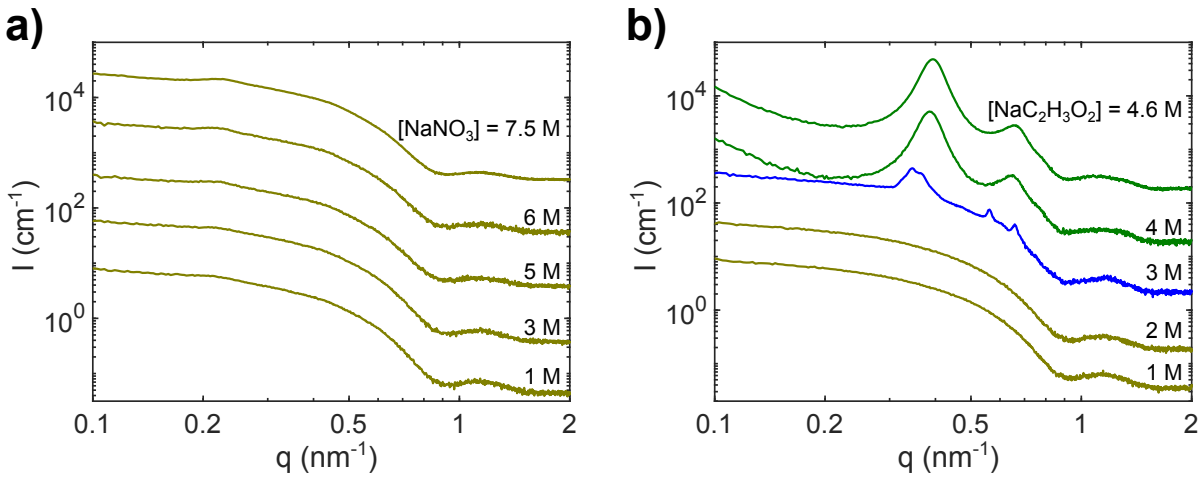

Figure 9.6: Scattered intensities of DNA-NPs in solutions of sodium salts with different anions, including sodium nitrate (a), and sodium acetate (b). Weak ordering is apparent in calcium nitrate solutions, with a small intensity modulation corresponding to $D_{nn} \sim 35$ nm appearing at high ionic strength. DNA-NP aggregation occurs in sodium acetate solutions, contrasting with the behavior observed in sodium chloride and nitrate solutions.

DNA-NP suspensions with fixed [$CaCl_2$] (200 mM) and varied [$NaNO_3$] and [$NaC_2H_3O_2$] were also measured, with results presented in **Figure 9.7**. Similarly to behavior observed in NaCl and LiCl solutions, both the nitrate and acetate salts interfere with $CaCl_2$-induced DNA-NP clustering when added in low concentration, with sodium nitrate increasing apparent D_{nn} values and sodium acetate eliminating ordering entirely. However, in contrast to the chloride salts, where the monovalent salt additions switch to favoring cluster compression above 0.5 M, this change does not occur in sodium acetate and sodium nitrate solutions until significantly higher concentrations (4 M and 3 M, respectively). Also, DNA-NPs do not precipitate in solutions of 200 mM $CaCl_2$ and 7 M sodium nitrate, whereas they do in solutions of 200 mM $CaCl_2$ and more than 3 M sodium acetate. Thus, the "salting out" effects described in Chapter 6 are influenced

considerably by anion type, with the chloride ion apparently being a stronger precipitant than nitrate or acetate anions. These differences could potentially arise from factors such as anion charge density or hydration, or different interactions with cations or the DNA-NP surface.

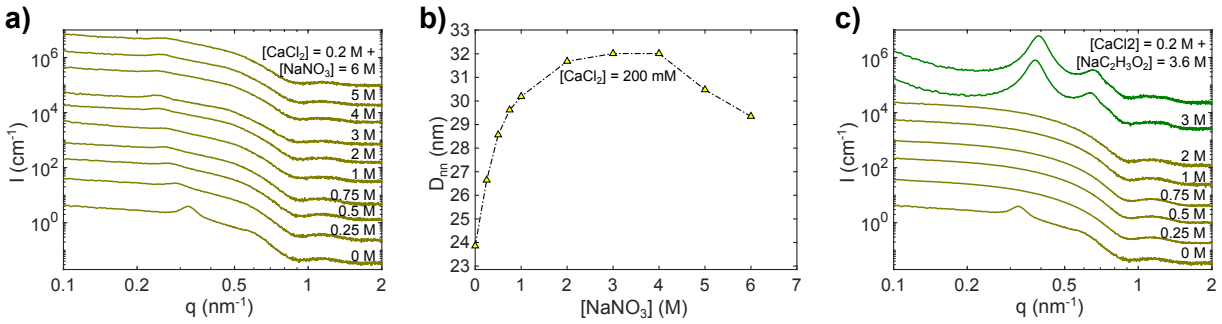

Figure 9.7: Assembly of T35-grafted DNA-NPs in aqueous solutions with fixed (200 mM) concentration of $CaCl_2$ and varied concentrations of sodium salts. (a) Scattered X-ray intensity of DNA-NPs with added sodium nitrate. Phases and interparticle separations (D_{nn}) are summarized in (b). $NaNO_3$ appears to weaken CaCl2-induced ordering until very high (> 4 M) concentrations. (c) Scattered X-ray intensity of DNA-NPs with added sodium acetate. Low concentrations of sodium acetate eliminate apparent ordering, but high concentrations induced precipitation.

9.4. Trivalent Cations: Lanthanum chloride ($LaCl_3$)

The monovalent and divalent cations utilized thus far do not precipitate free DNA in aqueous solutions at room temperature; in contrast, cations with valency of 3 or greater generally precipitate DNA[233]. Owing to their higher charge, electrostatic interactions between trivalent cations and phosphates of DNA are expected to be stronger. It is not readily apparent how the effects of bulk ionic correlations will influence these stronger electrostatic forces.

Here, preliminary tests of how salts of trivalent cations interact with DNA-NPs are conducted, specifically utilizing lanthanum chloride ($LaCl_3$). Thus, T35-DNA-NPs were dispersed in aqueous solutions of varying [$LaCl_3$] and [NaCl], sealed in capillaries, and characterized with SAXS/WAXS at beamline 5-ID-D of the APS.

Results of these SAXS experiments on DNA-NP samples precipitated by $LaCl_3$ are provided in **Figure 9.8**. No structuring is observed for DNA-NPs below the crystallization threshold, whereas DNA-NPs above this boundary (0.2 mM) form aggregates with little-to-no apparent long-range order, with structure factors featuring exceptionally broad correlation peaks. While deduction of interparticle separations is currently only approximate for these highly disordered structures, D_{nn} values appear to increase modestly with [$LaCl_3$], contrasting with the effects of other tested salts. It should be noted that higher valency cations may result in "overcharging" of the DNA surface[132, 273], potentially explaining the present behavior. At sufficient $LaCl_3$ concentrations (> 2.5 M), DNA-NPs redisperse into solution, restoring the red color of the freely suspended DNA-NPs and eliminating apparent ordering. Interestingly, correlations between ions appear potent enough to overcome the apparently strong interaction between trivalent cations and DNA.

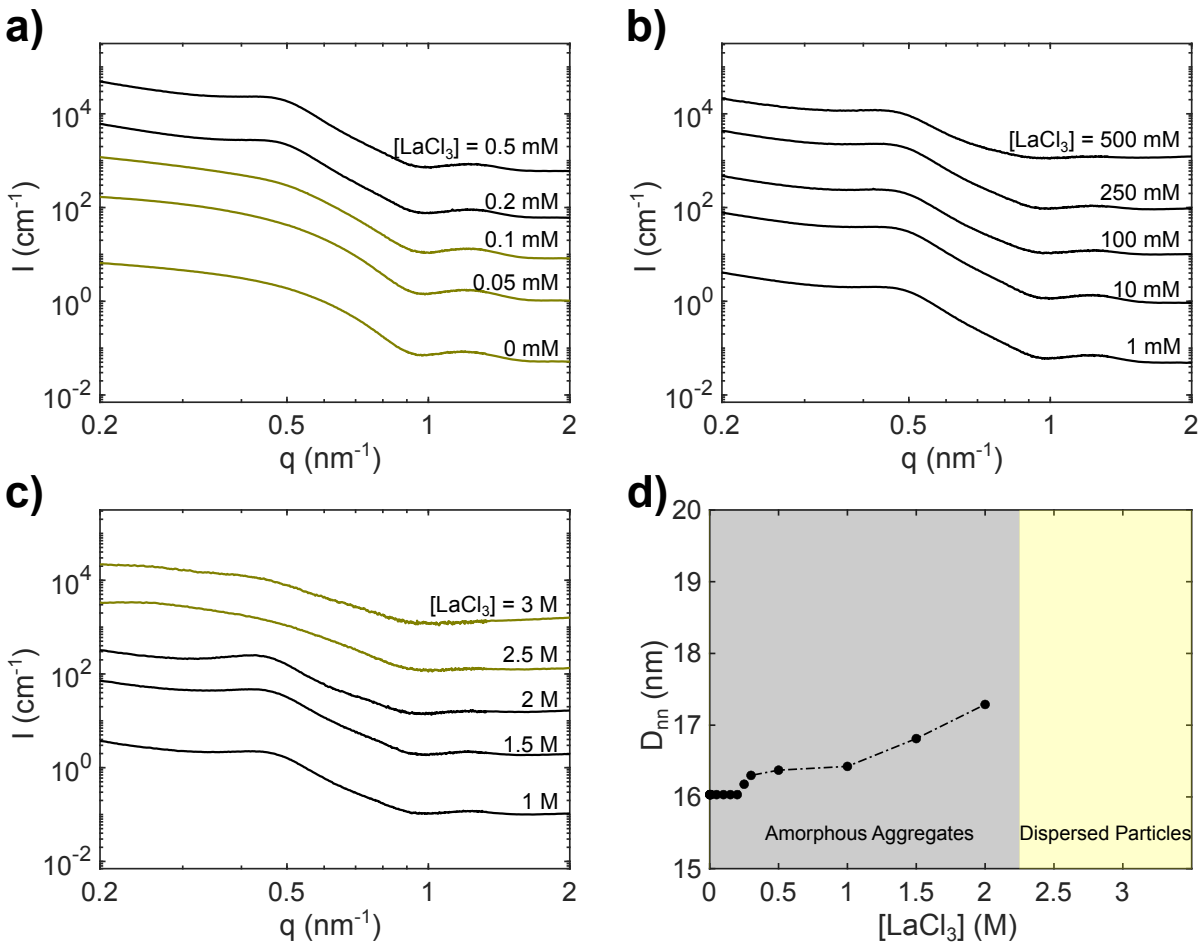

Figure 9.8: Assembly of T35-grafted DNA-NPs in aqueous solutions of $LaCl_3$ (a-c) Scattered X-ray intensity of DNA-NPs at low (a), intermediate (b), and high (c) [$LaCl_3$]. Phases and interparticle separations (D_{nn}) are summarized in (d). DNA-NPs aggregate in solutions of low [$LaCl_3$], forming amorphous precipitates that swell modestly with increasing salt concentration. At high concentrations (> 2.5 M), DNA-NP aggregates disperse, and particles return to being suspended in the solution.

Preliminary experiments revealed that DNA-NPs rapidly aggregate into precipitates of visible dimensions in dilute solutions of $LaCl_3$ (concentration > 0.2 mM); these aggregates did not disperse upon dilution of the solution, reflecting that La^{3+}-DNA interaction is strong-enough in dilute solution to be apparently irreversible, contrasting with the effects of monovalent and divalent cations. Re-dispersal of the aggregates formed by $LaCl_3$ was possible via the addition of NaCl, which would be expected to screen the attractive lanthanum-DNA interaction; this

prompted interest as to whether NaCl would induce "salting in" and "salting out" effects in this system as well. Thus, T35-DNA-NPs were also dispersed in aqueous solutions of varying [$LaCl_3$] and [NaCl] and characterized with SAXS/WAXS. **Figure 9.9** demonstrates that the effect of NaCl on $LaCl_3$-induced precipitation resembles that which it had on precipitation by low concentrations of divalent salts. Modest (~1 M) NaCl concentrations impair precipitation, resulting in the formation of pre-crystalline clusters with notably higher interparticle separations than in the amorphous aggregates formed in 0.2 mM or 1 mM $LaCl_3$ solutions. Beyond this concentration, however, additional NaCl decreases D_{nn} values, even leading to re-precipitation of the DNA-NPs. Thus, the mixed effects of monovalent salts appear to not be restricted to solutions containing divalent cations.

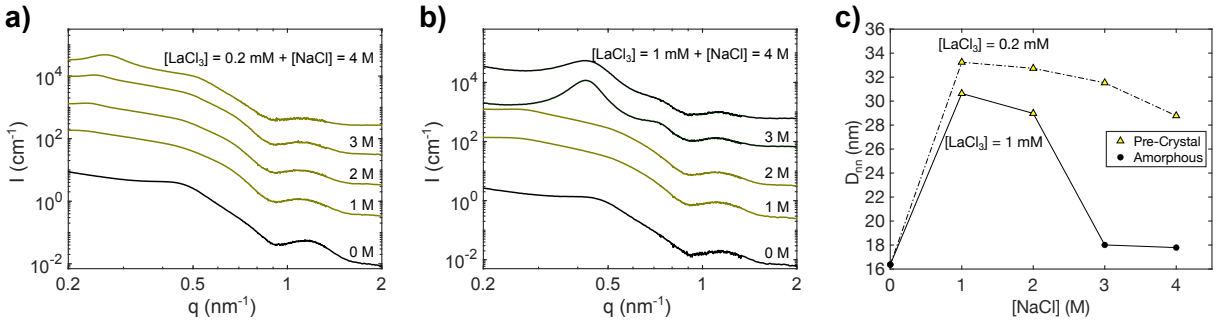

Figure 9.9: Assembly of T35-grafted DNA-NPs in aqueous solutions of $LaCl_3$ and NaCl. (a-b) Scattered X-ray intensity of DNA-NPs at different [NaCl], in the presence of 0.2 (a) or 1 mM (b) $LaCl_3$. Phases and interparticle separations (D_{nn}) are summarized in (c). While NaCl interferes with La^{3+}-induced aggregations at low concentration, cluster contraction or re-aggregation occur at high [NaCl].

9.5 Conclusions

Here, we have broadened our study of the DNA-NP system to include a number of additional salts. While evidence of long-ranged repulsive interactions in concentrated solutions of monovalent salts was not obtained, it was established that stable suspensions of DNA-NPs

could be prepared in such solutions by utilizing nitrate salts, highlighting their viability for future studies. The influence of bulk ion correlations was found to be potent enough to disrupt the powerful electrostatic interactions between trivalent cations and DNA, further evidencing the necessity of accounting for these effects in concentrated electrolytes, even in the presence of strong interactions. Finally, the influence of the utilized anion in the present system has been unambiguously demonstrated. The apparent tendencies for precipitation exhibited by sulfate, acetate, and chloride salts, and the lack thereof exhibited by nitrate salts, may naturally draw attention of the Hofmeister series for "salting out" effects[50]. However, it appears that the effects of the anions vary not just with the identity of the cation, but also with the concentration of the salt tested. Future investigations into the varied manifestation of bulk ion correlations in solutions of differing cation-anion pairs will likely provide critical information into predicting salt-induced effects in a more general context.

Chapter 10: Summary and Outlook

10.1. Summary

This thesis has characterized the interactions between DNA-grafted nanoparticles in a wide variety of electrolytes. Our approach combined scattering experiments with molecular dynamics simulations to probe DNA-NP and solution structure across a range of length scales, developing a comprehensive description of how the distributions of ions and solvent manifest as forces governing interactions between charged macromolecules. The influence of a number of electrolyte characteristics, including concentration, solvent, temperature, cation identity, and anion identity, were interrogated, enabling the validation of the theories developed here.

To provide an overview: divalent alkaline earth cations, in particular Ca^{2+}, are attracted electrostatically to the negatively charged backbones of grafted DNA chains, where they disrupt the solvent shells of the macromolecules. The cation-enriched atmosphere surrounding the DNA molecules generates attractive forces via interactions with the atmospheres of adjacent DNA, leading to assembly of the DNA-NPs. These attractions rapidly increasing in strength as divalent cation concentration increases (as evidenced by resistance to other potentially competing salts and thermally induced melting). Within the assemblies, the structures are dictated by the configurations of, and interactions between, the DNA chains, which manifest as structural phase transitions. These configurations and interactions are determined by a balancing of cation-induced attraction and solvent interactions, which can be tuned by varying temperature, solvent composition, and ionic strength. Of particular significance to this work are the correlations between electrolyte ions that arise at high concentration; at high ion densities, cation distribution becomes restricted by the large number of ions, leading to a disruption in the attractive forces

between DNA that drive expansion of the structures with added salt. The principles outlined here may have applications in the characterization of life at extreme conditions and the development of resilient and/or stimuli-responsive materials. While concentrated electrolytes remain complex, and even "mysterious" systems, this work provides experimental evidence that should aid the collective effort to understand "salt water".

10.2. Outlook/Future Work

This work establishes a number of promising directions for future research. To begin, additional studies on the FCC-to-BCC transitions analyzed in Chapter 5 could yield a series of insightful demonstrations. As mentioned, synchrotron SAXS measurements near (or at) the concentration boundary between the two phases could decisively establish the mechanism by which the structures interconvert. *In situ* SAXS experiments, where DNA-NP crystals are allowed to diffuse into regions of varied [$CaCl_2$] (as could be achieved with a salinity gradient), could also be useful. Cryogenic electron microscopy studies could provide additional information about structures that have converted between the two lattice types, such as the presence of defects. The assembly of nanoparticles grafted with slightly longer or shorter DNA could be tested at higher concentrations, to further clarify the role of the shell in structural determination. Finally, while neutron scattering measurements are time-and-resource-intensive, SANS measurements at additional salt concentrations, potentially with higher DNA-NP concentrations, would allow for a more rigorous *in situ* characterization of DNA shell extent; samples in $SrCl_2$ are particular promising candidates, as the lack of precipitation of the assemblies would minimize issues during long measurement times.

While The 3-dimensional system studied here allows convenient probing of the "bulk" electrolyte, the dispersal of the DNA-NPs with random orientations in solution measurements

effectively angle-averages the sample, potentially obscuring information about DNA configuration. In order to gain additional information about DNA brushes in electrolytes of varied concentration, planar DNA brushes on gold films could be prepared. The extension of the DNA molecules into solutions could then be measured using a number of techniques, including neutron reflectivity X-ray standing wave analysis, quartz crystal microbalance measurements. Lateral brush inhomogeneities could be resolved with liquid Atomic force microscopy. Additionally, it stands to reason that gold-coated AFM tips could be grafted with a thiolated DNA brush as well. Preparation of such functionalized tips could enable the measurement of the force between DNA brushes.

Studies on other DNA-based systems in concentrated electrolytes could test the generality of the phenomena analyzed here. For example, DNA-NP superlattices assembled via base pairing interactions could be assembled, followed by transfer into concentrated solutions of salts such as $CaCl_2$. Measuring the contraction and swelling of these structures via SAXS would establish whether DNA in base-pairing configurations will also respond to ion correlations. More generally, highly informative WAXS experiments could be conducted on any DNA-dense phase that can be prepared on a macroscopic scale in solution. If clear separation between bulk functionalization and bulk solution could be achieved, scanning x-ray microdiffraction[274] could be utilized to compare the ionic ordering in the DNA-dense phase to that of the bulk electrolyte. While very large DNA-NP superlattices may be suitable, other options include DNA-based hydrogels[275].

Finally, the obvious must be stated: there are plenty more salts out there to test. Particularly mysterious at this time is the apparently strong influence of the anion. In principle the SAXS, WAXS and MD experiments described here using chloride salts could be performed

substituting acetate, sulfates, nitrates, bromides, and perchlorate salts (among others). While that could keep a researcher busy for a while, increasing structural complexity of the anion may warrant the incorporation of spectroscopy techniques, such as X-ray absorption spectroscopy, may provide necessary insight on the local interactions between anions and other solution components.

Appendix

A.1. Extended DNA-AuNP Functionalization and Characterization

A.1.0. Definition of OD

The term "OD" denotes optical density at 260 nm, which is defined as the optical absorbance at 260 nm of a 1 mL solution of DNA in a 1 cm path length cuvette. This is a generally useful + standardized way of providing quantities of DNA, but is important to note that, since the absorption coefficients of nucleotides vary, the same OD of one oligo will not correspond to the same molar quantity of another. This might create issues if you attempt to adapt the functionalization protocol to DNA of a radically different molecular weight.

Also, do keep in mind that the absorption values provided by the Nanodrop are calculated in reference to what the absorbance measured would be in 1 mL solution. So, remember that you need to multiply this value by the volume of your sample (in mL) to obtain the OD.

A.1.1. Reduction of Thiolated DNA

Reduction can be carried out using wo different reducing agents: DTT and TCEP. While the former is commonly utilized, the latter holds some advantages. For comparison, the protocol for using either will be provided:

DTT (instructions are for using NAP-5 columns):

1. Add 1 mL DI water to your lyophilized DNA. Then vortex for 30 seconds and sonicate for 1 minute.

2. Measure the absorbance at 260 nm of the DNA. Since the volume is 1 mL, this value will be the OD.
3. Pipette as many volume equivalents of 15 OD as you need each into 1.5 mL centrifuge tubes. ($Volume(ml) = \frac{15\ OD}{Stock\ OD} * 1\ mL\ stock\ volume$
4. Place the tubes (with cap open) in a Centrivap. Depending on volume, evaporation can take anywhere from 30 minutes to 2 hours
5. While the samples spin make a 50 mM or 100 mM* DTT soluion, either in pH 7.4 phosphate buffer, or 170 mM Na2HPO4 and water. DTT doesn't work at low pH. You'll need 300 µl of this DTT solution (100 µl DTT/ 5OD).
6. After the DNA solutions sit for 30 minutes add 200 µl DI water, and proceed to the next step (ideally put them on the column around 1 hour).

TCEP

1. Add 1 mL DI water to your lyophilized DNA. Then vortex for 30 seconds and sonicate for 1 minute.
2. Measure the absorbance at 260 nm of the DNA. Since the volume is 1 mL, this value will be the OD.
3. Pipette the volume equivalents of OD you need into tubes. Consider the number of columns you will need in the following step

   ($Volume(ml) = \frac{15\ OD}{Stock\ OD} * 1\ mL\ stock\ volume$
4. Pipette the volume equivalents of OD you need into tubes. Consider the number of columns you will need in the following step

5. Add DI water and TCEP to the DNA solutions to make a final volume equivalent to the input of your NAP column and 20 mM TCEP (typically this means diluting the 0.5 M TCEP stock by 250x).
6. Proceed to the next step immediately, as the reaction with TCEP only needs to go for 15-30 minutes.

Using TCEP is faster, more scalable (no centrivap step) and doesn't require the preparation of fresh stock solutions every time. Additionally, DTT tends to degrade in Oxygen, so there's a chance every bottle used is slightly different

*100 mM is more commonly utilized. However, after a series of nanoparticles crashed during functionalization, the issue was isolated to DTT making it through the filtration column and cross-linking the particles [276]. Cutting to 50 mM seems to minimize this risk.

A.1.2. Gel Filtration

For this step, you can use NAP-5, NAP-10, or NAP-25 Sephadex columns to separate the DNA from the reducing agent. These columns operate on the principle that small molecules (reducing agent) pass through more slowly than the DNA. Prepare labeled tubes that can hold the DNA post filtration.

Table 0.1: Usage specifications for NAP columns.

Column	Loaded Volume (mL)	Eluted (mL)	Equilibration Volume (mL)	Max OD per tube
NAP-5	0.5	1	10	15
NAP-10	1	1.5	15	30
NAP-25	2.5	3.5	25	65

1. Mount columns vertically on some sort of support stand with racks and/or clamps, positioned so that liquid can drip out of the column into a sink or waste beaker.
2. Remove the caps from the top and bottoms of the column (s). NAP-25 may require scissors. Allow the buffer to drip out.
3. In 3-5 increments, add the volume of DI water specified by "Equilibration Volume" (**Table 0.1**) to the columns, and let it drip out. This equilibrates the column. Try not to let them dry out.
4. For one column at a time, add the DNA solution ("loaded volume") and allow to seep into the column.
5. Add the "Eluted volume" of DI water, and immediately begin collecting the fraction eluted from the column. This will contain the DNA. Try not to collect more than the eluted volume (the last few drops are most likely to contain the unwanted molecules
6. Measure the volume eluted using a pipette.
7. Measure the concentration using the Nanodrop (2 µl of the eluate). Calculate OD by multiply this value by the volume. If yield was less than 90%, something might have gone wrong.
8. Move promptly to begin the functionalization process

A.1.3. Functionalizing and Salt Aging

1. For each OD of DNA in your solution, prepare 1 mL AuNP solution (use as obtained from Ted Pella). Before adding the DNA, add 0.1 µl per ml AuNP of 0.1% w/w tween solution in water. Prepare these in 50 mL tubes with caps.

2. After adding the DNA solution, vortex the suspensions for 1 minute, and allow to incubate at room temperature overnight. If the color of the suspensions change to purple or blue, the nanoparticles are crashing, and functionalization has failed.
3. Quantities for the salt aging process are easily calculated using the various spreadsheets left in the "Synthesis and Purification" folder. For completeness, the procedure will be described. **Figure 0.1** provides example values for Step 6-9.
4. Prepare 5M NaCl, 1% SDS, and 0.1% SDS solutions in water.
5. Add 10µl of **1% SDS (in water)** per ml of suspension (e.g., 100 µl for 10 mL). Vortex vigorously for 30 seconds and let sit for 30 minutes.
6. Add 1 mL **0.1% SDS (in water)** to each tube. Then add enough 5 M NaCl to increase the concentration of the AuNP suspension to 0.05 M NaCl. Vortex vigorously for 30 seconds and let sit for 30 minutes.
7. Calculate the volume of 5 NaCl needed to increase the concentration to 0.1 M. First, add $1/10^{th}$ this calculated volume of 0.1% SDS, then add the NaCl. Vortex vigorously for 30 seconds and let sit for 30 minutes.
8. Repeat the previous step but increase [NaCl] to 0.2M instead.
9. Repeat step 8 until [NaCl] is 1 M. The time between salt addition can be increased to 1 hour when [NaCl] is above 0.6M.
10. If using TCEP, don't let the particles sit overnight at high salt. Proceed immediately to filtration.

Int C (c1)	Int V (v1)	5 M (c2)	salt V (v2)	Fnl C (c3)	0.1 % SDS	Fnl V (v1+v2+SDS)
0	14.9480	5	**0.1510**	0.05	**1.0000**	16.0990
0.05	16.0990	5	**0.1643**	0.1	**0.0164**	16.2797
0.1	16.2797	5	**0.3392**	0.2	**0.0339**	16.6528
0.2	16.6528	5	**0.3543**	0.3	**0.0354**	17.0425
0.3	17.0425	5	**0.3705**	0.4	**0.0370**	17.4501
0.4	17.4501	5	**0.3878**	0.5	**0.0388**	17.8766
0.5	17.8766	5	**0.4063**	0.6	**0.0406**	18.3235
0.6	18.3235	5	**0.4261**	0.7	**0.0426**	18.7923
0.7	18.7923	5	**0.4474**	0.8	**0.0447**	19.2844
0.8	19.2844	5	**0.4704**	0.9	**0.0470**	19.8018
0.9	19.8018	5	**0.4950**	1	**0.0495**	20.3464

Figure 0.1: Example utilization of the salt aging spreadsheet. Bolded quantities are added to the solution. All volumes are in mL.

A.1.4. Spin Filtering and Centrifugation

Excess DNA and salt now need to be removed with spin filtering and centrifugation.

1. Obtain Amicon Ultra-15 centrifugal filters (50 kDa or 100 kDa weight cutoff)
2. Load 12 ml of functionalized nanoparticles per filter (15 mL if using swinging bucket centrifuge).
3. Spin at 5000 RCF (4000 RCF for swinging bucket centrifuge) for 5 minutes. If using fixed-angle centrifuge, ensure the fritted panels are positioned parallel to the direction of rotation.
4. Remove the solution that passed through filter by picking the filter up and pouring into an appropriate waste receptacle.
5. Add 10 mL water (13 mL on swinging bucket) or the equivalent volume of nanoparticles if filters are in short supply.
6. Repeat step 3-5.
7. Spin at 5000 RCF (4000 RCF for swinging bucket centrifuge) for 30-40 minutes. If using fixed-angle centrifuge.

8. Remove concentrated DNA-NP solutions with pipette and move to 1.5 mL centrifuge tubes. Pipette 0.02% SDS into filters to extract any stuck particles. Fill tubes to total volume 1.5 mL with 0.02% SDS.
9. Centrifuge at max speed at 4°C for 1.5-3 hours.
10. Remove the supernatant (ideally hue is not darker than a light pink).
11. Fill tubes with DI water to 1.5 mL, pipetting up and down to disperse "pelleted" nanoparticle phase. It's ok to store the nanoparticles overnight in a 4°C fridge at this step.
12. Centrifuge at Centrifuge at max speed at 4°C for 3+ hours. Then remove supernatant and add DI water as in previous step.
13. Repeat step 12 1-2 times.
14. Centrifuge at Centrifuge at max speed at 4°C for 3+ hours. If the samples need to be very concentrated, consider running 12+ hours overnight.
15. Remove as much supernatant as possible without disturbing nanoparticle pellet.
16. Combine concentrated nanoparticles from equivalent tubes into stock solution.
17. Measure volume of product with pipette and concentration with UV-Vis (1:500 dilution)
18. Store stock in 4°C fridge

A.1.5 Oligreen Assay Determination of DNA Loading

1. Make a 100 μL 5 nM dilution of each functionalized AuNP of interest. The concentration is important here, so it's probably worth it to measure. One way to do this is to prepare a nominally 10nM solution from the concentrate, and measure a 5-fold

dilution of that working solution via UV-Vis. Then, add enough water to bring the concentration to 5nM.

2. Make 1mL of a 1 μM solution of the DNA-of-interest in DI water. Again, this is worth being precise with, so measure the concentration with UV-Vis and adjust accordingly. You only need 100 μL, so this is a big excess.
3. Mix 100 μL of 5 nM DNA-NPs with 100 μL of 40 mM potassium cyanide. Heat the solution to 50°C until the color disappears; this does not take very long.
4. In a 96-well clear bottom black plate, add 25 μL of the dissolved gold solution to three wells and add 75 μL of water. You can do more than 3 wells if you want better statistics, but you'll need to make an extra 100 μL of Oligreen solution per. **Figure 0.2** provides an example plate layout.
5. For the DNA standard curve, add 0, 1, 2, 4, 8, 12, 16, and 20 μL 1 μM DNA to each well, water up to 87.5 μL, and 12.5 μL of 40 mM potassium cyanide.
6. Dilute the oligreen reagent 200X in 1X TE buffer. Add 100 μL of oligreen reagent to each well. You need 1.1mL per particle type you're testing, so make 1.2mL per.

25 μL NP/KCN 75 μL Water 100 μL Oligreen	25 μL NP/KCN 75 μL Water 100 μL Oligreen	25 μL NP/KCN 75 μL Water 100 μL Oligreen					
0 μL DNA 87.5 μL Water 12.5 μL KCN 100 μL Oligreen	1 μL DNA 86.5 μL Water 12.5 μL KCN 100 μL Oligreen	2 μL DNA 85.5 μL Water 12.5 μL KCN 100 μL Oligreen	4 μL DNA 83.5 μL Water 12.5 μL KCN 100 μL Oligreen	8 μL DNA 79.5 μL Water 12.5 μL KCN 100 μL Oligreen	12 μL DNA 75.5 μL Water 12.5 μL KCN 100 μL Oligreen	16 μL DNA 71.5 μL Water 12.5 μL KCN 100 μL Oligreen	20 μL DNA 67.5 μL Water 12.5 μL KCN 100 μL Oligreen

Figure 0.2: Example volumes used in Oligreen assy. Each cell of the table denotes a well on the plate.

7. Measure the fluorescence at 520 nm with a 480 nm excitation. This can be done via the left computer connected to the plate reader. Select the wells with no DNA or

nanoparticles in them as blanks. Save the results as an Excel File and email it to yourself.

8. For analysis, calculate the average, standard deviation, and the St.dev/Average for each particle type in Excel.
9. Create a linear trendline by plotting fluorescence vs concentration in nM for each DNA dilution series. Since the total volumes are 200 µL, and you added 1µM DNA solutions, simply multiply the volume added to the well by 5 nM/µL to get these values.
10. Calculate the average amount of DNA in the wells containing dissolved nanoparticles by fitting the value to the trendline.
11. Divide this concentration by the particle concentration per well (0.3125 nM) to get the loading per particle.
12. Multiplying the St.dev/Average by the loading will give the error range for the loading.

References

1. Conway, B. E., *Electrochemical supercapacitors: scientific fundamentals and technological applications*. Springer Science & Business Media: 2013.
2. Armand, M.; Tarascon, J.-M., Building better batteries. *Nature* **2008,** *451* (7179), 652-657.
3. Yan, W.; Huang, S.; Stenby, E. H., Measurement and modeling of CO2 solubility in NaCl brine and CO2–saturated NaCl brine density. *International Journal of Greenhouse Gas Control* **2011,** *5* (6), 1460-1477.
4. Burant, A.; Lowry, G. V.; Karamalidis, A. K., Measurement and modeling of Setschenow constants for selected hydrophilic compounds in NaCl and CaCl2 simulated carbon storage brines. *Accounts of Chemical Research* **2017,** *50* (6), 1332-1341.
5. Matkovich, C. E.; Christian, G. D., Salting-out of acetone from water. Basis of a new solvent extraction system. *analytical Chemistry* **1973,** *45* (11), 1915-1921.
6. Duong-Ly, K. C.; Gabelli, S. B., Salting out of proteins using ammonium sulfate precipitation. In *Method Enzymol*, Elsevier: 2014; Vol. 541, pp 85-94.
7. Zhang, H.; Dasbiswas, K.; Ludwig, N. B.; Han, G.; Lee, B.; Vaikuntanathan, S.; Talapin, D. V., Stable colloids in molten inorganic salts. *Nature* **2017,** *542* (7641), 328-+.
8. Kamysbayev, V.; Srivastava, V.; Ludwig, N. B.; Borkiewicz, O. J.; Zhang, H.; Ilavsky, J.; Lee, B.; Chapman, K. W.; Vaikuntanathan, S.; Talapin, D. V., Nanocrystals in Molten Salts and Ionic Liquids: Experimental Observation of Ionic Correlations Extending beyond the Debye Length. *ACS Nano* **2019,** *13* (5), 5760-5770.
9. Zhang, T.; Davidson, A.; Bryant, S. L.; Huh, C. In *Nanoparticle-Stabilized Emulsions for Applications in Enhanced Oil Recovery*, SPE Improved Oil Recovery Symposium, 2010.
10. Séon, L.; Lavalle, P.; Schaaf, P.; Boulmedais, F., Polyelectrolyte multilayers: a versatile tool for preparing antimicrobial coatings. *Langmuir* **2015,** *31* (47), 12856-12872.
11. DasSarma, S.; Arora, P., Halophiles. *e LS* **2001**.
12. Zajc, J.; Džeroski, S.; Kocev, D.; Oren, A.; Sonjak, S.; Tkavc, R.; Gunde-Cimerman, N., Chaophilic or chaotolerant fungi: a new category of extremophiles? *Frontiers in microbiology* **2014,** *5*, 121677.
13. Wennerstrom, H.; Estrada, E. V.; Danielsson, J.; Oliveberg, M., Colloidal stability of the living cell. *P Natl Acad Sci USA* **2020,** *117* (19), 10113-10121.
14. Wennerström, H., Life in a saturated salt environment; a colloidal perspective. *JCIS Open* **2024**, 100109.
15. Walker, D. A.; Kowalczyk, B.; de la Cruz, M. O.; Grzybowski, B. A., Electrostatics at the nanoscale. *Nanoscale* **2011,** *3* (4), 1316-1344.
16. Grier, D. G., Colloids - A surprisingly attractive couple. *Nature* **1998,** *393* (6686), 621-+.
17. Li, Y. H.; Girard, M.; Shen, M.; Millan, J. A.; de la Cruz, M. O., Strong attractions and repulsions mediated by monovalent salts. *P Natl Acad Sci USA* **2017,** *114* (45), 11838-11843.
18. Bloomfield, V. A., DNA condensation by multivalent cations. *Biopolymers* **1997,** *44* (3), 269-282.
19. Domanico, P. L.; Tse-Dinh, Y. C., Mechanistic studies on E. coli DNA topoisomerase I: divalent ion effects. *Journal of inorganic biochemistry* **1991,** *42* (2), 87-96.
20. Traeger, J. C.; Schwartz, D. K., Interplay of electrostatic repulsion and surface grafting density on surface-mediated DNA hybridization. *J Colloid Interf Sci* **2020,** *566*, 369-374.

21. Wanunu, M.; Morrison, W.; Rabin, Y.; Grosberg, A. Y.; Meller, A., Electrostatic focusing of unlabelled DNA into nanoscale pores using a salt gradient. *Nat Nanotechnol* **2010,** *5* (2), 160-165.
22. Kohll, A. X.; Antkowiak, P. L.; Chen, W. D.; Nguyen, B. H.; Stark, W. J.; Ceze, L.; Strauss, K.; Grass, R. N., Stabilizing synthetic DNA for long-term data storage with earth alkaline salts. *Chem Commun* **2020,** *56* (25), 3613-3616.
23. Debye, P.; Huckel, E., The theory of electrolytes I. The lowering of the freezing point and related occurrences. *Phys Z* **1923,** *24*, 185-206.
24. Grahame, D. C., The Electrical Double Layer and the Theory of Electrocapillarity. *Chemical Reviews* **1947,** *41* (3), 441-501.
25. Kjellander, R., A multiple decay-length extension of the Debye–Hückel theory: to achieve high accuracy also for concentrated solutions and explain under-screening in dilute symmetric electrolytes. *Physical Chemistry Chemical Physics* **2020,** *22* (41), 23952-23985.
26. Verwey, E. J. W., Theory of the Stability of Lyophobic Colloids. *J Phys Colloid Chem* **1947,** *51* (3), 631-636.
27. Kirkwood, J. G.; Poirier, J. C., The Statistical Mechanical Basis of the Debye-Huckel Theory of Strong Electrolytes. *J Phys Chem-Us* **1954,** *58* (8), 591-596.
28. Kirkwood, J. G., Statistical mechanics of liquid solutions. *Chemical Reviews* **1936,** *19* (3), 275-307.
29. Attard, P., Asymptotic Analysis of Primitive Model Electrolytes and the Electrical Double-Layer. *Phys Rev E* **1993,** *48* (5), 3604-3621.
30. Cao, T.; Szilagyi, I.; Oncsik, T.; Borkovec, M.; Trefalt, G., Aggregation of Colloidal Particles in the Presence of Multivalent Colons: The Inverse Schulze-Hardy Rule. *Langmuir* **2015,** *31* (24), 6610-6614.
31. Grahame, D. C., Diffuse Double Layer Theory for Electrolytes of Unsymmetrical Valence Types. *J Chem Phys* **1953,** *21* (6), 1054-1060.
32. McBride, A.; Kohonen, M.; Attard, P., The screening length of charge-asymmetric electrolytes: A hypernetted chain calculation. *J Chem Phys* **1998,** *109* (6), 2423-2428.
33. Ulander, J.; Kjellander, R., Screening and asymptotic decay of pair distributions in asymmetric electrolytes. *J Chem Phys* **1998,** *109* (21), 9508-9522.
34. Blum, L.; Hoye, J. S., Mean Spherical Model for Asymmetric Electrolytes .2. Thermodynamic Properties and Pair Correlation-Function. *J Phys Chem-Us* **1977,** *81* (13), 1311-1317.
35. Israelachvili, J.; Gebbie, M.; Valtiner, M.; Banquy, X.; Fox, E.; Henderson, W., Ionic liquids behave as dilute electrolyte solutions. *Abstr Pap Am Chem S* **2014,** *248*.
36. Gebbie, M. A.; Dobbs, H. A.; Valtiner, M.; Israelachvili, J. N., Long-range electrostatic screening in ionic liquids. *P Natl Acad Sci USA* **2015,** *112* (24), 7432-7437.
37. Dobbs, H.; Gebbie, M.; Valtiner, M.; Banquy, X.; Berkson, Z.; Degen, G.; Kristiansen, K.; Israelachvili, J., Long-range electrostatic forces in ionic liquids. *Abstr Pap Am Chem S* **2018,** *255*.
38. Smith, A. M.; Lee, A. A.; Perkin, S., The Electrostatic Screening Length in Concentrated Electrolytes Increases with Concentration. *J Phys Chem Lett* **2016,** *7* (12), 2157-2163.
39. Lee, A. A.; Perez-Martinez, C. S.; Smith, A. M.; Perkin, S., Underscreening in concentrated electrolytes. *Faraday Discussions* **2017,** *199*, 239-259.

40. Lee, A. A.; Perez-Martinez, C. S.; Smith, A. M.; Perkin, S., Scaling Analysis of the Screening Length in Concentrated Electrolytes. *Physical Review Letters* **2017,** *119* (2).
41. Gaddam, P.; Ducker, W., Electrostatic Screening Length in Concentrated Salt Solutions. *Langmuir* **2019,** *35* (17), 5719-5727.
42. Hjalmarsson, N.; Atkin, R.; Rutland, M. W., Switchable long-range double layer force observed in a protic ionic liquid. *Chem Commun* **2017,** *53* (3), 647-650.
43. Cats, P.; Evans, R.; Hartel, A.; van Roij, R., Primitive model electrolytes in the near and far field: Decay lengths from DFT and simulations. *J Chem Phys* **2021,** *154* (12).
44. Anousheh, N.; Solis, F. J.; Jadhao, V., Ionic structure and decay length in highly concentrated confined electrolytes. *Aip Adv* **2020,** *10* (12).
45. Zeman, J.; Kondrat, S.; Holm, C., Ionic screening in bulk and under confinement. *J Chem Phys* **2021,** *155* (20).
46. Coles, S. W.; Park, C.; Nikam, R.; Kanduc, M.; Dzubiella, J.; Rotenberg, B., Correlation Length in Concentrated Electrolytes: Insights from All-Atom Molecular Dynamics Simulations. *J Phys Chem B* **2020,** *124* (9), 1778-1786.
47. Zeman, J.; Kondrat, S.; Holm, C., Bulk ionic screening lengths from extremely large-scale molecular dynamics simulations. *Chem Commun* **2020,** *56* (100), 15635-15638.
48. Setschenow, J., Über die konstitution der salzlösungen auf grund ihres verhaltens zu kohlensäure. *Zeitschrift für Physikalische Chemie* **1889,** *4* (1), 117-125.
49. Cohn, E. J., The physical chemistry of the proteins. *Physiological Reviews* **1925,** *5* (3), 349-437.
50. Hofmeister, F., On the understanding of the effects of salts. *Arch. Exp. Pathol. Pharmakol.(Leipzig)* **1888,** *24*, 247-260.
51. Cox, W.; Wolfenden, J. H., The viscosity of strong electrolytes measured by a differential method. *Proceedings of the Royal Society of London. Series A, Containing Papers of a Mathematical and Physical Character* **1934,** *145* (855), 475-488.
52. Marcus, Y., Effect of ions on the structure of water: structure making and breaking. *Chemical reviews* **2009,** *109* (3), 1346-1370.
53. Zhou, H. X., Interactions of macromolecules with salt ions: an electrostatic theory for the Hofmeister effect. *Proteins: Structure, Function, and Bioinformatics* **2005,** *61* (1), 69-78.
54. Jungwirth, P.; Cremer, P. S., Beyond hofmeister. *Nature chemistry* **2014,** *6* (4), 261-263.
55. Gregory, K. P.; Elliott, G. R.; Robertson, H.; Kumar, A.; Wanless, E. J.; Webber, G. B.; Craig, V. S.; Andersson, G. G.; Page, A. J., Understanding specific ion effects and the Hofmeister series. *Physical Chemistry Chemical Physics* **2022,** *24* (21), 12682-12718.
56. Salis, A.; Ninham, B. W., Models and mechanisms of Hofmeister effects in electrolyte solutions, and colloid and protein systems revisited. *Chemical Society Reviews* **2014,** *43* (21), 7358-7377.
57. Green, A. A., Studies in the physical chemistry of the proteins: X. The solubility of hemoglobin in solutions of chlorides and sulfates of varying concentration. *Journal of Biological Chemistry* **1932,** *95* (1), 47-66.
58. Green, A. A.; Hughes, W. L., [10] Protein fractionation on the basis of solubility in aqueous solutions of salts and organic solvents. **1955**.
59. Bianchi, E.; Blaak, R.; Likos, C. N., Patchy colloids: state of the art and perspectives. *Physical Chemistry Chemical Physics* **2011,** *13* (14), 6397-6410.

60. Ballauff, M., Spherical polyelectrolyte brushes. *Prog Polym Sci* **2007,** *32* (10), 1135-1151.
61. Bracha, D.; Karzbrun, E.; Shemer, G.; Pincus, P. A.; Bar-Ziv, R. H., Entropy-driven collective interactions in DNA brushes on a biochip. *P Natl Acad Sci USA* **2013,** *110* (12), 4534-4538.
62. Zhulina, E. B.; Borisov, O. V.; Birshtein, T. M., Structure of Grafted Polyelectrolyte Layer. *J Phys Ii* **1992,** *2* (1), 63-74.
63. Yu, J.; Mao, J.; Yuan, G. C.; Satija, S.; Jiang, Z.; Chen, W.; Tirrell, M., Structure of Polyelectrolyte Brushes in the Presence of Multivalent Counterions. *Macromolecules* **2016,** *49* (15), 5609-5617.
64. Yu, J.; Jackson, N. E.; Xu, X.; Brettmann, B. K.; Ruths, M.; de Pablo, J. J.; Tirrell, M., Multivalent ions induce lateral structural inhomogeneities in polyelectrolyte brushes. *Sci Adv* **2017,** *3* (12).
65. Farina, R.; Laugel, N.; Pincus, P.; Tirrell, M., Brushes of strong polyelectrolytes in mixed mono- and tri-valent ionic media at fixed total ionic strengths. *Soft Matter* **2013,** *9* (44), 10458-10472.
66. Parak, W. J.; Pellegrino, T.; Micheel, C. M.; Gerion, D.; Williams, S. C.; Alivisatos, A. P., Conformation of oligonucleotides attached to gold nanocrystals probed by gel electrophoresis. *Nano Lett* **2003,** *3* (1), 33-36.
67. Hariharan, R.; Biver, C.; Russel, W. B., Ionic strength effects in polyelectrolyte brushes: The counterion correction. *Macromolecules* **1998,** *31* (21), 7514-7518.
68. Hariharan, R.; Biver, C.; Mays, J.; Russel, W. B., Ionic strength and curvature effects in flat and highly curved polyelectrolyte brushes. *Macromolecules* **1998,** *31* (21), 7506-7513.
69. Pincus, P., Colloid Stabilization with Grafted Polyelectrolytes. *Macromolecules* **1991,** *24* (10), 2912-2919.
70. Argillier, J. F.; Tirrell, M., Adsorption of Water-Soluble Ionic Hydrophobic Diblock Copolymer on a Hydrophobic Surface. *Theor Chim Acta* **1992,** *82* (5), 343-350.
71. Zhulina, E. B.; Birshtein, T. M.; Borisov, O. V., Curved polymer and polyelectrolyte brushes beyond the Daoud-Cotton model. *Eur Phys J E* **2006,** *20* (3), 243-256.
72. Guo, X.; Ballauff, M., Spherical polyelectrolyte brushes: Comparison between annealed and quenched brushes. *Phys Rev E* **2001,** *64* (5).
73. Guo, X.; Ballauff, M., Spatial dimensions of colloidal polyelectrolyte brushes as determined by dynamic light scattering. *Langmuir* **2000,** *16* (23), 8719-8726.
74. Forster, S.; Hermsdorf, N.; Bottcher, C.; Lindner, P., Structure of polyelectrolyte block copolymer micelles. *Macromolecules* **2002,** *35* (10), 4096-4105.
75. Muller, F.; Delsanti, M.; Auvray, L.; Yang, J.; Chen, Y. J.; Mays, J. W.; Deme, B.; Tirrell, M.; Guenoun, P., Ordering of urchin-like charged copolymer micelles: Electrostatic, packing and polyelectrolyte correlations. *Eur Phys J E* **2000,** *3* (1), 45-53.
76. Korobko, A. V.; Jesse, W.; Lapp, A.; Egelhaaf, S. U.; van der Maarel, J. R. C., Structure of strongly interacting polyelectrolyte diblock copolymer micelles. *J Chem Phys* **2005,** *122* (2).
77. Korobko, A. V.; Jesse, W.; Egelhaaf, S. U.; Lapp, A.; van der Maarel, J. R. C., Do spherical polyelectrolyte brushes interdigitate? *Physical Review Letters* **2004,** *93* (17).

78. Li, N. K.; Fuss, W. H.; Tang, L.; Gu, R. P.; Chilkoti, A.; Zauscher, S.; Yingling, Y. G., Prediction of solvent-induced morphological changes of polyelectrolyte diblock copolymer micelles. *Soft Matter* **2015,** *11* (42), 8236-8245.
79. Tan, S. J.; Kahn, J. S.; Derrien, T. L.; Campolongo, M. J.; Zhao, M.; Smilgies, D. M.; Luo, D., Crystallization of DNA-Capped Gold Nanoparticles in High-Concentration, Divalent Salt Environments. *Angew Chem Int Edit* **2014,** *53* (5), 1316-1319.
80. Srivastava, S.; Chhabra, A.; Gang, O., Effect of mono- and multi-valent ionic environments on the in-lattice nanoparticle-grafted single-stranded DNA. *Soft Matter* **2022,** *18* (3), 526-534.
81. Lee, J.; Moesari, E.; Dandamudi, C. B.; Beniah, G.; Chang, B.; Iqbal, M.; Fei, Y. P.; Zhou, N. J.; Ellison, C. J.; Johnston, K. P., Behavior of Spherical Poly(2-acrylamido-2-methylpropanesulfonate) Polyelectrolyte Brushes on Silica Nanoparticles up to Extreme Salinity with Weak Divalent Cation Binding at Ambient and High Temperature. *Macromolecules* **2017,** *50* (19), 7699-7711.
82. Hurst, S. J.; Lytton-Jean, A. K. R.; Mirkin, C. A., Maximizing DNA loading on a range of gold nanoparticle sizes. *Analytical Chemistry* **2006,** *78* (24), 8313-8318.
83. Rosi, N. L.; Mirkin, C. A., Nanostructures in biodiagnostics. *Chemical Reviews* **2005,** *105* (4), 1547-1562.
84. Nykypanchuk, D.; Maye, M. M.; van der Lelie, D.; Gang, O., DNA-guided crystallization of colloidal nanoparticles. *Nature* **2008,** *451* (7178), 549-552.
85. Zhou, W. H.; Saran, R.; Liu, J. W., Metal Sensing by DNA. *Chemical Reviews* **2017,** *117* (12), 8272-8325.
86. Storhofff, J. J.; Elghanian, R.; Mirkin, C. A.; Letsinger, R. L., Sequence-dependent stability of DNA-modified gold nanoparticles. *Langmuir* **2002,** *18* (17), 6666-6670.
87. Krishnamoorthy, K.; Hoffmann, K.; Kewalramani, S.; Brodin, J. D.; Moreau, L. M.; Mirkin, C. A.; De la Cruz, M. O.; Bedzyk, M. J., Defining the Structure of a Protein-Spherical Nucleic Acid Conjugate and Its Counterionic Cloud. *Acs Central Science* **2018,** *4* (3), 378-386.
88. Kewalramani, S.; Zwanikken, J. W.; Macfarlane, R. J.; Leung, C. Y.; de la Cruz, M. O.; Mirkin, C. A.; Bedzyk, M. J., Counterion Distribution Surrounding Spherical Nucleic Acid-Au Nanoparticle Conjugates Probed by Small-Angle X-ray Scattering. *Acs Nano* **2013,** *7* (12), 11301-11309.
89. Heo, J. H.; Cho, H. H.; Lee, J. H., Surfactant-free nanoparticle DNA complexes with ultrahigh stability against salt for environmental and biological sensing. *Analyst* **2014,** *139* (22), 5936-5944.
90. Samanta, D.; Iscen, A.; Laramy, C. R.; Ebrahimi, S. B.; Bujold, K. E.; Schatz, G. C.; Mirkin, C. A., Multivalent Cation-Induced Actuation of DNA-Mediated Colloidal Superlattices. *Journal of the American Chemical Society* **2019,** *141* (51), 19973-19977.
91. Lee, J.; Huh, J. H.; Lee, S., DNA Base Pair Stacking Crystallization of Gold Colloids. *Langmuir* **2020,** *36* (19), 5118-5125.
92. Zhang, H. H.; Wang, W. J.; Hagen, N.; Kuzmenko, I.; Akinc, M.; Travesset, A.; Mallapragada, S.; Vaknin, D., Self-Assembly of DNA Functionalized Gold Nanoparticles at the Liquid-Vapor Interface. *Adv Mater Interfaces* **2016,** *3* (16).
93. Kewalramani, S.; Guerrero-Garcia, G. I.; Moreau, L. M.; Zwanikken, J. W.; Mirkin, C. A.; de la Cruz, M. O.; Bedzyk, M. J., Electrolyte-Mediated Assembly of Charged Nanoparticles. *Acs Central Science* **2016,** *2* (4), 219-224.

94. Hurst, S. J.; Lytton-Jean, A. K.; Mirkin, C. A., Maximizing DNA loading on a range of gold nanoparticle sizes. *Analytical chemistry* **2006,** *78* (24), 8313-8318.
95. Weigand, S. J.; Keane, D. T., DND-CAT's new triple area detector system for simultaneous data collection at multiple length scales. *Nuclear Instruments and Methods in Physics Research Section A: Accelerators, Spectrometers, Detectors and Associated Equipment* **2011,** *649* (1), 61-63.
96. Squires, G. L., *Introduction to the theory of thermal neutron scattering*. Courier Corporation: 1996.
97. Jacrot, B., The study of biological structures by neutron scattering from solution. *Reports on progress in physics* **1976,** *39* (10), 911.
98. Ingle Jr, J. D.; Crouch, S. R., Spectrochemical analysis. **1988**.
99. Schmid, F. X., Biological macromolecules: UV-visible spectrophotometry. *e LS* **2001**.
100. Huang, X.; El-Sayed, M. A., Gold nanoparticles: Optical properties and implementations in cancer diagnosis and photothermal therapy. *Journal of advanced research* **2010,** *1* (1), 13-28.
101. Haiss, W.; Thanh, N. T.; Aveyard, J.; Fernig, D. G., Determination of size and concentration of gold nanoparticles from UV− Vis spectra. *Analytical chemistry* **2007,** *79* (11), 4215-4221.
102. Hutter, E.; Fendler, J. H., Exploitation of localized surface plasmon resonance. *Advanced materials* **2004,** *16* (19), 1685-1706.
103. Storhoff, J. J.; Lazarides, A. A.; Mucic, R. C.; Mirkin, C. A.; Letsinger, R. L.; Schatz, G. C., What controls the optical properties of DNA-linked gold nanoparticle assemblies? *Journal of the American Chemical Society* **2000,** *122* (19), 4640-4650.
104. Lazarides, A. A.; Schatz, G. C., DNA-linked metal nanosphere materials: Structural basis for the optical properties. *The Journal of Physical Chemistry B* **2000,** *104* (3), 460-467.
105. Reinertsen, R. J.; Kewalramani, S.; Jiménez-Ángeles, F.; Weigand, S. J.; Bedzyk, M. J.; Olvera de la Cruz, M., Reexpansion of charged nanoparticle assemblies in concentrated electrolytes. *Proceedings of the National Academy of Sciences* **2024,** *121* (6), e2316537121.
106. Zang, X. N.; Shen, C. W.; Sanghadasa, M.; Lin, L. W., High-Voltage Supercapacitors Based on Aqueous Electrolytes. *Chemelectrochem* **2019,** *6* (4), 976-988.
107. Gonzalez-Mozuelos, P.; Yeom, M. S.; de la Cruz, M. O., Molecular multivalent electrolytes: microstructure and screening lengths. *Eur Phys J E* **2005,** *16* (2), 167-178.
108. Jing, Y. F.; Jadhao, V.; Zwanikken, J. W.; de la Cruz, M. O., Ionic structure in liquids confined by dielectric interfaces. *J Chem Phys* **2015,** *143* (19).
109. Lee, S. S.; Koishi, A.; Bourg, I. C.; Fenter, P., Ion correlations drive charge overscreening and heterogeneous nucleation at solid-aqueous electrolyte interfaces. *P Natl Acad Sci USA* **2021,** *118* (32).
110. Gebbie, M. A.; Valtiner, M.; Banquy, X.; Fox, E. T.; Henderson, W. A.; Israelachvili, J. N., Ionic liquids behave as dilute electrolyte solutions. *P Natl Acad Sci USA* **2013,** *110* (24), 9674-9679.
111. Kumar, S.; Cats, P.; Alotaibi, M. B.; Ayirala, S. C.; Yousef, A. A.; van Roij, R.; Siretanu, I.; Mugele, F., Absence of anomalous underscreening in highly concentrated aqueous electrolytes confined between smooth silica surfaces. *J Colloid Interf Sci* **2022,** *622*, 819-827.
112. Härtel, A.; Bültmann, M.; Coupette, F., Anomalous Underscreening in the Restricted Primitive Model. *Physical Review Letters* **2023,** *130* (10), 108202.

113. Beaucage, S.; Caruthers, M. H., Deoxynucleoside phosphoramidites—a new class of key intermediates for deoxypolynucleotide synthesis. *Tetrahedron letters* **1981,** *22* (20), 1859-1862.
114. Owczarzy, R.; Tataurov, A. V.; Wu, Y.; Manthey, J. A.; McQuisten, K. A.; Almabrazi, H. G.; Pedersen, K. F.; Lin, Y.; Garretson, J.; McEntaggart, N. O., IDT SciTools: a suite for analysis and design of nucleic acid oligomers. *Nucleic Acids Res* **2008,** *36* (suppl_2), W163-W169.
115. Chen, Y.; Tokuda, J. M.; Topping, T.; Sutton, J. L.; Meisburger, S. P.; Pabit, S. A.; Gloss, L. M.; Pollack, L., Revealing transient structures of nucleosomes as DNA unwinds. *Nucleic Acids Res* **2014,** *42* (13), 8767-8776.
116. Als-Nielsen, J.; McMorrow, D., *Elements of modern X-ray physics*. John Wiley & Sons: 2011.
117. Förster, S.; Timmann, A.; Konrad, M.; Schellbach, C.; Meyer, A.; Funari, S.; Mulvaney, P.; Knott, R., Scattering curves of ordered mesoscopic materials. *The Journal of Physical Chemistry B* **2005,** *109* (4), 1347-1360.
118. Kinnibrugh, T.; Fister, T., Structure of Sulfuric Acid Solutions Using Pair Distribution Function Analysis. *The Journal of Physical Chemistry B* **2022,** *126* (16), 3099-3106.
119. Yang, W. H.; Schatz, G. C.; Vanduyne, R. P., Discrete Dipole Approximation for Calculating Extinction and Raman Intensities for Small Particles with Arbitrary Shapes. *J Chem Phys* **1995,** *103* (3), 869-875.
120. Finney, J. L., Random Packings and Structure of Simple Liquids .1. Geometry of Random Close Packing. *Proc R Soc Lon Ser-A* **1970,** *319* (1539), 479-&.
121. Sirota, E. B.; Ou-Yang, H. D.; Sinha, S. K.; Chaikin, P. M.; Axe, J. D.; Fujii, Y., Complete phase diagram of a charged colloidal system: A synchro- tron x-ray scattering study. *Physical Review Letters* **1989,** *62* (13), 1524-1527.
122. Mcconnell, G. A.; Gast, A. P.; Huang, J. S.; Smith, S. D., Disorder-Order Transitions in Soft-Sphere Polymer Micelles. *Physical Review Letters* **1993,** *71* (13), 2102-2105.
123. Yun, H.; Yu, J. W.; Lee, Y. J.; Kim, J. S.; Park, C. H.; Nam, C.; Han, J.; Heo, T. Y.; Cho, S. H.; Lee, D. C.; Lee, W. B.; Stein, G. E.; Kim, B. J., Symmetry Transitions of Polymer-Grafted Nanoparticles: Grafting Density Effect. *Chem Mater* **2019,** *31* (14), 5264-5273.
124. Reinertsen, R. J.; Jimenez-Angeles, F.; Kewalramani, S.; Bedzyk, M. J.; de la Cruz, M. O., Transformations in crystals of DNA-functionalized nanoparticles by electrolytes. *Faraday Discussions* **2023**.
125. Hansen, J.-P.; Verlet, L., Phase Transitions of the Lennard-Jones System. *Physical Review* **1969,** *184* (1), 151-161.
126. Bai, Y.; Greenfeld, M.; Travers, K. J.; Chu, V. B.; Lipfert, J.; Doniach, S.; Herschlag, D., Quantitative and comprehensive decomposition of the ion atmosphere around nucleic acids. *J Am Chem Soc* **2007,** *129* (48), 14981-14988.
127. Ahmad, R.; Arakawa, H.; Tajmir-Riahi, H. A., A comparative study of DNA complexation with Mg(II) and Ca(II) in aqueous solution: Major and minor grooves bindings. *Biophysical Journal* **2003,** *84* (4), 2460-2466.
128. Long, M. P.; Alland, S.; Martin, M. E.; Isborn, C. M., Molecular dynamics simulations of alkaline earth metal ions binding to DNA reveal ion size and hydration effects. *Physical Chemistry Chemical Physics* **2020,** *22* (10), 5584-5596.

129. De La Cruz, M. O.; Belloni, L.; Delsanti, M.; Dalbiez, J.; Spalla, O.; Drifford, M., Precipitation of highly charged polyelectrolyte solutions in the presence of multivalent salts. *The Journal of chemical physics* **1995,** *103* (13), 5781-5791.
130. Raspaud, E.; de la Cruz, M. O.; Sikorav, J. L.; Livolant, F., Precipitation of DNA by polyamines: A polyelectrolyte behavior. *Biophysical Journal* **1998,** *74* (1), 381-393.
131. Nguyen, T. T.; Rouzina, I.; Shklovskii, B. I., Reentrant condensation of DNA induced by multivalent counterions. *The Journal of chemical physics* **2000,** *112* (5), 2562-2568.
132. Besteman, K.; Van Eijk, K.; Lemay, S., Charge inversion accompanies DNA condensation by multivalent ions. *Nature Physics* **2007,** *3* (9), 641-644.
133. Sing, C. E.; Zwanikken, J. W.; Olvera de la Cruz, M., Effect of ion–ion correlations on polyelectrolyte gel collapse and reentrant swelling. *Macromolecules* **2013,** *46* (12), 5053-5065.
134. Solis, F. J.; De La Cruz, M. O., Flexible linear polyelectrolytes in multivalent salt solutions: Solubility conditions. *EPJ direct* **2000,** *2*, 1-18.
135. *CRC Handbook of Chemistry and Physics*. CRC Press: 2023; Vol. 104.
136. Jalilehvand, F.; Spangberg, D.; Lindqvist-Reis, P.; Hermansson, K.; Persson, I.; Sandstrom, M., Hydration of the calcium ion. An EXAFS, large-angle X-ray scattering, and molecular dynamics simulation study. *Journal of the American Chemical Society* **2001,** *123* (3), 431-441.
137. Badyal, Y. S.; Barnes, A. C.; Cuello, G. J.; Simonson, J. M., Understanding the effects of concentration on the solvation structure of Ca2+ in aqueous solutions. II: Insights into longer range order from neutron diffraction isotope substitution. *J Phys Chem A* **2004,** *108* (52), 11819-11827.
138. Marques, M. A.; Cabaco, M. I.; Marques, M. I. D.; Gaspar, A. M., Intermediate-range order in aqueous solutions of salts constituted of divalent ions combined with monovalent counter-ions. *J Phys-Condens Mat* **2002,** *14* (32), 7427-7448.
139. Gaspar, A. M.; Marques, M. A.; Cabaco, M. I.; Marques, M. I. D.; Buslaps, T.; Honkimaki, V., X-ray diffraction investigations of concentrated aqueous solutions of calcium halides. *J Mol Liq* **2004,** *110* (1-3), 15-22.
140. Fetisov, E. O.; Mundy, C. J.; Schenter, G. K.; Benmore, C. J.; Fulton, J. L.; Kathmann, S. M., Nanometer-Scale Correlations in Aqueous Salt Solutions. *J Phys Chem Lett* **2020,** *11* (7), 2598-2604.
141. Friesen, S.; Hefter, G.; Buchner, R., Cation hydration and ion pairing in aqueous solutions of MgCl2 and CaCl2. *The Journal of Physical Chemistry B* **2019,** *123* (4), 891-900.
142. Rudolph, W. W.; Irmer, G., Hydration of the calcium(II) ion in an aqueous solution of common anions (ClO4-, Cl-, Br-, and NO3-). *Dalton T* **2013,** *42* (11), 3919-3935.
143. Safran, S. A.; Pincus, P. A., Scaling perspectives of underscreening in concentrated electrolyte solutions. *Soft Matter* **2023,** *19* (41), 7907-7911.
144. Wyman, J., The dielectric constant of mixtures of ethyl alcohol and water from-5 to 40(o). *Journal of the American Chemical Society* **1931,** *53*, 3292-3301.
145. Laanait, N.; Mihaylov, M.; Hou, B. Y.; Yu, H.; Vanysek, P.; Meron, M.; Lin, B. H.; Benjamin, I.; Schlossman, M. L., Tuning ion correlations at an electrified soft interface. *P Natl Acad Sci USA* **2012,** *109* (50), 20326-20331.
146. Arscott, P. G.; Ma, C. L.; Wenner, J. R.; Bloomfield, V. A., DNA Condensation by Cobalt Hexaammine(Iii) in Alcohol-Water Mixtures - Dielectric-Constant and Other Solvent Effects. *Biopolymers* **1995,** *36* (3), 345-364.

147. Bald, A.; Szejgis, A.; Barczyńska, J.; Piekarski, H., Effect of ionic association on the B coefficient for CaCl2 in ethanol-water mixtures at 298.15 K. *Physics and Chemistry of Liquids* **1999,** *37* (2), 125-135.
148. Liu, G. M.; Parsons, D.; Craig, V. S. J., Re-entrant swelling and redissolution of polyelectrolytes arises from an increased electrostatic decay length at high salt concentrations. *J Colloid Interf Sci* **2020,** *579*, 369-378.
149. Shannon, R. D., Revised effective ionic radii and systematic studies of interatomic distances in halides and chalcogenides. *Acta crystallographica section A: crystal physics, diffraction, theoretical and general crystallography* **1976,** *32* (5), 751-767.
150. Páll, S.; Zhmurov, A.; Bauer, P.; Abraham, M.; Lundborg, M.; Gray, A.; Hess, B.; Lindahl, E., Heterogeneous parallelization and acceleration of molecular dynamics simulations in GROMACS. *The Journal of Chemical Physics* **2020,** *153* (13), 134110.
151. Hess, B.; Kutzner, C.; van der Spoel, D.; Lindahl, E., GROMACS 4: Algorithms for Highly Efficient, Load-Balanced, and Scalable Molecular Simulation. *Journal of Chemical Theory and Computation* **2008,** *4* (3), 435-447.
152. Jiménez-Ángeles, F.; Lozada-Cassou, M., On the regimes of charge reversal. *The Journal of Chemical Physics* **2008,** *128* (17).
153. Páll, S.; Zhmurov, A.; Bauer, P.; Abraham, M.; Lundborg, M.; Gray, A.; Hess, B.; Lindahl, E., Heterogeneous parallelization and acceleration of molecular dynamics simulations in GROMACS. *The Journal of Chemical Physics* **2020,** *153* (13).
154. Powles, J. G.; Baker, S. E.; Evans, W. A. B., The chemical potential in atomically inhomogeneous fluids in external force fields by computer simulation. *The Journal of Chemical Physics* **1994,** *101* (5), 4098-4102.
155. Reinertsen, R. J.-E.; Jiménez-Ángeles, F.; Kewalramani, S.; Bedzyk, M.; de la Cruz, M. O., Transformations in crystals of DNA-functionalized nanoparticles by electrolytes. *Faraday Discussions* **2024,** *249*, 408-423.
156. Russel, W. B.; Russel, W.; Saville, D. A.; Schowalter, W. R., *Colloidal dispersions*. Cambridge university press: 1991.
157. Verwey, E. J. W., Theory of the Stability of Lyophobic Colloids. *The Journal of Physical and Colloid Chemistry* **1947,** *51* (3), 631-636.
158. Derjaguin, B.; Landau, L., Theory of the stability of strongly charged lyophobic sols and of the adhesion of strongly charged particles in solutions of electrolytes. *Progress in Surface Science* **1993,** *43* (1), 30-59.
159. Yethiraj, A.; van Blaaderen, A., A colloidal model system with an interaction tunable from hard sphere to soft and dipolar. *Nature* **2003,** *421* (6922), 513-517.
160. Gast, A. P.; Russel, W. B., Simple Ordering in Complex Fluids. *Physics Today* **1998,** *51* (12), 24-30.
161. Thomas, P., Crystallization kinetics of repulsive colloidal spheres. *Journal of Physics: Condensed Matter* **1999,** *11* (28), R323.
162. Robbins, M. O.; Kremer, K.; Grest, G. S., Phase-Diagram and Dynamics of Yukawa Systems. *J Chem Phys* **1988,** *88* (5), 3286-3312.
163. Kremer, K.; Robbins, M. O.; Grest, G. S., Phase-Diagram of Yukawa Systems - Model for Charge-Stabilized Colloids. *Physical Review Letters* **1986,** *57* (21), 2694-2697.

164. Sirota, E. B.; Ouyang, H. D.; Sinha, S. K.; Chaikin, P. M.; Axe, J. D.; Fujii, Y., Complete Phase-Diagram of a Charged Colloidal System - a Synchrotron X-Ray-Scattering Study. *Phys Rev Lett* **1989,** *62* (13), 1524-1527.
165. Bian, T.; Gardin, A.; Gemen, J.; Houben, L.; Perego, C.; Lee, B.; Elad, N.; Chu, Z.; Pavan, G. M.; Klajn, R., Electrostatic co-assembly of nanoparticles with oppositely charged small molecules into static and dynamic superstructures. *Nature Chemistry* **2021,** *13* (10), 940-949.
166. Lin, Y.; Olvera de la Cruz, M., Sublattice melting in binary superionic colloidal crystals. *Physical Review E* **2020,** *101* (3), 032603.
167. Yun, H.; Lee, Y. J.; Xu, M.; Lee, D. C.; Stein, G. E.; Kim, B. J., Softness- and Size-Dependent Packing Symmetries of Polymer-Grafted Nanoparticles. *Acs Nano* **2020,** *14* (8), 9644-9651.
168. Boles, M. A.; Talapin, D. V., Many-Body Effects in Nanocrystal Superlattices: Departure from Sphere Packing Explains Stability of Binary Phases. *Journal of the American Chemical Society* **2015,** *137* (13), 4494-4502.
169. Thaner, R. V.; Kim, Y.; Li, T. I. N. G.; Macfarlane, R. J.; Nguyen, S. T.; Olvera de la Cruz, M.; Mirkin, C. A., Entropy-Driven Crystallization Behavior in DNA-Mediated Nanoparticle Assembly. *Nano Letters* **2015,** *15* (8), 5545-5551.
170. Korgel, B. A.; Fitzmaurice, D., Small-angle x-ray-scattering study of silver-nanocrystal disorder-order phase transitions. *Phys Rev B* **1999,** *59* (22), 14191-14201.
171. Goodfellow, B. W.; Yu, Y. X.; Bosoy, C. A.; Smilgies, D. M.; Korgel, B. A., The Role of Ligand Packing Frustration in Body-Centered Cubic (bcc) Superlattices of Colloidal Nanocrystals. *J Phys Chem Lett* **2015,** *6* (13), 2406-2412.
172. Lodge, T. P.; Bang, J.; Park, M. J.; Char, K., Origin of the thermoreversible fcc-bcc transition in block copolymer solutions. *Physical Review Letters* **2004,** *92* (14).
173. Weidman, M. C.; Smilgies, D. M.; Tisdale, W. A., Kinetics of the self-assembly of nanocrystal superlattices measured by real-time in situ X-ray scattering. *Nat Mater* **2016,** *15* (7), 775-+.
174. Schmitt, J.; Hajiw, S.; Lecchi, A.; Degrouard, J.; Salonen, A.; Imperor-Clerc, M.; Pansu, B., Formation of Superlattices of Gold Nanoparticles Using Ostwald Ripening in Emulsions: Transition from fcc to bcc Structure. *J Phys Chem B* **2016,** *120* (25), 5759-5766.
175. Lee, B.; Littrell, K.; Sha, Y. C.; Shevchenko, E. V., Revealing the Effects of the Non-solvent on the Ligand Shell of Nanoparticles and Their Crystallization. *Journal of the American Chemical Society* **2019,** *141* (42), 16651-16662.
176. Bian, K. F.; Choi, J. J.; Kaushik, A.; Clancy, P.; Smilgies, D. M.; Hanrath, T., Shape-Anisotropy Driven Symmetry Transformations in Nanocrystal Superlattice Polymorphs. *Acs Nano* **2011,** *5* (4), 2815-2823.
177. Goodfellow, B. W.; Korgel, B. A., Reversible Solvent Vapor-Mediated Phase Changes in Nanocrystal Superlattices. *Acs Nano* **2011,** *5* (4), 2419-2424.
178. Kaushik, A. P.; Clancy, P., Solvent-driven symmetry of self-assembled nanocrystal superlatticesA computational study. *J Comput Chem* **2013,** *34* (7), 523-532.
179. Missoni, L. L.; Tagliazucchi, M., The Phase Behavior of Nanoparticle Superlattices in the Presence of a Solvent. *Acs Nano* **2020,** *14* (5), 5649-5658.

180. Zhang, L.; Bailey, J. B.; Subramanian, R. H.; Groisman, A.; Tezcan, F. A., Hyperexpandable, self-healing macromolecular crystals with integrated polymer networks. *Nature* **2018,** *557* (7703), 86-91.
181. Heller, W. T.; Urban, V. S.; Lynn, G. W.; Weiss, K. L.; O'Neill, H. M.; Pingali, S. V.; Qian, S.; Littrell, K. C.; Melnichenko, Y. B.; Buchanan, M. V., The Bio-SANS instrument at the high flux isotope reactor of Oak Ridge National Laboratory. *Journal of Applied Crystallography* **2014,** *47* (4), 1238-1246.
182. Qian, S.; Pingali, S. V.; Weiss, K. L.; Urban, V.; O'neill, H. M.; Langan, P., Neutron scattering for biological research: progress at the bio-SANS beam line. *Oak Ridge National Lab.(ORNL), Oak ridge, TN (United States). High flux* **2016**.
183. Heller, W. T.; Hetrick, J.; Bilheux, J.; Calvo, J. M. B.; Chen, W.-R.; DeBeer-Schmitt, L.; Do, C.; Doucet, M.; Fitzsimmons, M. R.; Godoy, W. F., drtsans: The data reduction toolkit for small-angle neutron scattering at Oak Ridge National Laboratory. *SoftwareX* **2022,** *19*, 101101.
184. Kewalramani, S.; Guerrero-García, G. I.; Moreau, L. M.; Zwanikken, J. W.; Mirkin, C. A.; Olvera de la Cruz, M.; Bedzyk, M. J., Electrolyte-mediated assembly of charged nanoparticles. *ACS central science* **2016,** *2* (4), 219-224.
185. Atkins, P. W.; De Paula, J.; Keeler, J., *Atkins' physical chemistry*. Oxford university press: 2023.
186. Ehlen, A.; Lopez-Rios, H.; De La Cruz, M. O., Metallization of colloidal crystals. *Physical Review Materials* **2021,** *5* (11), 115601.
187. Xia, J.; Lee, M.; Santos, P. J.; Horst, N.; Macfarlane, R. J.; Guo, H.; Travesset, A., Nanocomposite tectons as unifying systems for nanoparticle assembly. *Soft Matter* **2022,** *18* (11), 2176-2192.
188. Yee, D. W.; Lee, M. S.; An, J. Y.; Macfarlane, R. J., Reversible Diffusionless Phase Transitions in 3D Nanoparticle Superlattices. *Journal of the American Chemical Society* **2023,** *145* (11), 6051-6056.
189. Bain, E. C.; Dunkirk, N., The nature of martensite. *trans. AIME* **1924,** *70* (1), 25-47.
190. Cacace, M. G.; Landau, E. M.; Ramsden, J. J., The Hofmeister series: salt and solvent effects on interfacial phenomena. *Q Rev Biophys* **1997,** *30* (3), 241-277.
191. Yang, W. J.; Lu, J. X.; Gilbert, E. P.; Knott, R.; He, L. Z.; Cheng, W. L., Probing Soft Corona Structures of DNA-Capped Nanoparticles by Small Angle Neutron Scattering. *J Phys Chem C* **2015,** *119* (32), 18773-18778.
192. Neidle, S.; Sanderson, M., *Principles of nucleic acid structure*. Academic Press: 2021.
193. Kewalramani, S.; Guerrero-Garcia, G. I.; Moreau, L. M.; Zwanikken, J. W.; Mirkin, C. A.; Olvera de la Cruz, M.; Bedzyk, M. J., Electrolyte-Mediated Assembly of Charged Nanoparticles. *ACS Cent Sci* **2016,** *2* (4), 219-24.
194. Wittemann, A.; Drechsler, M.; Talmon, Y.; Ballauff, M., High elongation of polyelectrolyte chains in the osmotic limit of spherical polyelectrolyte brushes: A study by cryogenic transmission electron microscopy. *Journal of the American Chemical Society* **2005,** *127* (27), 9688-9689.
195. Li, Y.; Girard, M.; Shen, M.; Millan, J. A.; Olvera de la Cruz, M., Strong attractions and repulsions mediated by monovalent salts. *Proceedings of the National Academy of Sciences* **2017,** *114* (45), 11838-11843.

196. Jiménez-Ángeles, F.; Odriozola, G.; Lozada-Cassou, M., Electrolyte distribution around two like-charged rods: Their effective attractive interaction and angular dependent charge reversal. *The Journal of Chemical Physics* **2006,** *124* (13), 134902.
197. Qiao, B.; Jiménez-Ángeles, F.; Nguyen, T. D.; Olvera de la Cruz, M., Water follows polar and nonpolar protein surface domains. *Proc Natl Acad Sci U S A* **2019,** *116* (39), 19274-19281.
198. Jiménez-Ángeles, F.; Firoozabadi, A., Hydrophobic Hydration and the Effect of NaCl Salt in the Adsorption of Hydrocarbons and Surfactants on Clathrate Hydrates. *ACS Cent Sci* **2018,** *4* (7), 820-831.
199. Kirkwood, J. G., Statistical Mechanics of Fluid Mixtures. *The Journal of Chemical Physics* **1935,** *3* (5), 300-313.
200. Frenkel, D., *Understanding molecular simulation : from algorithms to applications*. Second edition. San Diego, Calif. ; London : Academic, [2002] ©2002: 2002.
201. Brooks, B. R.; Brooks III, C. L.; Mackerell Jr, A. D.; Nilsson, L.; Petrella, R. J.; Roux, B.; Won, Y.; Archontis, G.; Bartels, C.; Boresch, S., CHARMM: the biomolecular simulation program. *Journal of computational chemistry* **2009,** *30* (10), 1545-1614.
202. Lee, J.; Cheng, X.; Swails, J. M.; Yeom, M. S.; Eastman, P. K.; Lemkul, J. A.; Wei, S.; Buckner, J.; Jeong, J. C.; Qi, Y., CHARMM-GUI input generator for NAMD, GROMACS, AMBER, OpenMM, and CHARMM/OpenMM simulations using the CHARMM36 additive force field. *Journal of chemical theory and computation* **2016,** *12* (1), 405-413.
203. Arnott, S.; Smith, P. C.; Chandrasekaran, R., Atomic coordinates and molecular conformations for DNA-DNA, RNA-RNA, and DNA-RNA helices. In *CRC Handbook of biochemistry and molecular biology*, CRC Press: 2019; pp 411-422.
204. Lipps, H. J.; Rhodes, D., G-quadruplex structures: in vivo evidence and function. *Trends in cell biology* **2009,** *19* (8), 414-422.
205. Karlin, K. D., Metalloenzymes, structural motifs, and inorganic models. *Science* **1993,** *261* (5122), 701-708.
206. Matsarskaia, O.; Roosen-Runge, F.; Schreiber, F., Multivalent ions and biomolecules: Attempting a comprehensive perspective. *ChemPhysChem* **2020,** *21* (16), 1742-1767.
207. Dudev, T.; Lim, C., Competition among metal ions for protein binding sites: determinants of metal ion selectivity in proteins. *Chemical reviews* **2014,** *114* (1), 538-556.
208. Weisbuch, G.; Gueron, M., Polyelectrolyte theory. 3. The surface potential in mixed-salt solutions. *The Journal of Physical Chemistry* **1981,** *85* (5), 517-525.
209. Rouzina, I.; Bloomfield, V. A., Competitive electrostatic binding of charged ligands to polyelectrolytes: practical approach using the non-linear Poisson-Boltzmann equation. *Biophysical chemistry* **1997,** *64* (1-3), 139-155.
210. Bacquet, R. J.; Rossky, P. J., Ionic distributions and competitive association in DNA/mixed salt solutions. *The Journal of Physical Chemistry* **1988,** *92* (12), 3604-3612.
211. Raspaud, E.; De La Cruz, M. O.; Sikorav, J.-L.; Livolant, F., Precipitation of DNA by polyamines: a polyelectrolyte behavior. *Biophysical journal* **1998,** *74* (1), 381-393.
212. Braunlin, W.; Strick, T.; Record Jr, M., Equilibrium dialysis studies of polyamine binding to DNA. *Biopolymers: Original Research on Biomolecules* **1982,** *21* (7), 1301-1314.
213. Wang, X.; Spencer, H. G., Calcium alginate gels: formation and stability in the presence of an inert electrolyte. *Polymer* **1998,** *39* (13), 2759-2764.

214. Ben-Yaakov, D.; Andelman, D.; Podgornik, R.; Harries, D., Ion-specific hydration effects: Extending the Poisson-Boltzmann theory. *Current Opinion in Colloid & Interface Science* **2011,** *16* (6), 542-550.
215. Grochowski, P.; Trylska, J., Continuum molecular electrostatics, salt effects, and counterion binding—a review of the Poisson–Boltzmann theory and its modifications. *Biopolymers: Original Research on Biomolecules* **2008,** *89* (2), 93-113.
216. Yguerabide, J.; Yguerabide, E. E., Light-scattering submicroscopic particles as highly fluorescent analogs and their use as tracer labels in clinical and biological applications: II. Experimental characterization. *Analytical biochemistry* **1998,** *262* (2), 157-176.
217. Cutler, J. I.; Auyeung, E.; Mirkin, C. A., Spherical nucleic acids. *Journal of the American Chemical Society* **2012,** *134* (3), 1376-1391.
218. Hyde, A. M.; Zultanski, S. L.; Waldman, J. H.; Zhong, Y.-L.; Shevlin, M.; Peng, F., General principles and strategies for salting-out informed by the Hofmeister series. *Organic Process Research & Development* **2017,** *21* (9), 1355-1370.
219. Skou, S.; Gillilan, R. E.; Ando, N., Synchrotron-based small-angle X-ray scattering of proteins in solution. *Nature protocols* **2014,** *9* (7), 1727-1739.
220. Acerbo, A. S.; Cook, M. J.; Gillilan, R. E., Upgrade of MacCHESS facility for X-ray scattering of biological macromolecules in solution. *Journal of synchrotron radiation* **2015,** *22* (1), 180-186.
221. Hopkins, J. B.; Gillilan, R. E.; Skou, S., BioXTAS RAW: improvements to a free open-source program for small-angle X-ray scattering data reduction and analysis. *Journal of applied crystallography* **2017,** *50* (5), 1545-1553.
222. Hansen, J.-P.; Verlet, L., Phase transitions of the Lennard-Jones system. *physical Review* **1969,** *184* (1), 151.
223. Yang, W. H.; Schatz, G. C.; Van Duyne, R. P., Discrete dipole approximation for calculating extinction and Raman intensities for small particles with arbitrary shapes. *The Journal of chemical physics* **1995,** *103* (3), 869-875.
224. Finney, J., Random packings and the structure of simple liquids. I. The geometry of random close packing. *Proceedings of the Royal Society of London. A. Mathematical and Physical Sciences* **1970,** *319* (1539), 479-493.
225. Sirota, E.; Ou-Yang, H.; Sinha, S.; Chaikin, P.; Axe, J.; Fujii, Y., Complete phase diagram of a charged colloidal system: A synchro-tron x-ray scattering study. *Physical review letters* **1989,** *62* (13), 1524.
226. Collins, K. D., The behavior of ions in water is controlled by their water affinity. *Q Rev Biophys* **2019,** *52*, e11.
227. McLAUGHLIN, S.; Mulrine, N.; Gresalfi, T.; Vaio, G.; McLAUGHLIN, A., Adsorption of divalent cations to bilayer membranes containing phosphatidylserine. *The Journal of general physiology* **1981,** *77* (4), 445-473.
228. Perez-Martinez, C. S.; Smith, A. M.; Perkin, S., Underscreening in concentrated electrolytes. *Faraday discussions* **2017,** *199*, 239-259.
229. Andresen, K.; Das, R.; Park, H. Y.; Smith, H.; Kwok, L. W.; Lamb, J. S.; Kirkland, E.; Herschlag, D.; Finkelstein, K.; Pollack, L., Spatial distribution of competing ions around DNA in solution. *Physical review letters* **2004,** *93* (24), 248103.
230. Arakawa, T.; Timasheff, S. N., Theory of Protein Solubility. *Method Enzymol* **1985,** *114*, 49-77.

231. Wolf, B.; Hanlon, S., Structural transitions of deoxyribonucleic acid in aqueous electrolyte solutions. II. Role of hydration. *Biochemistry* **1975,** *14* (8), 1661-1670.
232. Ma, C. Y.; Pezzotti, S.; Schwaab, G.; Gebala, M.; Herschlag, D.; Havenith, M., Cation enrichment in the ion atmosphere is promoted by local hydration of DNA. *Physical Chemistry Chemical Physics* **2021,** *23* (40), 23203-23213.
233. Bloomfield, V. A., DNA condensation by multivalent cations. *Biopolymers: Original Research on Biomolecules* **1997,** *44* (3), 269-282.
234. Hanke, M.; Hansen, N.; Chen, R.; Grundmeier, G.; Fahmy, K.; Keller, A., Salting-out of DNA origami nanostructures by ammonium sulfate. *International Journal of Molecular Sciences* **2022,** *23* (5), 2817.
235. Giubertoni, G.; Bonn, M.; Woutersen, S., D2O as an Imperfect Replacement for H2O: Problem or Opportunity for Protein Research? *The Journal of Physical Chemistry B* **2023,** *127* (38), 8086-8094.
236. Zhou, W.; Saran, R.; Liu, J., Metal sensing by DNA. *Chemical reviews* **2017,** *117* (12), 8272-8325.
237. Liang, H.; Zhang, X.-B.; Lv, Y.; Gong, L.; Wang, R.; Zhu, X.; Yang, R.; Tan, W., Functional DNA-containing nanomaterials: cellular applications in biosensing, imaging, and targeted therapy. *Accounts of chemical research* **2014,** *47* (6), 1891-1901.
238. Nordstrom, L. J.; Clark, C. A.; Andersen, B.; Champlin, S. M.; Schwinefus, J. J., Effect of ethylene glycol, urea, and N-methylated glycines on DNA thermal stability: the role of DNA base pair composition and hydration. *Biochemistry* **2006,** *45* (31), 9604-9614.
239. Del Vecchio, P.; Esposito, D.; Ricchi, L.; Barone, G., The effects of polyols on the thermal stability of calf thymus DNA. *International journal of biological macromolecules* **1999,** *24* (4), 361-369.
240. McDuffie Jr, G.; Quinn, R.; Litovitz, T., Dielectric properties of glycerol—Water mixtures. *The Journal of Chemical Physics* **1962,** *37* (2), 239-242.
241. Hayashi, Y.; Katsumoto, Y.; Omori, S.; Kishii, N.; Yasuda, A., Liquid structure of the urea− water system studied by dielectric spectroscopy. *The Journal of Physical Chemistry B* **2007,** *111* (5), 1076-1080.
242. Roundy, D.; Rogers, M., Exploring the thermodynamics of a rubber band. *American Journal of Physics* **2013,** *81* (1), 20-23.
243. Callister, W. D.; Rethwisch, D. G.; Blicblau, A.; Bruggeman, K.; Cortie, M.; Long, J.; Hart, J.; Marceau, R.; Mitchell, R., *Materials science and engineering: an introduction*. John wiley & sons New York: 2007; Vol. 7.
244. Miller, W.; Smith, C.; Mackenzie, D.; Evans, K., Negative thermal expansion: a review. *Journal of materials science* **2009,** *44*, 5441-5451.
245. Rechtsman, M. C.; Stillinger, F. H.; Torquato, S., Negative thermal expansion in single-component systems with isotropic interactions. *The Journal of Physical Chemistry A* **2007,** *111* (49), 12816-12821.
246. Kim, H. J.; Wang, W. J.; Mallapragada, S.; Travesset, A.; Vaknin, D., Nanoparticle Superlattices with Negative Thermal Expansion (NTE) Coefficients. *J Phys Chem C* **2021,** *125* (18), 10090-10095.
247. Clark, E.; Lipson, J., LCST and UCST behavior in polymer solutions and blends. *Polymer* **2012,** *53* (2), 536-545.

248. Alberti, S.; Gladfelter, A.; Mittag, T., Considerations and challenges in studying liquid-liquid phase separation and biomolecular condensates. *Cell* **2019,** *176* (3), 419-434.
249. Pullara, P.; Alshareedah, I.; Banerjee, P. R., Temperature-dependent reentrant phase transition of RNA–polycation mixtures. *Soft Matter* **2022,** *18* (7), 1342-1349.
250. Merindol, R.; Loescher, S.; Samanta, A.; Walther, A., Pathway-controlled formation of mesostructured all-DNA colloids and superstructures. *Nat Nanotechnol* **2018,** *13* (8), 730-+.
251. Jin, R.; Wu, G.; Li, Z.; Mirkin, C. A.; Schatz, G. C., What controls the melting properties of DNA-linked gold nanoparticle assemblies? *Journal of the American Chemical Society* **2003,** *125* (6), 1643-1654.
252. Seuring, J.; Agarwal, S., Polymers with upper critical solution temperature in aqueous solution: Unexpected properties from known building blocks. ACS Publications: 2013.
253. Ermoshkin, A.; Kudlay, A.; Olvera de La Cruz, M., Thermoreversible crosslinking of polyelectrolyte chains. *The Journal of chemical physics* **2004,** *120* (24), 11930-11940.
254. Jia, X.; Chen, D.; Jiang, M., Preparation of PEO-b-P2VPH+–S 2 O 8 2− micelles in water and their reversible UCST and redox-responsive behavior. *Chem Commun* **2006,** (16), 1736-1738.
255. Saeki, S.; Kuwahara, N.; Nakata, M.; Kaneko, M., Upper and lower critical solution temperatures in poly (ethylene glycol) solutions. *Polymer* **1976,** *17* (8), 685-689.
256. Huffman, A. S.; Afrassiabi, A.; Dong, L. C., Thermally reversible hydrogels: II. Delivery and selective removal of substances from aqueous solutions. *Journal of controlled release* **1986,** *4* (3), 213-222.
257. Dormidontova, E. E., Role of competitive PEO− water and water− water hydrogen bonding in aqueous solution PEO behavior. *Macromolecules* **2002,** *35* (3), 987-1001.
258. Huddleston, J. G.; Willauer, H. D.; Rogers, R. D., Phase diagram data for several PEG+ salt aqueous biphasic systems at 25 C. *Journal of Chemical & Engineering Data* **2003,** *48* (5), 1230-1236.
259. Zavitsas, A. A., Aqueous solutions of calcium ions: hydration numbers and the effect of temperature. *The Journal of Physical Chemistry B* **2005,** *109* (43), 20636-20640.
260. Yang, T.; Luo, Z.; Tian, Y.; Qian, C.; Duan, Y., Design strategies of AuNPs-based nucleic acid colorimetric biosensors. *TrAC Trends in Analytical Chemistry* **2020,** *124*, 115795.
261. Park, S. Y.; Lytton-Jean, A. K.; Lee, B.; Weigand, S.; Schatz, G. C.; Mirkin, C. A., DNA-programmable nanoparticle crystallization. In *Spherical Nucleic Acids*, Jenny Stanford Publishing: 2020; pp 515-525.
262. Srivastava, A.; Timsina, R.; Heo, S.; Dewage, S. W.; Kirmizialtin, S.; Qiu, X., Structure-guided DNA–DNA attraction mediated by divalent cations. *Nucleic Acids Res* **2020,** *48* (13), 7018-7026.
263. Kelly, K. L.; Coronado, E.; Zhao, L. L.; Schatz, G. C., The optical properties of metal nanoparticles: the influence of size, shape, and dielectric environment. ACS Publications: 2003; Vol. 107, pp 668-677.
264. Lee, J.; Lee, S., Non-invasive, reliable, and fast quantification of DNA loading on gold nanoparticles by a one-step optical measurement. *Analytical chemistry* **2023,** *95* (3), 1856-1866.
265. Jishkariani, D.; Diroll, B. T.; Cargnello, M.; Klein, D. R.; Hough, L. A.; Murray, C. B.; Donnio, B., Dendron-Mediated Engineering of Interparticle Separation and Self-Assembly in Dendronized Gold Nanoparticles Superlattices. *Journal of the American Chemical Society* **2015,** *137* (33), 10728-10734.

266. Shevchenko, E. V.; Talapin, D. V.; Kotov, N. A.; O'Brien, S.; Murray, C. B., Structural diversity in binary nanoparticle superlattices. *Nature* **2006,** *439* (7072), 55-59.
267. Macfarlane, R. J.; Lee, B.; Jones, M. R.; Harris, N.; Schatz, G. C.; Mirkin, C. A., Nanoparticle Superlattice Engineering with DNA. *Science* **2011,** *334* (6053), 204-208.
268. Auer, S.; Frenkel, D., Suppression of crystal nucleation in polydisperse colloids due to increase of the surface free energy. *Nature* **2001,** *413* (6857), 711-713.
269. Macfarlane, R. J.; Jones, M. R.; Senesi, A. J.; Young, K. L.; Lee, B.; Wu, J.; Mirkin, C. A., Establishing the design rules for DNA-mediated programmable colloidal crystallization. *Angew Chem Int Ed Engl* **2010,** *49* (27), 4589-92.
270. Pusey, P. N.; Vanmegen, W.; Bartlett, P.; Ackerson, B. J.; Rarity, J. G.; Underwood, S. M., Structure of Crystals of Hard Colloidal Spheres. *Physical Review Letters* **1989,** *63* (25), 2753-2756.
271. Wilson, A. J. C.; Bradley, A. J., Imperfections in the structure of cobalt II. Mathematical treatment of proposed structure. *Proceedings of the Royal Society of London. Series A. Mathematical and Physical Sciences* **1942,** *180* (982), 277-285.
272. Rumble, J. R. B. T. J. D. M. J., *CRC handbook of chemistry and physics : a ready-reference book of chemical and physical data*. 2021.
273. Raspaud, E.; Pelta, J.; De Frutos, M.; Livolant, F., Solubility and charge inversion of complexes of DNA and basic proteins. *Physical review letters* **2006,** *97* (6), 068103.
274. Liu, J.; Makowski, L., Scanning x-ray microdiffraction: In situ molecular imaging of tissue and materials. *Current Opinion in Structural Biology* **2022,** *75*, 102421.
275. Um, S. H.; Lee, J. B.; Park, N.; Kwon, S. Y.; Umbach, C. C.; Luo, D., Enzyme-catalysed assembly of DNA hydrogel. *Nat Mater* **2006,** *5* (10), 797-801.
276. Tsai, D.-H.; Cho, T. J.; DelRio, F. W.; Gorham, J. M.; Zheng, J.; Tan, J.; Zachariah, M. R.; Hackley, V. A., Controlled formation and characterization of dithiothreitol-conjugated gold nanoparticle clusters. *Langmuir* **2014,** *30* (12), 3397-3405.